


This item was submitted to Loughborough University as a PhD thesis by the author and is made available in the Institutional Repository (<https://dspace.lboro.ac.uk/>) under the following Creative Commons Licence conditions.




CC creative commons
COMMONS DEED


Attribution-NonCommercial-NoDerivs 2.5


You are free:

- to copy, distribute, display, and perform the work

Under the following conditions:

 **Attribution.** You must attribute the work in the manner specified by the author or licensor.

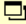
 **Noncommercial.** You may not use this work for commercial purposes.

 **No Derivative Works.** You may not alter, transform, or build upon this work.

- For any reuse or distribution, you must make clear to others the license terms of this work.
- Any of these conditions can be waived if you get permission from the copyright holder.

Your fair use and other rights are in no way affected by the above.

This is a human-readable summary of the [Legal Code \(the full license\)](#).

[Disclaimer](#) 

For the full text of this licence, please go to:
<http://creativecommons.org/licenses/by-nc-nd/2.5/>

BLDSC no :- DX 90199

LOUGHBOROUGH
UNIVERSITY OF TECHNOLOGY
LIBRARY

AUTHOR/FILING TITLE

WALSH, T J

ACCESSION/COPY NO.

040015551

VOL. NO.

CLASS MARK

- 9 JAN 1998

14 MAR 2000

- 2 NOV 1998

14 APR 2000

- 8 DEC 1998

2-15 JAN 1999

- 10 FEB 1999

- 1 MAR 1999

040015551 6



Capillary Properties of Model Pores

by

Tim J Walsh

A Doctoral Thesis

Submitted in partial fulfilment of the requirements
for the award of
Doctor of Philosophy of the Loughborough University of Technology

1 August 1989

© by T. J. Walsh, 1989

Loughborough University of Technology Library	
Date	Jan 90
Class	
Acc. No.	040015551

Abstract

Liquid menisci in small pores exhibit a curved surface across which there is a significant pressure difference. The capillary properties of such surfaces are important in many areas of science and technology. Pores of uniform section can be broadly classified according to whether the perimeter is smooth (as in cylindrical tubes) or angular (as in triangular tubes). A meniscus that is entirely bounded by the pore walls has a curvature that is inversely proportional to the tubes' hydraulic radius. A meniscus in an angular tube, however, has liquid wedges in the corners and this reduces the effective area of the pore. In the past it has been difficult to calculate the curvatures, of this class of menisci. Some recent studies have shown that a relatively straightforward, but hitherto neglected, method originated by Mayer & Stowe (1965) and Princen (1969a) can be applied to analyse wedging menisci. However, the method has lacked a comprehensive experimental verification.

This investigation follows on from the previously limited studies. A standardised method for the application of the analysis is described, the results from which are compared to observations made using modified experimental procedures. The behaviour of the capillary surfaces formed in several model pores are analysed with the method. The model systems studied are rectangular ducts, the pores formed by a rod in an angled corner, by two contacting rods and a plate and the space between a rod and a plate. For the latter two shapes the analysis is extended to include systems of mixed wettability which have a particular bearing on enhanced oil recovery operations. Experiments in which curvatures are inferred from observations of capillary rise, are performed using two comparative techniques. An involved procedure confirms predictions of meniscus curvature to within 0.3%. Use of a more straightforward, though less accurate, technique enables variations of curvature with tube shape or contact angle(s) to be conveniently studied. Results obtained are excellent and confirm the theory within the determined experimental errors.

In addition the analysis has been extended to predict more complex meniscus behaviour. The tubular space formed by three rods and a plate gives rise to a whole family of meniscus shapes. With certain geometries a capillary surface regards the tube as a pore doublet where the behaviour in one neighbouring pore depends on that in the other. The capillary properties of this model system shed light on the behaviour of adjacent pores in a porous medium undergoing drainage (or desorption). Experiments show excellent agreement with predictions of meniscus shapes, curvatures and, most interestingly, points of spontaneous transition from one meniscus shape to another. The system also has a potential future application because one particular arrangement of rods produces a meniscus with a curvature virtually independent of the geometry. This makes it suitable for producing a standard meniscus of known curvature.

Acknowledgements

I am greatly indebted to my Supervisor, Geoff Mason, for convincing me to stay on and write up this work. My thanks for his understanding and valued help during the last three years. I would like to express my gratitude to Brian Buffham, my Director of Research, and Brian Brooks, the Head of the Department.

Thanks also to Jack Burton who's excellent and precise machining of apparatus has enabled such accurate results to be presented here.

My family provided much needed encouragement and support for which I am very grateful. Thanks go particularly to my mother who helped me in the latter stages of the preparation of this manuscript.

My thanks to the lecturers, staff, fellow research students and secretaries in the department who have all helped to make my time in Loughborough so rewarding.

Contents

Abstract	ii
Acknowledgements	iii
Certificate of Originality	iv
Chapter 1 Introduction	1
Chapter 2 Chemistry of Interfaces	6
2.1 Introduction	6
2.2 Surface tension	6
2.3 Thermodynamic description of an interface	7
2.3.1 The interface	7
2.3.2 Interfacial tension at a plane interface	8
2.3.3 Free energy of an interface	10
2.4 Liquid interfaces	11
2.4.1 The Laplace equation	11
2.4.2 The Kelvin equation	15
2.4.3 Capillary rise and surface tension measurement	16
2.5 Solid surfaces	22
2.5.1 The solid surface	22
2.5.2 Surface roughness	23
2.5.3 Other surface defects	24
2.6 The solid/gas interface (adsorption of gases)	25
2.6.1 Adsorption Isotherms	26
2.7 The solid/liquid interface	27
2.7.1 Free energy of fluid interfaces bound by a solid	28
2.7.2 Wetting	29
2.7.3 Contact Angle	30
2.7.4 The Gauss equation of capillarity	31
2.7.5 Spreading and Contact Angle	32
2.7.6 Contact Angle Hysteresis	34
2.7.6.1 Wenzel's theory	36

2.7.6.2 Cassie's theory	37
2.7.7 The measurement of contact angles	40
2.8 Summary	41
Chapter 3 Porous Materials	42
3.1 Introduction	42
3.2 Characterisation of porous materials	43
3.2.1 Classification by pore size	45
3.2.2 Porosity	46
3.2.3 Saturation and saturation states	46
3.2.4 Capillary pressure curves	46
3.2.4.1 General form of capillary pressure data	48
3.2.4.2 The pF scale	49
3.2.5 Adsorption-desorption pressure curves	50
3.3 Models of the pore space	50
3.3.1 Classification of pore space models	51
3.4 Models of interfacial configurations	52
3.4.1 Hydraulic radius models	54
3.4.2 The Haines incircle approximation	54
3.4.3 The Mayer & Stowe - Princen analysis	55
3.4.4 The Dodds approximation	56
3.5 Hysteresis in porous materials	57
3.5.1 Contact angle hysteresis and one dimensional models	57
3.5.1.1 Porosimetry	58
3.5.1.2 Kelvin analysis	59
3.5.1.3 Thermoporometry	59
3.5.1.4 The Leverett j-function	60
3.5.2 Independent behaviour and zero dimensional models	62
3.5.2.1 The ink bottle effect	62
3.5.2.2 The Independent Domain Theory	64
3.5.3 Dependent behaviour and two and three dimensional models	65
3.6 Summary	67
Chapter 4 Interfacial configurations	68
4.1 Introduction	68
4.2 Classification of interfacial configurations	70
4.3 Review of past solutions	71
4.3.1 Axisymmetric interfaces	71
4.3.1.1 Surfaces bound by uniform geometry	71

4.3.1.2 Surfaces bound by converging-diverging geometry	73
4.3.2 Non-axisymmetric interfaces	74
4.3.2.1 Surfaces bound by uniform geometry	74
4.3.2.2 Surfaces bounded by converging-diverging geometry	78
4.4 Summary	78
Chapter 5 Review of past applications of the MS-P method	80
5.1 Introduction	80
5.2 Mercury porosimetry	80
5.2.1 Mayer & Stowe's study	80
5.2.2 Further studies	82
5.3 Capillary rise	83
5.3.1 Princen's studies	83
5.3.2 Studies of Mason & co-workers	85
5.4 Fluid/fluid displacement	87
5.5 Summary	89
Chapter 6 Theory and analytical procedures	90
6.1 Introduction	90
6.2 Terminology	91
6.3 The Mayer & Stowe - Princen theory	94
6.3.1 Curvature calculation for non-wedging systems	94
6.3.1.1 Energy balance approach	95
6.3.1.2 Force balance approach	96
6.3.1.3 Derivation from the Gauss equation	96
6.3.2 Curvature in wedging systems: the MS-P equation	97
6.3.2.1 Energy balance approach	98
6.3.2.2 Force balance approach	99
6.3.2.3 Derivation from the Gauss equation	100
6.4 Application of the MS-P equation	101
6.4.1 Analytical solutions	103
6.4.1.1 Equilateral triangle with a perfectly wetting liquid	103
6.4.1.2 n-agon tubes with variable wetting	105
6.4.2 Non-analytical solutions	106
6.4.2.1 Microcomputer solution technique	108
Chapter 7 Experimental apparatus and procedures	113
7.1 Introduction	113
7.2 Apparatus	114

7.2.1 General description	114
7.2.2 Cell design	114
7.2.3 The cathetometer	118
7.2.4 Slate-topped concrete bench and pillar	119
7.2.5 Pore construction components	119
7.2.5.1 HSS drill blanks	120
7.2.5.2 Needle rollers	121
7.2.5.3 Teflon rods	121
7.2.5.4 Spacers	122
7.3 The test liquids.	122
7.3.1 Perfectly wetting experiments	122
7.3.2 Non-zero contact angle experiments	122
7.4 Experimental procedure	123
7.4.1 General considerations	124
7.4.2 Selection of rods	124
7.4.3 Cell assembly	125
7.4.4 Arrangement of apparatus	125
7.4.5 Measurement of capillary rise	125
7.5 Determination of curvatures	128
7.6 Meniscus configurations investigated	130
Chapter 8 Curvatures in the standard configurations	131
8.1 Introduction	131
8.2 Experimental	132
8.2.1 Determination of curvatures	134
8.3 Results	135
8.3.1 The basic findings	135
8.3.2. Analysis of results	138
8.3.2.1 Gravitational distortion of menisci	139
8.3.2.2 Dimensional errors	148
8.3.2.3 Other systematic errors	148
8.3.3 Comparison of results with Mason et al's studies	149
8.3.4 Bearing on the general experimental method	150
Chapter 9 Investigations under perfectly wetting conditions	152
9.1 Introduction	152
9.2 Rectangular ducts	153
9.2.1 Theory	153
9.2.2 Experimental	156

9.2.2.1 Cell design	157
9.2.2.2 Determination of aspect ratio.	159
9.2.3 Results	159
9.3 One rod away from a plate	162
9.3.1 Theory	162
9.3.2 Experimental	164
9.3.2.1 Cell design	164
9.3.2.2 Cell assembly	166
9.3.2.3 Point of measurement of height of rise	167
9.3.3. Results	167
9.4 One rod in a corner	170
9.4.1 Theory	170
9.4.3 Experimental	172
9.4.3.1 Cell design	173
9.4.3.2 Measurement of corner angle	173
9.4.4 Results	175
9.5 Two unequal rods and a plate	178
9.5.1. Theory	179
9.5.2 Experimental	181
9.5.2.1 Cell assembly	182
9.5.3 Results	182
Chapter 10 Investigations with non-zero contact angle	184
10.1 Introduction	184
10.2 One rod away from a plate	185
10.2.1 Theory	185
10.2.2 Experimental	188
10.2.2.1 Cell assembly	189
10.2.2.2 Measurement of capillary rise	189
10.2.3 Results	192
10.3 Two equal rods and a plate	195
10.3.1 Theory	195
10.3.2 Experimental	198
10.3.3 Results	200
Chapter 11 Investigations with neighbours - three rods and a plate	205
11.1 Introduction	205
11.2 Theory	205
11.2.1 Analysis for effective areas and perimeters	209

11.2.2 Solution of equations	219
11.3 Experimental	221
11.3.1 Cell design	222
11.3.1.1 Intermediate and low ϕ design	222
11.3.1.2 High ϕ design	223
11.3.2 Measurement of half angle	225
11.3.3 Point of measurement of height of rise	226
11.4 Results	228
11.4.1 Three equal rods	228
11.4.2 Unequal rods symmetrically arranged	232
11.4.3 Unequal rods non-symmetrically arranged	235
11.4.4 General observations	237
Chapter 12 Principal findings, further work and conclusions	240
12.1 Application of the MS-P theory	240
12.2 Experimental apparatus and procedures	241
12.3 Standard configurations and the full comparative method	242
12.4 Investigations with the simplified comparative method	243
12.4.1 Perfectly wetting conditions	243
12.4.2 Non-zero contact angle	244
12.4.3 Investigations with neighbours	246
12.5 Further work	246
12.6 Conclusions	247
Bibliography	249
Nomenclature	255
Appendices	258

CHAPTER 1

Introduction

The phenomenon of the capillary rise of liquids in cylindrical tubes is familiar to school pupils everywhere. The simple school physics experiments illustrate only a small part a broad and sometimes complex science called *capillarity*. The study of capillarity originates in the earliest days of modern science and many eminent pioneering scientists have been involved in its development. Leonardo da Vinci is known to have observed capillary rise in the 15th century and the equations for rise in cylindrical tubes were known before the 18th century, but it was in the 19th century that the fundamental relationships were proposed in general form by, amongst others, Laplace, Gauss, Young, Lord Kelvin and Gibbs - all now famous names.

Derived from the Latin for hair, the term capillarity encompasses a wide subject area concerning fluid interfaces. Studies are performed in all the major scientific disciplines by chemists, physicists, mathematicians, biologists and engineers. Applications are also diverse; detergency, oil recovery, soil studies, the waterproofing of fabrics and even the design of storage tanks for spacecraft are but a few examples. Although there is no strict definition, capillarity can be said to concern the properties of systems having at least two fluid phases separated by an interface. Usually one or more solid surfaces bounds the interface.

A liquid interface in a capillary or pore normally exhibits a curved surface, or meniscus, across which there is a pressure difference. This pressure difference, usually called the capillary pressure, is proportional to the curvature of the surface and the interfacial, or surface, tension between the two phases comprising the interface. For a given tube shape and wetting condition, or contact angle, the mean curvature varies inversely with tube size. These relations are central to methods of interfacial tension and contact angle measurement and are also used to determine other liquid properties such as the solderability of metals and alloys.

Today the most important area for the application of capillarity is in the study of porous materials, of which there are many occurring naturally in the environment. In addition there are numerous synthetic media employed by modern technology. A large economic stimulus for research in the area has arisen from the need to develop enhanced oil recovery (EOR) techniques. The properties of a porous material that is partially saturated with a liquid are dominated by the behaviour of the liquid menisci in the pore space. The basic equations of capillarity are also used in characterising a porous material by processes such as mercury-intrusion porosimetry or the desorption of capillary

condensed gases because they relate the capillary pressure measured across an interface to the size of a model pore; the actual pore shapes usually being irregular. Alternatively, the pore size and interfacial tension may be known and the capillary pressure may be the variable to be determined, as for example in two phase laminar flow or in predictions of the behaviour of blobs of crude oil when treated with surfactant.

In situations when gravity is not significant the solution of the fundamental equations of capillarity is fairly straightforward as a meniscus will have constant mean curvature, but their applications have been restricted due to difficulties in obtaining solutions for particular geometries and contact angles. In the applications mentioned above a pore is frequently assumed to have a circular cross-section so that the curvature of the menisci contained in the pores may be easily deduced. If the pore geometry is obviously more complex, for example of converging-diverging section (akin to an egg timer's shape - see Figure 1.1), simple approximations are usually used for the curvature. An example is the well known Haines incircle approximation.

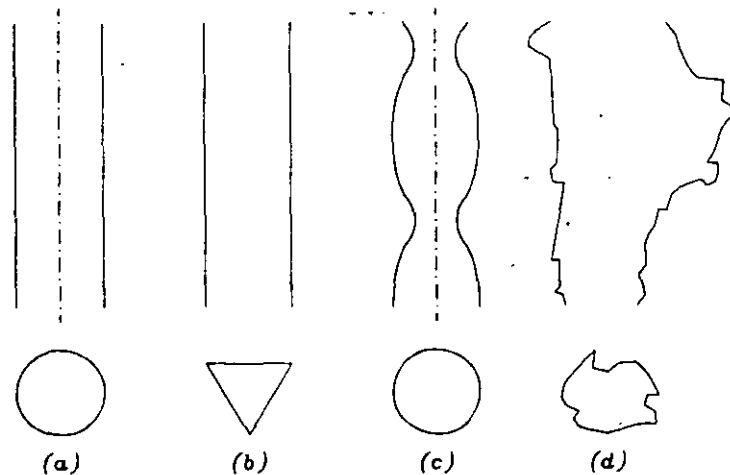


Figure 1.1 - Classification of tube shapes. (a) A cylindrical tube; uniform and axisymmetric. (b) A triangular tube; an example of a uniform non-axisymmetric tube. (c) An "egg timer" like example of a converging-diverging axisymmetric tube. (d) An irregular tub of converging-diverging non-axisymmetric shape.

In fact the shape of a meniscus in a pore of non-circular section, such as that formed by contacting spheres, is quite complex. Mathematically the interface is one of constant mean curvature or, when gravity is important, one of minimum surface energy, which meets the boundary conditions. These boundary conditions are the solid geometry and the contact angle which the liquid makes with the solid. There have been many attempts to solve the basic equation to yield particular interfacial configurations. Almost all the past work has concentrated on the behaviour of axisymmetric drops and bubbles where the axis of symmetry greatly simplifies the problem to one that solves relatively easily with the use of numerical integration techniques.

Only recently, with the availability of powerful computers, have solutions been attempted for the more widespread non-axisymmetric surfaces (Fig. 1.1), but the systems investigated must be carefully selected and the solid surface must comprise simple geometric elements. The time involved in arriving at such solutions is still so great that it is not a convenient method to use on a regular basis. Much of the complexity in these solutions arises from considering the interfaces to be distorted by gravity, to be in converging-diverging and/or non-axisymmetric geometry. There is, however, a virtually neglected class of non-axisymmetric interfaces for which solutions can be relatively easily obtained if gravity effects are small - those in uniform non-axisymmetric tubes.

Examined in this thesis is a method first put forward by Mayer & Stowe (as it turns out, mistakenly) for pores formed by contacting spheres and subsequently, but independently, by Princen (correctly) for tubes given by parallel cylindrical rods. Unfortunately this method has remained largely unused since its inception primarily because no attempt was made by the authors to validate their theory by experiment, apart from a single experiment reported by Princen. In addition the authors also obscured the true usefulness of their analyses by applying them to inappropriate systems. The theories proposed by Mayer & Stowe and Princen, here referred to as the MS-P method, give identical results. Mayer & Stowe assumed their analysis was exact for the menisci between contacting spheres whereas it applies exactly to uniform tubes. Whilst subsequent studies have shown it to provide a useful approximation at zero contact angle, it can be expected that errors in calculated curvatures will increase significantly with increasing contact angle. Princen too hid the power and exactness of the method by applying it approximately to gravity distorted menisci, although he did apply the analysis to uniform geometries.

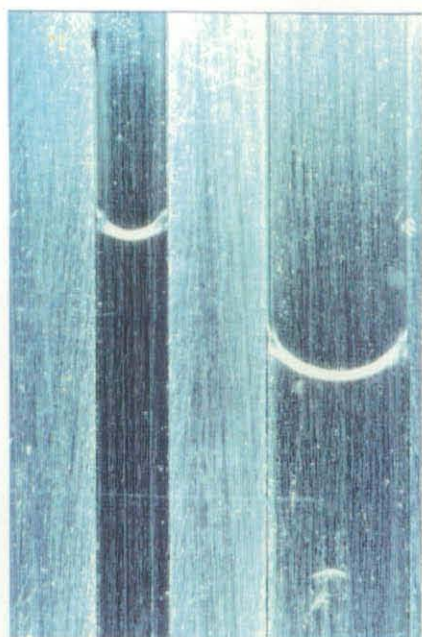
Although possible applications of the method were cited soon after Princen's work, its potential has remained unfulfilled. Only recently have attempts been made to test the theory and these only for relatively simple systems. However, the method is gradually finding more widespread applications. It was the objective of the work reported here to calculate the meniscus behaviour in some non-axisymmetric uniform pores and to test the validity of the theory's predictions. In addition the limited published work that involves the method will be brought together and further potential applications suggested.

Obtaining solutions with the MS-P method is relatively straightforward, but this does not mean that the meniscus behaviour is simple as it transpires that multiple solutions are possible. Some work on utilizing the method had already been conducted by the supervisor of this work, Mason, prior to the start of this investigation, establishing the basic principles of the experimental procedures and indicating the validity of the theory in the limited number of systems they studied. This study is a continuation of the work of Mason and co-workers, its purpose to confirm, and hopefully improve upon, past results and to extend the analyses to look at the effects on meniscus behaviour of both

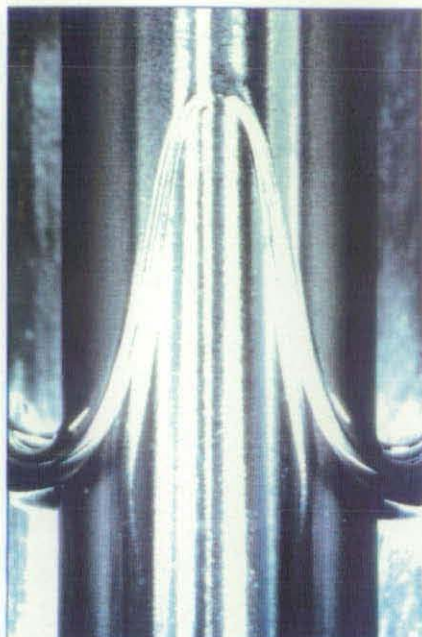
partial and mixed wettability and of interactions between neighbouring pores. Figure 1.2 shows some examples of the menisci investigated during the course of the study - the legend is given below *.

The structure of the thesis broadly follows that of the above outline. After a discussion of the relevant aspects of surface chemistry in which the fundamental equations of capillarity will be introduced, a brief overview is given of the most important area of application; porous materials. Attention will then turn to a review of alternative methods of interfacial configuration determination before the limited number of past investigations involving the MS-P method itself are discussed. The second part of the thesis is devoted to the application of the theory and its validation in specific systems. The investigative procedures are detailed before the particular experimental results are given. Conclusions will be drawn from these results.

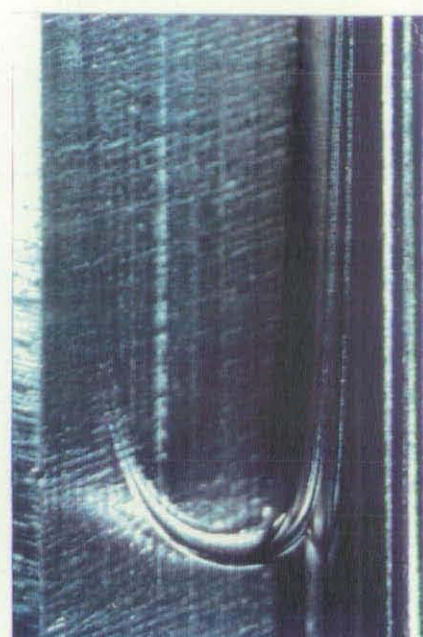
*Figure 1.2 - Menisci in uniform non-axisymmetric model pores. The photographs show the menisci formed when a wetting liquid, isooctane, undergoes capillary rise in the various tube shapes. (a) Rectangular ducts, high aspect ratio ($d/R = 5.14$ and 3.85 - *c.f.* section 9.2). (b) One rod away from a plate, low normalised spacing ($1/4$ " rod, 15 thou. shims $d/R = 0.06$ - *c.f.* section 9.3). (c) Rod in a 30° corner ($1/8$ " rod - *c.f.* section 9.4). (d) Two equal rods and a plate (2×3 mm rods - *c.f.* section 9.5). (e) Three unequal rods and a plate, symmetrically arranged, high half angle ($2 \times 1/16$ " + $1 \times 1/8$ " rods - see chapter 11). (f) Three equal rods and a plate, intermediate half angle ($3 \times 1/8$ " rods - see chapter 11). (g) - (i) Three unequal rods and a plate, non-symmetrically arranged, intermediate, high and very high halfangles ($2 \times 3/32$ " + $1 \times 3/64$ " rods - see chapter 11)



(a)



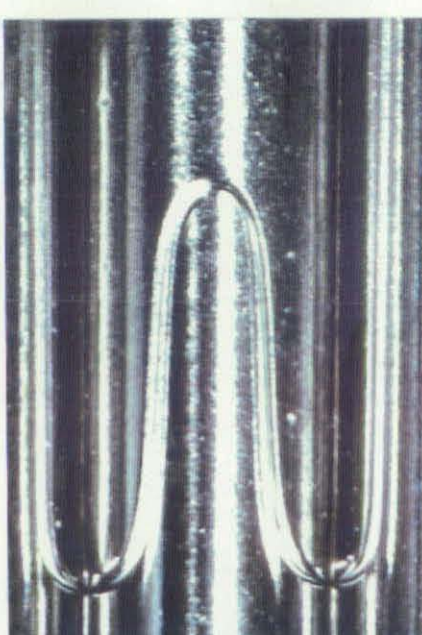
(b)



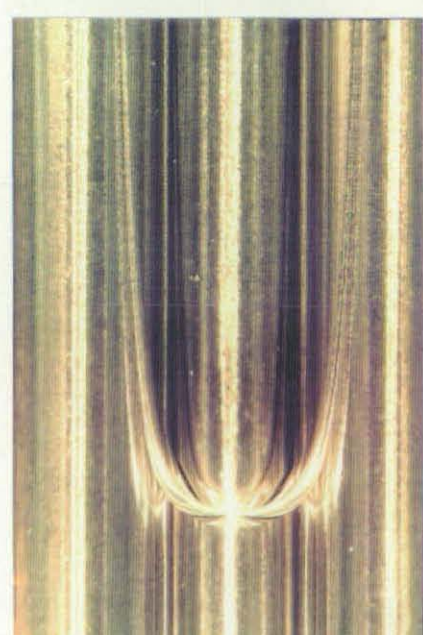
(c)



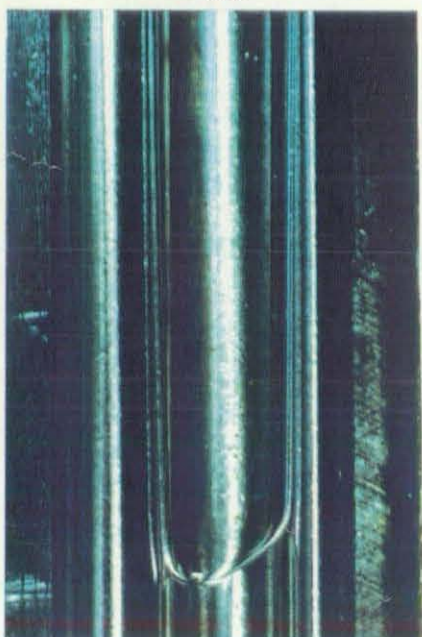
(d)



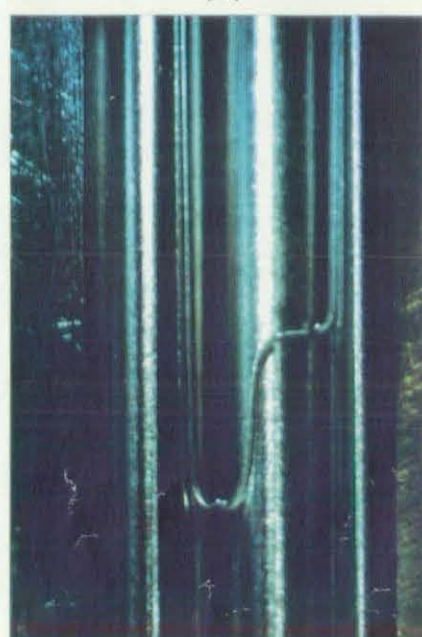
(e)



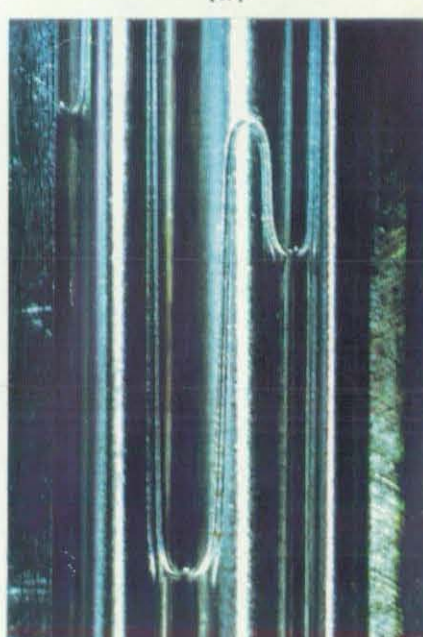
(f)



(g)



(h)



(i)

CHAPTER 2

Chemistry of interfaces

2.1 INTRODUCTION

The behaviour of fluids in a capillary or porous material, is essentially determined by interfaces between fluid and fluid; be it liquid/liquid or liquid/gas, and fluid and solid. It is a prerequisite of the idea of an "interface" to have "surfaces" which can come into contact.

Thomas Young (1805) and Josiah Gibbs (1872) introduced the fundamental concepts of surface chemistry. Young related the mechanical properties of the "surface" to those of a hypothetical stretched membrane, he described the tension in this "membrane" as the *surface tension*. Its position allowed a simple mechanical model to describe the complex region between two bulk phases in contact. In order to describe this region thermodynamically Gibbs conceived a two dimensional geometrical surface; the *Gibbs dividing surface*.

The developments of these two eminent scientists should not be underestimated just because they happened comparatively early in the history of modern science, before many of today's measuring techniques and the theories of molecular science were known. Other scientists of the nineteenth century involved in surface chemistry include the well known names of Laplace, Dupre, Rayleigh, Gauss, Poisson and Kelvin.

2.2 SURFACE TENSION

Nowadays with established theories of the molecular nature of liquids, surface tension can be more rigorously defined. Consider a drop of liquid surrounded by its vapour. A molecule in the interior of the liquid experiences the attraction of all the molecules around it. Due to the symmetry of attraction, there is no resultant force on the molecules in the bulk. In the surface the molecules are attracted more strongly by the dense liquid than the rare vapour. This difference in attraction causes the liquid to behave as though it were enclosed in Young's "stretched membrane". Work must be done to raise molecules to the boundary when the surface is extended. The work done against the molecular forces during this process is called the work required against surface tension.

The units of surface tension are force per unit length or energy per unit area. These are dimensionally identical. The energy units can be appreciated if surface tension is expressed as a measure of the free energy of a material in contact with its own vapour, hence the equivalent term of *surface free energy*. When a liquid is in contact with a substance other than its own vapour (a gas, immiscible liquid or a solid) the now interfacial free energy is called the *interfacial tension*.

The interchangeability of the two terms and their units can be illustrated by considering a soap film stretched over a wire frame as shown in Figure 2.1. If one end of the frame is mobile, as shown by the arrow, it will be noticed experimentally that there is a force acting in a direction opposite to the arrow. If the value of this force per unit length is denoted σ , the work done in extending the surface a distance, dx , is

$$W = \sigma dx = \sigma dA \quad (2.1)$$

where $dA = l dx$ and so denotes the change in area. Thus σ appears to be an energy per unit area. The usual units of ergs/cm² (SI J/m²) or dynes/cm (SI N/m) can thus be seen to be identical.

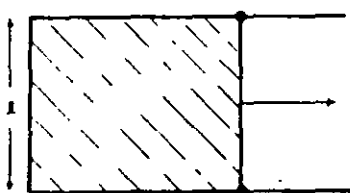


Figure 2.1 - Wire frame supporting a soap film.

2.3 THERMODYNAMIC DESCRIPTION OF AN INTERFACE

Gibbs' original thermodynamic treatment of interfaces has since been elucidated by van der Waals and Bakker, as discussed by Guggenheim (1967). Below the term "interface" is defined and some thermodynamics relevant to capillarity, to which reference will be made later, is given. A complete description of the thermodynamics of interfaces is not required here, but the interested reader may refer to Guggenheim's book.

2.3.1 The interface

The junction between two homogeneous bulk phases is often described as a two dimensional plane without thickness. Although this is a useful approximation for many calculations, the interface is in fact, a region between two phases where molecules of

each exist together. Across this region there is a gradual change in any thermodynamic property. Unless the two phases are completely miscible, the region's thickness is finite due to the limited range of the intermolecular forces. These interactions have been identified by Fowkes (1965) and include dispersion forces (London - van der Waals forces), hydrogen bonds, dipole - dipole interactions, π bonds, dipole induced dipole interactions, donor acceptor bonds and electrostatic interactions. Dispersion forces are usually dominant. Surface and interfacial tensions are direct measures of the intermolecular forces, which may extend over distances of 1 - 100 molecular diameters (Jaycock & Parfitt 1987) before behaviour reflects that of the bulk material.

An "interface" with both area and thickness should more properly be called an *interphase*, and this may exist in the solid, liquid or gaseous states. The term "surface" is usually only applied when one of the phases is a gas or a vapour. The interphase is imagined as being submicroscopic in thickness, about 1 to 10 nm (Jaycock & Parfitt 1987). However, it is common practice throughout the literature to use the terms interface and interphase (and sometimes surface) interchangeably and this convention is followed in the rest of this text.

Dupre (1869) developed the relationship between the interfacial tension and the individual surface tensions, which for a planar liquid/liquid interface is;

$$W_{L_1L_2} = \sigma_{L_1V} + \sigma_{L_2V} - \sigma_{L_1L_2} \quad (2.2)$$

where

$W_{L_1L_2}$	=	work of adhesion
σ_{L_1V}	=	surface tension of liquid 1
σ_{L_2V}	=	surface tension of liquid 2
$\sigma_{L_1L_2}$	=	interfacial tension

The work of adhesion may be visualised as the amount of work required to separate unit area of interface between liquids L_1 and L_2 . A sign convention is adopted such that when work is done on the system it is positive. Thus when new surface is created, energy is consumed and when interface area is decreased, energy is released.

2.3.2 Interfacial tension at a plane interface

Consider two homogeneous bulk phases, α and β , separated by an interfacial layer, s , (Fig. 2.2). The boundary between the interphase and bulk phase α is AA' and that between the interphase and phase β is BB' .

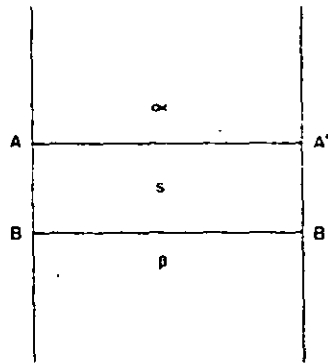


Figure 2.2 - Definition of an interphase.

The properties of the plane interphase are assumed to be uniform in any plane parallel to AA' or BB' , but not in any other plane in the interphase. At or near the plane AA' the properties of s are identical with those of α . Moving from AA' to BB' represents a gradual change in the properties of the interphase, from those of α to those of β .

The interphase described may be treated as a thermodynamic system, either *open* or in certain cases *closed*. A thermodynamic system is defined as open if both energy and matter may be transferred across the boundaries of that system. It is closed if no matter is allowed to move across the boundary.

The thermodynamics of an interphase differ from those of a bulk phase in that work must be done against interfacial tension. In the bulk phase the force across any unit area is equal in all directions, as is the pressure, but in the interphase the force is not the same in all directions.

If a plane is chosen perpendicular to AA' then the situation is different from that in the bulk phase. Let this plane be represented by a rectangle of height τ , the thickness of the interphase (AB), and of length, l , perpendicular to the plane of the diagram. The force across this plane will be equal to

$$P\tau l - \sigma l$$

The difference in sign being the difference between the work done on the system by the pressure, P , and the work done by the system against the interfacial tension forces. The interfacial volume, V , is defined as

$$V = \tau A$$

where A is the interfacial area. If the thickness is increased by $d\tau$, the area by dA and the volume by dV with the material content remaining unaltered then the work done on the interphase across the planes AA' and BB' is $-PA d\tau$. The work done by forces parallel to the planes AA' and BB' is independent of the shape of the perimeter, which can for

simplicity be assumed to be a rectangle. Consequently the work done on the interphase by the latter forces is $-(P\tau - \sigma)dA$ and the total work done, dW , is given by the sum

$$\begin{aligned} dW &= -PA d\tau - (P\tau - \sigma)dA \\ &= -P(A d\tau + \tau dA) + \sigma dA \\ &= -PdV + \sigma dA \end{aligned} \quad (2.3)$$

Equation 2.3 is the analogous work term for an interphase which corresponds to the three dimensional $-PdV$ for a bulk phase.

2.3.3 Free energy of an interface

a) Closed systems

Consider a closed planar interface that is of fixed composition with σ , the interfacial tension (or tangential stress), as an intensive variable (as are for example temperature and pressure). Introducing the first law of thermodynamics through the equation

$$dU = dQ + dW \quad (2.4)$$

and the second law through

$$dQ_{reversible} = TdS \quad (2.5)$$

Combining equation 2.3 with the above yields

$$dU = TdS - PdV + \sigma dA \quad (2.6)$$

The usual thermodynamic function definitions are:

$$\text{enthalpy} \quad H = U + PV \quad (2.7)$$

$$\text{free energy} \quad F = U - TS \quad (2.8)$$

$$\text{Gibbs free energy} \quad G = H - TS = U + PV - TS \quad (2.9)$$

Considering the free energy first. Differentiation of 2.8 gives

$$dF = dU - TdS - SdT \quad (2.10)$$

which on substitution gives

$$dF = -SdT - PdV + \sigma dA \quad (2.11)$$

and consequently

$$\left[\frac{\partial F}{\partial A} \right]_{T,V} = \sigma \quad (2.12)$$

$$\left[\frac{\partial F}{\partial T} \right]_{V,A} = -S \quad (2.13)$$

$$\left[\frac{\partial F}{\partial V} \right]_{T,A} = -P \quad (2.14)$$

At constant temperature

$$\begin{aligned}
 dA &= dU - TdS \\
 &= -W_{\max} \\
 &= -PdV + \sigma dA
 \end{aligned}
 \tag{2.15}$$

if no other work other than that associated with volume and area changes is involved. Similarly differentiation and substitution on 2.7 and 2.9 yields

$$dH = TdS + VdP + \sigma dA \tag{2.16}$$

$$dG = -SdT + VdP + \sigma dA \tag{2.17}$$

b) Open systems

For an open system, with varying composition, where μ_i and n_i are the chemical potential and number of moles of component i , respectively then

$$dU = TdS - PdV + \sigma dA + \sum_i \mu_i dn_i \tag{2.18}$$

Hence $dH = TdS + VdP + \sigma dA + \sum_i \mu_i dn_i \tag{2.19}$

$$dF = -SdT - PdV + \sigma dA + \sum_i \mu_i dn_i \tag{2.20}$$

$$dG = -SdT + VdP + \sigma dA + \sum_i \mu_i dn_i \tag{2.21}$$

2.4 LIQUID INTERFACES

When considering capillary rise, planar liquid surfaces are rarely present, rather the surface or interface is curved. Non-planar surfaces can give rise to variations in vapour pressure above the liquid and pressure differences across the curved interface. These problems were tackled in the 19th century by Lord Kelvin (1871) and Laplace (1805), who derived the equations that bear their names.

In the following three sections the two fundamental equations of capillarity are discussed together with the application of the Laplace equation to capillary rise in cylindrical capillaries and surface tension measurement. The more complex solutions are reviewed in a later section.

2.4.1 The Laplace equation

The derivation of the Laplace (or Young-Laplace) equation can be approached via a second illustration involving a soap film. Consider a soap bubble filled with air of radius, r , in the absence of any external field (e.g. electrical or gravitational), as shown in Figure 2.3.

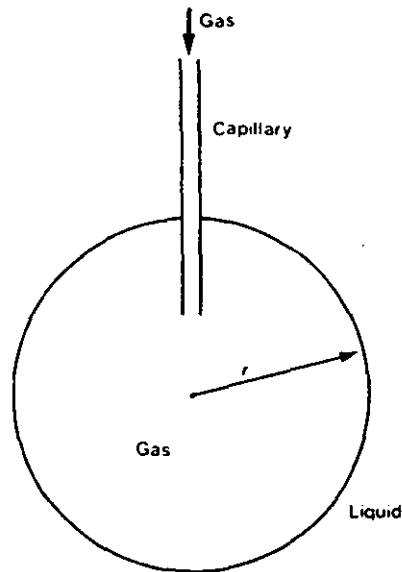


Figure 2.3 - A bubble of gas in a liquid

If the bubble is enlarged by introducing additional gas then the work done can be expressed in terms of that done against the forces of surface tension and in increasing the volume of the drop. In section 2.3.3 the free energy of a planar interface at constant temperature was derived as

$$dF = -PdV + \sigma dA \quad (2.15)$$

This will remain true for curved interfaces so long as σ is unaffected by curvature. Applied to the soap bubble (at equilibrium i.e. $dA = 0$) 2.15 becomes;

$$\sigma dA = \Delta P dV \quad (2.22)$$

where ΔP is the change in pressure across the bubble surface. The volume and surface area of the bubble are given by $\frac{4\pi r^3}{3}$ and $4\pi r^2$ respectively, thus $dV = 4\pi r^2 dr$ and $dA = 8\pi r dr$. Hence

$$dA = \frac{2dV}{r} \quad (2.23)$$

Substitution in equation 2.22 gives

$$\Delta P = \frac{2\sigma}{r} \quad (2.24)$$

Equation 2.24 is the form of the Laplace equation for a spherical surface, and shows that the smaller the bubble, the greater is the pressure of the air inside as compared to that surrounding the bubble. This accounts for the behaviour of the two different sized bubbles connected as in Figure 2.4, the small bubble is seen to inflate the larger one until mechanical equilibrium is reached (dotted lines) such that the radii of curvature are equal.

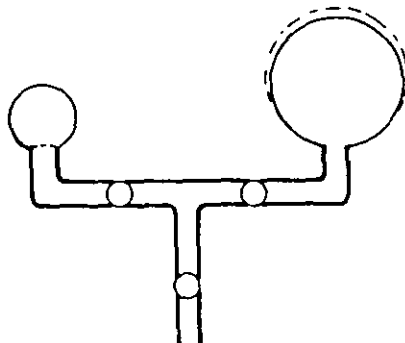


Figure 2.4 - Illustration of the Laplace equation.

In 1805 both Laplace and Young published a general relationship for the pressure across a curved interface of which equation 2.24 is a specific case for spherical surfaces. Generally it is necessary to invoke two radii of curvature to describe the degree to which a surface is curved (these are equal for a sphere).

Adamson (1976) gives a description of how radii of curvature are obtained for an arbitrarily curved surface.

"One erects a normal to the surface at the point in question and then passes a plane through the surface and containing the normal. The line of intersection in general will be curved, and the radius of curvature is that for a circle tangent to the line at the point involved. The second radius of curvature is obtained by passing a second plane through the surface, also containing the normal, but perpendicular to the first plane. This gives a second line of intersection and a second radius of curvature."

"If the first plane is rotated through a full circle, the first radius of curvature will go through a maximum, and its value at this maximum is called the principal radius of curvature. The second principal radius of curvature is then that in the second plane kept at right angles to the first."

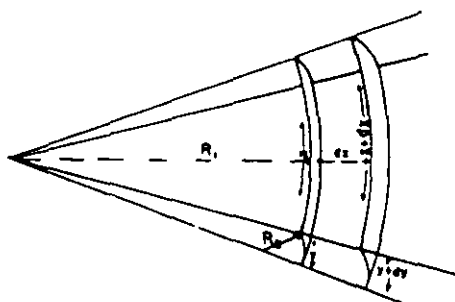


Figure 2.5 -A section of an arbitrarily curved surface.

Consider the section of surface shown in Figure 2.5. The two radii of curvature are indicated by r_1 and r_2 . The size of the section is such that the radii remain effectively constant. The surface is displaced a small amount, resulting in a change in area of dA , given by

$$\begin{aligned} dA &= (x + dx)(y + dy) - xy \\ &= xdy + ydx \end{aligned} \quad (2.25)$$

The work of formation of this additional area is then;

$$dW = \sigma(xdy + ydx) \quad (2.26)$$

As with a spherical surface there is also work performed against the pressure difference across the surface, it acts on area, xy , through a distance, dz , giving an expression for the work done:

$$dW = \Delta P xy dz \quad (2.27)$$

Comparing similar triangles reveals

$$(x + dx)/(r_1 + dz) = x/r_1 \quad \text{or} \quad dx = x dz/r_1 \quad (2.28)$$

$$\text{and} \quad (y + dy)/(r_2 + dz) = y/r_2 \quad \text{or} \quad dy = y dz/r_2 \quad (2.29)$$

For the surface to be in mechanical equilibrium then the two work terms must be equal, equating 2.26 and 2.27 and substituting for dx and dy gives

$$\Delta P = \sigma \left(\frac{1}{r_1} + \frac{1}{r_2} \right) \quad (2.30)$$

Equation 2.30 is a general statement of the *Laplace equation*. It is the fundamental equation of capillarity, it dictates the shape of all macroscopic menisci and from it come all techniques for the determination of interfacial configurations.

2.4.2 The Kelvin equation

The Kelvin equation describes the change in vapour pressure over an interface produced by variations in curvature and is the second fundamental equation of surface chemistry. The equation may be explicitly derived by thermodynamic reasoning.

Consider the effect of atomising a quantity of bulk liquid. The interface would be greatly increased by such a process, and since the interfacial free energy is greater than the bulk free energy, work will have to be done on the system in order to carry out the process. In consequence the chemical potential of the material of the drops will be larger than that of the bulk liquid, and there will be a corresponding increase in vapour pressure over a convex liquid surface. Unlike the Laplace phenomena an open system must be considered.

In section 2.3.3 the Gibbs free energy of an interface was expressed as

$$dG = -SdT + VdP + \sigma dA + \sum_i \mu_i dn_i \quad (2.21)$$

This equation gives rise to the definition of chemical potential

$$\mu_i = \left[\frac{\partial G}{\partial n_i} \right]_{n_j, T, P, A} \quad (2.31)$$

Whilst this definition is useful in the description of the transport of a material across a planar interface, for small spherical droplet the addition of material must necessarily cause a change in A . The associated volume change can be written

$$dV = \sum_i v_i dn_i \quad (2.32)$$

where v_i is the partial molar volume of the i th component of the liquid. In deriving the Laplace equation an expression for dA was deduced (equation 2.23), combination with 2.32 gives

$$dA = \sum_i \frac{2v_i}{r} dn_i \quad (2.33)$$

Substituting for dA in equation 2.21 yields

$$dG = -SdT + VdP + \sum_i \left[\frac{2v_i \sigma}{r} + \mu_i \right] dn_i \quad (2.34)$$

The chemical potential μ_i^o of the i th component in the drop is thus

$$\mu_i^o = \left[\frac{\delta G}{\delta n_i} \right]_{n_j, T, P} = \frac{2v_i \sigma}{r} + \mu_i \quad (2.35)$$

or

$$\mu_i^o - \mu_i = \frac{2v_i \sigma}{r} \quad (2.36)$$

Now the chemical potential terms for the planar and curved interfaces may be written as

$$\mu_i = \mu_i^\ominus + RT \ln P_i \quad (2.37)$$

and
$$\mu_i^\circ = \mu_i^\ominus + RT \ln P_i^\circ \quad (2.38)$$

where P_i is the vapour pressure over a planar interface and P_i° that over a curved interface. If these relations are substituted in equation 2.36 then

$$\ln \frac{P_i^\circ}{P_i} = \frac{2v_i\sigma}{rRT} \quad (2.39)$$

which is a statement of the *Kelvin equation*.

If instead of a drop of liquid in a vapour, a bubble of vapour in a liquid were considered then the radius of curvature is assumed to be negative. Dropping the subscripts and allowing for an arbitrarily curved surface the equation may now be written in the familiar form

$$\ln \frac{P}{P^\circ} = \frac{v\sigma}{RT} \left(\frac{1}{r_1} + \frac{1}{r_2} \right) \quad (2.40)$$

Although of a firm thermodynamic basis for macroscopic systems the validity of the Kelvin equation when the interface dimensions approach molecular sizes is the subject of an on-going debate. Lisgarten *et al.* (1971) have reviewed attempts at validation. Claims have been made for the equations' accuracy at radii of curvature of only a few molecular diameters (Fisher & Israelachvili 1981) but the uncertainty remains (Everett 1988).

2.4.3 Capillary rise and surface tension measurement

The capillary rise of liquids in cylindrical tubes is considered one of the most accurate methods of measuring surface tension (to hundredths of a percent - Jaycock & Parfitt 1987), partly because the theory has been worked out to a high degree of precision and partly because the experiment can be closely controlled. On the other hand, the capillary rise method is only applicable when the interfacial tension is constant and the liquid or solution completely wets the capillary tube (that is the contact angle is zero). In addition, there must be fairly large volumes of liquid available. Consequently there are many other methods of measuring surface tension, the most common are summarised in Table 2.1.

Table 2.1 Methods of measuring the surface tension of single liquids and solutions.

Method	Suitability	
	Pure liquids	Solutions
Capillary height	Very satisfactory when the capillary wets reproducibly.	Difficult when the contact angle is not 0° or variable.
Sessile drop	Very satisfactory.	Very useful for studying surface ageing.
Pendent drop	Very satisfactory but has experimental difficulties.	Useful for studying surface ageing.
Wilhelmy plate	With a good experimental set up, very accurate and convenient.	Provides accurate data on surface ageing.
Maximum pull on a cylinder	Very satisfactory. Easy to operate with simple apparatus.	Satisfactory if used with care and small displacements near maximum pull.
Maximum pull on a cone	Similar to cylinder method, but since the cone constant is universal, the results are easier to calculate.	
Du Noüy ring	Satisfactory	Unsatisfactory
Drop weight or drop volume	Very satisfactory	Poor when ageing effects suspected.
Maximum bubble pressure	Has experimental problems but useful where other methods are difficult to use.	Gives problems with ageing solutions.

All the methods in Table 2.1 rely on the application of the Laplace equation for a given interface shape. The solution of the Laplace equation can be difficult for other than two dimensional cylindrical menisci where one of the principal radii of curvature is infinite, or spherical menisci, where both radii are equal, as in equation 2.6. Solution is helped considerably if the interface shape possesses axial symmetry as, for example, do pendent and sessile drops. Except for the Wilhelmy plate method (cylindrical menisci), all methods shown in Table 2.1 are based on axially symmetric menisci. These more complex solutions to the Laplace equation are discussed later (see section 5.2).

It is not within the scope of this study to report details of the numerous methods of surface tension measurement, these may be found in the standard texts on surface chemistry (such as Jaycock & Parfitt 1987, Adamson 1976 or Bikerman 1970). However, the consideration of the capillary rise method introduces important relationships on which the experiments in this study are based.

Capillary rise in tubes is a well known phenomenon, its science was developed in the 19th century and involved some notable scientists of the day, such as Poisson and Mathieu. Liquid rises, or is depressed, in tubes due to the pressure difference created by a curved surface. A liquid rises in a tube if the contact angle, that is the angle with which

the liquid interface meets the solid wall, is less than 90° and it is depressed if the angle is greater than 90° . Figures 2.6 and 2.7 show situations where the contact angle is zero and 180° respectively. It is worth noting that the radii of curvature will always lie on the high pressure side of the interface, provided the meniscus is *clastic*: a meniscus that has radii of curvature that are of opposite sign is said to be *anticlastic* (van Brackel & Heertjes 1978).

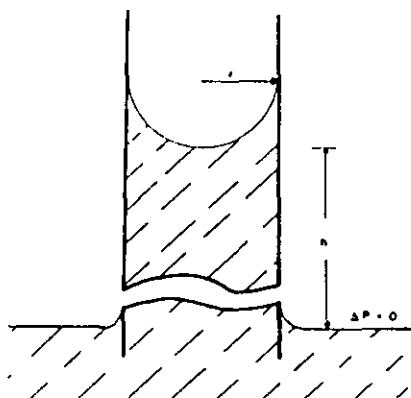


Figure 2.6 - Capillary rise of a liquid in cylindrical tube.

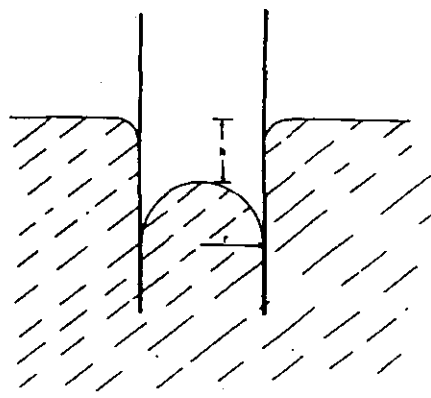


Figure 2.7 - Capillary depression.

For the situation shown in Figure 2.6, if the tube radius is small and the liquid completely wets the wall (a contact angle of zero) then the meniscus will be approximately hemispherical. So from the Laplace equation 2.30:

$$\Delta P = 2\sigma/R \quad (2.41)$$

where R is the radius of the tube, of equal magnitude to the two principal radii of curvature, r . For the system to be stable, the pressure difference across the interface must be balanced by the hydrostatic pressure drop. If the liquid above the (convenient to measure) height, h , is neglected then the hydrostatic head for the meniscus above the *planar* surface of the liquid is given by;

$$\Delta P = h\rho g$$

where ρ is the relative density difference, defined as the density inside the meniscus profile minus that outside it, and g is the acceleration due to gravity. Equating the hydrostatic head terms gives

$$hR = 2\sigma/\rho g \quad (2.42)$$

The term $2\sigma/\rho g$ is constant at a given temperature and defines the *capillary constant*, a :

$$a^2 = 2\sigma/\rho g \quad (2.43)$$

where a has units of length. Engineers often prefer to use a dimensionless parameter, the *Bond number*, given by

$$B = gL^2\rho/\sigma \quad (2.44)$$

where L is a characteristic reference length of the system under consideration. Both the capillary constant and the Bond number give a measure of the ratio of viscous to capillary forces.

For the general case where the liquid meets the wall with contact angle θ , the radii of curvature no longer equate to the tube radius. Consideration of the geometry in Figure 2.6 yields;

$$\begin{aligned} r &= R \cos \theta \\ \text{so } \Delta P &= h\rho g = 2\sigma/r \\ &= 2\sigma \cos \theta/R \end{aligned} \quad (2.45)$$

Equation 2.45 is commonly known as the *Washburn equation* (after Washburn 1921). For surface tension measurement the equation is written:

$$\sigma = Rh\rho g/2 \cos \theta \quad (2.46)$$

which, using the definition of the capillary constant (equation 2.43), becomes

$$a^2 = Rh/\cos \theta \quad (2.47)$$

Equation 2.43 was known before the 18th century and, although not strictly correct, it works well for small bore capillaries. The first correction to it came from Jurin (1718). Usually capillary rise is measured to the bottom of a meniscus as this is the most convenient point. However, the bottom of a meniscus does not correspond to its mean curvature. In a capillary rise experiment a meniscus cannot satisfy the constant curvature condition assumed by the above theory as curvature varies directly with height due to the influence of gravity. The region spanned by the meniscus will always be of a measurably finite height unless the height of rise is incredibly large.

Jurin determined a first order correction to bring the measured level near to that corresponding to a menisci's *mean* curvature. Assuming the meniscus in a tube to be hemispherical, Jurin drew a plane across the meniscus where the volume of liquid held above the plane equalled the volume of space below it. Utilising simple geometry he arrived at a correction that amounts to the addition of one third of the tube radius to the height of the bottom of the meniscus. Thus

$$a^2 = R(h + R/3) \quad (2.48)$$

However, even in small tubes there is a deviation from the spherical caused by gravity. Lord Rayleigh (1915) obtained a series approximation for nearly spherical

menisci in tubes up to a diameter of about 1 mm for water, equivalent to a R/h ratio of 0.02. He expressed the capillary constant as;

$$a^2 = R(h + R/3 - 0.1288R^2/h + 0.1312R^3/h^2 \dots) \quad (2.49)$$

Hagen and Desains (see Rayleigh 1915) had previously obtained a similar result by considering the meniscus to be elliptical:

$$a^2 = R(h + R/3 - 0.1111R^2/h + 0.0741R^3/h^2 \dots) \quad (2.50)$$

These correction factors are actually very small, even at the limit of $R/h = 0.02$ the total multiplication factor only amounts to 1.007. If the Jurin correction is used alone it is only in error by + 0.005%, equivalent to an error of about 1 μm in the measurement of R and h .

For cases where $h \ll R$, as in very wide tubes, Rayleigh obtained a different series approximation:

$$\frac{R\sqrt{2}}{a} - \ln\left(\frac{a}{h\sqrt{2}}\right) = 0.8381 + 0.2798\frac{a}{R\sqrt{2}} + 0.5\ln\left(\frac{R\sqrt{2}}{a}\right) \quad (2.51)$$

This equation can be used to show that for a 5 cm diameter tube and water the capillary rise is in the order of 1 μm . This equation has been validated for $R\sqrt{2}/a > 6$, equivalent to water in tubes of greater than 32mm diameter.

A more comprehensive approach was developed by Bashforth and Adams (1883) and later extended by Sugden (1921), to cover the range of R/h values not covered by Rayleigh's equations. Its basis is an axially symmetric figure of revolution. At the apex the two radii of curvature must be equal. For capillary rise the apex is at the bottom of the meniscus. If the radii of curvature at the apex are both b , and the height from the apex of a general point on the surface is z , where $z = y - h$ as shown in Figure 2.8.

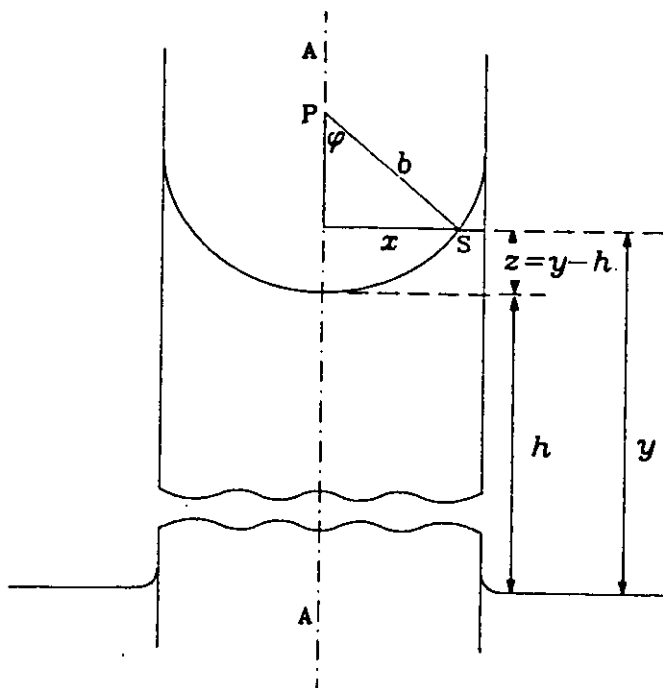


Figure 2.8 - The meniscus in a capillary as a figure of revolution.

The Laplace equation (2.30) can be written in the form,

$$\sigma \left(\frac{1}{r_1} + \frac{1}{r_2} \right) = \rho g z + 2\sigma/b \quad (2.52)$$

So at $z = 0$, $\Delta P = 2\sigma/b$ and at any other value of z the change in ΔP is given by a change in $\rho g z$. At a point S, on the surface where r_1 and r_2 are the radii of curvature, r_1 in the plane of the paper and r_2 in a plane perpendicular to the plane of the paper, and ϕ is the angle between the tangent at S and the vertical. The length PS corresponds to $r_2 = x/\sin \phi$ and this radius rotates around the symmetrical axis AA'. Equation 2.52 can now be written in a dimensionless form;

$$\frac{1}{(r_1/b)} + \frac{\sin \phi}{(x/b)} = 2 + \beta(z/b) \quad (2.53)$$

where
$$\beta = \rho g b^2 / \sigma = 2b^2/a^2 \quad (2.54)$$

The parameter, β , defines the shape of the meniscus, being positive for oblate figures; sessile drops, captive bubbles and a meniscus in capillary rise. β is negative for prolate figures such as pendent drops, emerging bubbles and menisci in capillary depression.

Before the days of computers Bashforth and Adams obtained solutions for equation 2.53. Their results were given as tables of values of x/b and z/b for closely spaced values of β and ϕ . For a given β value, a plot of z/b versus x/b reveals the profile of a particular figure of revolution satisfying equation 2.53. The tables can be used in an iterative fashion to obtain surface tension values from data collected from various measuring techniques

including capillary rise. Sugden presents the tables of Bashforth and Adams and his own extension in terms of tube radius. Values of R/b are given for closely spaced values of R/a . The tables may also be employed to yield corrected heights of rise in tubes of varying diameter and with liquids of various contact angles. Table 2.2 shows the relative accuracy of the various approximations used to interpret capillary rise data described above. Sugden's tables give the most accurate results for $R/h > 0.03$.

Table 2.2 Comparison of the methods of calculating capillary rise results in the form $a^2 = rhxF$

r/h	Jurin term	Rayleigh term	Hagen term	Sugden's Tables
	F	F	F	F
0.000 01	1.000 0	1.000 0	1.000 0	1.000 0
0.000 1	1.000 0	1.000 0	1.000 0	1.000 1
0.001	1.000 3	1.000 3	1.000 3	1.000 3
0.01	1.003 3	1.003 3	1.003 3	1.003 2
0.03	1.010 0	1.009 9	1.009 9	1.010 0
0.06	1.020 0	1.019 6	1.019 6	1.019 6
0.10	1.033 3	1.032 2	1.032 3	1.032 1
0.15	1.050 0	1.047 5	1.047 8	1.047 2
0.20	1.066 7	1.062 6	1.062 8	1.062 2
0.50	1.166 7	1.151 0	1.148 2	1.144 4
0.70	1.233 3	1.215 6	1.204 3	1.194 2
1.00	1.333 3	1.336 7	1.296 3	1.263 6

Today, with the advent of powerful microcomputers the hassle of the hand calculations can be negated. Boucher *et al.* (1987) have published such a program, covering an extensive range of meniscus configurations.

2.5 SOLID SURFACES

All curved fluid interfaces interact with the solid surfaces that surround them. Quantifying the way in which they interact is vital if a meaningful solution is to be found, hence an understanding of the fundamentals of solid surfaces is required.

Descriptions of solid surfaces as applied to capillarity have recently been reviewed by Good (1979) and Morrow (1970), whilst standard texts, such as Adamson (1976) and Jaycock and Parfitt (1987), also cover the area in more detail than can be afforded here.

2.5.1 The solid surface

Solids possess cohesion, that is they remain the same shape unless changed by external forces, due to the much larger intermolecular attraction forces than those in liquids or gases. Many solid objects are so familiar that they tend to be thought of as thermodynamically stable, which generally they are not. If solid surfaces were in

thermodynamic equilibrium (i.e. possessing minimum energy) then common processes such as annealing and sintering would not be possible. A 10p piece is in a thermodynamically unstable state, yet no observable change occurs in a conceivable time-span, for entirely kinetic reasons.

Solids have a considerable range of surface free energies*. Surface energy is likely to vary from place to place across the surface and at any particular point the surface tension need not be the same in all directions as is the case with a liquid surface. These surface energies are not usually measurable. However, values have been calculated for pure, perfect crystals (see Jaycock & Parfitt 1987), but are of little practical value, since it is virtually impossible to grow a crystal free from impurity and structural defects that the calculation assumes.

Essentially the shapes of solids are determined more by past history than surface tension forces. There are exceptions, however, these concern solids near their melting point. An example is the fusing together of ice cubes in a bucket in a freezer, they develop a "neck" at the points of contact.

It has been possible to characterise some solids on the basis of their specific surface energies as either "high energy" or "low energy" (Fox & Zisman 1950). Substances which have surface energies of the same order as most liquids ($< 100 \text{ ergs/cm}^2$), mainly organic polymers such as teflon (PTFE), are described as *low energy solids*. Most hard solids, such as rocks, with specific surface energies in the range 500 to 5000 ergs/cm^2 are referred to as *high energy solids*. Certain properties of a solid surface can be determined if the solid is characterised in this way (Good 1979).

The above discussion illustrates some of the difficulties involved in treating solid surfaces theoretically. If the solid surface cannot be adequately treated then obviously the study of solid/fluid(s) interfaces will also lack thermodynamic clarity.

2.5.2 Surface roughness

This term also has been noted as having a somewhat unclear meaning in the literature (Bikerman 1970), but the degree of roughness of a surface is important in capillary applications particularly where the liquid does not completely wet the solid. However, the concept of rough and smooth is subject to the closeness of the observation. For instance, you could be happily cycling along reflecting on the "smooth" surface of the road until you fall off and are grazed by the "roughness" of the tarmac.

* Morrow (1970) notes that there is no accepted terminology for the surface energies of solid surfaces and that the terms, surface tension, superficial tension, interfacial tension, adhesion tension, surface stress, stress tension, surface free energy, superficial densities of energy, specific free energy, free surface energy, surface energy, surface energy density, Helmholtz free energy, surface Helmholtz free energy, specific surface free energy, pure surface energy, actual surface energy, theoretical free surface energy, free energy of formation and relative surface free energy have all appeared in the literature on solid surfaces.

There is a level of variation at which the term "roughness" becomes inappropriate. A surface that is flat on a molecular scale is almost unattainable. Good (1979) cites carefully cleaved mica as the only probable exception, but all atoms and molecules vibrate with a measurable amplitude. So in general roughness is confined to changes in the surface representing movements of the surface larger than the interatomic distances (Jaycock & Parfitt 1987), and one criterion for an ideal solid surface is that it is smooth to a molecular level.

All the solid surfaces used in this study were prepared in some way; sawn, cut, turned, polished, ground or chemically treated. These methods all leave the surface rough. The simplest method for describing the degree to which these surfaces are rough is the *roughness factor*, r_w , given by Wenzel (1936) as

$$r_w = \frac{\text{actual surface area}}{\text{geometric surface area}} \quad (2.55)$$

where the geometrical surface is that measured in the plane of the interface corresponding to the surface area of a smooth interface.

Wenzel's ratio tells us nothing about the appearance of the roughness, and there is no consensus in the literature on formal descriptions that are more detailed. Bikerman (1970) gives a general method based upon the relative heights of hills and valleys and certain idealised configurations have been analysed by Johnson & Dettre (1964a, b) and by Eick *et al.* (1975). The distribution of hills and valleys will affect the behaviour of liquids in contact with that surface as will the degree to which ridges and valleys are parallel or organised into ranges (Jaycock & Parfitt 1987, Carroll 1984). It may be that in the future fractal analysis will be utilized to offer a more realistic description of solid surfaces (see Mandelbrot 1977).

2.5.3 Other surface defects

Other well known departures from the ideal solid surface are elastic distortion, the swelling of the solid by a liquid that wets the surface and the degree and extent of surface heterogeneity (Good 1979). There are three acknowledged causes for the heterogeneous nature of common surfaces:

- i) Differing chemical composition of matter on the surface. Either components essential to a material (as with steel) or surface impurities (nearly always present).
- ii) Different crystallographic faces on a chemically homogeneous solid (more correctly described as a homotactic solid in substances containing more than one type of atom (Jaycock & Parfitt 1987)). This may be visualised as the

difference in the density of atom packing in a (100) plane to that in a (111) plane or the presence of different kinds of molecular groups exposed in different planes.

iii) The existence of grain boundaries, crystal edges or corners and steps or ledges. Dislocations give rise to high energy sites where they intersect a surface, disturbing the uniformity.

Thus all surfaces that are not *homogeneous, uniform or homotactic* may be described as heterogeneous.

2.6 THE SOLID/GAS INTERFACE (ADSORPTION OF GASES)

The term *sorption* is commonly encountered in capillary applications. It is usually encountered with a prefix; commonly ab-, ad- or de-. The term is used to denote the separation of a chemical species between bulk and interface. *Absorption* generally applies to the solution of gases in liquids. Whereas *adsorption* refers to the concentration of a substance on a surface, such as the molecules or of a dissolved or a suspended substance on the surface of a solid. *Desorption* is the reverse of the latter mechanism.

In the context of capillarity, absorption is of little importance. Adsorption/desorption processes are however, directly relevant. Adsorption is often defined in terms of degrees of freedom. A molecule or atom, an *adsorbate*, is drawn towards a surface, an *adsorbent*, by the intermolecular attractive forces between them. This process results in a net decrease in the internal energy of the system as a whole. If the translational kinetic energy of the adsorbate is less than the adsorption energy the molecule will be "caught" on the surface. A molecule or atom is adsorbed if it has lost at least one degree of translational freedom.

If the forces causing loss of translational freedom are essentially London - van der Waals forces and electrical field - dipole interactions then the process is called *physical adsorption*. *Chemisorption* involves the formation of chemical bonds which results in much larger energies or heats of adsorption, typically 80 - 400 KJ/mol of adsorbate as compared to 0 - 40 KJ/mol for physical adsorption (Jaycock & Parfitt 1987). A molecule adsorbed by chemisorption must, by necessity, first be physically adsorbed as chemical forces only act over a very short range. The transition from physical to chemical adsorption may be associated with an activation energy barrier.

Since the interface between an adsorbed phase and its gas is just like any other, there is an associated equilibrium between them, and this must represent a balance between adsorption and desorption rates. With physical adsorption these rates are obviously much larger than those associated with chemisorption and thus it is physical adsorption that is of interest when applying capillary models.

2.6.1 Adsorption isotherms

The volume of a gas or vapour, V , that is adsorbed increases with the equilibrium pressure, P , and the distribution is usually also temperature dependent giving a description of the process in terms of an adsorption function:

$$V = f(P, T) \quad (2.56)$$

where V is usually expressed as the equivalent volume of pure adsorbate at STP. An adsorption *isotherm* can thus be written as

$$V_T = f(P) \quad (2.57)$$

When a gas or vapour is adsorbed it does not necessarily remain as a gaseous layer, but may collect together to form liquid. This phenomena gives rise to the process of capillary condensation of gases in porous materials. Polanyi (1914) postulated three different cases which describe the state of the adsorbed film in terms of the critical temperature of the adsorbate, T_c :

Case I For $T \ll T_c$ the adsorbed film will be a liquid;

Case II $T < T_c$, at temperatures just below T_c the adsorbed layer will be a mixture of liquid and compressed gas;

Case III For $T > T_c$ the adsorbed phase is a compressed gas.

Early workers thought adsorption was limited to a single monolayer of adsorbate molecules and formulated their models accordingly (see for example that of Langmuir 1918). However, it was soon realised that adsorption did not usually stop at a monolayer and that multilayer adsorption is the norm when the relative pressure:

$$P/P^\circ > 0.1 \quad (2.58)$$

where P° is the saturation vapour pressure of the adsorbate.

Adsorption is normally reported graphically using isotherms. Brunauer (1945) noted five distinct types of isotherm (Figure 2.9). *Type I* describes the adsorption of a monolayer showing an asymptotic approach to the monolayer volume, reached at P° , and corresponds to Langmuir's isotherm. *Types II* and *III* show multilayer formation on surfaces of high and low adsorption potential respectively. Finally, *types IV* and *V* are analogous to *II* and *III*, but cover adsorption on porous materials. The adsorption is seen to level off at a pressure less than P° as it is limited by the volume of the pores. Both involve condensation phenomena and can show hysteresis.

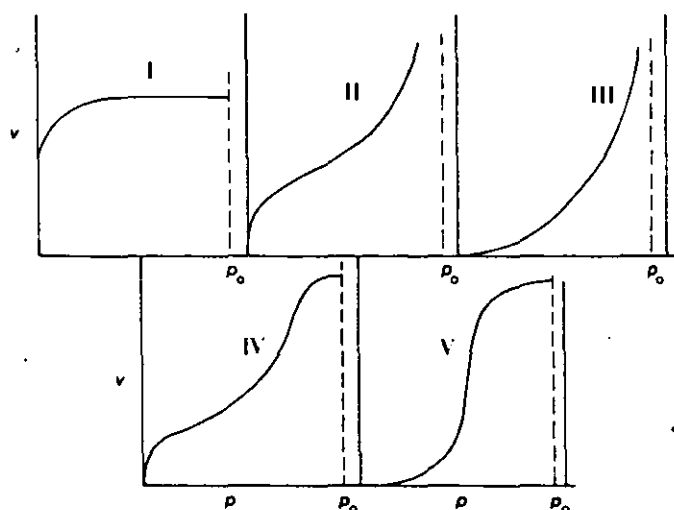


Figure 2.9 - Brunauer's (1945) classification of five types of adsorption isotherm.

Brunauer, Emmett and Teller (1938) (the latter of atomic bomb fame) developed the first successful multilayer adsorption model, commonly known as the *BET theory*. It is still in use today in the determination of solid surface areas, details of which may be found in any standard text on the subject. Adsorption/desorption methods are used in conjunction with capillary models for the determination of pore size distributions of some porous materials.

2.7 THE SOLID/LIQUID INTERFACE

Capillarity is the study of the macroscopic effects which arise at the point of contact between a liquid, or liquids and a solid. The physical aspects of this interface are manifest by the phenomena of wetting and spreading. The effects of the forces that act at the interface are governed by surface free energies and contact angles, which in turn depend on microscopic events at the interface with which they are associated.

Most of the following discussion and the experiments described later are concerned with pure liquids, as the forces involved in their molecular contact with a solid are better understood. However in many real situations involving the solid/liquid interface more than one component of a liquid phase needs to be considered. In addition, the surface geometry of the solid is often so complex as to preclude any exact mathematical treatment.

The literature concerned with the solid/liquid interface is extensive and no attempt is made to cover the entire field here. Wettability, as applied to oil recovery, has recently been reviewed by Anderson (1986a, b, c & 1987a, b). Contact angle phenomena and their measurement were the subject of reviews by Good (1979) and Neumann and Good (1979) respectively. The standard texts also cover this area in some detail.

2.7.1 Free energy of fluid interfaces bound by a solid

In section 2.3 an expression for the free (available) energy of a planar interphase was derived

$$dF = -SdT - PdV + \sigma dA + \sum_i \mu_i dn_i \quad (2.20)$$

In capillarity the usefulness of this relationship (and the corresponding expressions for enthalpy and Gibbs free energy) is limited as the fluid/fluid interfaces encountered are usually curved and bound, at least in part, by a solid surface. Equation 2.20 may be generalised via consideration of the situation in Figure 2.10. This system is defined by three "dividing" surfaces: that of the solid, S , the liquid, L , and the gas, G . Three different interfaces must now be considered: those between solid and gas, solid and liquid and liquid and gas.

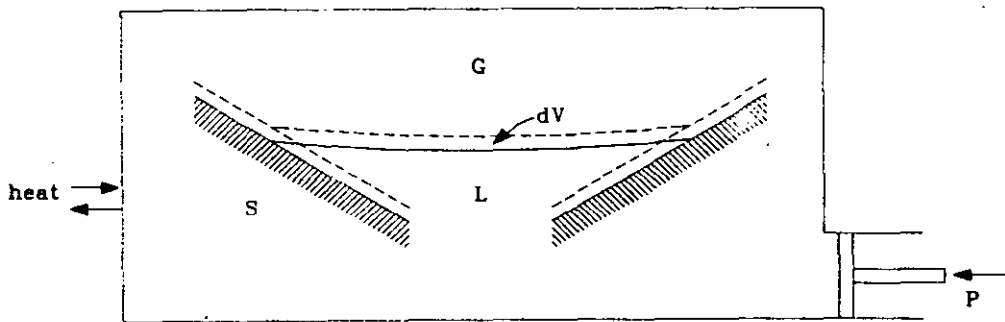


Figure 2.10 - An idealized system showing a small displacement of a liquid surface bound by solid and gas.

Equation 2.20 may be written (in the manner of Melrose 1966),

$$dF = -SdT - P_S dV_S - P_L dV_L - P_G dV_G + \sigma_{SL} dA_{SL} + \sigma_{SG} dA_{SG} + \sigma_{LG} dA_{LG} + \sum_i \mu_i dn_i \quad (2.59)$$

Several simplifying assumptions may be made for the model system shown in the Figure assuming variations to correspond to reversible, isothermal changes of state, in which no exchange of matter takes place (i.e. a closed system):

$$dT = 0$$

$$dV_S = 0$$

$$dn_i = 0$$

$$dA_{SG} = -dA_{LG}$$

and $dV_G = dV_{tot} - dV_L$

where $V_{tot} = V_S + V_L + V_G$

Substituting these relations in 2.59 yields

$$dF = -P_G dV_{tot} + (P_G - P_L) dV_L + (\sigma_{SL} - \sigma_{SG}) dA_{SL} + \sigma_{LG} dA_{LG} \quad (2.60)$$

Now from the first law of thermodynamics (equation 2.4) the total change in free energy is given by the external work, hence

$$dF = dF_{ext} = P_G dV_{tot} \quad (2.61)$$

Therefore we may write

$$(P_G - P_L) dV_L + (\sigma_{SL} - \sigma_{SG}) dA_{SL} + \sigma_{LG} dA_{LG} = 0 \quad (2.62)$$

Dropping the subscripts for the liquid and writing $P_L - P_G = \Delta P$ gives

$$\Delta P dV = \sigma dA + (\sigma_{SL} - \sigma_{SG}) dA_{SL} \quad (2.63)$$

Equation 2.63 describes the internal work performed and is a general equation that is very helpful in discussions on capillarity. For detailed analysis of the thermodynamics of interfaces as applied to capillarity the reader should refer to studies by Melrose (1966), Everett & Haynes (1972, 1975) and Boucher (1978).

2.7.2 Wetting

Wettability has been defined as "the tendency of one fluid to spread on or adhere to a solid surface in the presence of other immiscible fluids" (Anderson 1986b). Thus whenever a process involves the wetting of a solid by a liquid, three different interfaces are present. To illustrate this consider a rock/oil/water system, the interfaces are rock/oil, rock/water and water/oil. Any point where all three components meet is said to be on the *three phase line*. If the water preferentially wets the rock the solid is termed *water-wet*. Similarly the rock may be *oil-wet* if the rock is preferentially in contact with the oil. If the rock has no preference for either liquid it is termed as having *intermediate* or *neutral wettability*. It is important to note that the term wettability refers to the preference of the solid and does not necessarily refer to the fluid that is in contact with the solid at any given time.

The spontaneous imbibition (loosely this means suction - see later) of say, water into an water-wet pore occupied by oil indicates that the rock surface prefers to be in contact with water rather than oil. As the water imbibes into the pore an area of rock/oil interface is replaced by an equal area of rock/water interface. The changes in the total extent of each interface results in a net decrease in the total surface energy. Wetting is thus a thermodynamic process, and the magnitude of the free energy change involved

determines whether or not wetting will proceed spontaneously, at what rate and how far it can progress against any external forces, or alternatively, how large an external force is needed to overcome resistance to wetting.

The basic measure of the wetting properties of a liquid on a particular solid is provided by the *contact angle*, but it is not the only method of measuring wettability. Although relatively reliable in the simple systems in which they are measured, contact angles have, as yet, not proved superior to other methods when applied to porous materials or other geometrically complex systems that make up the majority of capillarity's practical applications. In these instances other quantitative techniques that have found widespread acceptance are the *imbibition and forced displacement, or Ammott method* and the *USBM wettability index* or even a combined *Ammott/USBM method*. These and many qualitative methods are described in Anderson's review.

2.7.3 Contact Angle

Contact angle is the wettability measurement employed in this study, so an understanding of its meaning, limitations and measurement is desirable. When a liquid is brought into contact with a flat solid surface the final shape taken up by the liquid depends on the relative magnitudes of the molecular forces that exist within the liquid (cohesive) and between the liquid and the solid (adhesive). Or in other words, the liquid spreads until equilibrium is obtained between the cohesive and adhesive forces.

The index of this effect is the contact angle which the liquid subtends with the solid, as shown in Figure 2.11. By convention the contact angle is measured through the more dense fluid. The angle varies between 0 and 180°. When the contact angle θ , is 0 the liquid is said to perfectly wet the solid. As the angle increases the liquid only partially wets the solid and the sessile drop of Figure 2.11 is part of a sphere, until at 180° no wetting is seen and the sessile drop is a complete sphere. Contact angles can also be observed in liquid/liquid/solid and liquid/liquid/gas systems.

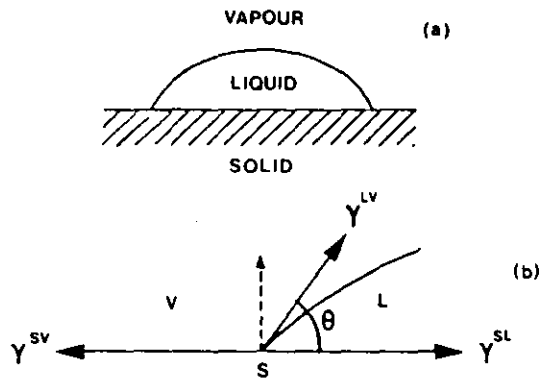


Figure 2.11 -The shape of a drop of liquid in contact with a solid surface when $\theta < 90^\circ$ (a), and the forces that exist at the three phase line (b).

A contact angle on a solid can only be defined with physical meaning when a unique tangent plane to the solid surface can be drawn; i.e. the plane through which the contact angle is measured must be "effectively flat" (Good 1979), on the scale of observation. In section 2.5 it was shown that a surface that is truly flat to a molecular level is a virtual impossibility. For contact angle purposes a surface may be said to be effectively flat only if contact angles measured on it give a single, unambiguous measurement (i.e. no hysteresis).

2.7.4 The Gauss equation of capillarity

The Gauss equation, first derived in the 19th century by Gauss (1830), has only comparatively recently found the widespread usage that has led to it being proposed as a fundamental equation of capillarity (as are the Kelvin and Laplace equations) (see Everett & Haynes 1972,1975, Iczkowski 1972, or Hwang 1977). The equation relates variations of fluid/fluid and solid/fluid interfacial areas with variations of liquid volume, the mean curvature of the liquid/gas interface and the contact angle.

The following derivation follows Hwang (1977). Consider a slight displacement of the liquid/gas interface shown previously in Figure 2.10. This displacement will cause a change in the liquid/gas interfacial area, dA , and an associated volume change, dV . This volume change is actually the volume swept by the meniscus during displacement.

A unit normal vector can be defined at every point on the liquid/gas interface, generating a continuous vector field within the volume element, dV . This enables the Gauss divergence theorem to be applied to the interface:

$$\iiint_{\partial V} (\nabla \cdot \mathbf{n}) dV = \iint_{\partial I} \mathbf{n} \cdot d\mathbf{A} + \iint_{\partial A_{SL}} \mathbf{n} \cdot d\mathbf{A} \quad (2.64)$$

In differential geometry, it can be shown that the divergence of a unit normal vector of any arbitrary surface is equal to the negative sum of the principal curvatures:

$$\nabla \cdot \mathbf{n} = -\left(\frac{1}{r_1} + \frac{1}{r_2}\right) = -J \quad (2.65)$$

Substituting this identity in 2.64 yields

$$\iiint_{\partial V} J dV = dA - \iint_{\partial A_{SL}} \cos \theta dA_{SL} \quad (2.66)$$

Defining

$$\langle J \rangle = \frac{\iiint_{\partial V} J dV}{\iiint_{\partial V} dV} \quad (2.67)$$

and

$$\langle \cos \theta \rangle = \frac{\iint_{\partial A_{SL}} \cos \theta dA_{SL}}{\iint_{\partial A_{SL}} dA_{SL}} \quad (2.68)$$

Equation 2.65 can be written as

$$\partial A = -\langle J \rangle \partial V + \langle \cos \theta \rangle \partial A_{SL} \quad (2.68)$$

At the limit $\partial V \rightarrow 0$ equation 2.68 is reduced to the differential form

$$J dV = dA - dA_{SL} \cos \theta \quad (2.69)$$

Which is a statement of the *Gauss equation of capillarity*. Note that although the equation may be applied to any surface the derivation assumes constant mean curvature and hence 2.69 is only valid for gravity free systems. Boucher (1980) has proposed a more general form:

$$\int J \partial V = dA - dA_{SL} \cos \theta \quad (2.70)$$

for changes of interfacial areas in systems where the volume changes by ∂V in dz .

2.7.5 Spreading and Contact Angle

It is generally found that liquids of low surface tension wet most solid surfaces ($\theta = 0$), whereas those with high surface energies usually give a finite contact angle. In the former case the molecular adhesion between solid and liquid is greater than the cohesion between the liquid molecules and in the latter it is the cohesion forces that are dominant.

The situation was illustrated in Figure 2.11. The relationship between contact angle and the individual surface energies was first considered by Young (1805). He postulated the relationship in words in his "*Essay on the Cohesion of Fluids*" (1805). Dupre (1869) later put it in mathematical terms. The expression may be deduced simply and directly from the Gauss equation.

Multiplication of the Gauss equation (2.69) by σ gives

$$\sigma J dV = \sigma dA - \sigma dA_{SL} \cos \theta \quad (2.70)$$

In section 2.7.1 an expression for the free energy of a fluid/fluid interface was derived;

$$\Delta P dV = \sigma dA + (\sigma_{SL} - \sigma_{SG}) dA_{SL} \quad (2.63)$$

simply comparing the coefficients of 2.70 and 2.63 yields

$$\Delta P = \sigma J \quad (2.30)$$

which is the Laplace equation and

$$\sigma_{SL} - \sigma_{SG} = \sigma \cos \theta \quad (2.71)$$

which is a statement of the *Young or Young-Dupre equation*. Note however that both these equations are more general than implied here. In particular they are valid for reversible changes which are not closed with respect to exchange of matter and the inclusion of gravitational effects, whilst complicating the derivations, does not affect the final results (Everett & Haynes 1972).

When applied to the solid/liquid/gas system the Dupre equation (2.2) is written as;

$$W_{SLV} = \sigma_{SG} + \sigma - \sigma_{SL} \quad (2.72)$$

where W_{SLG} is the work of adhesion. When combined with the Young equation the Dupre equation yields

$$W_{SLG} = \sigma(1 + \cos \theta) \quad (2.73)$$

This equation was that stated by Dupre in 1869. Another useful quantity is the adhesion tension, A_{SLG} . It was first used by Wenzel (1936) in his theory of surface roughness and is defined as

$$A_{SLG} = \sigma_{SG} - \sigma_{SL} = \sigma \cos \theta \quad (2.74)$$

It is worth noting that σ_{SG} refers to a solid surface in equilibrium with an adsorbed film of the gas or liquid vapour, and is not equal to the surface energy of the bare solid, σ_s . In terms of σ_s equation 2.71 becomes

$$\sigma_s = \sigma_{LG} \cos \theta + \sigma_{SL} + \pi \quad (2.75)$$

where $\pi = \sigma_s - \sigma_{SG}$ (2.76)

π is called the film pressure. It is still a matter of debate as to whether π is negligible on smooth, homogeneous, low energy surfaces. On nonhomogeneous, rough surfaces π will be appreciable (Good 1979).

It is perhaps worth noting that the general validity of the Young equation is still the subject of much debate. Equation 2.71 is exactly the same as that obtained by taking horizontal components of the surface forces (Fig. 2.11). It does not take the vertical component of the liquid surface tension, $\sigma \sin \theta$, into account, and there is evidence for the distortion of solid surfaces by this component. Michaels and Dean (1962) have shown that on soft solid surfaces a circular ridge is raised at the three phase line, further confirmation has been provided by Lester (1967) for mercury on mica, together with a theoretical treatment. On hard surfaces no visible effect is seen, but the surface tension component must be balanced by strain within the solid.

Young's equation does not hold when the contact angle is zero, and the imbalance of surface free energies is then defined by the spreading tension, S_{SLG} :

$$S_{SLG} = \sigma_{SG} - (\sigma + \sigma_{SL}) \quad (2.77)$$

The spreading tension is positive if spreading is accompanied by a decrease in surface free energy, that is if it is spontaneous.

Equations 2.73 and 2.74 are often far more useful than Young's equation since the latter contains two solid surface tensions which cannot be measured with any accuracy (as explained in section 2.5). As a consequence there have been virtually no successful attempts to verify the Young equation experimentally. In addition to the problems already discussed, other specific objections have been raised about the equation, but these are discussed elsewhere (see for example Bikerman 1970 and Morrow 1970).

To reiterate, the contact angle is only a fundamental property of the system when the surface of the solid is smooth, non-deformable and homogeneous with respect to surface energy and when the fluids are free of polar impurities. In such cases the equilibrium contact angle can be referred to as the *intrinsic contact angle*, θ_c , (Johnson & Dettre 1964a).

Fox and Zisman (1950) have shown that these conditions are closely met by pure liquids against air on the smoothed surfaces of certain low-energy organic polymers, including polytetrafluoroethylene (PTFE or teflon). Reproducible contact angles can be obtained that exhibit strong dependence on the surface tension of the liquid. A critical surface tension, σ_c , below which the contact angle will be zero, can be predicted from a plot of surface tension against $\cos \theta_c$ for a homologous series of liquids (Adamson 1976), although different series have been seen to give slightly different values of σ_c .

2.7.6 Contact Angle Hysteresis

Values of contact angles in most real systems depend on whether the three phase line is advancing or receding over the solid surface. It is generally found that a liquid drop on a surface can have many different stable contact angles. Those that are usually

measured are the maximum and minimum values corresponding to the recently advancing or recently receding conditions, as these are the most meaningful and reproducible. Since two fluids are involved, one fluid's advancing angle equates to the other's receding angle. The difference between the advancing angle, θ_a , and the receding angle, θ_r , is defined as the contact angle hysteresis, H_θ :

$$H_\theta = \theta_a - \theta_r \quad (2.78)$$

An every day example of this phenomena is that of the appearance of a rain drop on a dirty window, as shown in Figure 2.12. The effect can be quite large; for water on minerals hysteresis of 50° is common and a value of 154° has been recorded for mercury on steel.

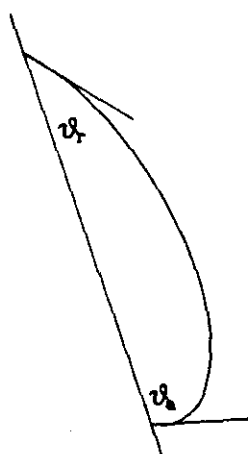


Figure 2.12 - Appearance of a rain drop on a dirty window.

Contact angle hysteresis was recognized before this century and three principal causes have been well documented (see for example Adamson 1976, Johnson & Dettre 1964a or Morrow 1970), these are:

- i) Surface roughness
- ii) Surface heterogeneity
- iii) Surface immobility on a macromolecular scale.

Surface roughness effects can be visualised by considering a horizontal but rough homogeneous plate. A liquid drop will generally be attached to a part of the surface that is not flat because the rough surface contains peaks and valleys. So the apparent contact angle, measured from the tangent to the horizontal plane of the surface, will be different to the true contact angle at the actual point of contact. The surface roughness will allow many metastable states of the drop to exist with differing contact angles.

Hysteresis due to surface heterogeneity can result from either heterogeneity in the solid surface as described in section 2.5 or from differential adsorption of wettability altering compounds and impurities in the liquid. Finally, surface immobility can cause hysteresis by preventing the fluid motion necessary for the contact angle to reach its equilibrium value. This problem is encountered in oil recovery operations; slow adsorption of a surfactant from the solid/liquid interface into the bulk liquid can cause hysteresis, some crudes actually form a solid film at the oil/water interface (Anderson 1986b).

Other factors affecting hysteresis have been documented, such as the dependence of contact angles on interface velocity (dynamic effects) (Morrow & Nguyen 1982, Larson *et al.* 1981). Good (1979) also reports diffusion, swelling and reorientation effects. However, it is principally surface roughness that relevant to this study and it is discussed in greater detail below.

2.7.6.1 Wenzel's theory

There have been several attempts to relate the surface roughness to contact angle. One of the earliest is that of Wenzel (1936). He introduced "effective adhesion tensions" (equation 2.74) to obtain a modified form of the Young equation, in which roughness changed the effective solid/vapour and solid/liquid surface tensions in proportion to his roughness factor, r_w , (equation 2.55). By combining the modified form with the actual Young equation Wenzel obtained a relationship between the intrinsic contact angle, θ_e , and the angle observed at a rough surface, θ^* ;

$$\cos \theta^* = r_w \cos \theta_e \quad (2.79)$$

Cassie (1948) and Shuttleworth & Bailey (1948) also arrived at this equation. However equation 2.79 takes no account of hysteresis, and it is the presence of hysteresis at rough surfaces that poses a fundamental objection to any theory of surface roughness based on equilibrium concepts (Morrow 1974).

In his experiments Wenzel notes that contact angles must be measured under water advancing conditions so as to obtain reproducible results relevant to the study of water-repellency, implying that equation 2.79 is applicable to advancing angles only. Variations in θ^* are put down to local changes in r_w .

According to equation 2.79 as surface roughness increases advancing contact angles decrease if $\theta < 90^\circ$, and increase if $\theta > 90^\circ$. Experimental data has been presented in an attempt to show the validity of Wenzel's theory, see for example Fox & Zisman (1950) but none have found the theory to be generally applicable.

The roughness ratio, r_w , is defined by Wenzel as an *independent* property of the solid. Shepard & Bartell (1953) and Morrow (1974), on paraffin wax and PTFE surfaces respectively, found a marked *dependence* of r_w on the intrinsic angle, θ_c . These more recent works also agreed that only at values of θ_c less than about 45° were contact angles seen to decrease with increasing surface roughness.

2.7.6.2 Cassie's theory

Working with patchy, heterogeneous, or composite, surfaces Cassie (1948) proposed that the equilibrium contact angle on such surfaces, θ_c , should be taken as an area weighted average such that,

$$\cos \theta_c = f_1 \cos \theta_1 + f_2 \cos \theta_2 \quad (2.80)$$

where f_1 and f_2 are the fractional areas occupied by the composite components 1 and 2. However θ_c can only be measured experimentally when hysteresis is absent, such as in the case of a flat surface with parallel bands of components 1 and 2 running parallel to liquid motion.

Cassie's theory has found application in water-repellency studies (see for example Adam 1958). The area f_2 becomes the fraction of open area and θ_1 the contact angle on a single fabric, hence,

$$\cos \theta_c = f_1 \cos \theta_1 - f_2 \quad (2.81)$$

Note that the negative sign results from the incorporation of Young's equation in equation 2.80.

Roughness and composite effects may both be manifest at the same time. For instance, if the contact angle is sufficiently large and the surface sufficiently rough, as in Figure 2.13, such that air becomes trapped by the liquid in-between surface asperities causing a composite effect, equation 2.81, on application of Wenzel's theory, becomes;

$$\cos \theta_{app} = r_w f_1 \cos \theta_1 - f_2 \quad (2.82)$$

where θ_{app} is the apparent contact angle.

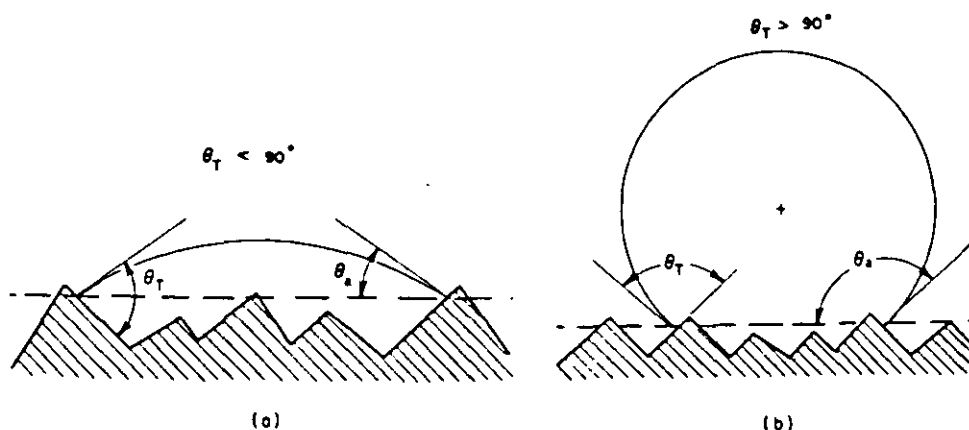


Figure 2.13 - Effects of surface roughness on apparent contact angle θ_{app} . θ_s is the contact angle measured on a smooth flat surface. (a) The droplet is the preferentially wetting fluid, so $\theta < 90^\circ$. (b) the droplet is the non-wetting fluid, so $\theta_s > 90^\circ$.

Although the relationships discussed above are useful in modelistic terms, they are difficult to apply to real systems as these are generally far more complex than the models. The *surface rugosity*, or the geometry of the surface roughness, plays an important part in determining the wetting behaviour and the extent of hysteresis (Anderson 1986b). For example a surface with a high roughness ratio, but with the roughness in the form of uniform ridges running parallel to the liquid motion, little or no hysteresis is seen. If the same ridges are perpendicular to the liquid motion hysteresis is at its maximum value.

Most real surfaces are rough, but in a haphazard manner, equivalent to a surface with random, intersecting systems of ridges. Shepard & Bartell (1953) successfully modelled such a surface as a regular array of pyramids and found that contact angles varied with the angle of inclination of the pyramids' faces, but not with their height, a conclusion subsequently confirmed elsewhere (Morrow 1974 and Tamai & Aratani 1972). Carroll (1984) discusses similar surface rugosity effects, but on cylinders as opposed to horizontal surfaces and arrives at the same conclusions.

Work of more general applicability and specifically relevant to this study is the detailed investigation of "*the Effects of Surface Roughness on Contact Angles*" by Morrow (1974). He used a series of liquids to quantify the effects of roughness on low energy PTFE surfaces. Using capillary tubes roughened with dolomite powders to measure contact angles from capillary rise, three distinct classes of contact angle hysteresis were found:

Class I behaviour, smoothed PTFE tubes gave essentially no hysteresis under advancing and receding conditions yielding the intrinsic contact angles.

Class II behaviour, the tubes as supplied by the manufacturer exhibited slight contact angle hysteresis that was empirically related to the intrinsic contact angle, see Figure 2.14. Slight roughening of the tubes did not change this behaviour.

Class III behaviour, with sufficient roughening of the internal surfaces of the tubes, class II behaviour was markedly increased to give class III behaviour, see Figure 2.15. This behaviour was obtained for a variety of roughness conditions and was found to be independent of the particle size of the abrasive dolomite powder, the extent of further roughening and possible composite surface effects. Class III behaviour was also empirically related to the intrinsic contact angles.

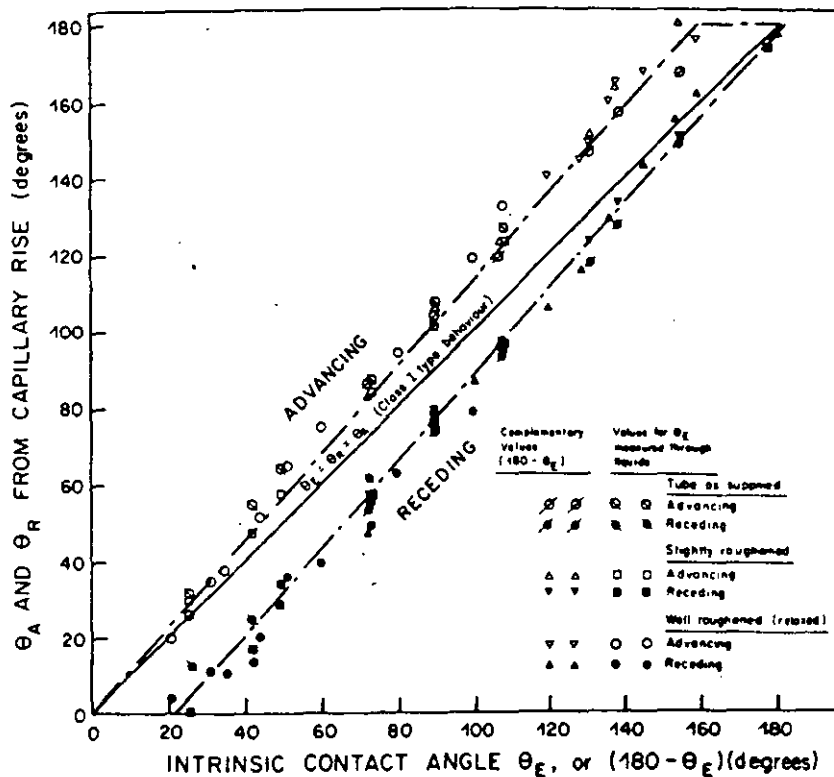


Figure 2.14 - Morrow's (1974) results from capillary tubes "as supplied" and slightly roughened exhibiting Class II behaviour.

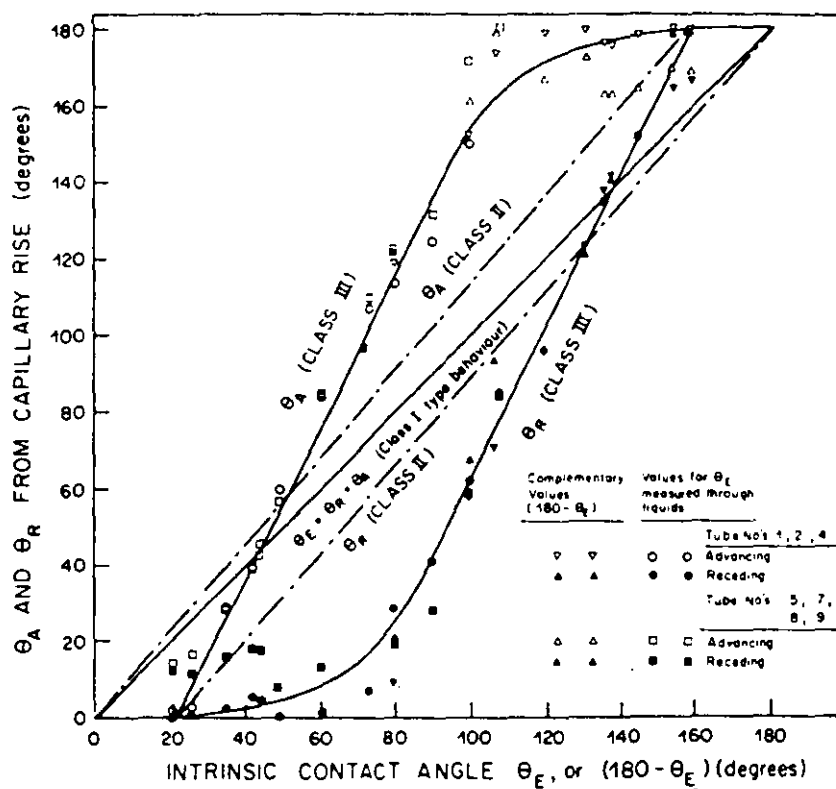


Figure 2.15 - Morrow's (1974) results from capillary tubes well roughened with dolomite powder that give rise to Class III behaviour.

Morrow's results are consistent in that when the angle observed at a smooth surface θ_s , is replaced by its complement, $180^\circ - \theta_s$, and the advancing and receding angles interchanged the results overlap the curves given by the results in their original form. Significantly Morrow found specific classes of hysteresis exhibiting reproducible values of θ_a and θ_r for wide ranges of surface roughness, and not a graduation in roughness effects. This enables his results to be employed without regard to the exact nature of the surface roughness. The work of Tamai & Aratani (1972) supports that of Morrow in that they found two-tiered hysteresis for mercury on silica plates, corresponding to classes I and III. The hysteresis was again independent of the grade of roughening abrasive, despite roughening giving up to a tenfold variation in the average height of the surface asperities.

2.7.7 The measurement of contact angles

Many different methods have been used to measure contact angles. Perhaps the most common is the direct measurement of θ by placing a drop on a horizontal plate and observing the angle at the three phase line (the sessile drop method), as previously

illustrated in Figure 2.11. Advancing and receding angles are obtained by adding or removing liquid from the drop and taking the maximum or minimum value before the three phase line moves.

Reasonably reproducible results can be obtained in this way (to within 0.3° , Jaycock & Parfitt 1987). However changes in the measured contact angle have been observed with variation in the curvature of the three phase line (i.e. a change in drop size). For example, water on a teflon sample gave a receding angle of about 95° for drops larger than 5 mm in diameter, but declined to about 80° if the drops were smaller than 1.5 mm. Similar effects have also occurred with advancing angles over the past 40 years and have yet to be satisfactorily explained.

Other popular methods for measuring contact angles include the tilting plate method, sessile bubbles, the vertical rod method, tensiometric methods, the cylinder method and the capillary rise method. Descriptions of these and other techniques can be found in reviews by Adamson (1976) and Neumann & Good (1979).

The choice of method depends greatly on the geometry of the solid system and on the quantity of liquid available. Techniques have been developed for specific systems where standard methods are inapplicable such as for fine textile fibres (Carroll 1976), and coal granules (Clark & Mason 1968).

Absolute values of θ_a and θ_r are not found, values differ by up to several degrees from laboratory to laboratory and with different measuring techniques. Values of contact angles on low energy surfaces are more reliable and reproducible than those on high energy surfaces. The author prefers those methods which involve indirect measurement of contact angle, over a larger perimeter, such as the capillary rise method, to those that employ direct measurement as they produce markedly less scatter.

The above discussion illustrates the limitations of contact angle measurement and that while a useful tool in the determination of the characteristics of the solid/liquid interface, contact angles are by necessity an approximation of the interface properties except on truly flat surfaces. Until hysteresis is properly understood, the uncertainties over contact angles will remain.

2.8 SUMMARY

Over the previous pages the basics of surface chemistry, as applied to capillarity, were discussed. The fundamental equations of capillarity - the Laplace, Young, Kelvin and Gauss equations - have been derived and points of debate about their application and validity noted. The concepts of interfacial tension, wettability and contact angle were defined and the limitations of each discussed in relation to the interfaces to which they apply. Attention is now directed towards the applications of capillarity.

CHAPTER 3

Porous materials

3.1 INTRODUCTION

A porous material may simply be defined as any solid with holes in it, that is it comprises a solid phase dispersed in such a way that a non-solid phase remains in-between. The solid phase is termed the *matrix*, and the non-solid phase the *pore space* (or void space), of the porous medium.

Porous materials occur widely in the natural environment and there are many synthetic media in use in the home and industry. They can be broadly classified as either *consolidated* or *unconsolidated*. Some examples of unconsolidated media are sand, glass beads, catalyst pellets, column packings and soils. Most naturally occurring rocks, like sandstone and limestone, are consolidated materials as are many man made materials like bricks, concrete, paper, membranes, adsorbents and textiles. Wood, human lungs and even insect hair are classifiable as porous media. The list of scientific disciplines involved in their study reflects the diversity of the materials: including biology, biophysics, soil physics, hydrology, catalysis, geology and chemical, building and petroleum engineering.

The shape of the pore space is usually very complex, consisting of irregularly shaped cavities or cracks connected together in an intricate and variable network. In order to describe a porous material it is usual to visualise the pore space to be made up of a number of interconnected "*pores*", although the reality of their concept is doubted by some authors (van Brackel 1975 and Everett 1988). A single pore is defined as a central cavity connected by one or more constrictions to neighbouring pores. The average number of connecting constrictions defines the *interconnectivity* or *branchiness* of the porous material. Porous materials are important in capillarity as when a porous medium is partially saturated with liquid the holes or pores act as capillaries and its properties are dominated by the behaviour of the liquid menisci in the pore space.

Obtaining fundamental information on the physical characteristics of porous solids like density; total porosity (and its sub-division into open and stacate (dead-end) pores); surface area (both accessible and inaccessible); wettability; pore size and pore size distribution; pore shape and connectivity is beset by many problems and uncertainties, in that even the simplest characteristics are difficult to measure in absolute terms due to the complex and irregular geometry.

On the other hand, the practical performance of a porous solid is important. Here the major concerns of technologists include adsorption-desorption processes, molecular sieving, permeability and fluid flow, drainage and imbibition (wetting and dewetting), catalytic properties and fluid-fluid displacement.

In principal characterisation and performance properties are linked, although in real systems the relationship is usually complicated. Tremendous effort within the literature has been devoted to the establishment of these relationships. As a consequence, many different characterisation techniques have been developed. Most are indirect, being based on some secondary, non-geometrical property related to the pore structure, but also relevant to the practical performance of the material.

The characterisation procedure normally involves the use of a model to represent the complex structure of the real pore system in a more mathematically tractable form. These models are nearly always a gross simplification of the real solid matrix, but are of value if they can rationalise experimental data.

Many of the practical applications of capillarity, and much of the economic stimulus for the on-going research to elucidate its fundamental relationships, involve porous media of some kind. At present an increasingly significant area of research arises from the need to apply secondary and tertiary oil recovery techniques (collectively EOR) to retrieve valuable oil left behind in the reservoirs by conventional drilling (so called primary recovery). Over the following pages some of the models are discussed in connection with the process explanations and characterisation techniques of which they form an integral part. A more complete description of porosity is beyond the scope of this study, but it is covered in detail elsewhere, for example see Dullien & Batra (1970), Modry & Svata (1973), Everett (1975), Gregg & Sing (1982) and Unger *et al.* (1988), although, as yet, there is no comprehensive standard text for the reader to refer.

3.2 CHARACTERISATION OF POROUS MATERIALS

Direct observation of the of the structures of porous media, or *stereology*, was previously of limited use in evaluating the performance of the media. However, it is expected that direct measurement will become increasingly important with the application of new techniques such as small angle X-ray scattering (SAXS) and small angle neutron scattering (SANS) which can give statistical information about pore structures in three dimensions.

Indirect characterisation techniques are normally employed to yield information that is directly relevant to the materials practical performance. There are three popular methods that are also particularly relevant here, namely adsorption-desorption, mercury porosimetry, and drainage-imbibition. All three techniques involve liquids entering or leaving pore space.

Adsorption-desorption. (Fig 3.1). In many adsorption- desorption processes a gas becomes capillary condensed in individual pores and is then evaporated from the pore space.

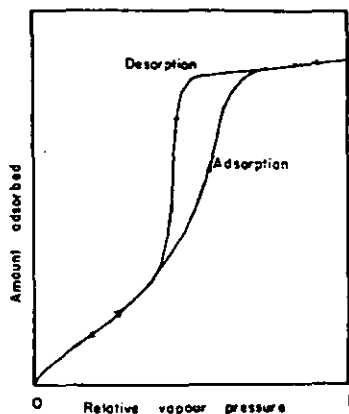


Figure 3.1 - A typical adsorption-desorption curve.

Mercury porosimetry. (Fig 3.2). In the analysis of pore structure by mercury porosimetry a non-wetting liquid, mercury, is forced into the pore space under pressure and then allowed to extrude again when pressure is relaxed.

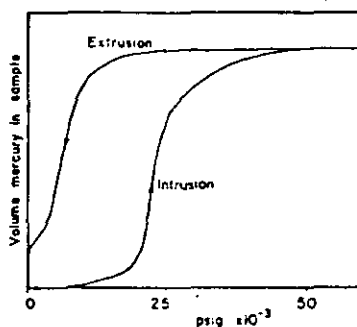


Figure 3.2 - An example of the capillary pressure curve obtained from mercury porosimetry experiments.

Drainage-imbibition. (Fig. 3.3). In drainage-imbibition processes a wetting liquid that initially fills the pore space is drained by the application of suction pressure and then allowed to imbibe again as the pressure deficiency is reduced.

These techniques are relatively simple experimentally and they can, when combined with an appropriate model, give parameters that accurately describe the pore space if the results are correctly interpreted. All three processes show similar behaviour if the results are plotted in a comparable way. They show a distinct *threshold* and *hysteresis* between filling and emptying (Fig. 3.4). Several explanations have been proposed for this behaviour (see section 3.5), but there is little doubt that it is caused by

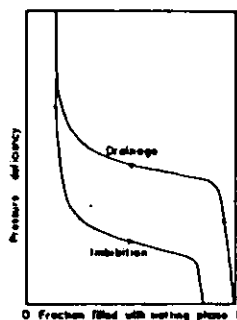


Figure 3.3 - A graph showing a typical capillary pressure curve obtained with a wetting liquid undergoing drainage followed by imbibition.

a combination of the properties of the liquid menisci and the complicated network of pores that make up a porous solid.

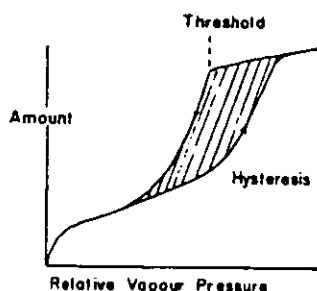


Figure 3.4 - A hysteresis curve showing a distinct threshold. Adsorption-desorption, mercury porosimetry and drainage-imbibition exhibit similar behaviour.

3.2.1 Classification by pore size

Most work on the pore sizes of finely porous materials has been based on measurements of desorption or fluid penetration. There is little overlap between each of these methods and stereological techniques. Pores are usually classified on the basis of their interaction with nitrogen adsorbate molecules in a manner reported by Gregg & Sing (1982) and recently recommended by IUPAC (the International Union of Pure and Applied Chemistry) (see Stacey 1988). Pores are divided roughly into the following groups based on mean pore width:

Micropores with dimensions < 2 nm

Mesopores in the range 2 - 50 nm

Macropores with dimensions > 50 nm.

Micropores have also been subdivided into ultramicropores (< 0.6 nm) and supermicropores (0.6 - 1.6 nm) to differentiate between adsorption mechanisms. Unlike smaller sized pores, macropores cannot be investigated using adsorption methods as they are too similar to plane surfaces for adsorption differences to be significant, but they can be examined using mercury porosimetry.

3.2.2 Porosity

The porosity of a material is defined as that fraction of the bulk volume of the material that is not occupied by the solid matrix. There are two common forms of porosity in use, *absolute porosity*, ϵ , and *effective porosity*, ϵ_{eff} . Absolute porosity is a measure of the total void space (including both open and stacate pores) with respect to the bulk volume. Effective porosity is the percentage of interconnected pore space (only the open pores). In other words, effective porosity is an indication of the conductivity to fluid, but not a measure of it.

3.2.3 Saturation and saturation states

The saturation of a porous material with respect to a particular fluid is defined as that fraction of pore space filled by the fluid. If the fluid is denoted by the subscript w the fractional saturation is given by

$$S_w = \frac{\text{volume of fluid in the medium}}{\text{total pore volume}} \quad (3.1)$$

and varies from 0 to 1. Fractional saturation usually refers to the wetting phase.

As the saturation of a porous medium increases three distinct fluid saturation states can be distinguished, namely *pendular*, *funicular* and *insular*. Figure 3.5 shows the situations for an air/water system where the porous media is in the form of an unconsolidated bed of granules. At very low saturations the wetting phase water, forms immobile rings around the contact points of the granules; these rings are called pendular rings and are toroidal in shape. At slightly higher saturations the wetting phase forms into a continuous body around the granules and is said to be in the funicular state. As the saturation is further increased a situation develops where the non-wetting fluid, air, can no longer exist in a continuous (funicular) phase and it breaks down into individual globules or ganglia. This dispersed condition is called the insular saturation state.

3.2.4 Capillary pressure curves

The void space in a porous solid usually contains many sharp recesses. If the wetting phase saturation is increased from an initially dry state the liquid will first collect in

An idealised apparatus for the measurement of capillary pressures for drainage-imbibition processes in porous solids is shown in Figure 3.6. Normally the medium is initially saturated with the wetting phase, in this case water, and in contact with a finely pored membrane which remains saturated with water. The pressure on the water, P_w , is the measured gas pressure acting on a frictionless piston. The non-wetting phase, oil, is in direct contact with the porous solid and its pressure is given by the gas pressure, P_{nw} , acting on a second piston. Usually one phase is kept at atmospheric pressure through the experiment. The capillary pressure, P_c , is given by

$$P_c = P_{nw} - P_w \quad (3.2)$$

The saturation of water in the solid is found from volumetric displacement measurements. The displacement of a volume of water, ΔV_w , is related to a saturation change, ΔS_w , by

$$\Delta V_w = V_b \epsilon \Delta S_w \quad (3.3)$$

where V_b is the bulk volume of the porous sample and ϵ its porosity. Each capillary pressure data point is obtained by holding the external pressure constant until fluid flow from the solid ceases. Volumetric displacement is indicated by the position of the piston acting on the water phase. Data points are usually referred to as capillary pressure equilibria, but this can be misleading as not all the stability requirements for equilibrium are met (Morrow 1970).

3.2.4.1 General form of capillary pressure data

The saturation changes which result from changes in capillary pressure do not follow a unique functional relationship. A typical example of a set of capillary pressure curves is shown in Figure 3.7, although the exact form will depend on the individual media. Several terms are commonly used to describe them.

Irreducible saturation, S_{wi} : the volume of wetting phase retained at high pressures when the saturation is independent of further increases in the externally measured pressure.

Residual saturation, S_{or} : the volume of non-wetting phase which is entrapped when the capillary pressure is reduced from a high value to zero.

Drainage curve, D : the relationship characteristic of displacement of wetting phase from 100% saturation to the irreducible wetting phase saturation, S_{wi} .

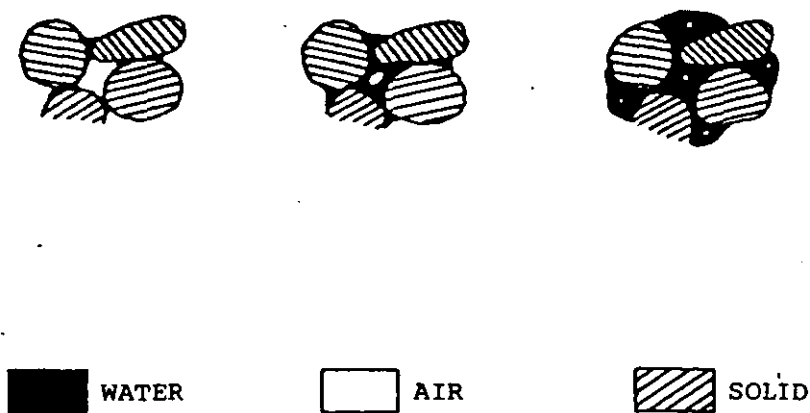


Figure 3.5 - Saturation states of porous media. On increasing the amount of fluid the saturation state changes from a pendular to funicular to insular.

these recesses to form *arc menisci* (pendular type rings). Further increases in saturation causes the radii of curvature of the fluid-fluid interface to alter, which consequently changes the pressure difference across the interface in accordance with the Laplace equation.

Wetting phase menisci are concave towards the non-wetting phase in porous solids, hence the pressure in the wetting phase just below the surface, is lower than the pressure in the non-wetting phase. So as the pressure differential across the porous material is lowered the wetting phase saturation increases. This pressure difference is known variously as, capillary suction, capillary tension, capillary potential or *capillary pressure*. Much valuable information about pore structure and flow properties can be gleaned from experimental curves relating capillary pressure to saturation - called *capillary pressure curves*.

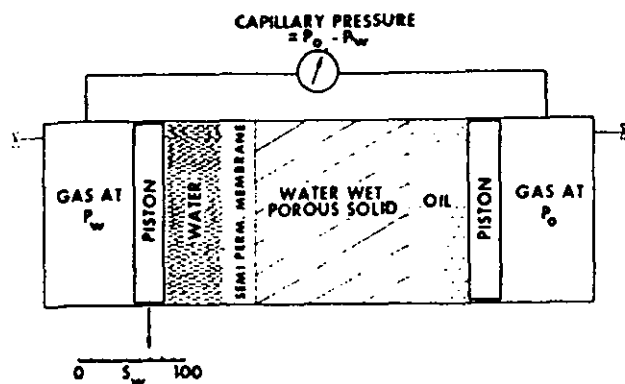


Figure 3.6 - Idealised capillary pressure apparatus.

Imbibition curve, I : the increase in wetting phase saturation from the irreducible wetting phase saturation to the residual non-wetting phase saturation, S_{or}

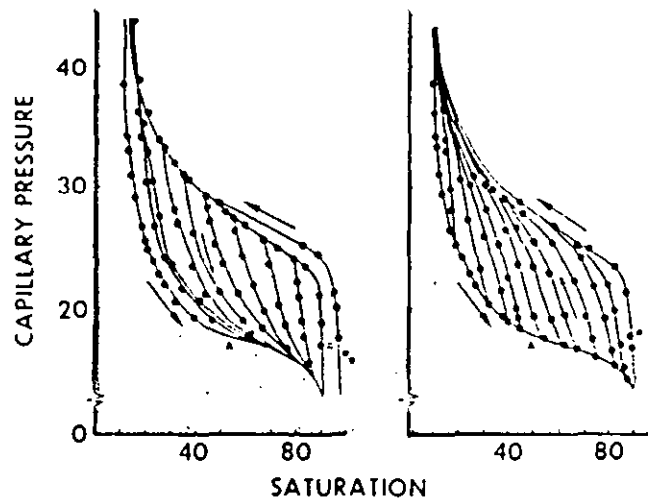


Figure 3.7 - Capillary pressure data for microbeads showing primary scanning curves in addition to the drainage and imbibition curves.

The drainage and imbibition curves constitute a closed and reproducible hysteresis loop, DI , and represent the extreme range over which hysteresis occurs. **Primary scanning curves** within the main hysteresis loop are obtained by reversing the direction of the pressure change at some intermediate point along either the drainage or imbibition curve. Similarly if the path along a primary scanning curve is reversed before the limit of the boundary curve is reached, another path is traversed. Such paths are known as **secondary scanning curves**.

3.2.4.2 The pF scale

Capillary pressures are sometimes expressed as an equivalent height of a column of water in ergs per unit weight, instead of the more usual units of energy per unit volume as in equation 2.52. Between the limits of saturation capillary potential expressed in this way can vary by a factor greater than a million. Hence the potential is often plotted on a logarithmic scale.

Schofield (1935) was the first to express capillary potential in terms of a log scale which he called the pF scale (analogous to the pH scale for acidity-alkalinity). The pF is defined as

$$pF = \log_{10} h_w \quad (3.4)$$

where h_w is the height of a liquid column of unit density which is equivalent to the capillary potential.

Drainage-imbibition of the sort described above is characteristic of meso- to macroporous materials. Mercury porosimetry is the reverse of this process, with extrusion corresponding to imbibition and intrusion to drainage. Mercury is a non-wetting liquid.

3.2.5 Adsorption-desorption pressure curves (sorption isotherms)

The adsorption of a gas by a porous material occurs in several stages as the relative vapour pressure, P/P° , the actual vapour pressure, P , as a fraction of the saturated vapour pressure, P° , is increased. Initially gas molecules adsorb at particular sites on the inner surface by the same mechanisms they adsorb to non-porous surfaces (section 2.6), to form first a monolayer and later multilayers. When these multilayers become sufficiently thick the adsorbed material behaves like a liquid and is said to be *capillary condensed*.

Eventually at the saturated vapour pressure the liquid fills all the pore space. During progressive equilibrium desorption (evaporation) hysteresis, analogous to that in drainage-imbibition, is seen as the relative vapour pressure is reduced. Results of experiments are plotted, as amount adsorbed versus relative vapour pressure, and typically appear like that shown on Figure 3.1. The adsorption portion of the hysteresis loop is analogous to imbibition whilst the desorption portion is similar to drainage.

3.3 MODELS OF PORE SPACE

To manipulate a physical process to produce the greatest efficiency requires that one must first understand the mechanisms underlying that process. With a seemingly incomprehensible system the first logical step is to simplify it to one that can be more readily understood. Newton did this in developing the theory of motion; the trajectory of a solid object of complex shape could be easily followed if the object was reduced to a point mass - thereby behaving in a manner akin to a ball - whose trajectory is simply followed. In short, Newton created a simplified *model* of a complicated system.

The brief description of porous material characterisation techniques given above is merely qualitative. To extract characteristic information from capillary pressure curves, such as pore size distribution, requires that the shapes of both the solid/fluid and fluid/fluid interfaces are known. To be of use practical characterisations of porous materials must yield parameters that describe the actual pore structure sufficiently well too allow explanations to be given of the process(es) under investigation.

It might be possible to obtain detailed mathematical maps of the topology of normal porous materials, but it would be impossible to predict the meniscus shapes inside the pore space. The relevant equation of capillarity could not be solved owing to the complex

and random nature of the solid geometry. Thus the problem for researchers is essentially to find not just one, but two models; one of the matrix and a second for the shape of the capillary surfaces in the modelled matrix.

The requirements of an effective pore space model are that it is simple enough to be amenable to theoretical treatment, whilst quantitatively capable of explaining the various interfacial, hydrodynamic and other properties of practical interest. A compromise is sought between oversimplification on the one hand and elaboration of the model to such an extent that the convenience is lost. Haynes (1975) states that the best justification for a rigorous theoretical treatment of a particular model is found when an experimental study of the same model is practicable - a seemingly obvious requirement, but it is often ignored.

Many models simply represent the pore structure as number of variously sized capillaries of some easily definable shape be they cylindrical, angular or made up of channels formed from parallel plates, arrays of parallel cylinders or packed spheres. These simple geometrical shapes enable the interfacial configurations to be easily calculated from the equations of capillarity, or simply approximated with the use of hydraulic or "insphere" radii.

Many different models have been used, but few pretend to rationalise all porous material processes. Fewer still give reliable quantitative explanations of a single process over the entire range of porous material types (van Brackel 1975). However the development of models has facilitated a much improved understanding of the mechanisms of many processes.

3.3.1 Classification of pore space models

The modeling of pore structure is not a recent phenomena. In the last century a soil physicist, C.S. Slichter (1897) published a model consisting of packed spheres in an attempt to evaluate the dependence of the saturated permeability of a soil on its particle size and porosity. Similar models are still in use today although no satisfactory explanation of the original problem has yet been offered in terms of a packed sphere model.

Pore space models have several other uses other than to characterise a medium. In the study of transport phenomena in porous materials (molecular diffusion, viscous flow, dispersion, fluid/fluid displacement, infiltration, drying and even heat conduction) models are used to obtain values of the transport coefficient (effective diffusion coefficient, permeability etc.) and, when applicable, the driving force (capillary pressure) for the transport equation. Models are employed to obtain particle size distributions and

to simulate sphere packings. Others are purely analytical devices for the definition of coefficients. Finally there are those that are used as overall descriptions of phenomena in which the macro- or microscopic pore structure is not accounted for.

In addition to simplifying the pore geometry most models make several other assumptions. Usually the solid must be homogeneous and isotropic; the pore space continuous; the solid interface fixed (no swelling or consolidation) and inert to the other phases; the number of phases and components restricted and only very simply initial and boundary conditions considered (one dimensional movement).

A comprehensive review of pore space models was given by van Brackel (1975) and Haynes (1975) discusses models used for porous material characterisation. More recently many current developments were discussed at the IUPAC conference (Unger *et al.* 1988). The models have been classified according to the number of geometrical parameters needed to describe them (Everett 1958) and with reference to the pore space interconnectivity by (van Brackel). The latter method is more comprehensive giving four classes:

i) One dimensional interconnectivity. This class includes the simplest and most common models; tubes in parallel or series; tubes with constrictions and adjacent slices (plates). The fluid may move in only one direction. Some examples are shown in Figure 3.8.

ii) Two dimensional interconnectivity. Broadly these comprise networked models of one dimensional models and consequently flow may occur in the plane of the network. See Figure 3.9.

iii) Three dimensional interconnectivity. Here flow also occurs in a plane perpendicular to the overall transport direction. These are the most promising type and include sphere packings, tetrahedral networks and tubes and junctions (bonds and sites or motorway and interchange) regularly or randomly arranged. See Figure 3.10.

iv) Strictly zero dimensional interconnectivity. Figure 3.11 shows some examples. These models consist of simple capillary elements used in explanations of particular phenomena, like ink bottle hysteresis or the independent domain theory (see section 3.5.2).

3.4 MODELS OF INTERFACIAL CONFIGURATIONS

The shapes of capillary surfaces are given by the fundamental equations of capillarity. In only a few simple cases is a trivial exact solution afforded by the Laplace or Kelvin equation. One such example is the case of the meniscus in a cylindrical tube under zero gravity conditions. Here the meniscus is part of a sphere and is described by

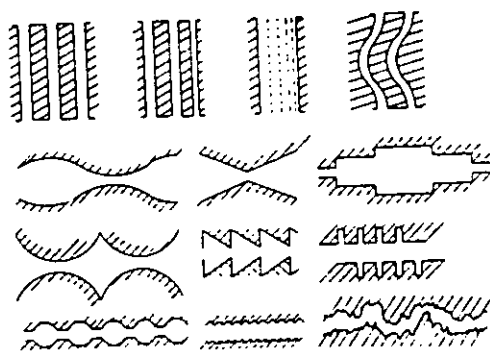


Figure 3.8 - Some elements of pore space models with one dimensional connectivity.

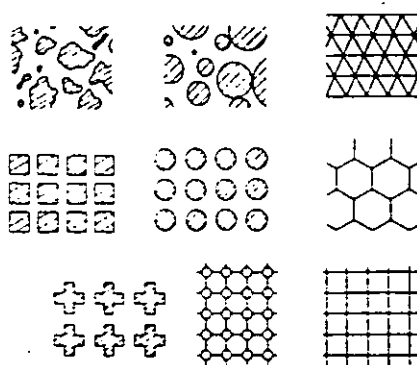


Figure 3.9 - Elements of pore space with two dimensional connectivity.

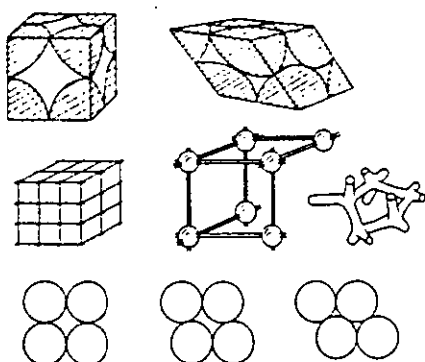


Figure 3.10 - Elements of pore space with two dimensional connectivity.

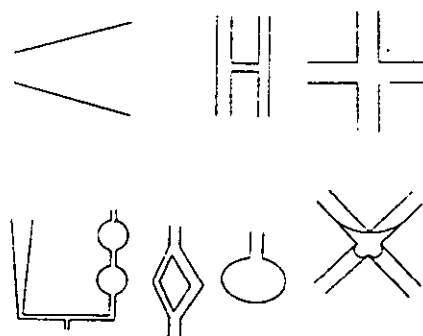


Figure 3.11 - Simple capillary models used in explanations of specific behaviour of porous media having strictly zero-dimensional interconnectivity.

a single radius of curvature (see section 2.4.3). The vast majority of proposed pore space models for capillary processes are made up of tubular cylindrical elements in order to facilitate this one parameter solution.

Solution for the exact shapes of capillary surfaces that are not given by a single radius of curvature involve complicated integrations of the Laplace equation even if simplifying assumptions are made. The effects of a gravitational field on fluid behaviour is always ignored in porous materials, the scale of the pore space ensuring that interfacial forces dominate (i.e. low Bond number - eq. 2.44). Even in pore space models comprising basic geometrical objects, such as spheres, determining the meniscus shape necessitates complicated numerical integrations that often require considerable computer time (see section 4.2).

The difficulties in predicting interface shapes has restricted development of non-cylinder based models (geometrically the most complicated pore models used are sphere packings). In those that have been employed the interfacial configuration is usually approximated, almost always as a zone of a sphere. The use of sphere approximations has been justified on the grounds that the matrix model is itself only an approximation of the actual pore space (van Brackel 1975). Thus the time involved in obtaining accurate interfacial configurations outweighs the benefits provided to the model. Van Brackel & Heertjes (1978) and Mason & Morrow (1984b) have reviewed methods for affecting approximation and the latter compared the results of each against experimental data from sphere packs.

3.4.1 Hydraulic radius models

In connection to porous materials the hydraulic radius, R_h has been defined as both the ratio of tube area to tube perimeter (Hwang 1977) and as that of pore volume to pore area (Anderson 1987a). For a capillary of cylindrical cross-section the tube and hydraulic radii are equivalent.

The hydraulic radius gives exact curvatures for menisci in uniform tubes when the sphere portion spans the entire cross-section of the tube (Carman 1941). Hwang (1977) attempted to extend its application to tubes containing angular corners (polygons, contacting cylinders etc.), but found his results differed significantly from the exact solutions of Princen (1969a). In wedge-shaped corners a wetting capillary surface must rise in the corners, in the manner derived by Concus & Finn (1969), in order to satisfy boundary conditions. Hence the complete tube cross-section is not spanned by the sphere portion. In the case of sphere packings this phenomena is manifest by the formation of pendular rings around points of contact. Commenting on Hwang's results, Mason & Morrow (1984b) found wide deviations for systems that form liquid wedges or rings. This was demonstrated by both experimental data and other semi-theoretical approximations.

Carman applied the hydraulic radius model to triangular pores given by close packing of equal spheres (closed triangular pores) and found, for a perfectly wetting liquid, a maximum normalised curvature of 19.5, in poor agreement with the accepted experimental value of approximately 11.4 for pore drainage (Haynes 1975).

3.4.2 The Haines incircle approximation

Haines (1927) arrived at an empirical approximation for interfacial configurations after observing capillary displacement in the various pore shapes that arise in regular sphere packings. He proposed that the curvature of a meniscus that just passes through

the central constriction of a pore (that associated with drainage) can be approximated by that of a sphere which just touches the spheres defining the pore throat. Essentially, Haines redefined the local geometry to that of a cylindrical tube.

Application of the Haines "incircle" or "insphere" approximation is straightforward and it has been employed in many studies concerning processes such as mercury porosimetry, sorption, drainage-imbibition and fluid/fluid displacement (see Haynes 1975). It has also been proposed that the curvature associated with imbibition can be modelled using the radius of the sphere that just touches the spheres defining the pore cavity (van Brackel 1975). However neither model is very precise. The maximum normalised curvature obtained in the triangular packing is 12.9.

3.4.3 The Mayer & Stowe - Princen analysis

The Mayer & Stowe - Princen theory, or the *MS-P theory* (named as such after Mason & Morrow 1984a), is a method for the determination of exact, one parameter, interfacial configurations of non-axisymmetric capillary surfaces in uniform tubes when gravitational forces are absent. It is the subject of the experiments conducted for this study and will be discussed in detail later (see chapter 5). The analysis was developed (separately) by Mayer & Stowe (1965) and Princen (1969a) as models for capillary surfaces in porous media. The following discussion serves as a brief historical background to the method and its application (further details are given in chapter 4).

a) Mayer & Stowe proposed what they believed to be an exact solution for the maximum curvature in regular sphere packings based upon what amounts to an integrated form of the Gauss equation (2.69). The cross-section of the meniscus in the pore throat is defined in part by circular arcs spanning the points of contact between the spheres. Pore shapes varied from the closed triangular to the closed square arrangement.

The underlying theory presented by Mayer & Stowe was queried at the time of publication by Melrose (1965a) and later by Haynes (1975) on the grounds that exact solution of the sphere problem must take into account the converging-diverging nature of the sphere geometry (see section 4.2). The analysis has however proved successful as a method of determining pore size distributions by mercury porosimetry (section 4.3)

b) Princen (1969b) arrived at an identical, but exact solution for the curvature between three contacting *cylinders* to that of Mayer & Stowe for closed triangular packings of spheres, reflecting the true nature of the Mayer & Stowe analysis. A normalised curvature of 11.3 is given by both analyses, much closer to the experimental value in triangular sphere packings, indicating the validity of the method as an approximation for curvatures in the regular sphere packing. Figure 3.12 shows the hydraulic, incircle and MS-P approximations compared with experimental data of

Hackett & Strettan (1928). Van Brackel & Heertjes (1978) have also found Princen's analysis to yield results closer to experimental data.

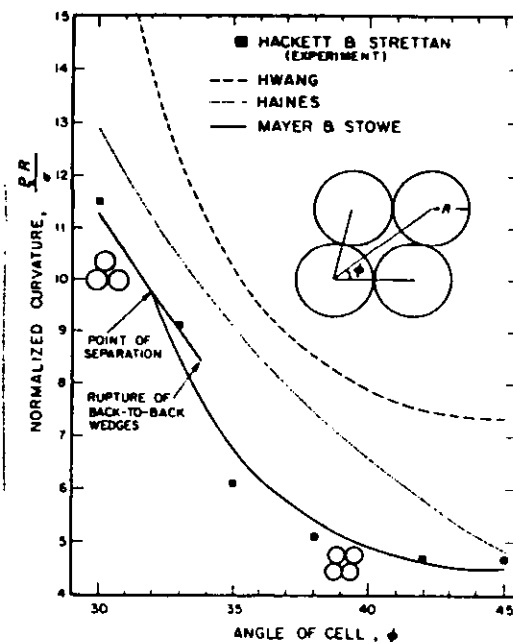


Figure 3.12 Comparison of the experimental results of Hackett & Strettan from sphere packs with the Haines incircle approximation, Hwang's hydraulic radius method and the MS-P method.

Princen was interested in capillary rise in bundles of rods where gravity plays a significant part. Here the analysis only approximates the height of rise, but is still of much greater accuracy than other methods available; the capillary tube and hydraulic radius models.

3.4.4 The Dodds approximation

Dodds (1978) noted the close agreement between Princen's results for rods and the experimental results of Hackett & Strettan (1928) for spheres. He went on to calculate displacement curvatures for pores formed by three cylinders with size and spacings varied. These configurations were then taken as models for pores found in sphere packings

Dodds also noted an approximate empirical relationship between his results and those given by the Haines incircle approximation,

$$r_{MS-P} = 0.875 r_{incircle} \quad (3.5)$$

suggesting a very simple approximation method. The factor 0.875 is derived from the ratio of MS-P to incircle curvatures for the closed triangular pore. However, Mason & Morrow (1984b) found a different relationship for equal, but variably spaced spheres.

$$C_{MS-P} = C_{incircle} - 1.5 \quad (3.6)$$

where C denotes the normalised curvature, R/r , the ratio of sphere radius to the radius of curvature. It appears that this type of correlation must only be applied selectively.

All the above modeling techniques for interfacial configurations have also been applied in situations where the contact angle is non-zero. The hydraulic radius and incircle approximations are simply multiplied by a $\cos \theta$ factor; agreement with experiment is poor (see below). Only the MS-P analysis uses a less trivial correction. There is some evidence that, although not providing as accurate an approximation as at zero contact angle, the MS-P analysis qualitatively agrees with experimental data from sphere packings (van Brackel & Heertjes 1978, Bell *et al.* 1981)

3.5 HYSTERESIS IN POROUS MATERIALS

Explanation of observed hysteresis in mercury porosimetry, drainage-imbibition and adsorption-desorption is central to the understanding of other processes involving the movement of fluid/fluid interfaces in porous materials. The following discussion illustrates the application of pore space and interfacial configuration models.

Physical characteristics of porous materials derived from capillary pressure curves or sorption isotherms, such as pore size distributions, can only be said to be realistic when the model from which they are determined is itself capable of explaining the observed hysteresis.

Hysteresis shown by liquids entering and leaving pore space cannot be explained as simply as that shown by liquids on non-porous materials (section 2.7.6). To date, hysteresis has been attributed to a number of possible causes, but is generally understood to be dependent on the interaction of wettability, pore geometry and saturation history. It is fair to say that at the present time a full understanding of the mechanisms of hysteresis is missing (Everett 1988).

3.5.1 Contact angle hysteresis and one dimensional models

Many attempts to characterise porous solids, model fluid flow or account for hysteresis in porous media have represented the pore space as assemblages of one dimensional tubes, most commonly by the capillary tube model. The spontaneous invasion of pore space by a wetting fluid is a manifestation of the same capillary forces that cause capillary rise in thin tubes, where the capillary pressure is given by the Washburn equation:

$$P_c = \frac{2\sigma \cos \theta}{R} \quad (2.45)$$

It is common practice for pore size distributions to be determined using the capillary tube model by porosimetry, Kelvin analysis or, more recently, thermoporometry. The hydraulic radius model finds use in a more general sense to compare similar media.

3.5.1.1 Porosimetry

In mercury intrusion porosimetry non-wetting mercury is forced into the pore space under external pressure. This process is distinguished from suctional porosimetry where a wetting liquid is used. In either case, if all pores are equally accessible then, at a particular pressure, P_c^* , only those with constriction radii given by

$$R_p < \frac{2 \cos \theta}{J} \quad \text{where} \quad J = \frac{P_c^*}{\sigma}$$

will be filled. Each increment of applied pressure causes the next smaller group of pores to be filled.

The measurement of pore size in this way was first proposed by Washburn (1921), but did not find widespread acceptance until Ritter & Drake (1945) published the first experimental work. Intrusion pressures of up to 60,000 psi were used.

The analysis of the data of volume penetrated versus pressure is as follows. If dV is the volume of pores with radii between R_p and $R_p + dR_p$ and dV is related to R_p by some distribution function, $D(R_p)$ (usually normal or Gaussian), then

$$dV = D(R_p) dR_p \quad (3.7)$$

From the Laplace equation (2.30)

$$P_c dR_p + R_p dP_c = 0 \quad (3.8)$$

Combining 3.7 and 3.8 yields

$$D(R_p) = \frac{P_c dV}{R_p dP_c} \quad (3.9)$$

$D(R)$ is obtained from a plot of V versus P_c . The accessible pore volume and the surface area may also be determined from the data. Porosimetry (suctional, in addition to mercury) is used on meso- to macroporous materials. Capillary tube model results can compare well with BET analysis. It will not detect significant numbers of pores of less than 5 nm in size even if extended to sufficiently high pressures.

Mason (1988a) (and others) objects to the use of the capillary tube model in porosimetry as it gives pore size distributions in the region of the threshold (see Fig. 3.2) that are so narrow as to be unlikely. Other debate concerns which value of the contact angle to apply.

3.5.1.2 Kelvin analysis

Kelvin analysis is analogous to porosimetry but makes use of Kelvin phenomena in meso- to microporous media. The desorption branch of a nitrogen isotherm is used in conjunction with the Kelvin equation (2.40) to determine pore size distributions.

The original analysis with the capillary tube model is due to Cohan (1938). He assumed that the pore radius, R_p , was equal to the Kelvin radius, r_k , given by

$$r_k = -\frac{2\sigma v}{RT \ln(P/P^o)} \quad (3.10)$$

Current procedures recognize the requirement to add an adsorbed film thickness, t , to the Kelvin radius (see Adamson 1976) giving

$$R_p = r_k + t \quad (3.11)$$

In order to evaluate R_p values of t must be obtained from a standard isotherm that is either experimentally determined on a similar, but non-porous, surface or theoretically derived.

The accuracy of Kelvin analysis is in doubt over what thickness of adsorbed layer to add in addition to the on-going debate over the validity of the equation itself (section 2.4.2). Usually the contact angle is taken to be zero, but this assumption is also a matter of debate (Everett 1988).

3.5.1.3 Thermoporometry

A porous material characterisation technique only developed over the last decade, thermoporometry is a;

"method of textual characterisation which is based on the thermal analysis of the liquid/solid transformation of a pure capillary condensate inside a porous body" (Quinson & Brun 1988).

Broadly, the method takes advantage of triphasic systems: liquid/solid/vapour capillary condensates. When a porous solid is totally saturated the usually divariant triphasic system becomes univariant; the curvature of the gas-solid interface being zero.

Like porosimetry and Kelvin analysis the method can be used for pore size distribution, pore volume and surface area determination. It relies on equating the curvature of a solid/liquid interface, J , to the pore radius by a relationship between the curvature and the equilibrium temperature, T :

$$T = T_o - \int_T^{T_o} \frac{v_L}{\Delta S_T} d(\sigma_{LS} J_{LS}) \quad (3.12)$$

where T_o : normal temperature of the triphasic equilibrium
 σ_{LS} : surface tension of the liquid solid interface
 ΔS_T : molar entropy of fusion
 v_L : molar volume of the liquid
 and $J_{LS} = 2/R_n$

The thermoporometric radius, R_n , is again different to the pore radius, R_p , due to the existence of an interphase of thickness t made up of molecules which are not involved in the thermal effect of the change of state.

3.5.1.4 The Leverett j -function

Although the shapes of capillary pressure curves vary from material to material, they have several features in common and this has led to attempts to devise some general method to describe all such curves. Leverett (1941) approached the problem from the stand-point of dimensional analysis, reasoning that capillary pressure should depend upon porosity, ϵ , interfacial tension, σ , and some kind of mean pore radius. He defined a dimensionless function which is known as the Leverett j -function:

$$j(S_w) = \left(\frac{\sqrt{k/\epsilon}}{\sigma} \right) P_c(S_w) \quad (3.13)$$

where k is the permeability of the porous solid, as defined by Darcy's law, and relates to the ease with which a fluid may be made to flow through a material by an applied pressure gradient. The ratio of permeability to porosity is taken as being representative of a mean pore radius. The ratio is related to the hydraulic radius R_h , via the well known Darcy and Kozeny-Carman equations and is the ratio of the volume of pore space to the wetted area (Morrow 1970).

For a given wettability, the Leverett j -function should be the same for each set of geometrically and topologically similar porous media. The dimensionless "Leverett number" is also used by some authors (for example, Melrose & Brandner 1974):

$$N_{Le} = J\sqrt{k/\epsilon} \quad (3.14)$$

where $J = P_c/\sigma$; the curvature of a spherical meniscus.

The j -function finds application within the oil industry as a means by which the capillary pressure curves measured on different cores from the same reservoir can be compared (Anderson 1987a):

Most early investigators, such as Zsigmondy (1911), attempted to explain the hysteresis phenomena on the pressure-saturation curves in terms of contact angle hysteresis in cylindrical capillaries. Their analyses were shown to be deficient when hysteresis in porous materials was found to be exhibited by wetting liquids, a phenomena

not possible in capillary tubes (see for example Morrow 1976). However, the drainage of wetting liquids from bundles of capillary tubes has been successfully used to model drainage from real porous solids (see for example Washburn 1921, Purcell 1949). However, the model has proved incapable of successfully accounting for imbibition curves.

The simple capillary tube model is inadequate in at least three ways as a physical description of porous media (Larson 1981)

- i)* The form " $\cos \theta$ " does not adequately describe the wettability behaviour of real porous media.
- ii)* The model completely ignores the irregular geometry of real porous matrices.
- iii)* The model does not account for the branchiness of the actual pore space.

Despite the inadequacy of contact angles to fully describe capillary pressure hysteresis in porous materials, there is little doubt that wettability can be a major factor (Anderson 1987a). As described in section 2.7.6 the wettability which one fluid of a fluid pair displays towards a flat solid surface is difficult to quantify in terms of an unambiguous measurement of contact angle. The direct measurement of contact angle within a porous material has not yet been achieved. The analysis of contact angle phenomena in porous media is very complex and little experimental data exists.

Morrow, who's work on contact angle hysteresis on the rough surfaces of non-porous media (1974) was described previously, has however conducted extensive studies on contact angle phenomena in six sintered teflon porous media (1976). Air and the pure organic fluids employed in the earlier study were used to vary the wettability whilst the geometry was fixed. The use of PTFE media ensured that surfaces were chemically inert, homogeneous and of uniform wettability.

Among Morrow's findings were that drainage capillary pressure curves are almost independent of contact angle for $\theta < 50^\circ$ whilst imbibition curves showed no wettability effects for $\theta < 20^\circ$ (these results are supported by experiments on oil field cores: Anderson 1987a). He also found strong evidence that the flat surface contact angles for receding menisci θ_r , and for advancing menisci θ_a , are those angles operative during capillary invasion of porous media of homogeneous wettability, but that the situation is complicated by roughness and pore geometry.

On a smooth surface the contact angle is fixed, but on the sharp edges found in porous media this condition is relaxed and there are a wide range of possible contact angles (Good 1979). Morrow (1970) postulates that most of the three phase contact line

will be located at the sharp edges as at these edges the contact angle can vary without moving the position of the contact line. Thus pore geometry will influence the three phase line and can change the apparent contact angle.

Although porous systems cannot be classified according^{to} their operative contact angles they can be classified by their imbibition behaviour as wetted, intermediate or non-wetted (Anderson 1987a). Porous media need not exhibit uniform wettability over their entire internal surface. For example, surface heterogeneity within porous media is almost the norm for oil bearing rocks and is certainly responsible for the observed instances in which an oil field core imbibes both oil and water (Anderson 1987a).

Other, less regular, one dimensional models have been proposed for porosimetry and drainage-imbibition and can partially account for the irregular geometry of real porous materials. For example, Jenkins & Rao (1977) used an elliptical tube model for mercury porosimetry in which the curvature of a meniscus was found from the hydraulic radius of the tube. Different sized capillary tubes in series and cylindrical tubes with constrictions (Svata 1971) have also been employed as models, but again in conjunction with the Washburn equation.

A consequence of the normally irregular geometry of porous materials is that some wetting liquid is retained after drainage: the irreducible wetting phase saturation. In unconsolidated media most of this liquid is held as pendular rings around particulate contacts and as liquid wedges in consolidated media. No non-angular one-dimensional model can account for this phenomena as each model pore empties completely on drainage. Mason & Morrow (1989) have noted some success in this area by using a triangular pore model combined with an exact MS-P analysis for the interfacial configuration. The model shows a distinct threshold, a significant hysteresis between drainage and imbibition, and an irreducible wetting phase saturation. Angular models of this type also have the advantage that under partially wetting conditions the dependence of the MS-P curvature on contact angle is not given by the simplistic $\cos \theta$ factor, but depends upon the particular geometry.

Despite the proven failings of both the capillary tube model and/or contact angle hysteresis to account for capillary pressure (hydrostatic) hysteresis both still find widespread application. Its simplicity is attractive, and few of the more complex models provide quantitative results significantly closer to those observed in practice.

3.5.2 Independent behaviour and zero dimensional models

3.5.2.1 *The ink bottle effect*

Contact angle hysteresis, though important, cannot entirely account for capillary pressure hysteresis. A fluid pair for which the intrinsic contact angle, θ_c , is zero has no rough surface contact angle hysteresis yet considerable capillary pressure hysteresis is

still seen (Morrow 1976). At least part of this remaining hysteresis is attributable to what has become known as the *ink bottle effect* (see for example, Haines 1930 and Melrose 1975).

As a meniscus or two-fluid interface passes through the converging-diverging geometry that comprises an ink bottle pore, it is subjected to local expansions and contractions as the cross-section changes during motion. Consequently the meniscus is compelled to adopt instantaneous shapes which represent considerable departures from equilibrium. The meniscus passes through such shapes rapidly but continuously, and performs "*Haines jumps*" (so called after their discoverer, Haines 1927). An alternative designation of *rheon* has been suggested (Morrow 1970, Melrose & Brandner 1974). The accompanying energy dissipation is a source of capillary hysteresis. These jumps are manifested by pressure fluctuations during drainage or imbibition.

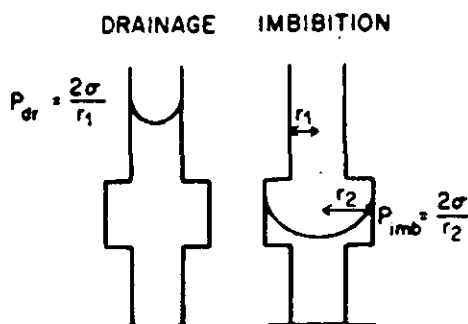


Figure 3.13 - Hysteresis in capillary rise due to pore geometry illustrating the ink bottle effect.

Consider a variable radius capillary tube with a circular cross-section as shown in Figure 3.13. To drain completely wetting fluid from the tube requires drawing the meniscus through small cross-sections. Thus the drainage capillary pressure is given by

$$P_{dr} = 2\sigma/r_1 \quad (3.15)$$

where r_1 is the radius of the smallest cross-section. The rheons correspond to a process in which the wetting phase saturation is decreasing and are called *xerons*. To imbibe, on the other hand, requires that the meniscus be drawn back through the larger cross-sections so that

$$P_{imb} = 2\sigma/r_2 \quad (3.16)$$

where r_2 is the radius of the largest cross-section. Here, the increasing wetting phase saturation classifies the rheons as *hydrions*. Since pores in real porous media are certainly of variable cross-section, ink bottle hysteresis is to be expected.

The pressure fluctuations caused by Haines jumps can be seen easily with converging-diverging capillaries and with packings of spheres (Morrow 1970). In media having very fine pores or particles these pressure fluctuations are generally too small to be observed, but ink bottle hysteresis will be present.

If an ink bottle pore is stacate (dead-end) then liquids may become entrapped. This phenomenon is particularly apparent with non wetting liquids such as mercury, used in porosimetry experiments (Adamson 1976), and oil ganglia in displacement studies (Anderson 1986b). Consideration of entrapment was a factor in the choice of mercury intrusion, as opposed to extrusion, for pore size distribution determination.

The ink bottle effect illustrates a mechanism of capillary pressure hysteresis, but converging-diverging models with only a one dimensional transport direction are still limited in accounting even qualitatively for hysteresis.

3.5.2.2 *The Independent Domain Theory*

Discussions of hysteresis indicate that information about the pore structure is contained not only in both the ascending and descending branches of the hysteresis loop, but also in the families of adsorption and desorption (or drainage and imbibition) scanning curves within the loop.

Hysteresis can be regarded as representing the macroscopic behaviour of a porous medium, whilst it is reasonable to assume that the mechanisms responsible for hysteresis must, like Haines jumps, occur at a microscopic level. Everett and co-workers (see Everett 1958) proposed such a mechanism where the net behaviour of the whole medium is governed by the average behaviour of a set of micro-systems or *domains*.

The independent domain theory can be thought of as an extension of the ink bottle effect. It regards the difference between the pressures at which ink bottle pores fill and empty as the prime cause of hysteresis. The interconnected void space within a medium are regarded as being sub-divided into a series of voids or cavities which are connected together via smaller openings usually called windows. If the cavities and windows vary in size, then for a small change in pressure only a small fraction of cavities will empty or fill.

Everett's domains consist of those elements of the medium that fill at a particular pressure, P_1 , and empty at another particular pressure, P_2 , independently of other elements. The associated volume change, V , is the third characteristic variable. A plot of the function $V(P_1, P_2)$ produces a surface in three dimensions from which it is possible, in theory, to calculate a family of adsorption scanning curves from a family of desorption curves and vice versa.

The independent domain model accounts qualitatively for a wide range of properties of systems exhibiting hysteresis. However it does not always give a satisfactory quantitative representation. The model has been verified in a number of systems including the wetting-dewetting of rocks (Lai *et al.* 1981) and in soils (Poulavassilis 1962), but it breaks down completely in others (see for example Topp & Miller 1966, Topp 1969, van Brackel & Heertjes 1978).

Morrow (1970) attributes the weakness of the independent domain theory to two fundamental causes:

- i) The assignment of draining and filling pressures to a given region can be unrealistic as displacement pressures are also determined by phase continuity and accessibility, so called *dependent* behaviour.
- ii) Pore space cannot be divided into volumetric zones which show one to one correspondence with respect to drainage and imbibition behaviour.

3.5.3 Dependent behaviour and two and three dimensional models

Problems in the independent domain theory centre on whether Everett's assumption that the domains are independent is justified. Independent behaviour is relatively obvious for the adsorption of a gas in porous media. The gas is able to penetrate into every connected cavity independently of the behaviour in neighbouring pores. However, many other processes exhibit *dependent behaviour*, such as network and pore blocking effects. In the desaturation of capillary condensed gases and drainage processes *pore blocking effects*, or *neighbouring pore effects*, can be important. This effect is illustrated in Figure 3.14, where a pore cannot empty until at least one of its near neighbours has emptied, indicating dependent or co-operative behaviour.

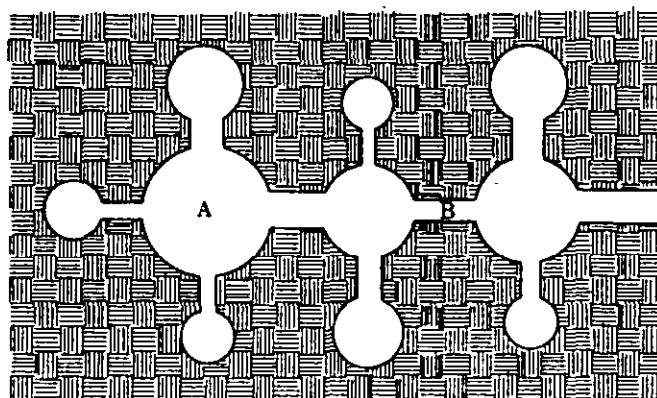


Figure 3.14 - Illustration of the "pore blocking effect". Pore A will empty when a meniscus can pass through throat constriction B. The drainage is thus not solely determined by the immediate characteristics of pore A, but depends on its "neighbour".

That pore blocking may account for the inaccuracies within the independent domain theory was recognized quite early at the Colston symposium by Barker (1958) and by Everett himself (1958). Since this time methods have been developed that account for pore blocking effects and liquid entrapment with the use of randomly interconnected models of the pore space.

Neighbouring pores may also cause distortions of pore size distributions. With the application of the MS-P theory in regular sphere packings Mason & Morrow (1984b) have shown that drainage of one pore can effect drainage of its neighbour by altering boundary conditions. This can result either in simultaneous drainage of both pores or, if the neighbouring pore remains filled, its drainage curvature may be reduced. Both these mechanisms will tend to cause pore sizes estimated from capillary pressure data to be narrower than that given by the geometrical structure of the packing.

Diametrically opposed to the independent domain theory is the idea that the whole of hysteresis can be explained by *network effects*. The implication is that each cavity within the pore structure has at least one window to it with the same radius of the cavity so that the filling and emptying of a single pore is reversible (Everett 1988). This has been demonstrated for a random sphere packing by Mason (1971).

Models made up of contacting spheres have several useful properties; including network effects (co-operative behaviour) and ink bottle hysteresis. The use of packed sphere models to account for hysteresis and other porous material phenomena has, like the capillary tube model, a long history. In 1897 a soil scientist, C.S. Slichter, published the first proposal for such a model, comprised of regular lattice packings of equal spheres. This model is now known as the *ideal soil model*. Slichter was attempting to calculate the dependence of the saturated permeability of a soil on its particle size and porosity. His attempt was only partially successful and until recently most work in this area has employed simpler models based on cylindrical tubes.

In the 1920's the ideal soil model was first applied to capillary pressure hysteresis by way of a long running controversy over points of mathematical detail between W.B. Haines (1925, 1927, 1928, 1930) and R.A. Fisher (1926, 1928). Haines had the last word, but boths' points were proven lacking in the end! Some years later packed sphere models were applied to hysteresis in capillary condensation (Higuti & Utsugi 1952, Carman 1953) and mercury porosimetry (Kruger 1958, Mayer & Stowe 1965, 1966). Development of the regular and random model continue to the present day in all three areas (see Haynes's 1975 review for details and for more recent developments Unger *et al.* 1988).

Sphere packed models have yet to yield much in the way of quantitative explanations of hysteresis in real media. They suffer from several drawbacks: there are no pore blocking effects in the regular model and also very little experimental data, whilst the theory for the irregular model remains thin, but the experiments numerous.

In common with other geometrically non-simple models it is very difficult to determine interfacial configurations of menisci. This has proved a major drawback to the development of packed sphere models (Haynes 1975).

Recent thinking on hydrostatic hysteresis in porous materials concludes that it seems more likely that the hysteresis mechanism in most porous media will be a combination of both network and domain behaviour. Aspects of the behaviour of a fluid in a porous medium can be determined using a two or three dimensional network model and statistical "*percolation theory*" (see for example Chatzis & Dullien 1977, Larson & Morrow 1981, Larson *et al.* 1981).

With the application of percolation theory, together with a model of the connectivity of the pore space in terms of a Bethe tree of sites (cavities) and bonds (windows), Mason (1988b) has shown that hysteresis depends on the distribution of both cavity and window sizes and on the connectivity of the network. Dependent behaviour in this model, is present except along the adsorption boundary curve and during the refilling of pores that have been emptied in a desorption scanning curve. A detailed analysis of experimental data obtained for xenon sorption in porous glass supports Mason's theory.

3.6 SUMMARY

The above discussion serves to broadly illuminate the study of porous materials - a major area of application of capillarity. The complicated relationships between characterisation on the one hand, and the practical performance of porous media on the other have been considered. The importance of modeling, both of the pore space and of the capillary surfaces it may contain, has been illustrated. The review concentrates on only one of the many processes to which models must be applied in order to comprehend observed phenomena. That the understanding of hysteresis is incomplete and some of the evidence contradictory is indicative of not only the wide diversity of porous material types, but of the complexity of fluid/fluid behaviour in the pore space.

CHAPTER 4

Interfacial configurations

4.1 INTRODUCTION

The shape of fluid/fluid interfaces are important in instances where the capillary properties of a liquid or liquids dominate. In chapter 3 many processes that occur in porous materials were shown to be dependant on capillary properties of liquids contained in the pore space. Outside the study of porous media the configurations of liquid interfaces are significant in diverse areas such as the shape and stability of liquid drops, the waterproofing of fabrics, solderability of electrical wires and the design of storage tanks for use in space.

Table 4.1 summarises some of the areas where interfacial configurations play a substantial part together with introductory references to the literature. Note that in many of the areas mentioned the detailed shape of the interface is not required, merely its mean curvature. Once the curvature is known other parameters can be obtained such as the volume of liquid, the surface area of the interface or the forces acting on the solid surfaces.

The shapes of the fluid interfaces encountered in the areas highlighted in the Table 4.1 vary from simple constant curvature surfaces - like drops in space - to highly complicated configurations such as those contained within many porous media. To theoretically predict the shape of any fluid interface requires the solution of the Laplace equation (or the Kelvin equation for adsorption phenomena).

In section 2.4.3 some solutions of the Laplace equation were given for menisci in cylindrical tubes, for both constant curvature and gravity distorted menisci, in the context of capillary rise. The approximate nature of some of the equations (for example the Rayleigh equations; 2.49 and 2.51) for these moderately simple systems is indicative of the difficulties encountered when predicting the shapes of more complicated menisci. It is in order to avoid these difficulties that such gross approximations are employed in some pore space models (section 3.4).

Since its inception in 1805 there have been many attempts to solve the Laplace equation to yield the exact shapes of liquid interfaces when their configuration is not straightforward. The majority of this work has involved the behaviour of drops and bubbles where an axis of rotational symmetry greatly simplifies the problem. Only recently have techniques been developed that, in principal, enable the computation of the shapes of fluid bodies that are neither rotationally or translationally symmetric. Much

Table 4.1 Areas where the interfacial configurations of fluid interfaces have an important role. Some specific applications are shown together with references containing details.

Subject	References
MEASUREMENT OF LIQUID PROPERTIES	
Interfacial tension	Jaycock & Parfitt '87
Contact angle	Neumann & Good '79
on fibres	Carroll '76, Herb <i>et al.</i> '83
Solderability	Schumacher <i>et al.</i> '45, Shipley '75
EQUILIBRIUM & STABILITY OF BUBBLES & DROPS	
Retention of pesticide sprays on leaves	Boucher '80 Michael & Williams '81
Condensation of drops in a condenser	Furmidge '62 Graham & Griffith '73
POROUS MATERIALS	
CHAPTER 3	
Enhanced oil recovery	Latil '80
Blob mobilisation	Mason & Yadav '83
Connate water distribution	Morrow '71
Threshold pressure	Thomas <i>et al.</i> '68
Behaviour of foams	Mast '72, Ransohoff <i>et al.</i> '87
Fluid flow	Greenkorn '83
Two phase laminar flow	Legait '83
Characterisation	
Porosimetry	see
Adsorption-desorption	chapter 3
Drainage-imbibition	
Wetting and Capillary rise	van Brackel '75
Sap rise in trees	Pickard '81
Wetting & wicking in paper & textiles	Princen '69b, Schwartz '69
Soil studies and hydrology	Emmerson <i>et al.</i> '78
Determination of soil saturation	Haines '25, Fisher '26
Deformation of moist soils	Haines '25, '27 Fisher '26
Adhesion of dust & powder to surfaces	Zimon '69
Dispersion of pigments & wetting of powders	Carman '53
Drying	Key '72
Film formation from latices	Sheetz '65, Mason '73
Heterogeneous catalysis	Youngquist '70
Liquid phase sintering of finely divided metals and polymers	Heady & Cahn '70
Mechanical dewatering of powders and sludge	Fricke <i>et al.</i> '73
Porous electrodes	Katan & Grens '71
Rising damp	Mason '74
Tensile strength of moist powders	Clark & Mason '67 Mason '72
Waterproofing of fabrics	Adam '58
MISCELLANEOUS	
Coating processes on wires and filaments	Carroll '84
Crystal growth from the melt	Tatarchenko '77
Detergency	Jaycock & Parfitt '87
Floation	Kitchener '77
Proposed Spacelab experiments	ESA '76
Storage tank design for use in space	Petrash & Otto '64

of the complexity of the various analyses arises from considering the interface to be distorted by gravity, to be in converging-diverging geometry or to be in non-axisymmetric tubes.

For fully three dimensional interfaces the Laplace equation must be solved in the form of a non-linear, partial differential equation for either specific or free boundary conditions. To date only a small number of successful studies have been published. These depend heavily on the choice of specific boundary conditions: the solid geometry, the location of the three phase line and the solid/fluid contact angle. The methods employed are too time consuming to be employed on a regular basis and it is for this reason that techniques giving quick, reliable approximations of interfacial configurations still find widespread applications.

Over the following pages, common solution methods for the shapes of capillary surfaces are discussed in terms of the geometry of the interface and the solid that bounds it. The limitations of the methods are highlighted. There appear to be no texts that cover this area adequately, but much of the information presented here is discussed in reviews by Boucher (1980) and Michael & Williams (1981) (axisymmetric surfaces) where details of the solution methods can be found. Brown (1979) gives a detailed analysis of finite element methods (FEMs) used for some non-axisymmetric surfaces.

4.2 CLASSIFICATION OF INTERFACIAL CONFIGURATIONS

Michael & Williams (1981) classify (axisymmetric) capillary surfaces according to the nature of the force field governing the *equilibrium*:

- i)* Menisci supporting a constant or zero pressure difference as, for example, with soap bubbles and interfaces between neutrally buoyant fluids.
- ii)* Interfaces between two fluids of different density in an external gravitational field, characteristic of drops or bubbles formed in immiscible fluids of different densities under ordinary terrestrial conditions.
- iii)* Equilibrium studies describing menisci formed at the surface of rotating bodies of fluid.
- iv)* Equilibrium of the meniscus under the action of electrostatic fields in which the electrical stresses enter into the force balance at the meniscus surface.

For the purposes of this study only the first two classes are considered, but in addition, the shape of the solid geometry bounding the meniscus is important as this determines

the nature of the problem - solution with free or fixed boundary conditions. Table 4.2 shows capillary surfaces classified in this way with indications of the degree of difficulty encountered when solving the Laplace equation.

The exact equations governing an interfacial configuration are definable, but can only be solved analytically for a few simple cases. Usually solution is effected using non-exact numerical integration techniques. The equations may require simplification, particularly with the more complicated shapes. The near-exact solutions referred to here are distinguished from the approximate configurations discussed in chapter 3 by the much reduced level of approximation.

4.3 REVIEW OF PAST SOLUTIONS

4.3.1 Axisymmetric interfaces

Classes 1 and 2 (Table 4.2) are comprehensively covered by the reviews and the following notes merely serve to illuminate the main solution methods and shapes covered.

4.3.1.1 Surfaces bound by uniform geometry

The simplest interfacial configurations are contained in this class - the classic example is the meniscus in a cylindrical capillary tube. Solution is moderately simple owing to the axis of symmetry and the uniform geometry.

a) Gravity free interfaces

Boucher (1980) gives the five basic meridians from which undistorted axisymmetric menisci take their shape. These capillary surfaces have *constant mean curvature* and are the cylinder, sphere, catenoid, nodoid and unduloid.

A meniscus bounded by a cylindrical tube is fully described by a single radius of curvature and is a sphere section. The Laplace equation may be written

$$\Delta P = 2\sigma/r \quad (2.24)$$

Fluid/fluid interfaces meeting a plane wall are also described by a single radius of curvature, that of a cylinder, the second principal radius of curvature being infinite, hence

$$\Delta P = \sigma/r \quad (4.1)$$

The Wilhemy plate method of interfacial tension and contact angle measurement makes use of this property.

The remaining meridians are obtained by rolling an ellipse or hyperbola along the axis of symmetry to solve a non-linear differential form of the Laplace equation where the mean curvature J , is given by

Table 4.2 Classification of interfacial configurations by rotational symmetry, the presence of an external force field, and shape of the solid geometry across the three phase line: degree of difficulty and common method(s) of solution are shown.

Shape of meniscus	Force field	Solid geometry bounding meniscus	
		Uniform (fixed boundary problems)	Converging-diverging (free boundary problems)
Axisymmetric surface	No	1 (a) Simple. Analytical solution.	2 (a) Moderately simple. Some analytical solutions.
	Yes	1 (b) Intermediate. Numerical solutions.	2 (b) Moderately complicated. Numerical or approximate solution
Non-Axisymmetric	No	3 (a) Moderately simple. MS-P theory (this study).	4 Very complicated.
	Yes	3 (b) Complicated. Numerical or approximate solution.	Few numerical solutions - mostly approximate.

$$2J = \frac{d^2y/dx^2}{\{1 + (dx/dy)^2\}^{3/2}} + \frac{dy/dx}{x\{1 + (dx/dy)^2\}^{1/2}} = \Delta P/\sigma \quad (4.2)$$

in cartesian coordinates. Equation 4.2 solves analytically for even quite complex interface shapes such as drops on cylindrical elements (Carroll 1976), but involves elliptical integrals of the first and second kind.

b) Gravity distorted interfaces

For a capillary surface in a gravitational field it is not possible to solve the Laplace equation analytically regardless of the geometry. The mean surface curvature now depends on the vertical position, z , but the interface has *minimum surface energy*.

Interfacial configurations are represented by rotated sections of distorted nodoid profiles - sessile drops and captive bubbles, distorted unduloid profiles - pendant drops and emergent bubbles, catenoid shapes - holms, and liquid bridges between solids - light and heavy bridges. To obtain the exact interface shape requires solution of eq. 4.2, but with an added term:

$$Bz + 2J_o L = \frac{d^2z/dx^2}{\{1 + (dx/dz)^2\}^{3/2}} + \frac{dz/dx}{x\{1 + (dx/dz)^2\}^{1/2}} \quad (4.3)$$

where $B = gL^2\rho/\sigma$ - the Bond number
 $L =$ some characteristic length of the system
 $J_o = J$ at $z = 0$

This equation can usually be solved by employing a numerical integration method such as that of Runge-Kutta-Merson or Adams-Bashforth-Moulton. Bakker (1928) reviewed early attempts at solution. The Bashforth and Adams tables (section 2.4.3) were obtained in this way. With the advent of powerful computers their tables have been updated and considerably extended: Paddy (1971) has made available a 400 page book of them and Boucher *et al.* (1987) a computer program. Huh & Scriven (1969) cover some surfaces that do not cross the axis of symmetry, called *unbounded menisci* (such as the rod-in-a-free-surface system).

In recent years many attempts have been made to compute the profiles of menisci not covered by the existing tables, see for example Pitts (1974), Michael & Williams (1976), Hartland & Hartley (1976), Boucher (1978) and Boucher & Evans (1980) (parts iv and xii of a series of solutions for various shapes). Sometimes boundary conditions must be restricted in order that the mathematics are tractable.

Another approach, that also appears to hold promise for systems lacking simple symmetry (see sections 4.3.3 and 4.3.4) is that of Orr *et al.* (1975a). They have presented a solution obtained by a *finite element method* (FEM) for the case of a rod-in-a-free-surface that shows good agreement with that of Huh & Scriven.

4.3.1.2 Surfaces bound by converging-diverging geometry

Solving for the shape of capillary surfaces in converging-diverging geometry (such as the space between spheres) requires the solution of equation 4.2 or 4.3 with a free boundary: the location of the three phase line not now known. This added difficulty has restricted the systems studied to those involving simple geometric shapes like spheres and cones.

a) Gravity free interfaces.

Each of the five constant curvature meridians have been applied to the problem of pendular rings between contacting spheres (or the half problem of a sphere and a plate). Clark, Haynes & Mason (1968) approximated the sphere-on-plate system by assuming that the liquid bridge configuration to be a cylindrical toroid instead of the actual nodoid. Mason & Clark (1965) had earlier given an exact solution for zero force fluid bridges between two unequal spheres (that formed with two immiscible liquids of equal density). In this case the bridge profile is an arc of a circle and the surface part of a sphere.

Melrose (1966) and Erle *et al.* (1971) gave some exact analytical solutions for nodoid and unduloid bridges between equal spheres, but the problem was not covered comprehensively until 1975. Orr *et al.* (1975b) gave analytic forms for constant curvature meridians of unduloids, catenoids and nodoids for all possible types of pendular rings between a sphere and a plate. By allowing for different contact angles at the sphere and plate Orr *et al.*'s analyses can also be applied to the two sphere system.

b) Gravity distorted interfaces

The shapes of capillary surfaces in this class can be obtained with similar methods to those of class 1 (b), but the equations have an extra degree of freedom that often forces simplifying assumptions to be made. Boucher and co-workers have applied phenomenological, thermodynamic and variational approaches, together with numerical computation to systems involving spheres (Boucher 1978, Boucher & Kent 1977a, 1978 see also Hotta *et al.* 1974) and cones (Boucher & Kent 1977b, Boucher & Jones 1982). Benjamin & Cocker (1984) have presented solutions for free boundary problems arising from liquid drops suspended by soap films.

4.3.2 Non-axisymmetric interfaces

When the geometry of a fluid/fluid interface and/or its fluid/solid boundary is not definable in simple mathematical terms (i.e. one parameter) the exact solution of the partial differential form of Laplace equation is, at best, difficult and, depending on the complexity of the geometry, can be impossible. To date very few successful studies predicting the shapes of non-axisymmetric interfaces have been published. Potential applications of these classes are however abundant, particularly within the field of porous materials*. The literature that is available has not been well reviewed although Brown (1979) and Concus & Finn (1974) discuss general problems relating to gravity distorted capillary surfaces in complex geometries.

4.3.2.1 Surfaces bound by uniform geometry

This class comprises any fluid/fluid interface that does not possess a rotational axis of symmetry, but that is bound by uniform non-axisymmetric geometry. Simple examples are a meniscus in a square tube or a surface between two spaced cylinders.

* The likelihood of a method being developed for the prediction of interface shapes in a porous material of non-trivial internal geometry is remote. The location of the three phase line is unknown *a priori* and the contact angle boundary condition is also free as the interface is likely to form at solid edges where the contact angle on a flat surface has no meaning (section 3.5.1). However the shapes of menisci in these classes could of considerable aid in simple and model media.

a) Gravity free interfaces

For any fluid interface where gravitational effects are negligible and the solid geometry non-converging-diverging a moderately simple, but non-trivial, method attributable to Mayer and Stowe (1965) and Princen (1969a) can be used. It is known as the *MS-P method* (after Mason & Morrow 1984a). It is exact for interfaces in this class, solves analytically for some simpler cases and by straightforward numerical *iteration* (not integration) in any system where the geometry can be defined. The experiments performed as part of this study examine the method, the basis of which will be discussed in detail later (Chapter 6)

The MS-P method can be applied to a wide variety of tube shapes, including configurations in which the cross-section does not define a closed region. It yields the exact shapes of the unbounded cylindrical menisci that form in wedge like corners or between spaced uniform elements and the mean curvature of other undistorted surface configurations. No other solution method has been employed for surfaces in this class when the boundary conditions give rise to unbounded menisci, called *wedging systems*. Exact curvatures may be found with the hydraulic radius method (section 3.4.1) if the system is *non-wedging*. Tables 4.1 and 4.3 detail all the systems for which the shapes of interfaces have been calculated with the method.

b) Gravity distorted surfaces

To predict the shape of a non-axisymmetric, gravity distorted meniscus requires the non-linear, second order, partial differential form of the Laplace equation to be solved in fully three dimensions. If in cartesian coordinates the elevation of the surface is $z = z(x, y)$ the mean curvature, J , is given by

$$2J = \frac{(1+z_y^2)z_{xx} - 2z_xz_yz_{xy} + (1+z_x^2)z_{yy}}{(1+z_x^2+z_y^2)^{3/2}} \equiv -\nabla \cdot \mathbf{N} \quad (4.4)$$

where the unit vector $\nabla \equiv \mathbf{i}\partial/\partial x + \mathbf{j}\partial/\partial y$

and $\mathbf{N} = (\mathbf{k} - \mathbf{i}z_x - \mathbf{j}z_y)/(1+z_x^2+z_y^2)^{1/2}$

Thus the form of the Laplace equation that must be solved is

$$Bz + 2J_oL = -\nabla \cdot \mathbf{N} \quad (4.5)$$

Hartland *et al.* (1982) avoided the problem posed by this equation by only considering slight deviations from asymmetry and obtained near-exact solutions for a cylindrical rod in a cylindrical tube. Full solutions in this class are few in number and then only for carefully selected configurations and boundary conditions. Most of these are attributable to a single "school" of authors.

Table 4.3 Closed interfacial configurations whose behaviour has been predicted by the MS-P method. All references shown contain the equations in solved form and all solutions are for geometry of uniform wettability.

Reference(s)	Solid geometry	Contact angle	Geometric variables
Princen '69b	Equilateral triangular tube	Zero	-
Singal & Somerton '70 Ransohoff <i>et al.</i> '87	Equilateral triangular tube	Variable	-
Mason & Morrow '89	Triangular tubes	Zero	Tube shape factor (area/perimeter ²)
Princen '69b	Square tube	Zero	-
Lenormand '81 Legait & Jacquin '82 Legait '83	Square tube	Variable	-
Lenormand <i>et al.</i> '83	Rectangular tubes	Zero	Tube aspect ratio (depth/width)
Mason & Morrow '84a	Kite shaped tube	Zero	-
Mason & Morrow '84a	Polygon tubes	Variable	No. of tube walls
Mason & Morrow '84a	Rod in a right-angled corner	Variable	-
Mason & Morrow '84a	Two equal rods and a plate	Zero	-
Mason & Morrow '83	Two equal rods and a plate	Variable	-
Mason <i>et al.</i> '88	Two unequal rods and a plate	Zero	Rod radius ratio
Mayer & Stowe '65	Three equal rods	Variable	-
Mason & Morrow '86	Four equal rods	Zero	Cell angle
Mayer & Stowe '65	Four equal rods	Variable	Cell angle

The few early studies were restricted to quite symmetrical configurations. Petrov & Chernous'ko (1966) used a numerical method of "local variation" to yield the shape of a capillary surface in a "rectangular parallelepiped". Concus & Finn (1969, 1970), mathematicians, were interested in the basic properties of the Laplace equation, they considered the shape of an open capillary surface in a wedge with varying corner and contact angles. They showed that at a corner or vertex the meniscus elevation is unbounded if the liquid surface cannot meet the contact angle boundary condition on the two solid surfaces that intersect there - a property utilised by the MS-P method.

Most of the remaining solutions in this class stem from the work of Orr and co-workers (see Orr *et al.* 1975a) who have successfully applied the *Galerkin finite element method* to such problems. This method of numerical integration has proved more suitable than finite difference techniques. However the mathematics involved is complicated and long durations of computer time are required for each solution. Broadly, the surface is

Table 4.4 Open interfacial configurations whose behaviour has been predicted by the MS-P method. All references shown contain the equations in solved form and all solutions are for geometry of uniform wettability.

Reference(s)	Solid geometry	Contact angle	Geometric variables
Princen '70b	Wedge	Variable	Angle at apex
Princen '69a Mason & Morrow '87	One rod away from a plate	Zero	Rod-plate spacing
Princen '69a	Two equal rods	Variable	Rod-rod spacing
Mason & Morrow '87	Two equal rods and a plate	Zero	Unequal rod-plate spacings
Mason & Morrow '84b	Three equal rods	Zero	Unequal rod-rod spacings
Princen '69b, '70	Three equal rods in an equilateral array	Variable	Rod-rod spacing
Princen '69b	Three equal rods in an infinite equilateral array	Variable	Rod-rod spacing
Dodds '78	Three unequal rods	Zero	Unequal rod-rod spacings
Princen '69b, '70a	Four equal rods in a square array	Variable	Rod-Rod spacing
Princen '69b	Four equal rods in an infinite square array	Variable	Rod-rod spacing

approximated by a set of small polygonal elements or subdomains (triangular and rectangular systems have been used). Inside each of the elements the solution is obtained by interpolating linearly between distinct values of the solution at nodes (corners) of the polygon. The solution moves stepwise from element to element. Relaxation techniques may also be required.

The FEM solutions do not give the mean curvature of the surface as their derivatives are only "piecewise continuous". The mean curvature may, however be estimated from the elevation and the Laplace equation itself. Difficulties arise with the FEM and unbounded menisci as the domains become of infinite extent. This problem has been overcome for rods-in-a-surface systems although no solution has been put forward for unbounded surfaces that can arise in the wedge like corners of angular tubes.

The following Class 3 (b) interfacial configurations have been found using this FEM: cylinders in an infinite square array (Orr *et al.* 1975a), and square pins in an infinite array (Orr 1976, Orr, Scriven and Chu 1977) at given spacings and for unbounded menisci around a single elliptical cylinder (Orr, Brown & Scriven 1977) and around two spaced circular cylinders. All the above solutions allow variation in contact angle.

Larkin (1967) attempted a solution for the seemingly simple case of a drop on an inclined plate using a finite difference method. His success was limited and he avoided the elliptic nature of the problem by sacrificing boundary conditions. However the problem aroused the interest of Orr and co-workers. Brown, Orr & Scriven (1980) published a full solution assuming the three phase line was of a known circular shape, this analysis was later confirmed in Japan (Tuskada *et al.* 1982). Lawal & Brown (1982a, b) extended the analysis to include drops whose line of contact has an oval shape. Even with this modification it has been shown that as a model of real drops the assumptions over the three phase line make applications very limited (Nguyen *et al.* 1987).

Recently Brown *et al.*'s analysis has been further extended by Rotenberg *et al.* (1984), who assumes that the drop is slowly sliding down the plate. Their boundary conditions along the line of contact are described in the form of a functional relationship between the contact angle and the velocity of the three phase line. They claim close agreement with observed drop profiles.

4.3.2.2 Surfaces bounded by converging-diverging geometry

Solution is now further complicated by the free solid boundary. To the best of my knowledge only one publication presents successful solutions of the Laplace equation for capillary surfaces in this class. Orr, Brown & Scriven (1977) propose solutions for gravity distorted interfaces formed between an infinite square array of cones and two different solutions for spheres in a three dimensional regular square array. Again the FEM was employed, but with an additional iterative routine required to locate the three phase line. The solutions for the spheres represent two distinct stable meniscus configurations for a given pressure at the datum level, depending upon which level of spheres is wetted by the interface.

Unlike the solutions they earlier obtained for simpler configurations, Orr *et al.* rely on substantial restrictions of the natural boundary conditions such as the contact angle. It remains to be seen whether these difficulties can be overcome and if the FEM finds applications elsewhere such as in detailed investigations with the ideal soil model and less regular porous media.

4.4 SUMMARY

Capillary surfaces have been classified according to their symmetry, the solid geometry by which they are bound and the presence of a force field. The solution of the Laplace equation for the interfacial configuration varies from being trivial to extremely complicated even though past studies concentrate on surfaces between geometrically simple solid objects.

The difficulties of solving the Laplace equation for gravity distorted surfaces or menisci in converging-diverging geometry accounts for the gross approximations of some interfacial configurations assumed in pore space models (section 3.4) and the relative simplicity of their solid components (section 3.3)

The above classification and the discussion that follows it show how the MS-P method fits into the study of interfacial configurations and illustrates the uniqueness of the method in the systems to which it may be applied.

CHAPTER 5

Review of past applications of the MS-P method

5.1 INTRODUCTION

The MS-P method was first proposed over twenty years ago, by Mayer & Stowe (1965) and separately by Princen (1969a), but for much of the intervening period it has been sparsely employed in the literature. The potential applications of the MS-P theory are numerous, covering many of the areas listed earlier in Table 4.1. This has not gone entirely unnoticed by all researchers, with the work of both Mayer & Stowe and Princen receiving citations, indicating its promise in several different areas of capillarity. As yet the method has only actually been applied in a few areas and then not extensively. Recent years have however seen growing utilisation of the method.

There have been four principal areas of application; those for which the method was originally developed - mercury porosimetry and capillary rise - and two other related areas in the study of porous materials - fluid/fluid displacement and in attempts to explain hysteresis.

In section 3.4 the Mayer & Stowe - Princen method was introduced through its application as an approximate model for interfacial configurations in porous materials. Chapter 4 has introduced the type of capillary surface whose exact shape the method can predict and illustrated how the method compliments other techniques for the determination of interfacial configurations. Before discussion of the theory in detail (in chapter 6) other previous applications are reviewed. Note that the relevant literature concerning capillary pressure hysteresis was reviewed in section 3.5.

5.2 MERCURY POROSIMETRY

5.2.1 Mayer & Stowe's study

Mayer & Stowe (1965) presented the first correct derivation of what is here called the MS-P theory*, but mistakenly thought it gave exact interfacial configurations in the

* Two years previously Frevel & Kressley (1963) had proposed a similar solution, but their expression of the Laplace equation (containing a $\cos \theta$ factor) is incorrect and their algebra mistaken. That the authors arrive at an identical equation to Mayer & Stowe must be regarded as somewhat fortuitous (see Haynes 1975).

converging-diverging geometry of regular sphere packings. Their analysis begins with a simplified form of the free energy expression for a fluid/fluid interface (eq. 2.59). Their relationship for the work associated with infinitesimal displacements of the surface reads

$$P_c^* dV = \sigma dA_{LV} + \sigma_{SL} dA_{SL} + \sigma_{SV} dA_{SV} \quad (5.1)$$

where P_c^* is the breakthrough, or threshold, pressure. Mayer & Stowe proceed by assuming that at the point of instability, beyond which a mercury interface passes spontaneously through the pore throat, the three phase line (SLV) lies in the plane containing the spheres centres that define the pore constriction (see Figure 5.1). Since the pore walls are approximately parallel near this plane it follows that the interface is of approximately constant shape. Thus dV will be proportional to A , the cross-section of the mercury in the plane of sphere centres, and the three dA terms will be proportional to the lengths of the perimeters in that plane of the liquid/vapour and liquid/solid interfaces, P_{LV} and P_{SL} respectively.

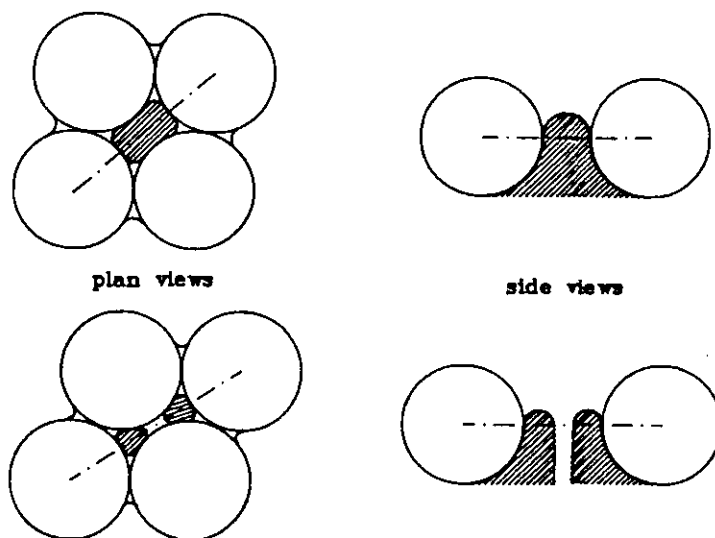


Figure 5.1 - Mayer & Stowe model for mercury intrusion between spherical particles.

By introducing the Young equation and making use of the fact that $dA_{SL} = -dA_{SV}$ Mayer & Stowe arrive at the expression

$$P_c A = \sigma(P_{LV} - P_{SL} \cos \theta) \quad (5.2)$$

Defining $P_{eff} = P_{LV} - P_{SL} \cos \theta$ gives;

$$P_c = \sigma \frac{P_{eff}}{A} \quad (5.3)$$

Note the similarity of equation 5.2 to the Gauss equation. Haynes (1975) comments that whereas the Gauss equation, relating area to interfacial curvature, J , is in differential form,

$$JdV = dA_{LV} - dA_{SL} \cos \theta \quad (2.69)$$

the Mayer & Stowe treatment implies an integrated form

$$JA = P_{LV} - P_{LS} \cos \theta \quad (5.4)$$

One further unsubstantiated assumption of the Mayer & Stowe analysis is that the intersections of the plane of sphere centres with the liquid/vapour interfaces are portions of circular arcs. The implication is that the pendular rings around the sphere contacts are toroidal when in fact they will be nodoidal (section 4.2.1.2).

Bell *et al.* (1981) note that for situations where $\cos \theta \neq 1$ (i.e. $\theta \neq 0, 180^\circ$) there will be significant deviation of the three phase line from the plane of sphere centres that will cause the actual curvature to differ from that calculated by Mayer & Stowe. Bell *et al.* conclude that in general this difference will be small, thereby explaining experimental confirmation of Mayer & Stowe's results at contact angles of 140° .

Mayer & Stowe proceed to show how porosimetry data can yield a particle size distribution with use of their results. The term P_{eff}/A is a function of the packing angle of the powder bed and the mercury contact angle. They calculated this ratio for all possible packing angles for pack porosities ranging from 0.25 to 0.48 and contact angles from 180° to 100° . Thus once the correct P_{eff}/A value is chosen from the Mayer & Stowe table the radius of the particles defining the pores which are penetrated can be directly derived from the experimental intrusion pressure.

At each intrusion pressure the mercury penetration volume is also registered. By expressing this volume as a percentage of the overall penetration volume measured at the end of the run, it is possible to derive a complete particle size distribution on a volume basis. Mayer & Stowe did not however conduct any experiments to verify their analysis.

5.2.2 Further studies

The Mayer & Stowe analysis has found uses in mercury porosimetry as an alternative to the Washburn model (section 3.5.1.1). Orr (1970) used mercury intrusion data and the analysis to obtain a particle size distribution for a powder with particle sizes in the range 10 to $120 \mu\text{m}$. His results showed qualitative agreement with those obtained from a Coulter Counter.

Savata & Zabransky (1970) compared results from the Mayer & Stowe analysis with size distributions measured by microscopy for five powders in the size range 1 to $100 \mu\text{m}$. Again the techniques were qualitatively in agreement. However powders with narrow size distributions showed markedly better agreement.

Stanley-Wood (1979) sized steel shot using mercury intrusion and sieve analysis and three other powders with mercury intrusion, sedimentation and electronmicroscopy techniques. For the steel shot agreement was excellent, whilst intrusion results from the other three powders fell between those from sedimentation and microscopy. In the course of his investigation Stanley-Wood extended the Mayer & Stowe tables to cover the porosities of his powders, which were in the range $0.64 < \epsilon < 0.75$, significantly outside the range of porosities given by regular sphere packings.

More recently Carli & Motta (1984) measured particle size distributions of four pharmaceutical powders whose particle sizes lay between 1 and 200 μm . They noted good agreement between the Mayer & Stowe results and various other sizing methods.

Smith and co-workers (1987a, b) have applied an approximate version of the MS-P theory to sphere packings. They base their analysis on two approximations in order to simplify the MS-P calculations. They employ Mason & Morrow's (1984b) empirical relationship between the curvature predicted by the MS-P theory and that estimated using the Haines incircle approximation (derived from data for liquids exhibiting zero contact angle in packings of equal spheres - section 3.4.4);

$$C_{MS-P} = C_{incircle} - 1.5 \quad (3.6)$$

To account for the mercury contact angle of 140° a novel empirical expression relating the ratio $C_{MS-P}(\theta = 140^\circ)$ to $C_{MS-P}(\theta = 180^\circ)$ as a truncated series in $C_{incircle}$ is used. Smith *et al.* conclude that the Mayer & Stowe analysis gives particle size distributions much wider than the actual values. However, considering the odd nature of their approximations and the lack of any direct comparison between the actual MS-P theory and their approximate method, their conclusions cannot be said to apply directly to the theory attributable to Mayer & Stowe.

5.3 CAPILLARY RISE

5.3.1 Princen's studies

Princen (1969a) arrived at the same expression for the capillary pressure across a curved interface as did Mayer & Stowe and correctly applied his theory to interfaces bound by uniform geometry where, in the absence of gravitational effects, it is exact. However, Princen's interest was capillary rise, specifically wetting and wicking in textiles, where gravitational forces are involved. This led Princen to stipulate that his analyses were only valid for systems in which the height of rise is well in excess of the capillaries' characteristic dimension (i.e. $h/R \gg 1$).

Princen's formulation of the theory is based on a force balance that equates the weight of a liquid column above a planar surface to the surface tension forces in the meniscus region. Expressing the weight of the column as;

$$F_1 = h\rho g A_{LV} \equiv P_c A_{LV} \quad (5.5)$$

and the surface tension forces by;

$$F_2 = \sigma(P_{LV} + P_{SL} \cos \theta) \quad (5.6)$$

the analysis can be seen to be equivalent to that of Mayer & Stowe. Equating 5.5 to 5.6 yields equation 5.3:

$$P_c = \sigma \frac{P_{eff}}{A} \quad (5.3)$$

Princen (1969a) gave results in tabular form for the meniscus between two equal rods separated by a distance, $2d$, in terms of normalised spacing, d/R , versus normalised curvature, R/r , for contact angles between 0 and 90° . Similar tables were presented for a single rod spaced from a plate (with $\theta = 0$) (1969a), three equally spaced cylindrical rods (1969b) and a graphical presentation for four equal rods in a square array (with $\theta = 0$) (1969b).

The three and four rod systems give rise to two distinct capillary profiles depending on the spacing. Princen calculated the curvatures for each of the three different menisci formed. Figure 5.2 shows the configurations Princen suggested for the four rod arrangement. At low spacings two types of meniscus coexist, Figure 5.2b, those in-between each pair of rods and that held between all four rods. Princen predicted the spacing at which transition occurred to a single meniscus (Fig 5.2d).

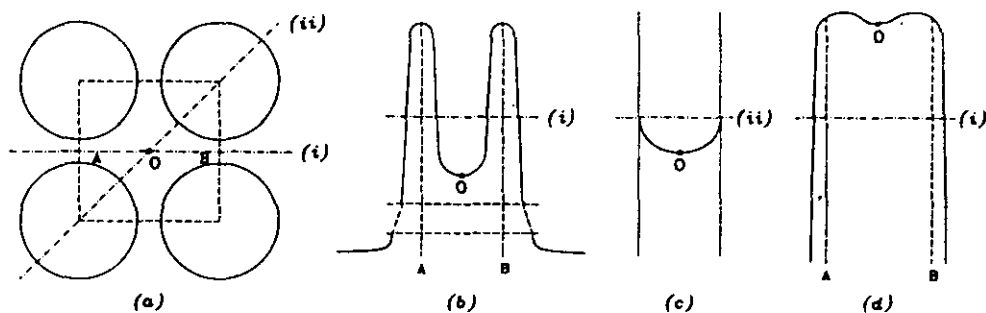


Figure 5.2 - Princen's suggestions for the capillary rise between four rods in a square array.
 (a) Horizontal cross section through four spaced rods.
 (b) Schematic capillary rise profile in a vertical section through line (i) for low rod separations.
 (c) Corresponding capillary rise profile in section through line (ii).
 (d) Schematic capillary rise profile through line (i) at larger rod separations.

Princen proceeded to extend his results to cover multicylinder systems, arranged in both hexagonal and square lattices. He suggested these systems could be used as models of textile yarns. The Haines incircle approximation was investigated and found to overestimate the curvatures of the concave, clastic, menisci between the three or four cylinders. However this approximation could not account at all for capillary rise between two spaced rods where the meniscus profile is partly convex; that is where the meniscus is anticlastic.

In addition to the detailed results given for open systems, Princen showed that his analysis can be applied to closed systems through the derivation of the relationships describing capillary rise in triangular and square tubes. Furthermore Princen (1970a) went on to consider horizontal assemblies of cylinders, now using an energy balance to calculate curvatures. He noted the existence of an additional stable state where the liquid column is "convex outward" - akin to unduloid drops that form on a single cylinder. The capillary forces resulting from the presence of liquid columns between cylinders were briefly discussed.

Princen's calculations for capillary rise between cylinders are extensive, but throughout his three papers the result of only a single experiment is presented. For a rod of radius 6.34 mm spaced 0.2 mm from a flat plate a height of rise of 13.3 mm was found with a perfectly wetting liquid (1969b). This result is about 3% less than that predicted and was used to show that the criterion $h/R \gg 1$ may be overly severe in certain cases.

Princen noted that his analysis could be employed to measure surface tensions and in a further paper (1970b) discussed applications to the grooved Wilhemy plate method. In the course of which he determined the curvature of a meniscus in a horizontal wedge shaped groove as a function of its height above the planar liquid surface.

5.3.2 Studies of Mason & co-workers

The fact that neither Mayer & Stowe or Princen published experimental verification has undoubtedly contributed to the sparse use of the MS-P method in the literature. The method's potential has been cited in studies ranging from sap rise in plants (Pickard 1981) to "fingering phenomena" in porous materials (Levine *et al.* 1977). Shortly after Princen's work Mason (1971) noted the potential of the analyses of both Mayer & Stowe and Princen as an approximation for the breakthrough curvature of menisci in sphere packings. However, uncertainties over the validity of the method led to the use of the Haines incircle approximation.

It was not until 1983 that the first experimental validation of the method was published. Mason *et al.* (1983) calculated the curvature of the closed meniscus formed between two equal rods and a flat plate using Princen's analysis. Validation of the predicted curvatures were conducted using capillary rise and bubble movement

experiments for both perfectly wetted systems and for systems that gave reproducible advancing and receding contact angles. At zero contact angle the curvatures determined from observed capillary rise were within 2.5% of those predicted, whilst the bubble movement results were within 5%. For the partially wetted system results were not so good, but all were within the estimated experimental error.

The promise shown by their first investigation led to by a more detailed study (Mason & Morrow 1984a) in which a refined apparatus was used. Measured curvatures for the two equal rod and plate configuration with a perfectly wetting liquid were within 1.5% of those predicted by the MS-P method. Similar agreement was found for a single rod in a right angled corner. Theoretical discussions on the conditions of pore geometry and contact angle which give rise to unbounded wedge-like menisci in corners were presented. These were illustrated by consideration of menisci in a kite shaped pore, polygonal tubes and pores formed by the rod-in-a-right-angled-corner. In this way Mason & Morrow were able to differentiate between uniform geometries where the curvature may be calculated from the hydraulic radius method - termed non-wedging systems - and those where the MS-P method must be employed - called wedging systems.

The validity of the MS-P method as applied to pore throats formed by spheres was studied by Mason & Morrow (1986). Pore throats formed from four ball bearings in a rhomboidal array with half angles in the range 30° (closed triangular) to 45° (square array) were investigated. A modified capillary rise technique was used to measure the maximum meniscus curvature; that at which the meniscus becomes unstable and spontaneously passes through the pore throat.

Experimental values of curvature were only 2 to 5% less than values calculated with the MS-P method for pores formed by rods in the corresponding array (with $\theta = 0$). For the closed triangular pore, discussed in section 3.4, a normalised curvature of 11.08 ± 0.2 was found, about 3% less than the accepted experimental value in sphere packings. Mason & Morrow also found good agreement between experiments and theory for mixed pores comprising rods and balls. As expected the more uniform the geometry (i.e. the more rods) the closer was the agreement.

Mason & Morrow (1987) proceeded to investigate pores with open cross-sections. An arrangement again comprising of two equal rods and a plate, but with either one or both rods spaced from the plate was studied. As with Princen's assemblies of cylinders, this system allows more than one stable state and several meniscus shapes depending on the arrangement of the rods. The authors also found metastable meniscus configurations. Agreement between observed and calculated curvatures were largely within experimental error, both in terms of the curvatures of specific menisci and in terms of the transitions from one meniscus profile to another with change in tube shape.

At some spacings when both rods are separated from the plate, three distinct stable meniscus configurations are possible, all having different curvatures. Mason & Morrow reason that whilst the configuration with the lowest curvature will be the most stable, the other metastable states are a possible cause of capillary pressure hysteresis in porous media, showing a mechanism distinct from generally accepted causes (section 3.5). However, they also warn that the fact that a curvature can be calculated for a specific meniscus type does not mean that the configuration will exist.

Further experimental validation was published by Mason, Morrow & Walsh (1988 - see appendix A) for the closed meniscus formed in a pore of two unequal rods and a plate. Excellent agreement between the MS-P theory and experiments was again found for rod radius ratios from 1 to 7. These results are a part of this study and are discussed in detail in section 8.6.

Want of experimental verification of the MS-P method has not prevented all researchers from using it. Van Brackel & Heertjes (1978) applied Princen's results for cylinders to the problem of capillary rise in regular sphere packings. Following Mayer & Stowe they assumed that the three phase line lies in the plane of sphere centres upon breakthrough. They noted some success by considering the anticlastic menisci between the contacting spheres (pendular rings) together with the concave, clastic menisci in the pore throats.

5.4 FLUID/FLUID DISPLACEMENT

Fluid/fluid flow in porous media is often described in terms of macroscopic laws where the actual geometry of the pore space is not considered. However, when capillary forces are dominant with respect to other forces involving viscosity and gravity, a macroscopic description is usually not sufficient. In these instances it is necessary to model the pore space using techniques discussed in section 3.3. As with proposed explanations of hysteresis (section 3.5) early work in the area concentrated on the simple capillary tube model, but this again proved inadequate in most cases. More recently interest in oil recovery has stimulated research involving angular tube models: here interfacial configurations are best determined with the MS-P theory. An advantage of such tubes is that, in common with real media, their angularity allows the wetting phase to by-pass blobs of non-wetting phase by flowing behind the wedge like (arc) menisci in the corners.

Singal & Somerton (1970) presented an entirely theoretical model for two phase laminar flow in porous media based on relationships derived for flow in triangular tubes. They use a modified version of Poiseuille's law to incorporate a capillary pressure term

in an expression for the mean velocity of flow. The capillary pressure is found using Princen's analysis together with the Laplace equation to yield the mean curvature in an equilateral triangular tube, giving;

$$P_c \equiv \frac{1.78\sigma(\cos\theta - 1)}{R_h} \quad (5.7)$$

where R_h is the hydraulic radius of the tube.

Legait & Jacquin (1982) and Legait (1983) were interested in tertiary oil recovery. They studied blob mobilisation by modelling two phase laminar flow in a constricted square capillary. The Mayer & Stowe analysis is applied to the square sectioned tubes under variable wetting conditions (but with $\theta < 45^\circ$ for which arc menisci exist). The curvature of the upstream and downstream fluid/fluid interfaces (with respect to the constriction) of the blob were determined according to the expression

$$J_i = F(\theta)/R(x) \quad (5.8)$$

where $R(x)$ is half the tube width at position x . $F(\theta)$ Was determined with the MS-P theory in terms of the fraction of tube area occupied by wetting fluid.

Equation 5.8 ignores the converging-diverging nature of the tube with the assumption of local uniformity in cross-section. This result was validated by comparison with experimental data given by Arriola *et al.* (1980), good agreement was found. Using the curvature function Legait was able to derive expressions for the volumetric flow rates of each phase and determine the conditions necessary for blob mobilisation through the constriction in terms of a critical capillary constant. Theoretical results compared well with experiments conducted in model capillaries.

Lenormand *et al.* (1983) studied the mechanism of the displacement of one fluid by another with reference to observations of drainage, imbibition and blob mobilisation in etched networks. Their model comprised a two dimensional network of rectangular tubes. Threshold pressures, at which non-wetting fluid enters a tube, were determined using the MS-P theory and the Laplace equation. A wetting phase contact angle of zero was used giving;

$$P_c^* = F(\epsilon)2\sigma\left(\frac{1}{x} + \frac{1}{y}\right) \quad (5.9)$$

where

$$F(\epsilon) = \frac{\epsilon(4 - \pi)}{2(1 + \epsilon)\{(1 + \epsilon) - \sqrt{(1 + \epsilon)^2 - \epsilon(4 - \pi)}\}} \quad (5.10)$$

and $\epsilon = x/y$ - the aspect ratio of the tube

Predicted threshold pressures were in good agreement with experimental data obtained from small networks

Ransohoff *et al.* (1987) were also concerned with oil recovery, but were interested in the snap-off of moving gas bubbles in various constricted non-circular capillaries. In oil recovery processes by foam flooding a primary mechanism of foam generation is the snap-off of non-wetting gas bubbles passing through constrictions in the pore space. It is the "curvature driven" flow of the wetting liquid along the capillary walls that controls the dynamics of this process.

The MS-P theory was employed by Ransohoff *et al.* to calculate meniscus curvatures in constrictions in equilateral triangular tubes. Use was also made of Mayer & Stowe's results for the breakthrough pressures in pore throats formed by three and four contacting spheres and Legait's results for the square tube. Ransohoff *et al.* proceed develop a "corner flow hydrodynamic theory" which they employ to calculate the time to snap-off for a moving bubble in terms of a function of the capillary constant, flow resistance and the shape of the constriction. Experiments in model capillaries confirmed their findings.

5.5 SUMMARY

The method of Mayer & Stowe and Princen has found only limited application in four areas of study. The sparse use of the method is, in part, accounted for by the lack of experimental verification in the uniform geometry systems in which the method applies. Only recently have the first steps been taken to rectify this.

Mayer & Stowe's original analysis was intended for use as a particle sizing model in mercury intrusion porosimetry. The method has since been qualitatively validated by several studies, although the analysis has not always been applied in the manner intended by Mayer & Stowe. Experiments indicate that, at least at zero contact angle, the MS-P theory gives good estimates of breakthrough curvatures between spheres.

Princen gave extensive analysis of capillary rise of various open and closed menisci in non-axisymmetric tubes using the MS-P method. He unfortunately conducted only a single experiment. Recent experiments of Mason and co-workers indicate that capillary rise of non-axisymmetric menisci in uniform tubes can, when gravity effects are small, be predicted accurately by the method, for the limited number of systems they have investigated.

Recent applications of the MS-P method to fluid/fluid flow and capillary pressure hysteresis in porous materials have shown the MS-P methods ability at elucidating real problems in a currently important area of research and has furnished further validation of the method. Many of the studies mentioned above will be discussed further in later chapters.

CHAPTER 6

Theory and analytical procedures

6.1 INTRODUCTION

The background material has been covered in the preceding chapters and attention is now focused on the Mayer & Stowe - Princen theory and its application in the present study. Table 6.1 details the tube geometries that are investigated in this study. The wettabilities and variables covered are also shown.

The shapes produced by liquid menisci in the non-axisymmetric tubes of complex configuration detailed in the table are generally complex themselves. To apply the MS-P theory to such systems requires that the general shape of the meniscus in the tube be estimated and to describe potential shapes it is necessary to have a terminology. Details of such a terminology are given below.

In the past, the theoretical relationships describing the shape of fluid interfaces in cylindrical capillary tubes have been approached via consideration of the energy or forces involved or by direct derivation from the Gauss equation of capillarity. All these methods

Table 6.1 Arrangements investigated in this study. Interfacial configurations are predicted with the MS-P theory and validity experiments conducted using the simplified comparative method (chapter 7). Details of each arrangement can be found in the sections indicated.

Solid geometry	Capillary Rise Profile(s)	Wettability	Variable	Section Reference
Rectangular ducts	Closed	Perfect	Tube aspect ratio	9.2
One rod away from a plate	Open	Perfect Partial	Rod-plate spacing Contact angle	9.3 10.2
One rod in a corner	Closed	Perfect	Corner angle	9.4
Two unequal rods and a plate	Closed	Perfect	Rod radius ratio	9.5
Two equal rods and a plate	Closed	Perfect Partial Mixed	- Contact angle Contact angle	8* 10.3 10.3
Three equal rods and a plate	Closed Various	Perfect Perfect	- Subtended angle	8* 11
Three unequal rods and a plate	Various	Perfect	Subtended angle	11
Symmetrical	Various	Perfect	Subtended angle	11
Non-symmetrical	Various	Perfect	Subtended angle	11

* Experiments using the *full* comparative method.

can also be utilised to derive the MS-P equation.

Except in a few simple cases, application of the MS-P theory to non-axisymmetric tubes results in a set of equations that do not possess a unique solution, nor may they be resolved analytically. Techniques for the application of the theory and for the solution of the resulting equations are illustrated with examples in the latter sections of the chapter.

6.2 TERMINOLOGY

The calculation of curvature by the MS-P method is relatively straightforward, but the problem is not trivial. Application of the theory requires that the basic arrangement of the liquid in a pore is known or at least estimated prior to solution. To aid discussion of possible arrangements it is helpful to have a terminology that covers the main features of meniscus configurations in uniform geometry capillaries.

Figure 6.1 shows the development of a terminology, as published by Mason & Morrow (1987), and Table 6.2 details the nomenclature. For menisci in the uniform tubes of Figure 6.1, the capillary pressure, and hence the interfacial curvature (equation 2.30), is a linear function of the height of rise.

Figure 6.1a shows the meniscus formed by a perfectly wetting liquid in a vertical cylindrical capillary. The meniscus spanning the tubular space is a simple example of a *main terminal meniscus* (MTM). In the vicinity of the MTM there is a rapid change in liquid content with height. The region directly above the MTM is filled with the non-wetting phase (gas) and is called the *dryside* (D) with respect to the MTM. Similarly, the region filled by the wetting phase (liquid) is referred to as the *wetside* (W). The system is termed *non-wedging* as the MTM is completely bounded by the solid perimeter of the tube. Under constant curvature conditions (when there is no distortion of the meniscus by external forces such as gravity) the MTM will be a perfect hemisphere.

The situation in the kite shaped capillary of Figure 6.1b differs in that the MTM now merges with a wedge of liquid caught in the corner formed because of the contacting straight sides. In contrast to the MTM, the liquid content in the wedge only changes slightly with height. The liquid in the wedge is bounded in the corner by an *arc meniscus* (AM). The MTM is now only partially bounded by the solid perimeter making this a *wedging system*.

In wedging systems the terms wetside (W) and dryside (D) are used in the general sense to describe the higher and lower liquid content sides of the MTM. When the solid perimeter bounds the liquid wedge as in Figure 6.1b the AM is referred to as a *closed arc meniscus* (CAM), and, as the CAM is on the dryside of the MTM, the full description of the AM is *dryside closed arc meniscus* (DCAM) with respect to the MTM.

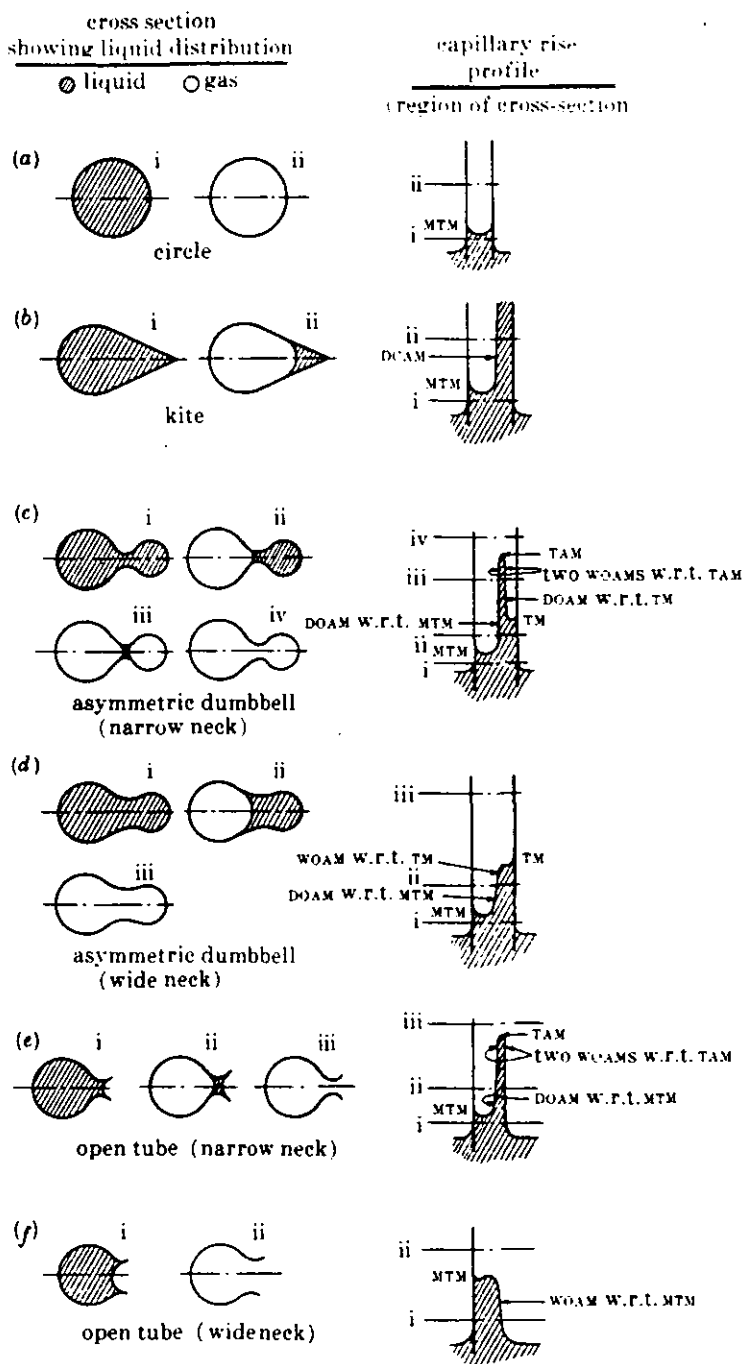


Figure 6.1 - Fluid distributions for capillary rise in various shapes of tube showing various types of arc and terminal menisci.

Under constant curvature conditions the liquid content in the wedge is fixed, the wedge having constant volume per unit length. In a mathematical sense the wedge will be infinitely long, and thus the radius of curvature of the AM in the vertical direction is infinite. The other principal radius of curvature (Fig. 6.1b ii) is the radius of a circular

Table 6.2 Nomenclature for the classification of menisci held in tubes of uniform cross-section.

A	arc	TAM	terminal arc meniscus
T	terminal	OAM	open arc meniscus
M	main (in main terminal meniscus only)	CAM	closed arc meniscus
D	dryside	DAM	dryside arc meniscus
W	wetside	WAM	wetside arc meniscus
O	open	DOAM	dryside open arc meniscus
C	closed	DCAM	dryside closed arc meniscus
AM	arc meniscus	WOAM	wetside open arc meniscus
TM	terminal meniscus	WCAM	wetside closed arc meniscus
MTM	main terminal meniscus		

arc; the cross-section of the wedge. As curvature is everywhere constant, the curvature of the AM (just the reciprocal of the radius of the circular arc) must equal that of the MTM, and its magnitude will be governed by its interaction with the MTM.

In a capillary rise experiment the curvature of the MTM can be determined directly from the height of rise. As it is affected by gravity, the curvature of the AM will also change in direct proportion to its height above the free liquid surface. However, in the vicinity of the MTM the curvatures of the AM and MTM will be approximately equal, so that in practice the curvature determined from capillary rise corresponds very closely to that of a meniscus of constant curvature. The validity of this assumption has been experimentally confirmed for systems where the distortion of the meniscus due to gravity is not excessive (Mason & Morrow 1984a).

Figure 6.1c shows an axisymmetric narrow necked dumb-bell capillary. The configuration taken up by the liquid profile exhibits three terminal menisci. The MTM spans the tubular space in the large diameter side of the dumb-bell profile. The shape is such that the liquid rises above the level of the MTM in the small diameter side. An abrupt change of liquid content with height marks the *terminal meniscus* (TM) of the small side. Above the MTM the liquid is bounded by an AM associated with the re-entrant solid surface and is referred to as an *open arc meniscus* (OAM). As the OAM is on the dryside of the MTM it is a *dryside open arc meniscus* (DOAM) with respect to the MTM.

Above the TM there is a second OAM associated with the liquid held in the constriction of the dumb-bell cross-section. This liquid is bounded by the two back-to-back OAMs which at a particular curvature form a *terminal arc meniscus* (TAM) as shown in Fig. 6.1c. Arc menisci are dryside or wetside with respect to a particular TM, so with respect to the TAM the back-to-back OAMs are termed *wetside open arc menisci* (WOAMs).

In Figure 6.1c the MTM and other TMs are at different heights and so of different curvatures. In a constant curvature system only one TM can be formed as only one curvature is possible. The TMs in the dumb-bell capillary coexist as gravity enables the system to have changing curvature. In the absence of gravity the interface is one of constant curvature and the volume of liquid per unit length on the dryside (or wet side) of a given terminal meniscus is constant. In practice, a particular TM together with its associated arc menisci will determine the curvature of that part of the system, and hence the liquid content per unit length on the dryside of the TM.

If the constriction in the dumb-bell is widened a situation arises where the curvature of the TAM is less than that of the TM in the small side. It is now impossible for the TAM and its associated back-to-back OAMs to be formed which results in the profile shown in Figure 6.1d.

In Figure 6.1e the small side of the dumb-bell profile has been removed and the OAM on the outer side of the neck now falls to join the free liquid surface. As the neck is widened the curvature (and hence height) of the TAM decreases until it merges with the MTM to give the profile shown in Figure 6.1f.

6.3 THE MAYER & STOWE - PRINCEN THEORY

In discussing the MS-P theory it is convenient to divide capillary systems into two groups according to the terminology. Non-wedging systems are those in which the terminal meniscus is completely bounded by the solid perimeter. The theory for these systems has long been known. A wedging system is any system in which one or more arc menisci are formed and it is for these systems that the MS-P theory is specifically appropriate.

In the following sections different ways of deriving the equation for curvature prediction in non-wedging systems are outlined. These methods are then extended to cover wedging systems, yielding the MS-P equation. It must be stressed here that the following analyses strictly only apply to menisci of *constant mean curvature* that are *bounded by uniform geometry*.

6.3.1 Curvature calculation for non-wedging systems

In predicting the curvature of a non-wedging meniscus in a pore of uniform cross-section, such as that shown in Figure 6.2, there are three possible approaches: an energy or force balance, utilising the Laplace and Young equations, or the direct application of the Gauss equation of capillarity.

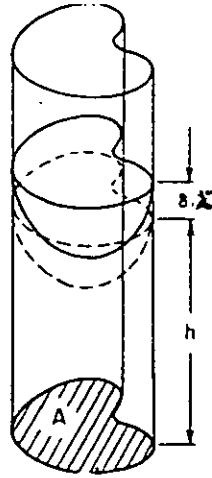


Figure 6.2 - An example of a uniform tube in which a meniscus is non-wedging.

6.3.1.1 Energy balance approach

At equilibrium a meniscus always attempts to adopt the curvature that gives the minimum surface energy for the particular boundary conditions. Consider the virtual works performed when the meniscus in Figure 6.2 is displaced by an infinitesimal distance, dx , from its equilibrium position. The virtual work required to lift the meniscus by dx is

$$dW_1 = P_c A dx \quad (6.1)$$

where the capillary pressure $P_c = \rho gh$, the hydrostatic head, and A is the projected area of the MTM, also the cross-sectional area of the tube. In the process of displacement the solid/liquid interface is extended by an element, dx , resulting in the wetting of an area of originally non-wetted solid surface, Pdx , where P is the perimeter of the tube. This virtual work is given by

$$dW_2 = P(\sigma_{SV} - \sigma_{SL})dx \quad (6.2)$$

The solid/vapour, σ_{SV} , and the solid/liquid, σ_{SL} , interfacial tensions cannot be directly measured, but their difference is related to the liquid/vapour interfacial tension, σ , and the contact angle, θ , via the Young equation:

$$\sigma_{SV} - \sigma_{SL} = \sigma \cos \theta \quad (2.71)$$

Hence $dW_2 = \sigma P \cos \theta dx$ (6.3)

Equating the two works of displacement, 6.1 and 6.3, yields

$$P_c A = \sigma P \cos \theta \quad (6.4)$$

The Laplace equation relates the capillary pressure to meniscus curvature by the relation

$$P_c = \sigma J \quad (2.30)$$

where J is the reciprocal of the meniscus's radius of curvature. Combining equations 2.30 and 6.4 gives

$$J = \left(\frac{P}{A} \right) \cos \theta$$

but the ratio perimeter to area is simply the inverse of the hydraulic radius of the capillary, R_h , so

$$J = \left(\frac{\cos \theta}{R_h} \right) \quad (6.5)$$

This result was examined by Carman (1941). He found that for near circular tubes and perfectly wetting liquids ($\theta = 0$) the equation fitted the experimental data of Schultze (1925a, b). However for other shapes the fit was not satisfactory. To quote Carman's explanation, this was because

"... where capillary walls form a sharp angle the edge of the meniscus shows a sharp local rise to a considerable height above the bottom of the meniscus."

This was a perceptive observation. Using the current terminology, Carman noted that equation 6.5 is adequate only when arc menisci are not present, i.e. for non-wedging systems.

6.3.1.2 Force balance approach

In section 2.4.3 the well known Washburn equation was derived via consideration of the forces on a meniscus in a cylindrical tube,

$$P_c = \frac{2\sigma \cos \theta}{R_T} \quad (2.45)$$

where R_T is the radius of the cylindrical tube, which in this case, is also twice the hydraulic radius of the tube. Incorporation of the Laplace equation and generalising the equation for arbitrarily shaped tubes yields equation 6.5,

$$J = \left(\frac{\cos \theta}{R_h} \right) \quad (6.5)$$

6.3.1.3 Derivation from the Gauss equation

The Gauss equation of capillarity relating the variation in interfacial area, dA_{LV} ,

to the associated volume change, dV , curvature and contact angle was derived in section 2.7.4;

$$dA_{LV} = -JdV + \cos\theta dA_{SL} \quad (2.69)$$

where dA_{SL} is the change in liquid/solid interfacial area.

Again consider a small displacement, dx , of the MTM in Figure 6.2. In the absence of AMs the projected area of the TM is equal to the cross-sectional area of the tube, A , which is constant along the length of the tube, hence

$$dA_{LV} = 0, \quad dV = A dx \text{ and } dA_{SL} = P dx$$

So equation 2.69 becomes,

$$0 = -J A dx + P \cos\theta dx$$

or

$$J = \left(\frac{P}{A}\right) \cos\theta = \left(\frac{\cos\theta}{R_h}\right) \quad (6.5)$$

6.3.2 Curvature in wedging systems: the MS-P equation

The Mayer & Stowe - Princen (MS-P) theory is exact only for calculations of curvature for non-gravity distorted menisci in uniform pores. In practice however, the theory is more versatile and has previously given accurate estimates of curvature for menisci slightly distorted by gravity in a variety of tube shapes, including configurations where the cross-section does not form a closed region. In certain circumstances the method has also yielded good approximations of measured curvatures of menisci in non-uniform tubes. The previous studies involving the MS-P method were discussed in detail in chapter 5.

The MS-P theory relies on equating the curvature found from a force or energy balance to the curvature of any arc menisci present in the system. At equilibrium the curvature of the AM(s) equals that of the TM in question. In applying the MS-P theory it is vital to choose an appropriate position to utilise this condition. At some distance above a TM (in practical terms this is only a few tube radii) the profile of an AM in the plane of cross-section becomes a circular arc of definable radius. The other radius of curvature, at right angles, is infinite. The choice of this position facilitates the solution of the overall meniscus curvature requiring consideration of only two dimensional geometry.

The MS-P equation can be derived by the same techniques employed for non-wedging systems, except that now the analyses must take into account the effect of the arc menisci. An arbitrary example of a wedging system is shown in Figure 6.3; an axe-shaped pore.

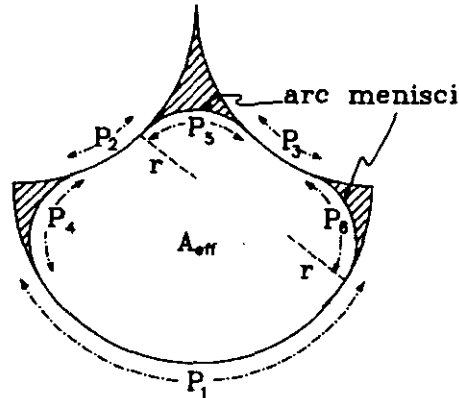


Figure 6.3 Illustration of the definition of A_{eff} , ΣP_S and ΣP_L for main terminal meniscus bounded in part by arc menisci in a uniform axed shaped tube. The solid perimeter, $\Sigma P_S = P_1 + P_2 + P_3$ and the liquid perimeter, $\Sigma P_L = P_4 + P_5 + P_6$.

The projected area of the MTM in Figure 6.3 is no longer simply the cross-sectional area of the tube as the AMs occupy the corners, reducing the effective projected area, A_{eff} , available to the MTM. The effective perimeter, P_{eff} , of the MTM must now be considered in parts: ΣP_S being the solid perimeter, and ΣP_L , the liquid perimeter. From Figure 6.3:

$$\Sigma P_S = P_1 + P_2 + P_3 \quad (6.6)$$

$$\Sigma P_L = P_4 + P_5 + P_6 \quad (6.7)$$

6.3.2.1 Energy balance approach

As in section 6.3.1.1 consider a small displacement, dx , of the MTM in Figure 6.3. The virtual work balance now yields

$$P_c A_{eff} dx = (\sigma_{SV} - \sigma_{SL}) \Sigma P_S dx + \sigma \Sigma P_L dx \quad (6.8)$$

The extra term, $\sigma \Sigma P_L dx$, accounts for the work done creating the new liquid perimeter. Incorporation of Young's equation gives

$$P_c A_{eff} = \sigma \Sigma P_S \cos \theta + \sigma \Sigma P_L \quad (6.9)$$

The principal radius of curvature of the AMs in the vertical direction is infinite, whilst the radius in the plane of cross-section is a circular arc of radius r (Figure 6.3). The arc radius is related to the capillary pressure using the Laplace equation,

$$P_c = \sigma/r \quad (2.30)$$

thus from equations 2.30 and 6.9

$$A_{eff}/r = \sum P_S \cos \theta + \sum P_L \quad (6.10)$$

and if the effective perimeter is defined as

$$P_{eff} = \sum P_S \cos \theta + \sum P_L \quad (6.11)$$

then equation 6.10 may be rearranged to give

$$P_{eff}r - A_{eff} = 0 \quad \text{or} \quad r = \frac{A_{eff}}{P_{eff}} \quad (6.12)$$

It is usual to normalise r with respect to some arbitrary tube characteristic dimension, R , giving

$$C = \frac{R}{r} = \frac{RP_{eff}}{A_{eff}} \quad (6.12)$$

where C is the *normalised* meniscus curvature. Equations 6.12 are statements of the *Mayer & Stowe - Princen equation*.

6.3.2.2 Force balance approach

The MS-P equation can also be derived via consideration of the forces acting on a TM. The weight of the liquid column in a tube is balanced by forces arising from interfacial tensions.

The weight of the column is simply the hydrostatic head multiplied by the effective area,

$$F_1 = h\rho g A_{eff} \quad (6.13)$$

The hydrostatic head is equivalent to the capillary pressure, P_c , so

$$F_1 = P_c A_{eff} \quad (6.14)$$

Acting in the opposite direction are forces arising from the contact of liquid with the solid perimeter;

$$F_{21} = \sigma \sum P_S \cos \theta \quad (6.15)$$

and that from the liquid surface not contacting the solid, $\sigma \sum P_L$, in Figure 6.3;

$$F_{22} = \sigma \sum P_L \quad (6.16)$$

Combining equations 6.13 to 6.16 yields

$$P_c A_{eff} = \sigma \sum P_S \cos \theta + \sigma \sum P_L \quad (6.10)$$

Equation 6.10 from section 6.3.2.1. Incorporation of the Laplace equation gives the MS-P

equation (eq. 6.12).

6.3.2.3 Derivation from the Gauss equation

To derive the MS-P equation from the Gauss equation of capillarity it is again necessary to include an extra term to account for the effect of the AMs. As before

$$dA_{LV} = - JdV + \cos\theta dA_{SL} \quad (2.69)$$

but the term dA_{LV} must now account for the change in liquid/vapour interface when the meniscus undergoes a small displacement, dx . As with non-wedging systems;

$$dV = A_{eff}dx$$

and $dA_{SL} = \sum P_S dx$

but $dA_{LV} = -\sum P_L dx$

and $J = 1/r$

Note the negative sign for the change in liquid/vapour area; interface is destroyed, not created. With these assumptions equation 2.69 becomes

$$A_{eff}/r = \sum P_L \cos\theta + \sum P_L$$

or $P_{eff}r - A_{eff} = 0 \quad (6.12)$

Note that if there are no AMs, equation 6.12 is equivalent to equation 6.5; i.e. the curvature equates to the inverse hydraulic radius of the tube.

By defining the effective area and perimeter in this way the interaction between the AMs and the MTM is accounted for. Neither the cross-sectional area of the AM, nor the solid perimeter wetted by the AM enter the expression for curvature. So the actual perimeter behind the AM could be any of a variety of alternative shapes and not affect the condition of the MTM.

The tubes shown earlier in Figure 6.1 are displayed again in Figure 6.4 with the effective areas hatched and the effective perimeters outlined. As before the prefixes W and D refer to a particular TM. DAMs act to hold up a TM, as does the solid perimeter. WAMs have radii of opposite signs to DAMs and thus pull down on a TM as in Figure 6.1f. As a consequence the contributions made by the liquid perimeters of WAMs to P_{eff} is negative.

To clarify the reasoning behind a WAMs negative contribution, consider the situation when the liquid surface of the WOAM in Figure 6.1f is replaced by a *completely non-wetting solid cylinder* ($\theta = 180^\circ$) of equal radius. As the shape of the liquid surface along the perimeter is unchanged the shape and height of rise of the MTM will remain the same. In calculating the contribution of this new surface to P_{eff} the nature of the downward force resulting from the WOAM becomes obvious:

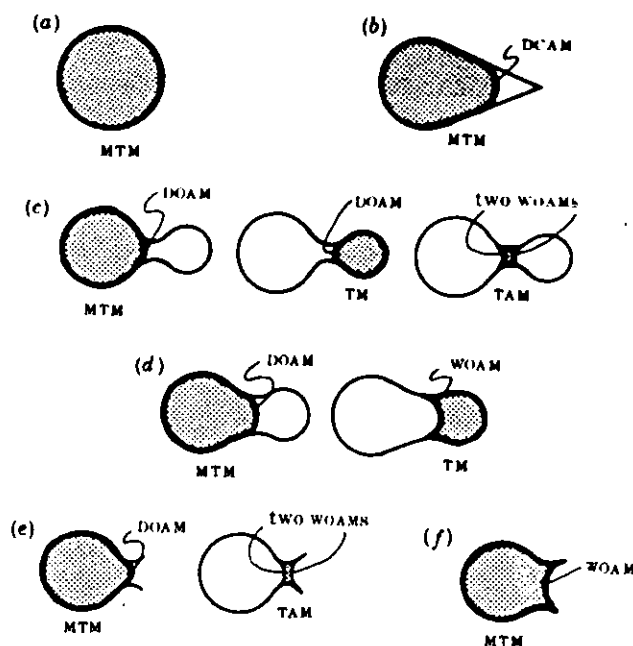


Figure 6.4 - Examples of A_{eff} and P_{eff} for the cross sections shown in Figure 6.1. A dryside open arc meniscus (DOAM) acts in the same sense as the wetted perimeter of the tube. A wetside open arc meniscus (WOAM) acts in the opposite sense.

$$\begin{aligned}
 P_{eff} &= P_w \cos(0) + P_{NW} \cos(180^\circ) \\
 &= P_w - P_{NW}
 \end{aligned}$$

where P_w is the wetted perimeter and P_{NW} , the non wetted perimeter.

Although any one of the three approaches of arriving at the MS-P equation is adequate, they are all of historical importance. Mayer & Stowe (1965) used the energy balance approach, whereas Princen (1969a) favoured the force balance. Derivation from the Gauss equation was Hwang's (1977) method, but he mistakenly thought the hydraulic radius method applicable to *all* uniform pores. Hwang did not account for the effect of the AMs and so omitted to include the liquid perimeter term. Consequently he found his results did not agree with those of Princen.

6.4 APPLICATION OF THE MS-P EQUATION

The MS-P method is a simple and elegant way of determining meniscus curvatures in the systems to which it applies. Mayer & Stowe (1965) and Princen (1969a) complicated the analysis by attempting to apply it to inappropriate systems.

Mayer & Stowe were interested in applying the analysis to converging-diverging pore geometries involving spheres when, in fact, their analysis was for tubes made up of uniform rods. Princen, though studying uniform tubes made up from rods, was interested in capillary rise which inevitably implies the distortion of menisci by gravity

and AMs of variable curvature. This led Princen to observe that his analysis was subject to the condition that the meniscus dimensions must be negligible when compared to the height of rise. Regardless, the MS-P theory is exact when applied to pores of uniform cross-section and menisci of constant mean curvature.

In principle, the application of the MS-P method is straightforward. Geometrical expressions for the effective area and perimeter, in terms of the pore dimensions and the radius of the arc menisci, need only be substituted into equation 3.10. However, the analysis depends critically on the prediction of whether or not, and where AMs exist in the particular geometry. For example, AMs never occur in circular cross-section tubes, but will always occur in tubes made up of cylinders in contact, unless the contact angle is exactly $\pi/2$ rad. (90°).

In pores of angular geometry, such as the kite-shaped tube of Figure 6.1b, the presence of an AM depends on the wetting properties of the liquid. In Figures 6.1c and d the width of the neck of the dumb-bell determines the existence of the OAMs, as the geometry is changed arc menisci may appear and disappear. To determine the existence or non-existence of AMs it is necessary to calculate the curvatures for each possible meniscus configuration and then assume that the meniscus will adopt the one with the lowest curvature; that having the minimum surface energy.

This method was used by both Mayer & Stowe and Princen, although neither stated it as a principle. It is not foolproof, as cases are possible where physically significant metastable menisci can exist (Mason & Morrow 1987). These menisci may be required to overcome an energy barrier before adopting a configuration of lower curvature.

To illustrate the techniques employed to solve the MS-P equation some geometrically simple pore shapes are discussed below. Similar solutions had been published prior to the studies of Mason and co-workers: Princen (1969b) has given solutions for menisci in equilateral triangular and square cross-sectioned tubes for perfectly wetting liquids. Concus (1974) published solutions for menisci in polygonal tubes for large contact angles. Both analyses are simplified as in the former AMs always exist and in the latter they never appear. Mason & Morrow (1984a) gave general solutions for menisci in polygonal tubes. These are discussed first as they produce analytical solutions for curvature which conveniently illustrate how menisci in wedging and non-wedging systems are analysed.

The technique for obtaining expressions for effective areas and perimeters is standardised throughout this study. With the relatively simple shapes discussed below the method may appear somewhat long-winded, but with the more complex geometries discussed later its versatility becomes apparent. Basically the cross-section of a pore, or a relevant part of it, is divided into a number of regions. Each region has an associated perimeter adjoining the meniscus and usually, an area and angle, all denoted by the region number. From these regions the required effective perimeter and area are easily derived.

6.4.1 Analytical solutions

6.4.1.1 Equilateral triangle with a perfectly wetting liquid

Figure 6.5 shows a meniscus in a uniform tube where the cross-section is an equilateral triangle - a three sided polygon. The characteristic dimension of the tube is chosen to be the radius of the inscribed circle, R . Although the problem can be solved for any contact angle, only the case of a perfectly wetting liquid is considered below. Figures 6.5a - c show the form of the meniscus. The MTM spans the centre of the tube, reaching its lowest point in the centre of the triangle, O , while the liquid rises in the corners to an infinite height, bound by AMs of radius r .

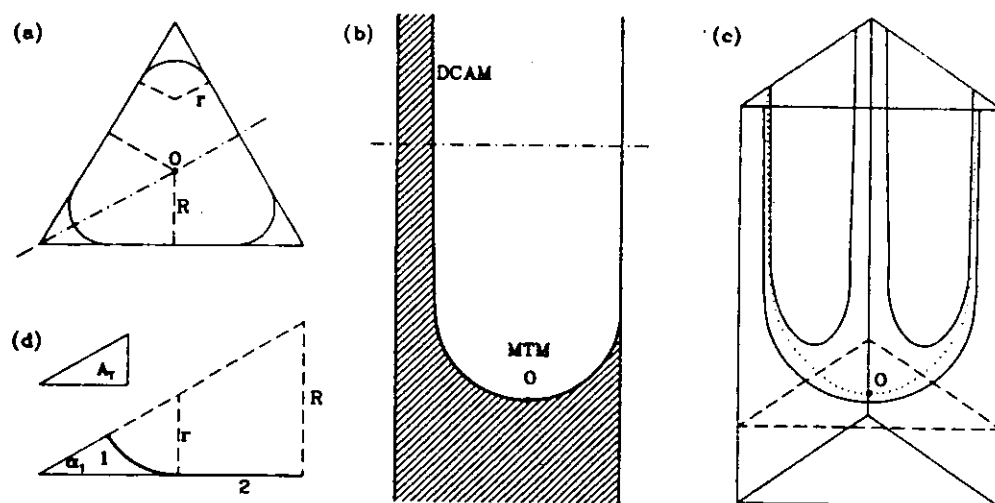


Figure 6.5 - Configuration of arc menisci in a uniform triangular tube (a). The MTM spans the centre of the tube reaching its lowest point in the centre of the tube (b). The liquid rises into the corners to an infinite height bound by AMs (c). The terminology required for the application of the MS-P theory is also shown (d).

The cross-section is polygonal and it is the ratio of area to perimeter that is required so only one corner sector need be analysed. Figure 6.5d shows a right-angled triangle; one sixth the area of the whole channel. Here, only two regions within the sector need be defined; numbered 1 and 2. The parameters of these regions may now be written down.

a) Angles

Only region 1 has an associated angle and, since this is part of a equilateral triangle;

$$\alpha_1 = \pi/6 \quad (6.17)$$

b) Perimeters

The perimeters of each section are obtained from simple trigonometry:

$$P_1 = 2\alpha_1 r \quad \text{Equations}$$

$$P_2 = (R - r) \cot \alpha_1 \quad 6.18$$

c) Areas

Only region 1 has an associated area, but the area of the whole sector, A_T , is also required:

$$A_T = \frac{1}{2} R^2 \cot \alpha_1 \quad \text{Equations}$$

$$A_1 = \frac{1}{2} r^2 \cot \alpha_1 \quad 6.19$$

d) Effective perimeter and area

It is now a simple matter to write the effective area and perimeter:

$$\begin{aligned} P_{eff} &= \sum P_S + \sum P_L \\ &= P_2 + P_1 \end{aligned} \quad (6.20)$$

and $A_{eff} = A_T - A_1 \quad (6.21)$

e) Solution of equations

The simultaneous equations 6.17 through 6.21 together with the MS-P equation itself (eq. 6.12) yield a quadratic equation in r , this may be normalised with respect to R giving

$$\left(\frac{\sqrt{3}}{2} - \frac{\pi}{6} \right) \left(\frac{r}{R} \right)^2 - \sqrt{3} \left(\frac{r}{R} \right) + \frac{\sqrt{3}}{2} = 0 \quad (6.22)$$

Hence $\frac{r}{R} = \frac{\sqrt{3} \pm \sqrt{\pi/3}}{\sqrt{3} - \pi/3}$

which yields solutions for r/R of 4.4955, which is physically impossible as it implies $r > R$, and 0.5625. So the normalised curvature of the meniscus in triangular channel under perfectly wetting conditions is

$$C_\Delta \approx 1.778$$

6.4.1.2 *n*-agon tubes with variable wetting

The solution for an equilateral triangular tube can be generalised for a *n*-sided polygon channel under variable wetting conditions. The analysis follows the same pattern as before, but the trigonometry is more complex.

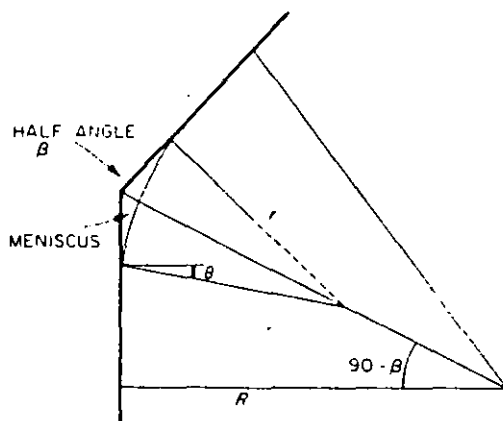


Figure 6.6 - Diagram of a corner of a polygonal sectioned tube. Depending on the contact angle, an arc meniscus (AM) may exist in the corner.

Consider the sector of an *n*-gon tube shown in Figure 6.6. The incircle radius, *R*, is again selected as the normalising dimension. Let the AM meet the wall with a given contact angle θ .

a) Angle

Let the half angle in the corner of the *n*-gon be β , hence

$$\alpha_1 = \beta \quad (6.23)$$

b) Perimeters

$$P_1 = (\pi/2 - \alpha_1 - \theta)r \quad \text{Equations}$$

$$P_2 = R \cot \alpha_1 - r(\cot \alpha_1 \cos \theta + \sin \theta) \quad 6.24$$

c) Areas

$$A_T = \frac{1}{2}R^2 \cot \alpha_1 \quad \text{Equations}$$

$$A_1 = \frac{1}{2}r^2(\cos^2 \theta \cot \alpha_1 - \cos \theta \sin \theta - (\pi/2 - \alpha_1 - \theta)) \quad 6.25$$

d) Solution of equations

Combining equations 6.23 to 6.25 with the MS-P equation,

$$P_{eff}r - A_{eff} = 0 \quad (6.12)$$

yields a quadratic of the form

$$\frac{1}{2}(\cos^2 \theta \cot \beta - \cos \theta \sin \theta - (\pi/2 - \beta - \theta))\left(\frac{r}{R}\right)^2 - \cos \theta \cot \beta \left(\frac{r}{R}\right) + \frac{1}{2} \cot \beta = 0 \quad (6.26)$$

Again there are two roots, only one of which is physically realistic. The other probably corresponds to menisci on the outside of the polygon.

When the coefficient of $(r/R)^2$ becomes zero then there are no real roots and

$$\theta + \beta = \pi/2$$

which represents the point where the AMs in the corners disappear. So the system will be wedging only if

$$\theta \leq \pi/2 - \beta$$

Hence for $\pi/2 > \theta > (\pi/2 - \beta)$ the AMs do not exist and equation 6.26 reduces to one where the curvature is given in terms of the inverse hydraulic radius,

$$\frac{A}{P} = \frac{R_h}{\cos \theta} = \frac{1}{J} \quad (6.27)$$

Under these conditions the MTM simply runs into the corners. Concus (1974) investigated menisci of this configuration and noted that equation 6.27 corresponds to the spherical meniscus in the polygon tube with incircle radius $R/\cos \theta$.

AMs will always exist if $\theta = 0$ unless $\beta = \pi/2$, which is the half angle in a polygon with an infinite number of sides or, in other words, a cylindrical tube. In Figure 6.7 the curvatures in three, four and infinite sided tubes of equal hydraulic radius are shown as a function of the contact angle, θ . As would be expected, no difference in curvature is seen between non-wedging menisci in polygons and those in a cylindrical tube of equivalent section. However, when the AMs form, the curvature in the polygons drops below that for a cylindrical tube. A triangular pore yields a lower curvature than a square pore at a given contact angle, implying that the height reached by the meniscus drops as the corners become more acute.

6.4.2 Non-analytical solutions

The MS-P equation usually cannot be solved analytically. Even for seemingly simple shapes, like that of a rod in a corner, the simultaneous equations in A_{eff} , P_{eff} and the MS-P equation prove to be unresolvable. To arrive at a value for curvature numerical or graphical techniques must be employed.

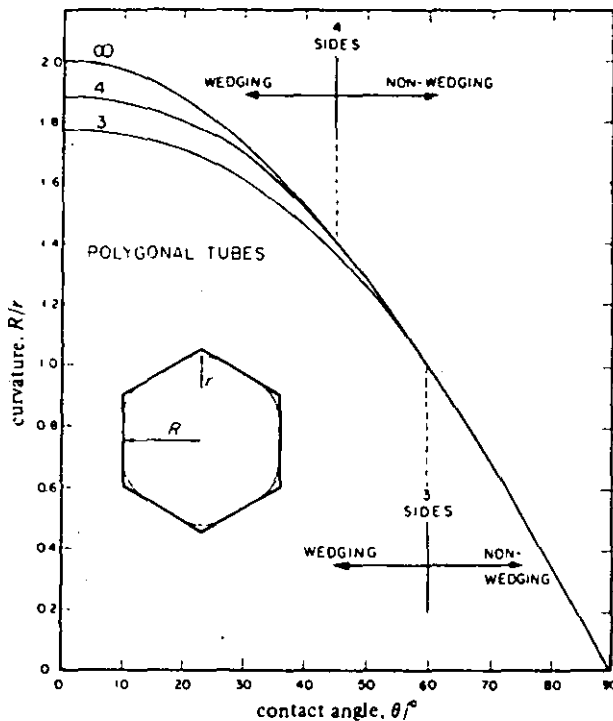


Figure 6.7 - Curvature of the meniscus in the n -agon tube normalised relative to the ratios of the insphere is given as a function of the contact angle. The infinite side number tube is simply a cylinder and the values agree with those for meniscus curvature in cylindrical tubes. When corners exist, the terminal menisci merge with arc menisci at low contact angles, and this reduces the curvature.

Figure 6.8 shows the graphical solution for the kite-shaped pore with the dimensions shown. The effective area to perimeter ratio is calculated for various prescribed values of r/R and, in this case, $\theta = 0$. A graph of $y = A_{eff}/RP_{eff}$ versus $y = r/R$ can then be plotted. The intersection of the line $y = r/R$ with $y = A_{eff}/RP_{eff}$ gives the value of r/R which is the solution to the equations.

At the point of intersection the value of A_{eff}/RP_{eff} is its maximum possible value, and hence also r 's. This confirms the equilibrium situation i.e. the meniscus has minimum curvature, corresponding to the minimum surface energy configuration for the particular boundary conditions.

Of the uniform tubes employed in the current study only the rectangular duct's equations solve analytically. For the remaining tubes numerical techniques provided the best solution mechanism as they are amenable to use on computers, enabling a large number of solutions to be found quickly. Below the numerical methods used here are described.

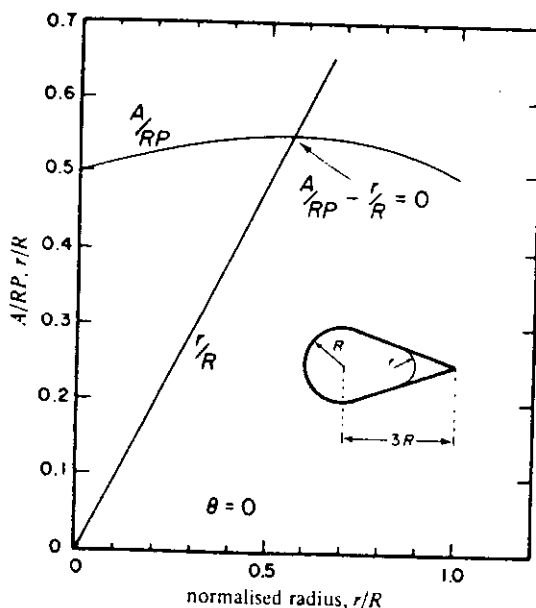


Figure 6.8 - Example of the graphical solution of the meniscus curvature for the kite-shaped pore shown. The intersection of the two lines gives the solution. The solution is always at the maximum value of A/RP .

6.4.2.1 Microcomputer solution technique

For the purposes of numerical solution the MS-P equation may be written;

$$F(r) = \frac{A_{eff}}{P_{eff}} - r = 0 \quad (6.28)$$

or

$$f(r) = \frac{A_{eff}}{P_{eff}} \quad (6.29)$$

The ratio A_{eff}/P_{eff} will comprise a number of simultaneous non-linear equations in terms of the arc radius, r , the geometry of the particular tube and, where relevant, the solid/liquid contact angle, θ . These equations do solve to give a unique value of r .

The form of equation 6.28 lends itself to solution by numerical methods. The requirements of which are not one, but multiple solutions in terms of a second variable, RR : either the contact angle or a characteristic dimension of the tube such as rod-plate spacing, rod radius ratio or tube aspect ratio. The resulting group of stepwise solutions for r in RR may be used to plot a graph of the function $r = f(RR)$ or, more often, $C = 1/f(RR)$ which may then be compared with experimental results.

Over the course of the study standard solution routines were developed, written in BASIC on a BBC microcomputer. Throughout emphasis was placed on obtaining the required solutions rather than computational elegance. The standard program was

structured so that on investigation of a new tube configuration all that is required is substitution of the relevant expressions for A_{eff}/P_{eff} and some minor adjustment of input and output routines.

Figure 6.9 shows a simplified flow chart. At given RR the radius of curvature, r , is iterated using successive bisection (internal halving) from initial "guesses" above and below the solution. The user is only required to make the initial guesses for the first solution in a set. Subsequent initial guesses are determined automatically by a process of intuitive reasoning and interpolation. Much of the complexity of the program arises in obtaining initial guesses for one solution from the solution that preceded it. Figure 6.9 shows a number of separate procedures (sub routines) each of which carries out a specific task.

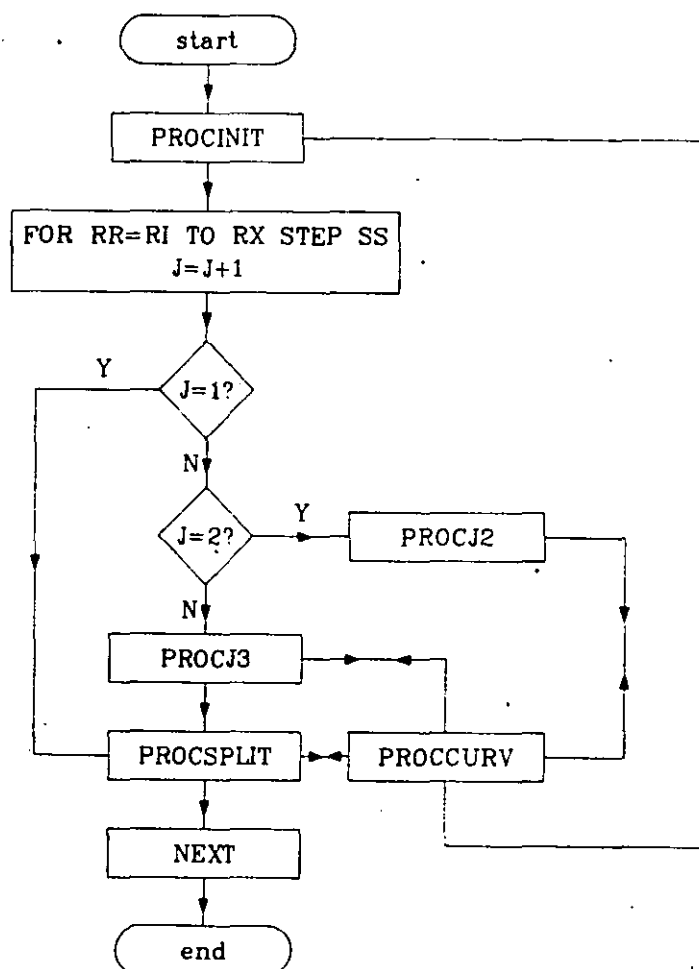


Figure 6.9 - A simplified flow chart illustrating the successive bisection and interpolation routines adopted for the numerical solution of the MS-P equation. This standard program was utilized for all tube shapes and wettabilities investigated with only minor adjustments required.

a) PROCCURV

The procedure, PROCCURV, contains the detailed equations that make up $F(r)$: those for the angles, areas and perimeters of the relevant regions required to calculate A_{eff}/P_{eff} . PROCCURV is sent a value of r and returns values of $F(r)$ and the iteration criteria, $R5$ and $R6$ (these criteria stop the iteration when sufficient accuracy has been achieved).

b) PROCINIT

PROCINIT initialises the program. The user is prompted to input the required information: the geometric constants, the minimum (RI) and maximum (RX) values of the characteristic dimension or contact angle (RR) and the interval or step size between solutions (SS). The program then asks for two guesses at the first solution, r_{RI} , to initialise the successive bisection iteration method: one above, $(r_0)_{RI}$, and one below, $(r_1)_{RI}$.

PROCINIT liaises with PROCCURV and displays the values of $F(r)_{RI}$ calculated with $(r_0)_{RI}$ and $(r_1)_{RI}$. Calculations will not proceed until one positive and one negative value of $F(r)_{RI}$ have been returned. In general, provided that the two initial guesses are close to the solution, r , the function $F(r)$ will be continuous between them, thereby enabling the solution to be found. In mathematical notation the conditions for convergence are;

$$F(r_0) < 0 \quad \text{Equations}$$

$$F(r_1) > 0 \quad \text{6.30}$$

and for $r_0 \leq r \leq r_1$ $F(r)$ is continuous.

PROCINIT also prints a record of the inputted information and the headings for a table of results before returning to the main program.

c) PROCSPLIT

PROCSPLIT carries out the iteration for r at the current value of the characteristic dimension or contact angle, RR , from given values of r_0 and r_1 . Iteration by successive bisection proceeds as follows:

$$r_2 = \frac{(r_1 + r_0)}{2} \quad \text{(6.31)}$$

PROCSPLIT liaises with PROCCURV which returns the value of $F(r_2)$. r_3 is then determined according to the sign of $F(r_2)$:

$$\text{If } F(r_2) < 0 \text{ then } r_3 = (r_0 + r_2)/2$$

$$\text{If } F(r_2) > 0 \text{ then } r_3 = (r_1 + r_2)/2$$

The value of $F(r_3)$ is now calculated and bisection repeated as above. Iteration continues until

$$\text{ABS}|F(r_n)| \leq 1 \times 10^{-5} r_{n-1} \quad \equiv \quad \text{ABS}|R5|, |R6| \quad \text{(6.32)}$$

The above iteration criteria ensure that values of curvature obtained are exact to three decimal places. Having determined the solution at r_{RR} PROCSPPLIT prints out results in tabular form of, among other parameters, the curvature of the meniscus in the tube shape defined by $RR; C_{RR}$:

d) PROCJ2

Procedure J2 is enacted only once to find the initial guesses for the second solution for r : that when $RR = RI + SS$. $(r_0)_{RI+SS}$ and $(r_1)_{RI+SS}$ are found by addition or subtraction of factors of r_{RI} from r_{RI} . The magnitude of the factor is gradually increased until;

$$F((r_0)_{RI+S}) > 0 \quad \text{and} \quad F((r_1)_{RI+S}) < 0 \quad (6.33)$$

e) PROCJ3

PROCJ3 finds initial guesses of the radius of curvature for the third and subsequent solutions. With two solutions already calculated on the function $r = F(RR)$ a first approximation of subsequent solutions can be interpolated;

$$r_{RR_n} \equiv r_{RR_{n-1}} + (r_{RR_{n-1}} - r_{RR_{n-2}}) \quad (6.34)$$

$F(r_{RR_n})$ is then calculated from PROCCURV. If $F(r_{RR_n}) > 0$ then $(r_0)_{RR_n} = r_{RR_n}$ and $(r_1)_{RR_n}$ is determined by adding factors of r_{RR_n} to r_{RR_n} until $F((r_1)_{RR_n}) < 0$. Similarly if $F(r_{RR_n}) < 0$ then $(r_0)_{RR_n} = r_{RR_n}$ and $(r_1)_{RR_n}$ is determined by subtracting factors of r_{RR_n} from r_{RR_n} until $F((r_1)_{RR_n}) < 0$. Use of this routine ensures that the two initial guesses are close to the solution. Once the guesses have been found the near-exact value of r_{RR_n} is determined by PROCSPPLIT.

The solution program described above works satisfactorily for solution of the MS-P equation, at least for the systems investigated here. An advantage of the successive bisection method, beyond its simplicity, is that the maximum error in the solution can always be quantified, being a maximum of half the difference of the last bisected interval. Thus

$$e_{\max} = \frac{(r_n - r_{n-1})}{2} \quad (6.35)$$

The techniques could certainly be improved with the application of more advanced numerical methods, having faster convergence, and faster computer languages. Application of alternative numerical methods should be approached with caution. In early work the secant method (a modification of the well known Newton-Raphson method, see Hosking 1978) was used to iterate r , but the one-sided approach to solution the method uses proved inadequate for instances where discontinuities in $F(r)$ were encountered.

Exactly where and why discontinuities occur in $F(r)$ was not pursued, but that this occurs was apparent with some pore configurations, particularly those requiring more complicated geometric descriptions. On occasions the successive bisection and interpolation method also "crashed", but this was overcome by reducing the step size for RR . The method has the advantage, over one-sided methods, that once the starting values have been correctly chosen convergence is assured.

The computer time required for each solution of r_{RR} was not excessive, varying between a few seconds and, at worst 3 to 4 minutes. An entire set of results describing the relation $C = 1/f(RR)$ can thus be determined in a matter of a few hours. The necessity for the user to make initial guesses for the first solution is a consequence of both the possibility of discontinuity and of the non-unique solution of r afforded by the equations. Otherwise fractions of the geometric size of the tube could have been employed as first guesses.

With each new meniscus or pore configuration the relevant equations were written into PROCCURV. When possible, the solutions given by the program were validated by comparison with previously published or calculated results. Often comparison could be made to results given in publications by Mason & co-workers, but usually only for a limiting value of r_{RR} .

To conclude, the successive bisection and interpolation method described above proved versatile enough to yield solutions of the MS-P equation for all the systems investigated here. Little alteration of the program was required for each new configuration and the convergence of the method was such that solutions were found in a satisfactory period of time. Details specific to particular configurations are discussed in the relevant results sections (chapters 8 to 11) and listings of the programs are given in the appendices; notation follows that employed here.

CHAPTER 7

Experimental apparatus and procedures

7.1 INTRODUCTION

The successful development of any new scientific theory, from its mathematical conception to its widespread acceptance and application, depends upon the validation of the theory over the range of conditions to which it applies. In validating the MS-P theory it is important to note that the theory is exact *only* for capillary surfaces of constant mean curvature - those surfaces undistorted by a gravitational field. It follows that the techniques used for the experiments must minimise the effects of gravity on the surfaces under investigation.

The most obvious approach is to conduct the experiments under zero gravity conditions. Indeed, some experiments on capillarity have been performed in space. Unfortunately, beside being prohibitively expensive, zero gravity experiments in space, drop towers or in aircraft on parabolic flight-paths are often unsuccessful. The capillary forces are usually so small that other phenomena, notably electrostatic forces, can seriously distort results (Haynes 1989).

If the experiments were conducted with a pair immiscible liquids of equal density then the effects of gravity will again be entirely eliminated, but there are serious drawbacks with this approach as well. The difference in interfacial tension between such a liquid pair is usually small and, to maintain constant curvature conditions, it is vital to match the densities precisely. As a consequence, successful experiments require fine temperature control of the *few* suitable liquid pairs available (Mason 1970).

A third approach centres not on eliminating gravity, but on reducing its effects relative to the capillary forces by making the pore geometry small. (Similar reasoning accounts for the *small* bore capillary tubes selected for school physics experiments). Recently this method has been successful in testing of the MS-P theory (Mason *et al.* 1983, 1984a, 1986, 1987 and 1988), but there are disadvantages. The smaller the pore geometry becomes the larger are the errors in fabricating the geometry. Conversely the effects of gravity become more appreciable as the pore is enlarged.

Past experiments discovered a scale of apparatus whereby the model pores could be made large enough to be mechanically accurate, whilst the height of rise in the pores was such that the meniscus surfaces were not overly effected by gravity. Although this amounts to a compromise, it fortunately allows enough variation of pore size to facilitate validation of the theory.

The experiments conducted here principally involved measuring the heights of rise of terminal menisci in uniform capillaries. The pores were made up in part by a number of cylindrical rods, or flat plates, and in part by a transparent plate (usually glass) through which the meniscus was observed with a cathetometer. Meniscus curvature was calculated from a simple equation. So long as the change in height over the region of the TM is small in comparison to the overall height of rise, the condition of constant curvature is satisfied. Furthermore, curvatures are measured by a comparative method, negating the need for temperature control.

In the following pages the general points stated above are elaborated and justified, details of apparatus are given and procedures discussed.

7.2 APPARATUS

7.2.1 General description

Figure 7.1 shows photographically the equipment used in the experiments to validate the MS-P theory. Broadly speaking, the apparatus comprises a pair of rectangular steel cell-blocks that contain the model pore and reservoir indicator cells (1). The cell-blocks connect, via Swagelock fittings and PTFE tube to each other and the main liquid reservoir (2), a PTFE beaker capable of providing a small positive head. The test cells and main reservoir are supported by separate laboratory jacks (3) enabling the height of the cells to be fixed at a comfortable viewing position and the menisci in the cells to be adjusted to a suitable level. The heights of the menisci in each cell are measured by a cathetometer (4) equipped with a tele/microscope capable of traversing both laterally and longitudinally, and a vernier scale accurate to 0.01 mm. The menisci are illuminated by a pair of lamps (5), each with two flexible optical fibre antennae. The apparatus stands on levelled, vibration free, slate-topped concrete benches. On the lower bench sits the cathetometer, fixed in position by two restraining clamps.

7.2.2 Cell design

The optimum design of a capillary rise experiment, for a given density difference and interfacial tension, involves a compromise between fabrication errors and distortion by gravity of the meniscus shape. As pore size is increased fabrication errors decrease, but gravitational distortion of the meniscus increases. Mason *et al.* (1984a) discovered a "*window of opportunity*" in the scale of the apparatus through which it is possible to measure curvatures in accurately fabricated pores, capable of holding menisci not unduly distorted by gravity.

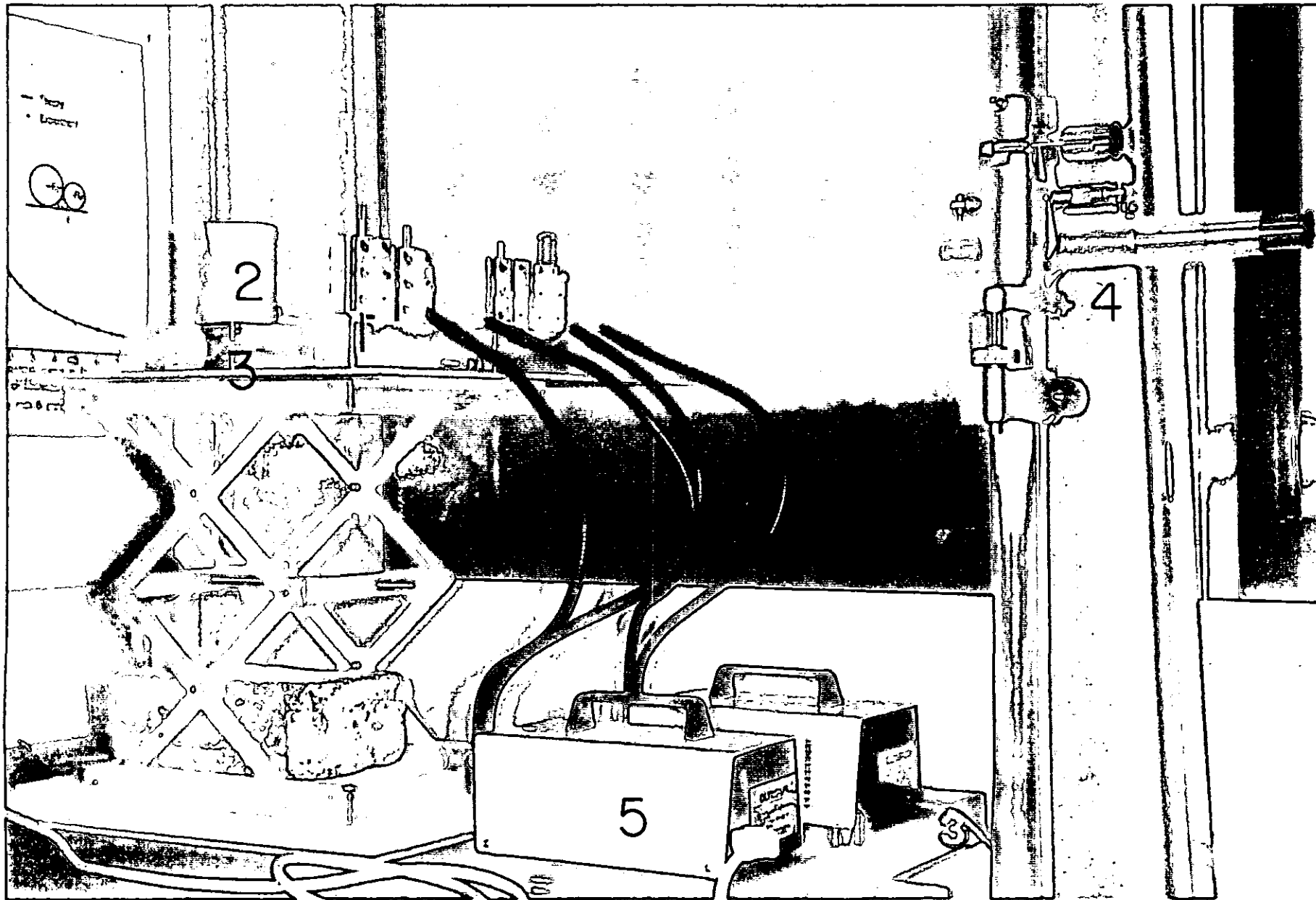


Figure 7.1 - Photographic depiction of the apparatus employed for the capillary rise experiments (see text).

Before they could specify the optimum cell dimensions, Mason *et al.* needed to know the limits of this "window". An experiment carried out by Mason and Morrow (1984a) showed that distortion of menisci in cylindrical capillaries becomes appreciable when the height of rise drops below about 7 mm (0.3") with isooctane; the liquid used for the majority of the experiments. A 7 mm rise roughly corresponds to a capillary of 1.5 mm (1/16") diameter. A similar experiment has been performed for the present study; further details can be found in chapter 8.

To accurately fabricate model pores of similar or smaller hydraulic radius as the 1.5 mm capillary tube is difficult. However fabrication errors can be largely eliminated if, instead of direct fabrication, the model pores are made up from precision elements that are considerably larger than the pore itself. All the pore configurations investigated here are made up of cylindrical rods and/or flat plates. When put together they create pores considerably smaller than themselves in which there is a much greater level of confidence in the geometric dimensions. Also, the meniscus is visible through the front flat plate!

Based on the experience of past studies, pores made up of rods between 1/32" and 3/8" (0.8 and 9.5 mm) usually give satisfactory results: exact limits will depend on the particular pore configuration. Having determined the limiting sizes of the model pores in variously fashioned cells, it became possible for Mason and Morrow (1986) to design a versatile cell arrangement: Figure 7.2.

Cell blanks are fashioned from an easily machinable aluminium alloy. The blanks, with a face measuring 2 1/4" by 1 1/2" (57 by 38 mm), are 3/4" (19 mm) thick and include a 5/8" (16 mm) connecting plug machined at the base. Each cell has a 1/4" (6 mm) glass window, 3/4" (19 mm) wide, which is held by clamps to the machined front face of the cell. A channel capable of accommodating rods in the required configuration is then machined from the front face.

A given cell, together with (usually) a reservoir level indicator cell (with a single 1/2" (12.7 mm) square channel), fits into a cell block. The block is simply a rectangular piece of alloy containing two holes to receive the connecting plugs of the cells and so hold them vertically in position; the clearance being sealed by PTFE 'O' rings. The cell block connects the cells via 1/8" (3 mm) fluid viaducts and is itself connected to the remainder of the system by flexible PTFE tubing of 1/16" (1.59 mm) I.D. This gives the apparatus a useful characteristic as the model pore and indicator cells are always in equilibrium with each other before the indicator cell equilibrates with the main liquid reservoir. The two cell-blocks are connected in parallel via a Swagelock "T" piece, to facilitate quicker stabilization after level changes.

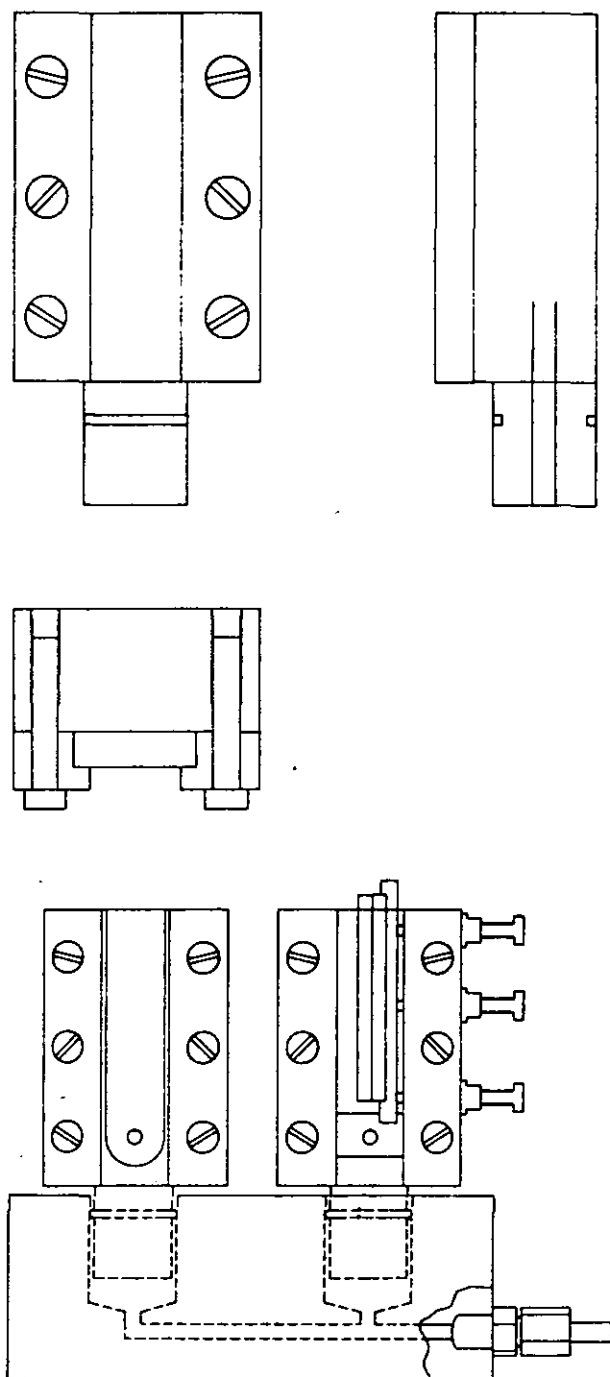


Figure 7.2 - Sketch of the standard "cell blanks" used to realise the rod and plate geometries of the theory (top). A channel with the specifications suiting the particular rod arrangement can be machined from the front face and clamps added as required. The cells fit into a cell block connected to the main liquid reservoir (below).

The early channel designs, by Mason and co-workers, required that the channels were of the exact depth and width to accommodate the rods in the desired positions. Results were not always satisfactory as even a machining error of a fraction of a thousandth of an inch (thou.), a typical engineering tolerance, could cause significant deviations from the prescribed geometry, usually because rods were not properly in contact.

The current design ensures rods contact by making the channels deeper and/or wider than required. Tightening screws can then be fitted to the back and/or side of the cells to clamp the rods in position. This approach has the added advantage that different rods may be used in the same cell to vary a particular pore shape or to give entirely different configurations. However, it sometimes becomes difficult to assemble the pores in the prescribed shape and it is necessary to use a process of trial and error until the correct position is achieved. If assembly of the pore becomes excessively complicated it is always possible to design a new cell specifically for that purpose. The clamping screws are fitted with plastic nuts, tightened against the outside of the cells, to prevent leakage along the threads.

It was occasionally necessary to fabricate cells of a different overall size to the standard blanks and sometimes parts of the channel needed to be made to more precise dimensions. Errors in the fabrication of the cells were small due to the use, by an experienced machinist, of a milling machine equipped with a digital read-out. Details of individual cell designs are given in the sections relating to each particular pore shape, but the principles of design and fabrication remain the same.

7.2.3 The cathetometer

In addition to accurately fabricated model pores, the success of the capillary rise experiments depends on precise measurements of heights of rise. Meniscus curvature is directly proportional to the observed heights, so any error in the readings is passed directly on to the measured curvature. Accurate readings require a versatile optical instrument; one capable of magnifying the menisci and traversing both laterally and longitudinally whilst maintaining the ability to record heights precisely, even when the focusing position is altered. Cathetometers are designed for this purpose, but they vary in quality and capability.

For some early experiments a cathetometer of antiquated design and uncertain quality was used. This was soon replaced by a modern precision instrument. The Gaertner M-912 horizontal-vertical cathetometer as shown in Figure 7.1. A substantial frame supports a precision 1 1/4" diameter meter rod between thrust bearings that enable rotation about the rod axis. A scale engraved on the rod reads to 0.5 mm. An alignment tele/microscope (the Gaertner M533HG) and carriage assembly mounted on the rod is

equipped with a vernier scale capable of reading to 0.01 mm (0.004"). A finely threaded screw situated on the carriage assembly provides fine, hysteresis free, vertical adjustment. This cathetometer is a special non-standard device obtained specially for this project.

The manufacturers claim that refocusing with the tele/microscope over the range 75 mm to 1.25 m (3" to 4 ft) will not alter a reading by more than .0025 mm (.001"); this is considerably better than an ordinary slide-focus scope which can give errors of 2.5 mm over the same range. The tele/microscope also has the advantages of a completely enclosed mechanism, so there is no danger of stray "fingers" coming into contact with it. Magnification is quoted at 17.5X at 75 mm dropping to 4X at 1.25 m; between 150 and 300 mm (6" to 1 ft), the extremes of the working distance used in the experiments, the scope provides adequate magnification.

7.2.4 Slate-topped concrete bench and pillar

The large slate-topped bench shown in Figure 7.1, provides an inert level surface to conduct the experiments on. The bench is sturdy enough to maintain its position if accidentally jolted and sits on lead shrouded rubber sheet which damps out vibration emanating from elsewhere in the building.

The bench was built to specifications supplied by Mason for his earlier work. I later designed the pillar to hold the Gaertner cathetometer, as unlike the old device, it was too large to site on the bench. The principles of the design of the pillar are basically the same as those for the bench: a slate slab is supported by adjustable discs (that enable the slate top to be levelled) on studs protruding from a rubber backed, ferroconcrete block (Fig. 7.3). The pillar requires, in addition to the supporting studs, a long stud which passes through the centre of the slab. To this a two-jawed clamp is attached to fix the cathetometer in position, once it's been levelled.

7.2.5 Pore construction components

Of the pore shapes investigated almost all are made up in part from cylindrical elements and all include a flat transparent window. The selection of the cylindrical rods was governed by three factors:

- i)* The rods had to be manufactured with a high degree of precision on diameter to give confidence in pore geometry.
- ii)* They were required to have a uniform surface finish so that wetting properties are reproducible.

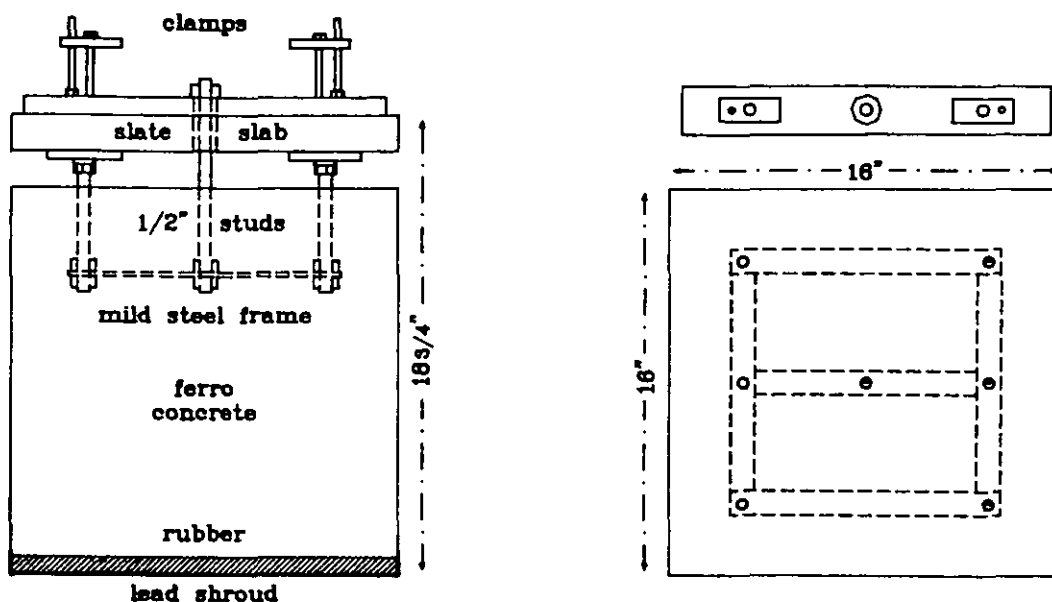


Figure 7.3 - Design of the slate-topped pillar required to support the cathetometer.

- iii) The rods needed to be available in suitable lengths over a range of diameters covering $1/32''$ to $3/8''$.

Two systems were chosen, one consisting of steel rods and glass windows to be used for perfectly wetting experiments ($\theta = 0$), the other being a teflon system used with liquids that produced known contact angles. Three different rod types were used in construction of the pores; their properties are discussed below.

7.2.5.1 HSS drill blanks

Hardened steel drill blanks, whose more usual applications are as arbors, punches, spindles or gauges, proved to be good construction elements; satisfying the requirements well. Steel, in common with other metals and hard solids, has a *high energy surface*; that is it has high surface energy. High energy surfaces are wet by most liquids against air, particularly by those with low surface tensions. In addition, steel can be made with smooth, homogeneous surfaces.

The steel used for the blanks is first hardened, then precision ground using a centreless grinder; the surface finish is bright. The blanks are available in extensive size ranges. Between the size limits imposed by the cell design ($1/32''$ to $5/16''$) the rods were obtained in a 10^{th} mm metric range and a $1/64^{\text{th}}$ imperial range. In addition a numbered range provides sizes that fall in-between those of the other ranges. Tolerances for the rod diameters of $+0$ to -0.02 mm (8 thou.) are claimed by the manufacturer (SKF & Dormer Tools Ltd.). The mean diameters of rods used were found by averaging

measurements taken with a digital micrometer along the rod length and around the axis. These drill blanks are useful because they come in a whole range of sizes; imperial, metric and number sizes. Their finish is not really good enough and they are always fractionally undersize.

7.2.5.2 Needle rollers

Needle rollers, as used in roller bearings, have to be made to high precision for their usual function. Also manufactured from hardened steel and precision ground and polished, but with a matt finish, the needle rollers made excellent construction components. However, they are not available in as an extensive range as the drill blanks (1 to 5 mm in increments of 0.5 mm), but their tolerance is better at $+0$ to -0.003 mm on diameter and measurements showed much less variation in diameter along a given rod. They are also not as long as drill blanks.

7.2.5.3 Teflon rods

Teflon (PTFE) has a *low energy surface* and has been shown to give reproducible wetting properties with a homologous series of liquids (Morrow 1974 or section 2.7.6). This is a rare quality among unprepared surfaces and led to the selection of teflon for experiments with non-zero contact angles.

In comparison to steel rods there are noticeable disadvantages in making pores from PTFE rods:

- i) Teflon rods are flexible and compressible which makes assembling a uniform pore a much more difficult operation.
- ii) The range of available sizes is restricted and ground PTFE rods couldn't be obtained with diameters less than 1/16". However, in this study only rod sizes greater than 1/8" proved successful.
- iii) Usually the rod is extruded and consequently has a very variable diameter. The rod is available ground, but grinding to high precision is not possible as PTFE is a soft material. Grinding also roughens the surface and can modify contact angle behaviour. The claimed diameter tolerance of the manufacturer, Dalau Ltd., of $+0.2$ to -0 mm along a 1 m length is also very poor, but for the short lengths employed in the experiments the variation was not so great. In fact diameter variation around the rod section was more of a problem than longitudinal variations.

In addition to the rods described above, all pores required a transparent window through which heights of rise are measured. For the wetting system a flat glass plate was used. However the teflon system usually required all pore surfaces to have identical

wetting properties. A thin, transparent film of a fully fluorinated polymer was stretched over the inner surface of a glass plate in these instances (transparent PTFE film is unavailable). The film, manufactured by Curtis Noll Corp. and supplied via the New Mexico Petroleum Recovery Research Centre (Socorro), was 0.05 mm thick with a tolerance of +0.005 - 0.000 mm and was available as loose roll and as self-adhesive tape.

7.2.5.4 Spacers

For some arrangements spacers were required to hold rods away from the plate or to alter cell width or depth. Usually brass precision engineering shimstock was used. The small pieces required were cut, or sawn, from 1 foot sq. sheets. To ensure these were flat and contained no burrs the edges were first filed down before the shim was clamped tight in a vice and left for several hours. Their thicknesses was then be measured with a micrometer.

7.3 THE TEST LIQUIDS

7.3.1 Perfectly wetting experiments

The wetting experiments required a liquid that wets steel and glass, exhibiting no deviation from the perfectly wet under advancing or receding conditions. Steel and glass are high energy solids and as such will be wet by most liquids spreading against a gas provided that the surfaces are clean. Isooctane was chosen because it satisfied the wetting conditions, but it also possesses some other useful properties:

- i) Isooctane has low viscosity making the time taken for equilibrium to be obtained in the small pores short.
- ii) It has low toxicity; no extra precautions were required for the experiments.
- iii) It made a useful cleaning fluid for the apparatus as it is a mild solvent.
- iv) In common with other organic solvents, isooctane is manufactured at high purity, but available at low cost.
- v) It evaporates when it leaks from between the metal-metal or metal-glass junctions and this obviates the need for special seals.

7.3.2 Non-zero contact angle experiments

For the partially wetting experiments the fluids were chosen to produce known contact angles. Following Morrow's (1974) work on the effects of surface roughness on contact angle, discussed in section 2.7.6, and experiments conducted by Mason *et al.*

(1983), the contact angles of several liquids, likely to pertain for the surface condition of the rods and film, were known. Of the three distinct classes found by Morrow the "as supplied" rod and film surfaces give class II behaviour.

Table 7.1 Contact angles and physical properties of the organic test liquids.

Test Liquid	Receding Angle θ_r (deg.)	Advancing Angle θ_a (deg.)	Surface Tension σ (dyn/cm)	Density ρ g/cm ³
Isooctane	4.6	29.6	18.7	0.6918
n-Dodecane	22.8	47.9	24.9	0.7430
n-Tetradecane	25.1	50.2	26.2	0.7599
Dioctyl Ether	30.8	55.9	24.8	0.8020
Hexachlorobutadiene	43.3	68.4	36.0	1.6820
α -Bromonaphthalene	58.1	83.2	43.0	1.4739

The fluids and their relevant physical properties are listed in Table 7.1. The documented surface tensions were confirmed by du Nouy tensiometer measurements. The receding and advancing contact angles, θ_r and θ_a , are related to the intrinsic angle, θ_c , according to Morrow's empirical equations:

Class II receding contact angles

$$0 < \theta_c < 22^\circ \quad \theta_r = 0 \quad \text{Equations}$$

$$22^\circ < \theta_c < 180^\circ \quad \theta_r = 1.14(\theta_c - 22^\circ) \quad 7.1$$

Class II advancing contact angles

$$0 < \theta_c < 158^\circ \quad \theta_a = 1.14\theta_c \quad \text{Equations}$$

$$158^\circ < \theta_c < 180^\circ \quad \theta_a = 180 \quad 7.2$$

Figure 2.14 showed Morrow's experimental results plotted together with the lines resulting from the equations above. It is noticeable that some of Morrow's experiments gave results more than 5° in error of those given by the equations, although the spread of results usually transposes the lines. Considering the well known difficulty of reproducing contact angles (section 2.7) the agreement is the best that can be expected.

7.4 EXPERIMENTAL PROCEDURE

The experiments principally involved measuring the height of capillary rise in pores of constant cross-section made up from rods and/or plates. The experimental procedure

remains essentially the same throughout, although some specific details differ from one pore shape to another; these points are discussed in the sections devoted to individual configurations (see later).

Some of the pore shapes listed in Table 6.1 had been selected for the experiments prior to the start of the investigation, while others arose as the study progressed, either from a previously investigated shape or from a simple desire to improve the versatility of the MS-P method. In this section the general experimental procedure and the determination of meniscus curvatures from measured heights of rise are discussed.

7.4.1 General considerations

Once a specific pore shape had been chosen a suitable test cell was sought to accommodate the rods in the desired configuration. If none of the available cells suited the shape then a new cell, designed specifically for the purpose, would be commissioned.

Prior to preceding with a set of experiments the height of the laboratory jack supporting the cells was adjusted to a suitable level and the spirit level on the cathetometer was checked over the lateral traverse. If not within the limits specified by the manufacturer the cathetometer would be re-levelled in the manner prescribed in its manual.

7.4.2 Selection of rods

Meniscus curvature is sensitive to small deviations in pore geometry so the selection of the rods that make up the geometry requires care. Each rod was measured at several points along its length and around its axis as there is often significant variation in a drill blanks' diameter. Measurements were taken with a digital micrometer accurate to 0.001 mm (0.0001"). Rods with noticeable tapering were rejected. The construction of a cell usually required two or more rods to be of equal diameter or in a specific ratio. So it was often necessary to measure many drill blanks, nominally of equal size or ratio, until suitable rods were found.

This problem was not encountered to the same degree with either the needle rollers or teflon rods, the former have a closer tolerance than drill blanks whilst the latter were cut from 2 m lengths of rod so the likelihood of significant differences between adjacent pieces was small. Rods selected for pore construction were thoroughly cleaned before assembly. Once clean the rods were handled with tweezers.

7.4.3 Cell assembly

As with the rods each cell was first cleaned with isooctane. Particular care was taken to ensure all swarf was removed from newly machined apparatus. Assembly of the test cells usually involved first arranging the rods in position against the transparent plate with the cell horizontal. The rods were then fixed in position by clamping screws or by wedging other rods behind those forming the pore or by a combination of both methods. Care was taken to ensure rods remained in contact with each other and/or the plate. Even steel rods will bend if too much pressure is applied by a clamping screw; these only needed to be hand tight (less so with teflon rods).

7.4.4 Arrangement of apparatus

For each experiment the apparatus comprised of four cells, usually two reservoir level indicator cells, the test cell and a "standard cell" (see later), arranged in the (connected in parallel) cell blocks with the indicator cells at either end, as shown in Figure 7.4. The cell blocks were positioned as close to the cathetometer as was practical and arranged so that both focus adjustment from one cell to another and the lateral traverse of the tele/microscope were at a minimum. This operation maximises the magnification of menisci whilst minimising any height measuring errors that may arise during refocusing.

7.4.5 Measurement of capillary rise

The assembled cells were filled by raising the main reservoir beaker, containing about 50 cm³ of test liquid, above the level of the cells, and holding it there until menisci appeared in all the cells. The beaker was then replaced on its laboratory jack and the menisci allowed to stabilise.

The optical fibre antennae were adjusted to give maximum illumination of the menisci in each cell. Satisfactory illumination of the menisci with ordinary lamps would have been difficult due to the multiple reflections from the rods. Even using the optical antennae, careful positioning was required. If the point of measurement is deep within a pore or the channel large, as with the indicator cell, obtaining adequate illumination can be very difficult. This sometimes led to significant experimental error. However it was usually possible to obtain reflections off the bottom of a meniscus by manipulating the antennae. These could then be sharply focused with the telescope.

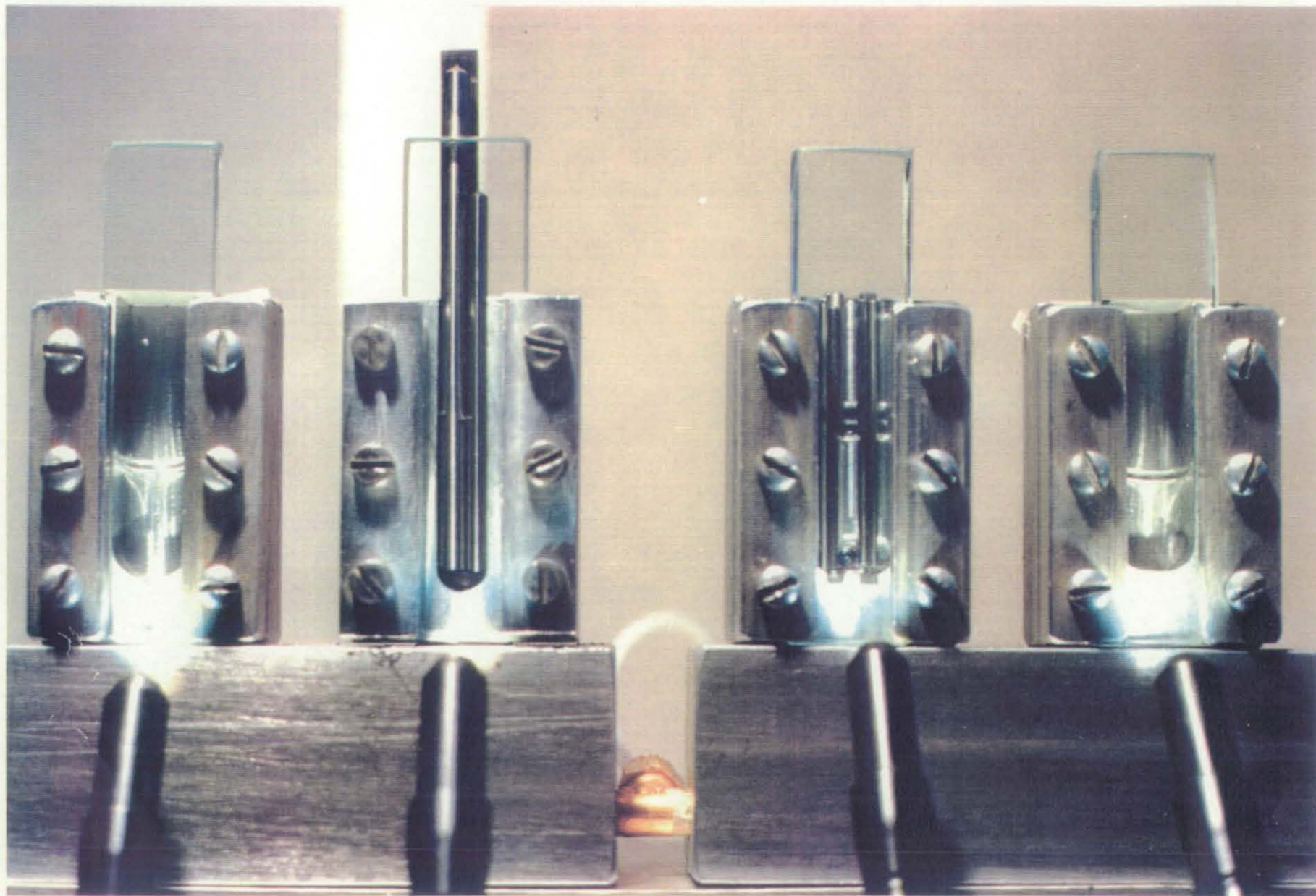


Figure 7.4 - Photograph showing the arrangement of the cells in a typical capillary rise experiment. Reservoir cells occupy the outermost positions whilst the test and standard cells can be seen in the middle.

By raising or lowering the jack supporting the main reservoir the levels of liquid in the cells could be increased or decreased to give either advancing or receding menisci as necessary. The apparatus has quite a slow response to level changes; typically taking 10 minutes or so to reach equilibrium. Figure 7.5 shows a graph of normalised capillary height versus time for a typical response with isooctane. Some of the more viscous liquids used could take considerably longer to equilibriate, sometimes in excess of half an hour. With a highly volatile liquid, like isooctane, evaporation is rapid. So, to prevent excessive losses and to maintain static heights of rise, the main liquid reservoir was always kept covered during experiments.

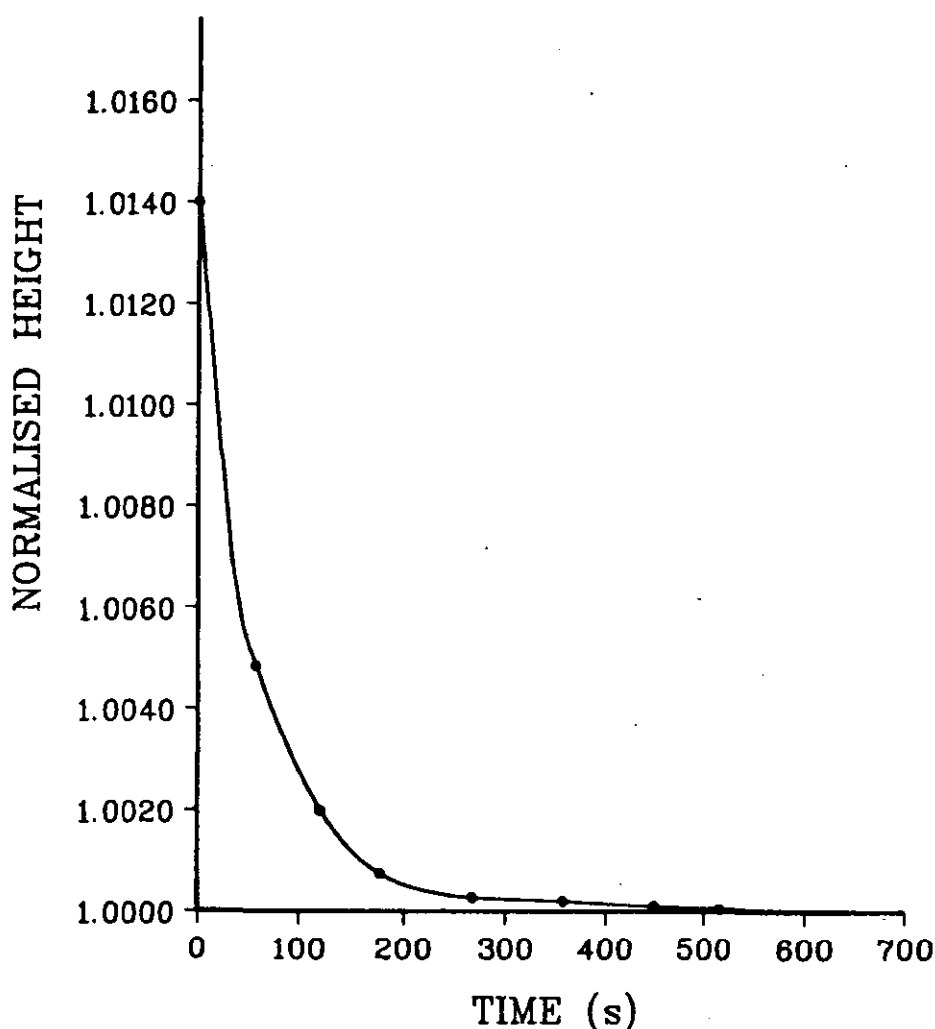


Figure 7.5 - Graph of the normalised height of rise versus response time for a typical experiment with isooctane. This shows that about 10 minutes is required for the system to stabilize after a change in reservoir level.

Before measuring heights of rise a check for leakage from the system was made, at first visually and then by placing pieces of dry tissue paper in the cell joins and around connecting points. If a paper became wet then that piece of apparatus was dismantled, checked and reassembled.

Once the liquid levels in the cells reached equilibrium all the meniscus heights; those in the test pores and the reservoir indicator cells; were measured with the cathetometer. The heights were read by first focusing on the cross-hairs and then focusing, without parallax, on the *bottommost point* of a meniscus.

Having two indicator cells, at either end of the cell assembly, provided a check on the equilibrium and on the accuracy of the cathetometer travel. Sometimes this system was abandoned in favour of one with two test cells, one indicator and a standard. The equilibrium was then checked by re-measuring the first level at the end of the reading sequence. In either case a significant difference in these readings required re-measurement at a later time. Non-attainment of equilibrium after several tries usually indicated a small leakage from the system not detected by the tissue paper.

Experimental errors were expected to be produced mainly through dimensional tolerances of the constructed pores. By taking readings at different levels within a given pore an estimate of the scatter due to dimensional deviations could be determined.

For experiments involving teflon components and partially wetting liquids a different procedure is required so that the heights of rise corresponding to both advancing and receding conditions are obtained. This modified method, which also contains a means of verifying the uncertain teflon pore geometry, is discussed later in section 10.2.

7.5 DETERMINATION OF CURVATURES

The experiments were designed so that no finer control of temperature was needed than that provided by the normal temperature control in the laboratory. This was achieved by using a standard cell, comprising of two equal rods and a plate, for which the normalised meniscus curvature was known. Employing this method meant that the relevant temperature dependant properties of the test liquid, in the form of the term $\rho g/\sigma$, could be determined from the readings for each run.

Referring back to chapter 2, section 2.4.3, the relationship between meniscus curvature and height of rise for a cylindrical capillary of radius R_T is,

$$\Delta h \rho g = 2\sigma/R_T \quad (2.42)$$

where Δh is the height of rise. The expression can be generalised for any capillary of uniform cross-section giving

$$\Delta h \rho g = C\sigma/R \quad (7.3)$$

where R is a characteristic pore dimension and C the *normalised* meniscus curvature (R/r).

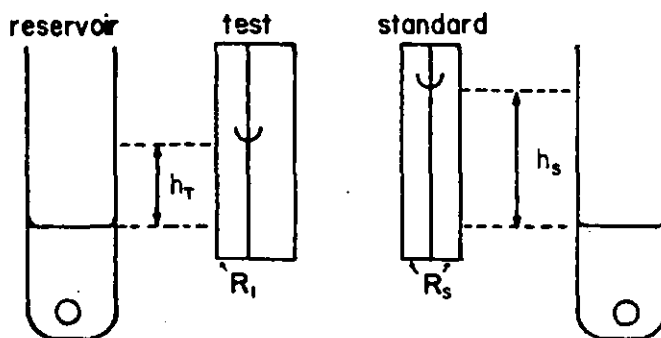


Figure 7.6 - Sketch of the various heights which must be measured in the capillary rise experiments.

Aside from minor corrections, the meniscus curvature of a given pore can now be determined. Taking the terminology from Figure 7.6 the curvature of the meniscus in the test cell (subscript t) is given by

$$\Delta h_t \rho g = C \sigma / R_t \quad (7.4)$$

and that of the standard (subscript s) by

$$\Delta h_s \rho g = C_s \sigma / R_s \quad (7.5)$$

combining 7.4 and 7.5 yields

$$\frac{\Delta h_t}{\Delta h_s} = \frac{C R_s}{R_t C_s}$$

or

$$C = C_s \frac{\Delta h_t R_t}{\Delta h_s R_s} \quad (7.6)$$

Note that the physical properties of the liquid (σ and ρ) have cancelled, this makes the method relatively insensitive to temperature changes. The normalised meniscus curvature in the standard, C_s , was found to be 6.94 ± 0.02 (see section 8.2). A correction needed to be added to account for the capillary rise in the indicator cell; determined to be 0.5 mm. So upon incorporation of these results 7.6 becomes

$$C = 6.94 \left(\frac{\Delta h_t + 0.5}{\Delta h_s + 0.5} \right) \frac{R_t}{R_s} = 6.94 \frac{\Delta h_{t,c} R_t}{\Delta h_{s,c} R_s} \quad (7.7)$$

with all measurements now in mm.

For the special case of near hemispherical menisci the curvature may be adjusted for gravity distortion by employment of the *Jurin* correction (see section 2.4.3). This gives rise to a further equation for curvature determination

$$C = 6.95 \left(\frac{\Delta h_t + 0.2 + h_{jt}}{\Delta h_s + 0.2 + h_{js}} \right) \frac{R_t}{R_s} = 6.94 \frac{\Delta h_t R_t}{\Delta h_s R_s} \quad (7.8)$$

where h_{jt} and h_{js} are the Jurin corrections for the heights of rise in the test and standard cells respectively. These and the constants in equation 7.8 are explained in section 8.2.

The curvature of the meniscus in the test cell can now be determined from either equation 7.7 or 7.8 and compared with the value predicted by the theory.

7.6 MENISCUS CONFIGURATIONS INVESTIGATED

During the course of this study the MS-P method has been tested in uniform, non-axisymmetric tubes of varying shapes with perfectly and partially wetting liquids; the latter in tubes of both fixed and mixed wettability. Several different tube shapes, made up from the rods and plates described in section 7.2.5, have been employed. Tube shapes were selected both in order to confirm results of past studies and to extend investigations into the behaviour of menisci with both open and closed profiles. Table 6.1 listed the tube configurations investigated together with the geometric variables and/or wetting conditions for which menisci behaviour has been studied.

For the presentation and discussion of results the different configurations are discussed in order of ascending complexity, although this was not the order in which the experiments were performed. Experiments involving the perfectly wetting liquid, isooctane, and tubes constructed from steel and glass components are reported in chapter 9. Selected tubes shapes from chapter 9 are treated again in chapter 10, but under partially wetting conditions for fixed wettability, with pores fabricated from teflon components, and/or for mixed wettability, with a combination of teflon and steel components. Finally, in chapter 11 investigations involving complex capillary surfaces where meniscus behaviour can be dependant on the behaviour of a neighbour are discussed; these are the so called "neighbouring pore" effects described in sections 3.5 and 5.3.2.

The next chapter begins the reportage of results with the discussion of experiments performed to determine the curvature of menisci in a limited number of pore shapes selected to act as "standards". It is against these standards that curvatures in the other pore shapes are measured, so their values are of crucial importance.

CHAPTER 8

Curvatures in the standard configurations

8.1 INTRODUCTION

In chapter 7 an experimental technique was set down for the determination of meniscus curvatures from measured heights of rise. By making use of a comparative method the required apparatus was greatly simplified as it no longer needed fine temperature control. However, the observed curvatures depend heavily on the predetermined curvature of a meniscus in a pore of "*standard*" configuration. The relationship is one of direct proportion (equation 7.7), so any errors in the standard's curvature will be carried-over as a systematic error to all the other experimentally measured curvatures. Confidence in the experimental results is therefore highly dependent on the level of confidence held in the standard's curvature.

If the technique described in chapter 7 is termed the "*simplified*" comparative method then to determine the standard's curvature a "*full*" comparative method is required. The full method employed here differs from the simplified method in the number of pores used to obtain a single curvature. Heights of rise in several *differently sized* pores of the *same* standard configuration are compared to those in a number of cylindrical capillary tubes for which the meniscus curvature is known. This approach lends to the results a high degree of confidence. Furthermore, these experiments are a thorough test of the comparative method and its reliance on the "window of opportunity" in the scale of apparatus. The experiments are able to quantify the scale of the pores where dimensional variations in pore section and gravitational distortion of menisci are both small. Some quantitative estimate can be made of the effect of these and other likely errors in the technique. The small, but significant correction that must be added to observed heights of rise for the capillary rise in the indicator cell is also a result of these experiments.

Results of two similar experiments have been published previously. For a standard pore comprising two equal rods and a plate, by Mason *et al.* (1983), Mason & Morrow (1984a) and for a rod in a right-angled corner by the same authors (1984a). The value of the meniscus curvature in the two rod configuration given in the latter paper has been used in some experiments for this study. Some results obtained using this value with the simplified method had shown significant improvement over those published in previous studies. It was thought that similar improvements might be found in the measured curvature of the meniscus in the standard pore.

The full comparative method compares heights of rise in cylindrical tubes to those in assembled pores. The question will naturally arise as to why a cylindrical tube, for which the meniscus curvature has long been known, is not itself used as a standard. The tubes used in these experiments are of the highest precision available, but the manufacturer's claimed bore tolerance of ± 0.25 mm over a 1.5 m length is hardly inspiring. My own measurements in the 10 cm lengths employed here showed a bore tolerance in the region of ± 0.01 mm (see Appendix B). The rods used to make up the assembled pores have a tolerance improved by a factor of 10. Hence, when correctly assembled a standard made up from rods is likely to be significantly more reliable than that provided by a single cylindrical tube. Two configurations were selected as standards:

a) Two equal rods and a plate

This configuration was selected as it had already been established as the usual standard for this study and so as to provide a comparison to Mason and co-workers' results. In 1983 Mason *et al.* found a value for the normalised curvature of the configuration of 7.00 ± 0.14 and later, with a modified apparatus, a value of 6.88 ± 0.02 was found (Mason & Morrow 1984a). Both these experiments used a large machined block containing milled channels designed to hold the rods (from 3 to 6 mm diameter) in position. This form of apparatus was seen as having significant disadvantages over the clamped method employed here. Details of meniscus shape and the derivation of the MS-P theoretical curvature for the configuration are detailed later in chapter 9.

b) Three equal rods and a plate

The possibility of using a three rod standard had not been considered before and only arose as a consequence of early experiments conducted with the configuration (see chapter 11 where the theory is also detailed). The predicted curve for curvature against subtended half-angle, ϕ , for three equal rods (Figure 11.16) shows an almost flat portion between $\phi = 52^\circ$ and $\phi = 60^\circ$; curvature varies by only 0.05 (about 0.15%). It is a simple matter to assemble rods such that the angle lies between these limits. It was hoped that the increased confidence in the mechanical accuracy of the pore would lead to a new common standard.

8.2 EXPERIMENTAL

The components of the apparatus and the procedures followed here remain largely unchanged from those discussed in chapter 7, but there are differences in scale. In place of two connected cell blocks a total of five blocks, connected in parallel, were needed for each run. They were arranged in a circular arc around the cathetometer. Two 1/2" cells held the five differently sized capillary tubes, seven cells held rods in the standard configuration and one was a reservoir indicator cell.

Where possible needle rollers were used as rods to make the pores; advantage being taken of their greater precision. Some "juggling" of rods from one cell to another was required in order that all seven sizes could be accommodated in the available cells. The capillary tubes were held in a vertical position by clamping them into cells in the same manner as the rods.

The diameters of the capillary tubes were determined by partially filling them with mercury and measuring both the length (with a travelling microscope) and weight of the mercury thread in several positions (see Appendix B).

Isooctane, was chosen as the wetting liquid for the experiments. The apparatus had a particularly slow response to level changes due to its physical size and menisci typically took 15 minutes or so to settle. The system never obtained a static equilibrium. Such a large surface area of the volatile isooctane was in contact with the atmosphere that evaporation was considerable even when cell top openings behind the pores were blocked with tissue.

Rectifying small leaks was now also more important than with the simplified experiments. Here several small leaks amount to a measurable height loss over the reading-taking period, whereas a single small leak is unnoticeable over the short reading period in the other experiments. Considerable effort was required to track down and rectify these leaks. Complete prevention of leaks/evaporation proved impossible. However, over each reading period all levels were observed to drop by the same amount, typically 0.1 mm in 10 minutes, indicating that levels in the cells were in equilibrium with each other.

The apparatus had two finer points. For the two-rod system two pores made up of rods of the same diameter were included, one at either end of the cell arrangement. This was not possible with the three rod system due to requirements of space, but two capillary tubes of the same size were included with both systems. This enabled a check on the equilibrium before taking readings and gave a check on the fabrication errors of the pores and on the accuracy of the horizontal travel of the cathetometer.

Errors in the measured heights of rise arising from the cathetometer were likely to be increased over those in the simplified experiments. The horizontal travel was, by necessity, greater and the telescope required more re-focusing from meniscus to meniscus as the cells could no longer be arranged such that all menisci were simultaneously in focus.

An experimental run consisted of measuring the levels of all the menisci, both in the test capillaries and the glass capillary tubes. This required focusing on and reading the levels of 14 or 15 menisci, a process that typically taking over 10 minutes (this compares with about 3 minutes for the two block system). Levels of menisci were corrected for the drop in height by re-measuring the first level in the sequence at the end and the reading period was timed. By assuming that an equal time was required for each

reading and that equilibrium between the cells is maintained the heights can be corrected to their levels at the start of the cycle. As a further safeguard the positions of the cells were interchanged between each run, thereby randomising any error.

Runs were repeated for several levels in the apparatus both as a check on the method and for an estimate of the scatter produced by dimensional variations. Rod sizes for the seven constructed capillaries were chosen to give heights of rise covering the range for which the experimental technique was thought to be valid, judged from earlier experiments to be roughly 5 to 25 mm.

For the two rod system this resulted in rods of nominal diameters 1/16" and 2, 2.5, 3, 3.5, 4 and 5 mm; the 1/16" rods were drill blanks whilst the others were needle rollers. The three rod configuration requires rods of smaller diameter for a given height of rise resulting in pores made up from rods with nominal diameters of 0.038, 0.0465 and 1/16" and 2, 2.5, 3 and 3.5 mm; again the imperially sized rods are drill blanks whilst the remainder are needle rollers. When assembled these rods gave subtended angles of 58.7°, 56.7°, 58.3°, 55.8°, 55.9°, 56.0° and 59.5° respectively.

Note that the rods selected for the three rod system are significantly smaller. When the three rods are assembled the pores are large compared to the two rod pores. The capillary tubes had mean diameters of 0.544, 0.622, 0.782, 0.860 and 1.186 mm and gave, as planned, heights of rise in the same range as the constructed tubes.

8.2.1 Determination of curvatures

Having obtained the heights of rise of each menisci above the measured level in the reservoir indicator cell, graphs of heights of rise versus reciprocal rod/tube radius could be drawn. From the gradients the curvatures can be determined. Also the two straight lines obtained should extrapolate to the same point on the height of rise axis, giving a measure of the height of rise in the reservoir indicator cell, h_o .

For the glass capillary tubes the height of rise, h_T , in a tube of radius, R_T , is given by;

$$h_T = h_o + \frac{2\sigma}{\rho g R_T} \equiv h_o + \frac{a^2}{R_T} \quad (8.1)$$

where 2 is the numerical value of the normalised curvature of a hemispherical meniscus in a cylindrical tube (see section 2.4.3) and other symbols carry their usual meanings. A plot of h_T versus $1/R_T$ is thus a straight line through h_o , with a gradient, G_T , of $2\sigma/\rho g$ ($= a^2$ the capillary constant).

The height of rise in the constructed pores, h_{R_i} , with rods of radius, R_i ($i = 2$ for the two-rod system etc.), is given by;

$$h_{R_i} = h_o + \frac{C_{R_i}\sigma}{\rho g R_i} \equiv h_o + \frac{C_{R_i}a^2}{2R_i} \quad (8.2)$$

where C_{R_i} is the normalised curvature of the given rod configuration. The gradient of the rod line, G_{R_i} , will thus be $C_{R_i}\sigma/\rho g R_i$. The curvature of the menisci in the assembled pores is related to the ratio of gradients by;

$$C_{R_i} = 2\frac{G_{R_i}}{G_T} \quad (8.3)$$

As with the simplified comparative method $\sigma/\rho g$ is a constant that cancels, making the method insensitive to temperature changes. In addition the change in curvature with height in the region of the TM caused by gravity will be largely compensated for by this method (see later).

8.3 RESULTS

Over the following pages the principal findings from these experiments are first given and then discussed in relation to this and previous studies. The effectiveness of the comparative method of curvature determination is revealed and a quantitative account is made of the errors inherent to the experimental technique. A detailed breakdown of results is included in Appendix B. ✓

8.3.1 The basic findings

Figures 8.1 and 8.2 show respectively, the results obtained using the two rods and plate and three rods and plate configurations. The data is plotted as graphs of heights of rise versus the reciprocal of rod or tube radius. Rather than reproduce all the data from each of the runs separately, the results from experimental runs conducted at five different levels in the apparatus have been condensed onto single graphs for each of the two configurations. The heights of rise shown refer to the height of the bottom of a TM above that measured in the reservoir indicator cell.

The straight lines drawn on the graphs were obtained by linear regression of the mean heights of rise in each of the tubes or constructed pores (excluding the zero height of rise in the indicator cell). All the data points from the five runs are shown. Detailed breakdowns of the results, including the linear regression findings for each run, can be found in Appendix B.

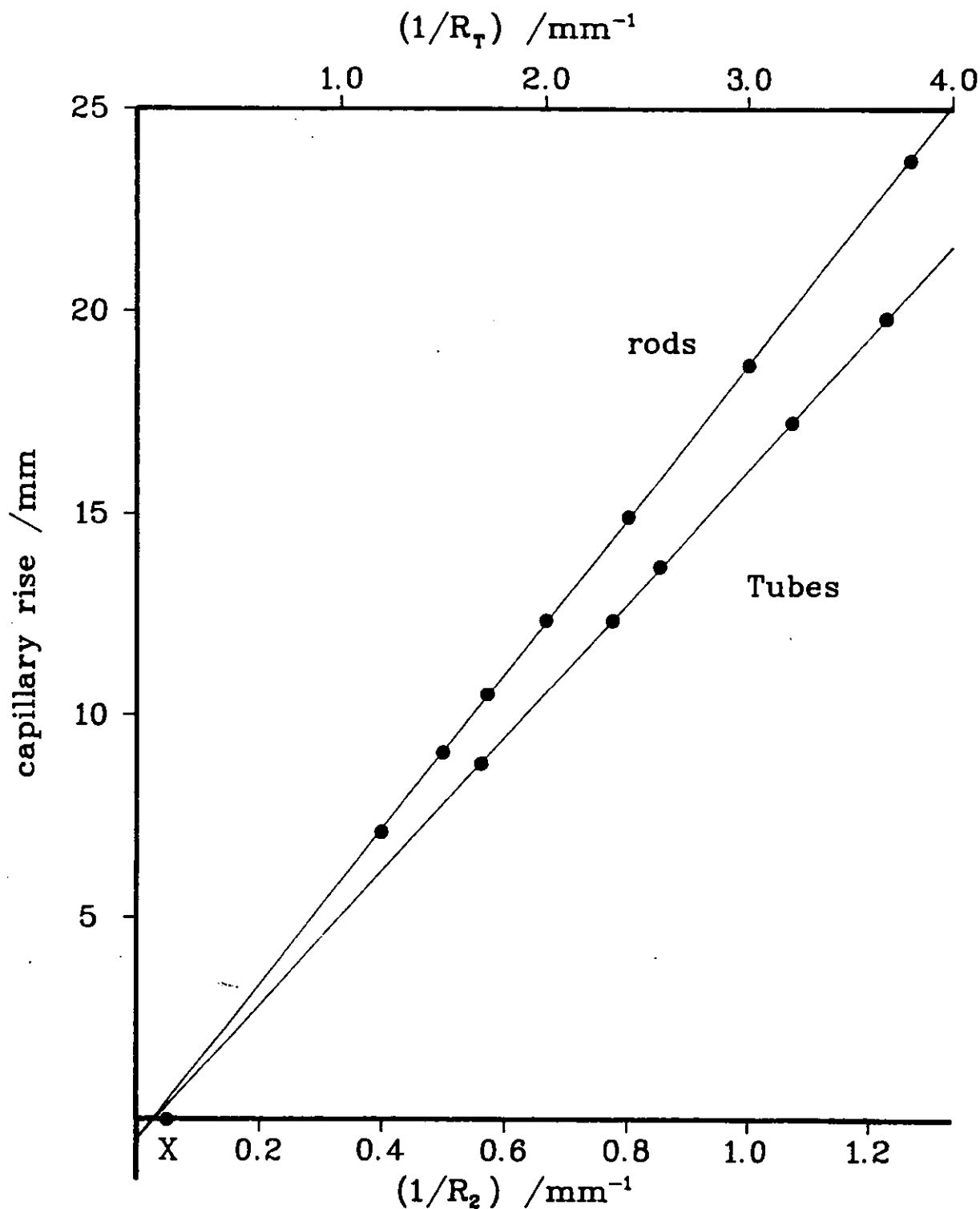


Figure 8.1 - Graph of the heights of rise against $1/R_T$ for the capillary tubes and against $1/R_2$ for the two-equal-rods-and-plate menisci. The scatter of points is mainly caused by dimensional variations in the pore sections over the five different levels at which measurements were taken. No correction has been made for the effects of gravity distortion on the menisci. Point X shows an approximate reciprocal equivalent tube radius for the square indicator cell. Its distance below the rod line indicates the severe distortion of the meniscus the cell contains.

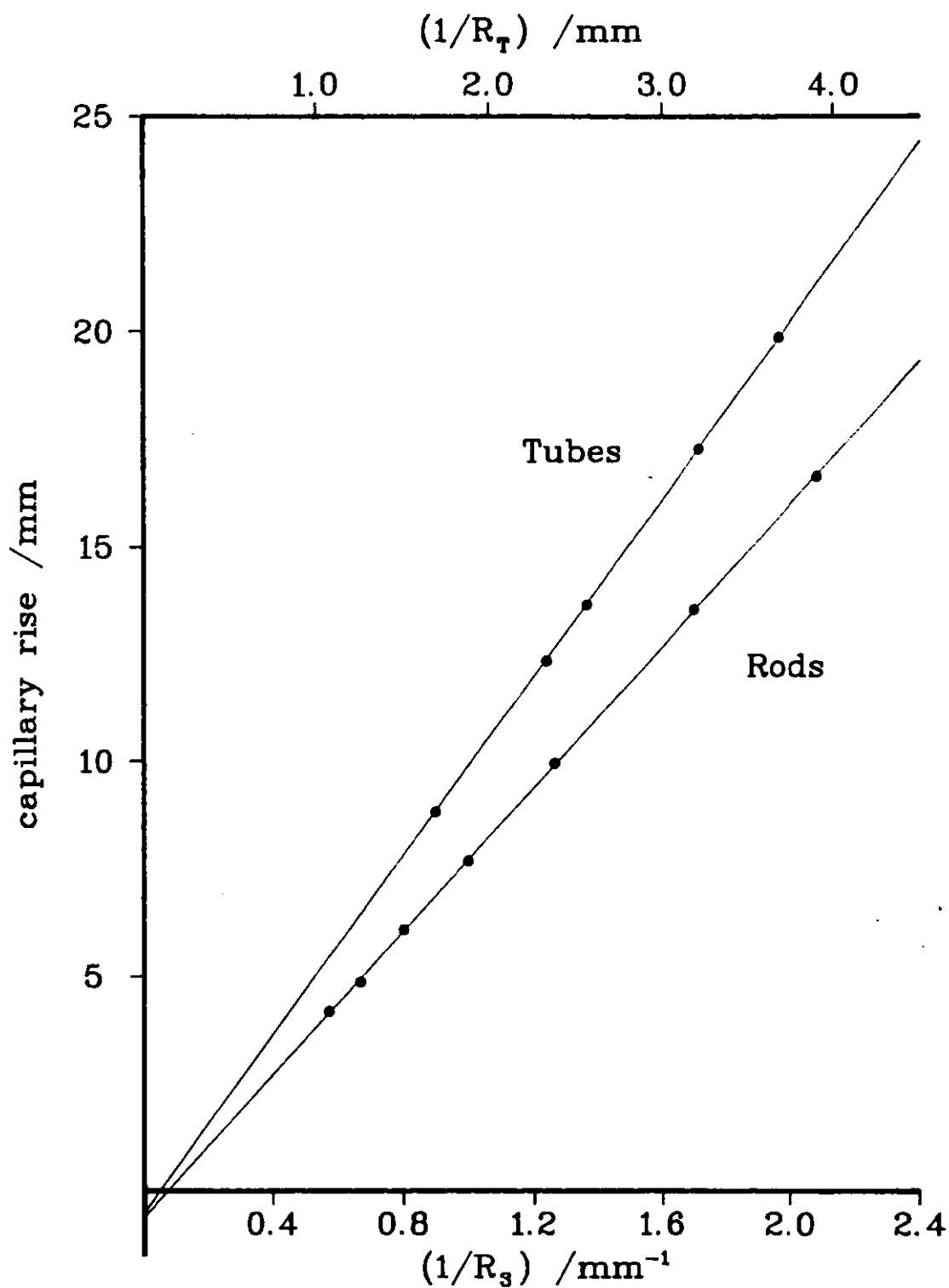


Figure 8.2 - Graph of the heights of rise against $1/R_T$ for the capillary tubes and against $1/R_3$ for the three-equal-rods-and-a-plate menisci. No correction has been made for the effects of gravity distortion on the menisci.

For all three pore shapes, the cylindrical tubes and both assembled arrangements, the data fits the imposed straight lines excellently with only a small scatter of points. This implies that, as expected, gravitational distortion of the menisci is small. The two lines on the graph extrapolate as expected to intercept at roughly the same point on the height axis, giving an estimate of the capillary rise in the indicator cell.

Using each of the gradients of the separate run lines of Figures 8.1 and 8.2 the normalised curvatures of the two and three rod systems were determined from equation 8.3. The values obtained were in the ranges $C_{R_2} = 6.94 \pm 0.02$ and $C_{R_3} = 3.00 \pm 0.02$. The theoretical values at zero contact angle obtained from the MS-P theory are $C_{R_2} = 6.970$ and $C_{R_3} = 2.96^*$ (refer to sections 9.5 and 11.2). The agreement, though not perfect, is very good at - 0.4 % and + 1.3 % respectively.

The numerical values obtained for the height of rise in the indicator cell ranged from an average of 0.5 mm for both the tubes and two rod system to 0.6 mm for the three rod configuration.

8.3.2. Analysis of results

Experiments in this section represent the most thorough test of the MS-P theory conducted in this study or published elsewhere. The experiments that follow this discussion use only one test cell to obtain an estimate of the meniscus curvature, whereas seven cells of varying size are used here. The single curvature obtained is the "standard" against which curvatures in the other configurations are measured. Hence, it is important to give these results a complete analysis and try to account for the discrepancy between the experimental and theoretical values.

Aside from the random errors generated by the measuring techniques two principal sources of error have been identified which are inherent to the experimental technique. Firstly there are errors arising from the distortion of the menisci by gravity, for which the MS-P theory takes no account. Secondly, due to the small physical size of the pores, there are likely to be fabrication errors arising from dimensional variations in the pore construction components. The scale of the apparatus was chosen to make these errors as small as possible. Three questions present themselves:

- What are the quantitative effects of these errors?
- Can they be made smaller?
- And are there any other significant systematic errors?

* This value is the mean for the range of curvatures found for subtended angles between 52° and 60°.

8.3.2.1 Gravitational distortion of menisci

In conducting these experiments capillary rise measurements have been used to estimate a curvature which is then compared to a theoretical value derived for surfaces of constant curvature. It has been assumed that errors arising from the distortion of the menisci are largely eliminated by the use of the comparative method. The reasoning being that with a similar height of rise the distortion of a meniscus in a tube will be roughly equivalent to that in an assembled pore. The selection of capillary tubes giving heights of rise in the same range as that exhibited by the constructed pores should have led to most of the effects of distortion cancelling when curvature is calculated from equation 8.3. This argument is constrained by two criteria:

- i) The menisci formed in the assembled pores need to be roughly the same shape as those in the tubes - concave and near hemispherical.
- ii) Distortion must nowhere be severe i.e. the data must closely fit a straight line on a graph of height versus reciprocal radius.

Distortion of menisci increases as pore size increases, so any severe distortion will be manifest by increasing deviations from the straight lines drawn on Figures 8.1 and 8.2 as reciprocal radius decreases. This is not apparent.

In order for the reader to clearly identify that menisci do become heavily distorted as the size of pore increases an approximate reciprocal tube radius has been plotted for the square indicator cell on the zero height of rise line, marked X on Fig. 8.1. This point falls well below the line, indicating the severe depression in capillary rise due to the decreased curvature resulting from distortion.

The effect of gravity distortion on the data shown in the Figures will be increasing depression of the heights of rise as pore size increases. The gradients, G_T and G_{R_i} , will all be slightly greater than would be given by undistorted menisci.

Two assumptions of the MS-P theory are not precisely met by capillary rise experiments due to the effects of gravity:

- i) The theory assumes that the MTM is of constant mean curvature whereas in practice the measured height of rise correspond to the minimum curvatures of a distorted menisci.
- ii) The theory requires that the AMs bound vertical liquid wedges in the corners, but in practice the wedges will be sloped in the region of the MTM due to the variation of curvature with height.

Below the above two factors are discussed and rough quantitative accounts made of their effect on observed curvatures.

a) Correction for minimum curvature

In capillary rise experiments terminal menisci cannot satisfy the constant curvature condition of the MS-P theory because the curvature varies directly with the height above a free liquid surface. The measurement of height of rise to the bottom of a terminal meniscus is an experimental convenience (it being a definable point of measurement), but it also corresponds to the minimum curvature of a distorted meniscus.

Closest to the theoretical value will be the average curvature of the meniscus. Only if the height change across the terminal meniscus is so small as to be unmeasurable will the height of rise read by the cathetometer yield the average curvature. This would require a height change through a TM of less than 0.01 mm. If apparatus were designed with this in mind then heights of rise in excess of 1 m would be needed and pores would have to be smaller than it is currently possible to make them. So, in practice, the capillary rise method will always yield TMs of measurably finite height.

A more accurate estimate of a TM's curvature can be found if the level in the meniscus that corresponds to its average curvature is used. This was the basis of a correction to capillary rise discussed in section 2.4.3 for cylindrical tubes. The average curvature is given by the level of a plane across the TM in such a position that the volume of liquid above the plane equals the volume of space below it. To apply this principle to wedging systems it must first be assumed that the arc menisci hold solid wedges and that the cross-section so obtained applies to the whole length of the tube.

Exact corrections can be made for the heights of rise in the cylindrical capillary tubes by application of Sugden's tables, but not to those in the assembled pores as their cross-sections are not circular. However, it is possible to apply a first-order correction for the effects of gravity on the TMs in the assembled pores by assuming the TMs to be hemispherical. This is the basis of the *Jurin correction*, h_j . In cylindrical tubes this correction is simply one third of the tube radius, R_T ;

$$h_j = R_T/3 \quad (8.4)$$

The correction is almost exact for the sizes of tubes used in the experiments where the menisci will be near hemispherical. The maximum difference between the Sugden and Jurin corrected heights of rise being only 0.05% with the largest tube, as illustrated by Table 8.1.

Applying the Jurin correction to the experimental data from the capillary tubes the height, h_{oc} , of the hypothetical planar liquid surface was re-determined by linear regression of these values against $1/R_T$. The TMs in the two and three rod assembled pores are not hemispherical, but bear a close enough resemblance to allow the correction

to be applied approximately. Firstly an *equivalent* tube radius, R_{Te} , was calculated from each average height of rise,

$$R_{Te} = \frac{G_{Tj}}{h_{R_i} + h_{oc}} \quad (8.5)$$

where G_{Tj} is the Jurin corrected gradient of the tube line.

Table 8.1 Jurin and Sugden corrections as applied to the heights of rise in the capillary tubes and the largest tubes employed for the two and three rod standards.

Nominal Diameter/ Equivalent Radius (mm)	Jurin Correction h_j (mm)	% of Height of Rise	Radius to Height Ratio R/h	Sugden Correction h_s (mm)	Over- correction by Jurin (%)
Tubes:					
0.5	0.09	0.4	0.014	0.09	0.00
0.6	0.10	0.6	0.018	0.10	0.00
0.78	0.13	0.9	0.028	0.13	0.00
0.8	0.14	1.1	0.034	0.14	0.01
1.2	0.20	2.2	0.064	0.19	0.02
Two Rods:					
0.72	0.24	3.3	0.094	0.23	0.14
Three Rods:					
1.20	0.40	9.1	0.261	0.37	0.76

This equivalent tube radius is the radius of a cylindrical capillary tube that would give the same height of rise as the assembled pore. One third of this radius was then added to observed heights of rise. For the two rod system the correction amounted to a maximum of 3.3% in the height of rise for the pore made from 5 mm rods. The maximum correction was greater in the three rod system owing to the smaller capillary rise, amounting to an increase of 9.1% in the height of rise in the 3.5 mm rod pore. Table 8.1 shows the effect of the correction on the largest pores together with a comparison with the exact correction (for tubes) provided by Sugden's tables. The simplicity of the Jurin correction is favoured over the accuracy of Sugden's tables. The application of the correction to non-axisymmetric pores is anyway an approximation.

Plots of the adjusted heights of rise versus reciprocal rod and tube radii (shown in Figures 8.3 and 8.4) again show excellent straight lines for all points. Both rod and tube gradients were shifted downwards, but the ratio of the gradients changed only slightly. Values of the normalised curvatures obtained in this way were, $C_{R_2} = 6.95 \pm 0.02$ and $C_{R_3} = 2.95 \pm 0.02$ (changes of +0.1 and -1.3% from the uncorrected data respectively). Both of the adjusted curvatures are closer to their theoretical values of 6.970 and 2.96 respectively.

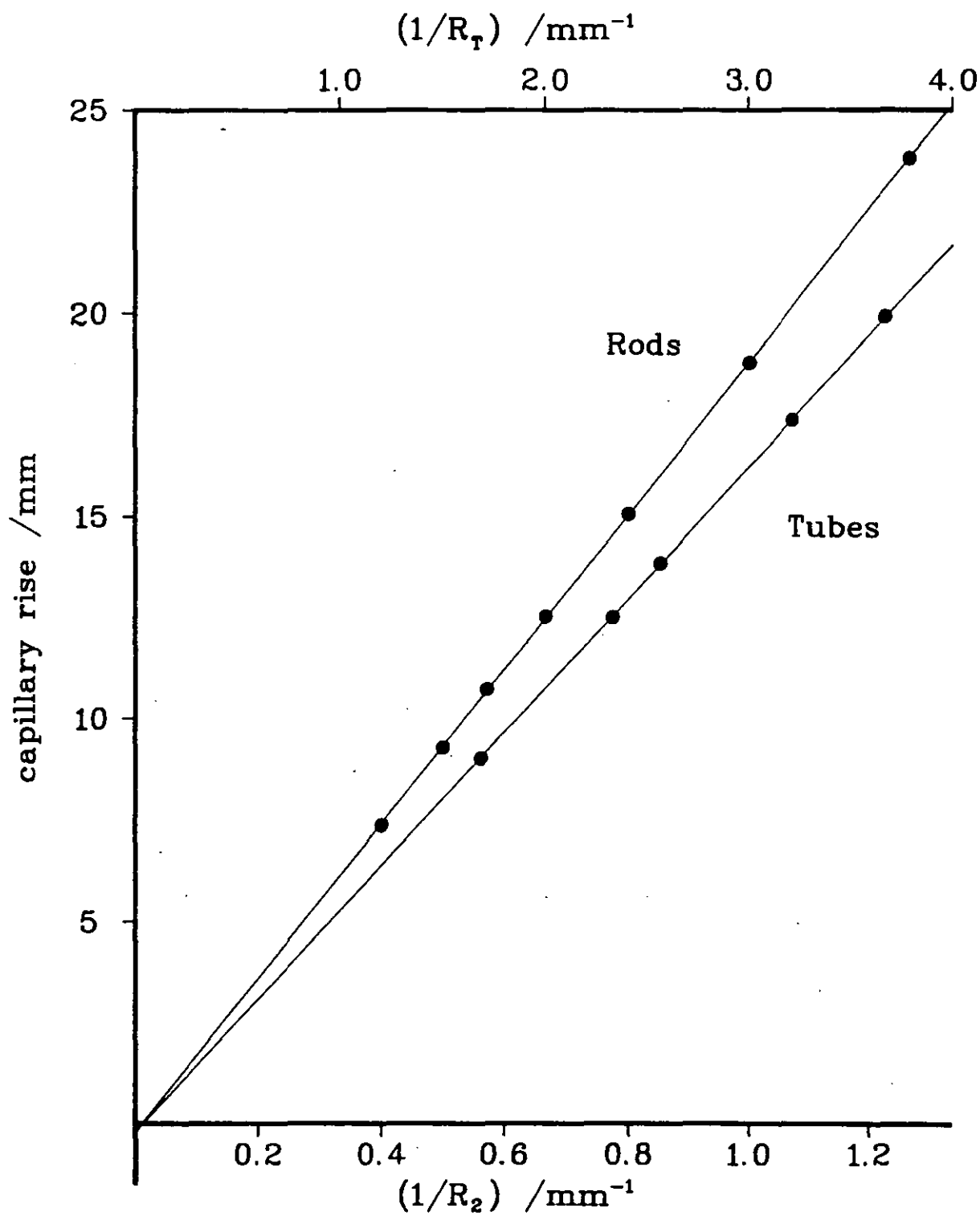


Figure 8.3 - Graph of the heights of rise plotted against the reciprocal of the tube and rod radii for the two-rods-and-plate experiments. A correction for the gravity distortion of the menisci has been applied to the results. The effect on the final ratio of line gradients is quite small as the changes are mostly self-correcting.

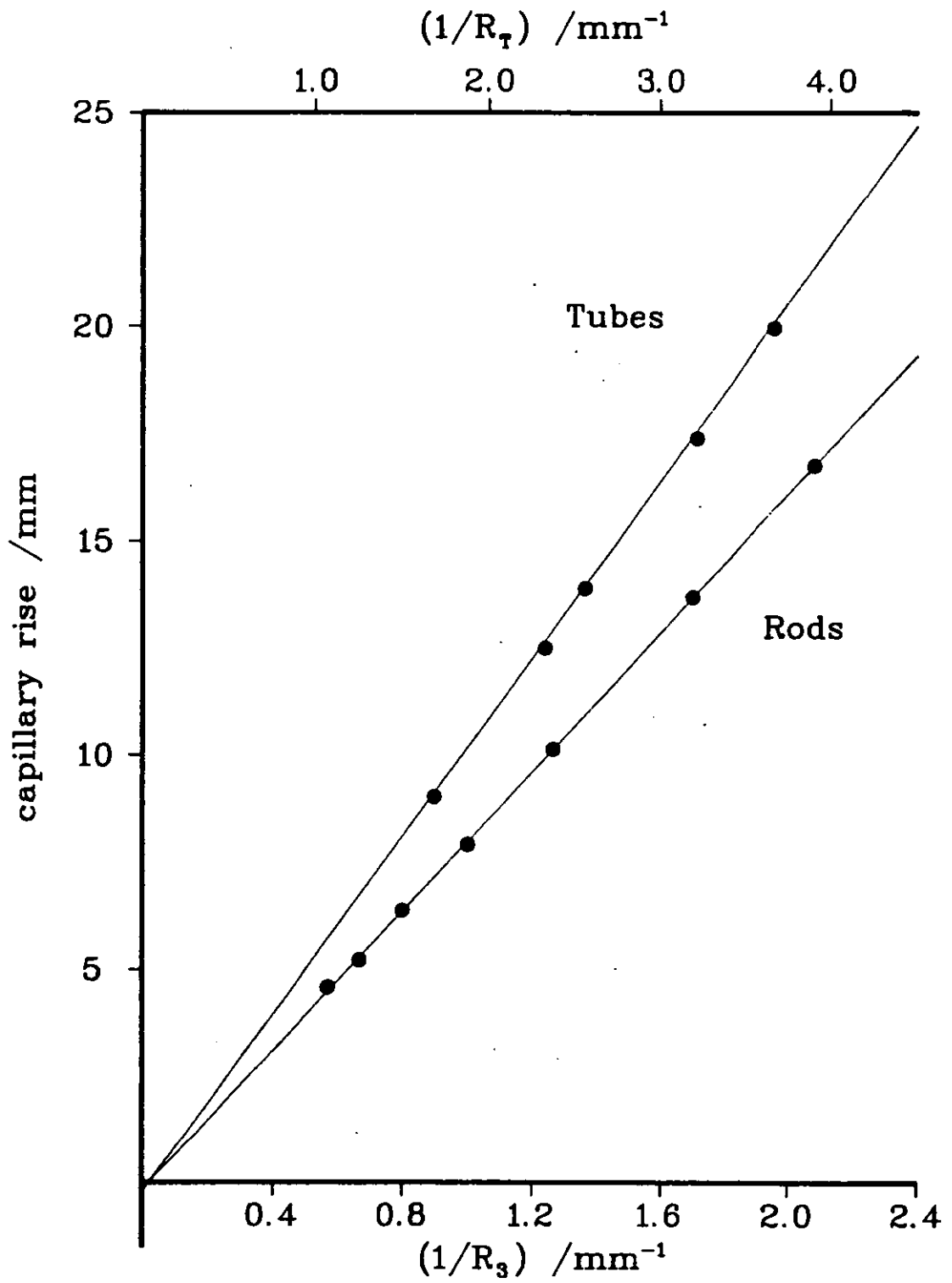


Figure 8.4 - Graph of the Jurin corrected heights of rise plotted against the reciprocal of the tube and rod radii for the three-rods-and-plate experiments.

That the two determinations of the curvature in the two-rod system, one involving a correction for gravity distortion and the other not, give such similar results can be attributed to the comparative method of measurement. The fact that the heights of rise in the tubes and the rod pores were roughly in the same range meant that meniscus distortion was also approximately equivalent. This hypothesis is supported by the intercepts of the rod and tube lines with the height of rise axis. The lines from the uncorrected data intercept the axis at the same place (to within 0.01 mm). If distortion of rod and tube menisci had been significantly different then the intercepts would not equate so closely.

After application of the Jurin correction the difference between the rod and tube intercepts is still small (0.02 mm) indicating the validity of the correction when applied to menisci between two rods and a plate (of this size range). The numerical value of the intercept, at approximately -0.2 mm is close to the height of rise predicted by Sugden's tables for a tube with the equivalent radius of the square indicator cell (0.15 mm - this is itself only an approximation as it applies to a cylindrical tube of equivalent area).

Heights of rise in the larger three rod pores fall well below the range encompassed by the rises in the tubes. It should therefore be expected that the distortion in these pores, and hence the gradient of the line, will be increased. The heavier distortion of menisci at these heights of rise (c.f. 4.5 mm) thus accounts for the rather high curvature given by the uncorrected data. This is borne out by the difference in intercepts; the rod line cutting the height axis 0.1 mm lower than the tube line. Put in other words the comparative method no longer accounts for gravity distortion when the ranges of heights of rise are not the same.

Once corrected, the rod and tube intercepts show better agreement, but with the rod line now crossing the height axis at a higher point than the tube line (0.07 mm difference). This indicates a slight over correction of the rod data and hence it is quite fortuitous that the corrected value compares so favourably with the theory.

In section 2.3.4 it was stated that the Jurin correction was valid only for the tube radius to height of rise ratio, $R/h \leq 0.02$ and that it amounts to a slight over-correction. Here we have employed the Jurin correction well over this limit to $R/h = 0.26$ with a 4.5 mm height of rise. Figure 8.5 shows plots of height of rise versus reciprocal tube radius for three cases:

- i)* The ideal case where there is no gravity distortion and the height of rise is given by $h_r = a^2/R_r$. The capillary constant, a^2 , of isooctane is used.
- ii)* The "real" case, determined by using Sugden's tables in reverse, shows the heights of rise that would be observed in practice.
- iii)* The third line shows the effect of Jurin's correction on Sugden's "real" data.

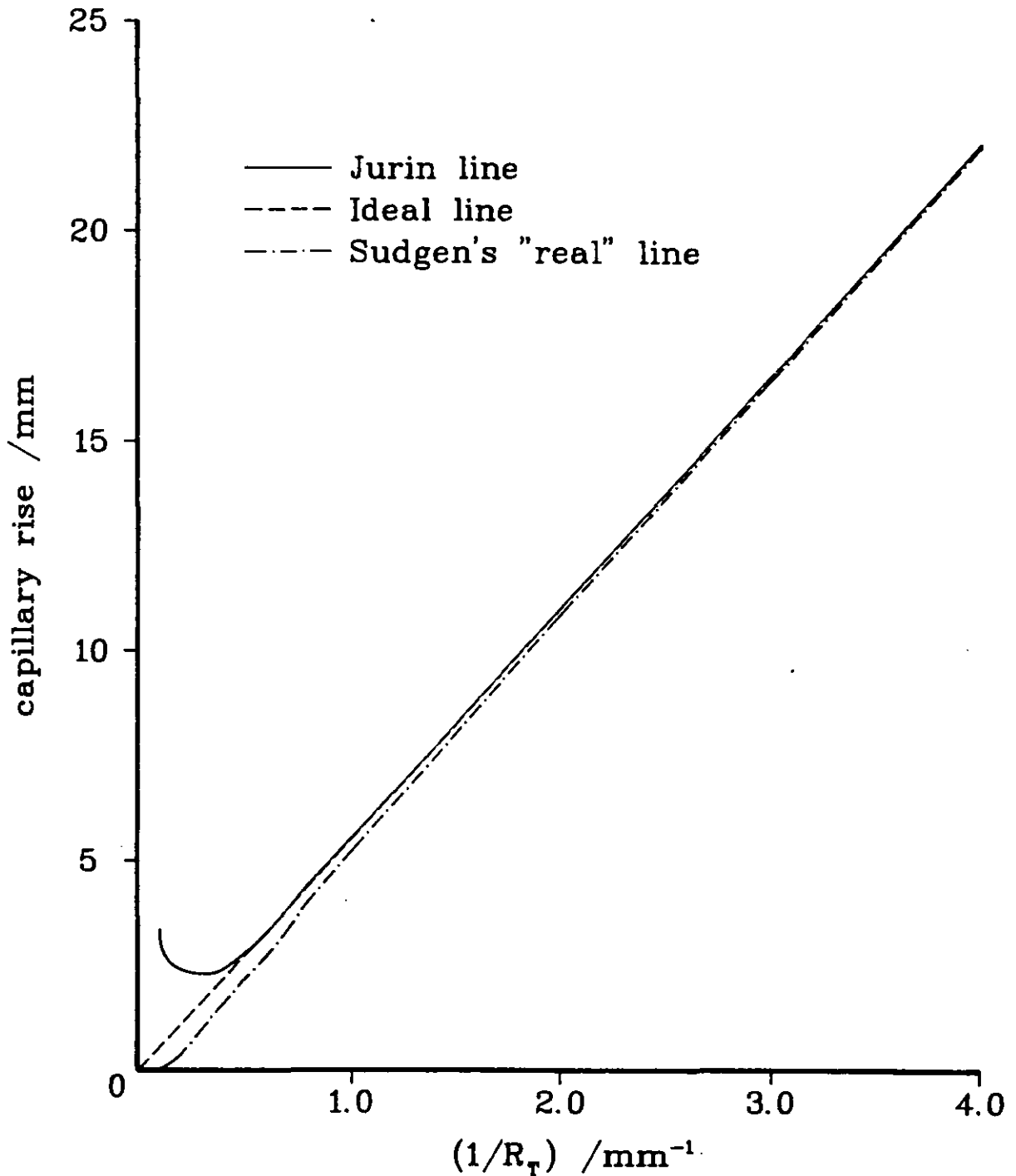


Figure 8.5 - Graph of theoretical heights of rise versus reciprocal tube radius. Three cases are shown

- (a) The 'ideal' line shows the heights of rise for undistorted menisci.
- (b) The 'real' case, determined from Sugden's tables, shows the gravity affected heights of rise that are observed in practice.
- (c) This curve shows the effect of Junn's correction on Sugden's 'real' data, only at very low heights of rise does this curve significantly depart from the 'ideal' line.

The "real" line shows, as expected, increasing deviation from the ideal as the tube radius increases. It can be seen that Jurin's correction only deviates substantially from the ideal when the height of rise drops below about 3 mm, a tube greater than 1.5 mm radius. The over-correction is always less than 0.1% for $R/h < 0.05$ and less than 1% for $R/h < 0.5$.

That the Jurin correction increasingly over-estimates the height of rise as the size of the tube increases can be appreciated if the changing shape of the meniscus is considered. With larger tube diameters the meniscus becomes more distorted; its shape changing from the initial hemisphere to an increasingly cube like form. The volume of liquid above a plane drawn $R/3$ from the bottom of the meniscus will be increasingly less than the volume of space below it.

If it is assumed that the curves of Figure 8.5 also apply to the menisci formed in the rod assemblies (and this would make a very useful experimental study) then it can be concluded that the "window" for which the current experimental technique is valid is considerably larger than was thought at the outset to the study. With heights of rise in excess of 3 mm the comparative technique would provide results close to those of the theory.

The three rod experiments have shown that the heights of rise do not even need to be in the same ranges for the method to estimate curvatures accurately provided a simple correction for meniscus distortion by gravity is added. However, it must be noted that the Jurin correction will only have any relevance where the menisci in the test pores are near-hemispherical. If this is so menisci will be similar in shape to those formed in cylindrical capillary tubes.

In summary, when the heights of rise in the tubes and rod pores are in the same range, as with the two rod system, then the comparative method will account for any over-correction. This was not the case with the three rod experiments and resulted in the heights being slightly depressed from the "ideal". It is not worth applying the more accurate corrections afforded by Sugden's tables to data from wedging systems as any corrections of this kind will not provide exact answers.

b) Correction for the slope of the liquid wedges

As a consequence of the relationship between meniscus curvature and height in capillary rise experiments, the liquid wedges held in the corners of the assembled pores will not, as the MS-P method assumes, be vertical. In practice the liquid wedges will slope outwards from the corners, the inclination to the vertical increasing with decreasing height above the free liquid surface (Figure 8.5). If, in the region of the MTM, the wedges slope with an angle, β , then as pore size is enlarged the magnitude of β increases in the region of the MTM. The effect will be a growing systematic deviation from the theory as the upward force from the wetted perimeter, ΣP_s , will become progressively less vertical, depressing observed heights of rise.

The curvatures in the two and three rod pores have been estimated by comparison with capillary tubes which do not hold wedging menisci. So the effect of the sloping wedges on observed curvatures found from the comparative method will be to slightly increase their values. The gradient of the rod line, G_{R_i} , is in fact greater than would be found had the wedges been vertical. The apparatus was scaled to keep gravitational effects small, but we need to know whether the sloping of the wedges has altered the results significantly.

A rough estimate of the effect can be made by making use of the MS-P analysis. By considering a small section across a meniscus the radius of curvature of the AMs at the top and bottom of a MTM can be estimated from,

$$r = \frac{a^2}{2h} \quad (8.7)$$

With the radius of curvature known at, say, positions 0.5 mm apart an estimate of the angle, β (Fig. 8.5), can be made for each wedge. The effect of the slope on meniscus curvature can be computed by inserting the cosine of the angle(s) into the relevant expression for the liquid perimeter, ΣP_L , in the MS-P analysis. The reduced curvature so obtained, $C_{R_i}^*$, can be used to calculate the suppression in the height of rise, Δh , caused by the wedge slope from;

$$\Delta h = \frac{a^2}{2R_i} (C_{R_i} - C_{R_i}^*) \quad (8.8)$$

The effect on the observed curvature can then be found from equation 8.3 by adding relevant Δh to each of the observed heights of rise. Table 8.2 shows the estimates obtained for the largest and smallest rods in the two-rod system.

Table 8.2 Effects of sloping wedges in the two-rods-and-plate standard.

Rod Diameter (mm)	Slope of Wedge		Reduced Curvature	Reduction In Height (mm)	Change In Height (%)
	Rod-Plate (deg)	Rod-Rod (deg)			
0.79	0.5	0.3	6.9698	0.001	0.00
5.0	5.0	3.0	6.9598	0.01	0.14

If the heights of rise are adjusted in this way the net effect on the curvatures obtained by the full comparative method is a reduction of 0.01 (0.15%) in that for the two-rod system. This is a roughly similar but reversed effect to the Jurin correction.

8.3.2.2 Dimensional errors

Deviations in the pore cross-sections from that given by the average dimensions of the pore construction components will pertain in both the constructed pores and the precision bore capillary tubes.

Variations in the diameter of the tubes are unlikely to have caused significant systematic deviations in the observed curvatures. This is because at the level of measurement the diameter of the tube may be greater or less than the average determined by the mercury thread method. Over the five runs any variations should largely cancel, producing a mean line whose gradient is close to that of totally uniform tubes having the average diameters.

However, for a pore formed by contacting rods the effect of dimensional variation is different. A rod will contact with its neighbour or the plate at points where its diameter is largest, leading to pores of greater cross-section than specified. Here we are assuming that measurement of the rod diameters have shown no significant tapering from top to bottom. Since the dimensional tolerances of the rods were found to be independent of diameter (see section 7.2.5), these variations will be more marked with smaller pores; i.e. dimensional errors will increase with decreasing pore size.

The dimensional errors can be quantified if the "equivalent tube" diameters are considered. For example, the equivalent tube radius of the pore formed by two 1/16" rods is 0.24 mm. The maximum variation in rod diameter was 0.002 mm. If all this error is passed on to the equivalent radius the corresponding drop in the observed height of rise amounts to 0.8%. With the largest rods, 5 mm diameter and 0.72 mm equivalent tube radius, the change in the observed height of rise is only 0.3% with rods of identical tolerance. The result of these dimensional variations will be to depress of the gradient of the rod line and hence the observed curvature by as much as 1%.

The overall effect of tolerance variation is always to make the constructed capillaries larger than their nominal sizes. This is consistent with observed curvatures being slightly lower than their theoretical values.

8.3.2.3 Other systematic errors

The two sources of error discussed above, namely those arising from gravity distortion and dimensional variations, can together account for the difference between observed and theoretical curvatures. However it is necessary to make some note of other potential sources of systematic error. Errors arising from the measurement of heights and diameters etc. will be random, leaving only errors that may arise from the surface condition of the pores.

One possible source of error is that of non-zero contact angle. The pore construction materials, steel and glass, are both high energy solids and as such will be perfectly wetted by isooctane. However, if the surfaces of the pore are contaminated with dirt and/or grease then non-zero contact angles may result. Even if the materials had remained contaminated after cleaning the resulting contact angles will be small, of the order of a few degrees. Isooctane on teflon, a low energy solid, produces a receding contact angle of less than 5° .

The effect of low contact angles on meniscus curvatures is small (see for example, Figure 10.5) resulting in only very slight reductions in value. Contact angles less than 5° produce reductions in curvature of less than 0.25%. The use of the comparative method of curvature determination will further reduced any error.

Another assumption of the theory that will not be exactly satisfied is that of the perfectly smooth solid surface (see section 2.7). On a macroscopic scale the surfaces of both the steel and glass are rough and hence the liquid will not always meet the plane of the solid surfaces tangentially. The angle of interception with the vertical plane of the solid surface will vary according to the surface condition at the three phase line. As a consequence the upward force resulting from the contact of the liquid with the solid perimeter will not be everywhere vertical, so lowering individual curvatures slightly. The effect will again be largely eliminated by the comparative method.

8.3.3 Comparison of results with Mason *et al*'s studies

Mason *et al.* (1983, 1984a) have published results from experiments similar, in most respects, to these. Their raw experimental data (1984a), uncorrected for distortion, yielded a value of 6.88 ± 0.02 for the normalised meniscus curvature in the two rod system. The value of 6.94 ± 0.02 obtained here compares favourably with Mason's value. The improved proximity of the experimental value found here to that predicted can be attributed to two improvements in the apparatus.

- i)* Mason used "precisely" machined channels, not clamps, to hold the rods in position. As explained in section 7.2 this arrangement is likely to lead to significantly greater dimensional errors as the rods may not touch the plate.
- ii)* The needle rollers that were, for the most part, used to assemble the pores are of significantly higher tolerance than the silver steel rods employed in Mason's experiments.

8.3.4 Bearing on the general experimental method

The experiments conducted here have been to determine the curvatures in certain "standard" pore shapes. In each case a total of twelve pores were used. This method yields accurate results in which there is a high degree of confidence. However, it would be impractical to conduct all experiments with the full comparative method, as it is both cumbersome and too time consuming.

In determining the curvatures of menisci in test pores of non-standard configurations only three measurements are required; the level in the test pore, that in a standard cell and the reference level in the reservoir indicator cell. The meniscus curvature is then determined as described in section 7.5, from a simple equation;

$$C = 6.94 \left(\frac{\Delta h_t + 0.5}{\Delta h_s + 0.5} \right) \frac{R_t}{R_s} \quad (7.7)$$

This method is termed the *simplified* comparative method and carries the same advantages as its *full* brother, but is also bound by some limitations as the accuracy of the method depends on the applicability of the standard's predetermined curvature. The multiplier, 6.94, is the mean value of the meniscus curvature in a pore formed by two equal rods and a plate for heights of rise in the range 7 to 24 mm. So the heights of rise in test and standard pores should be in this range.

The correction applied for the height of rise in the indicator cell, 0.5 mm, has no physical significance. It is simply an extrapolated value from the heights of rise given by the gravity distorted menisci in the pores (see Fig. 8.1). The correction accounts for the distortion only so long as the heights of rise in the test and standard pore are close to each other and their shapes broadly similar.

If the heights of rise differ by more than a few millimetres use of the simplified comparative method is not strictly valid. The degree of distortion of each meniscus will differ.

The validity of the correction is also doubtful when the test meniscus is of a markedly different shape to the near-hemispherical menisci produced in the standard arrangements. The value of the intercept will, in fact, vary slightly from configuration to configuration and with one liquid to another. However, the increased accuracy obtained from the full method could not be justified in terms of the time required obtaining it.

In those instances where the menisci in the test and standard are of similar shape there is no need to keep the heights of rise close. These experiments have shown that the Jurin correction provides an excellent compensation for distortion of *near hemispherical* menisci. In these cases the curvature is obtained by first adding the "true" correction for the height of rise in the indicator cell, determined at 0.2 mm from Figure

8.4. The Jurin correction, h_j , found from the equivalent tube radius, is then added giving the relationship for curvature in the test cell as;

$$C = 6.95 \left(\frac{\Delta h_t + h_{j_t} + 0.2}{\Delta h_s + h_{j_s} + 0.2} \right) \frac{R_t}{R_s} \quad (7.8)$$

Note that the gravity corrected value for the standard curvature is now used.

The above equation proved useful in some of the experiments (see later), but was inappropriate when the test TMs' were not concave. With some pore shapes other corrections seemed considerably more appropriate, these are discussed in the relevant sections. In these experiments the two principal effects of gravity, namely those arising from the measurement of minimum curvature and from the sloping of the wedges, broadly cancelled. Note that this will not necessarily be the case with the simplified method as both standard and test pore will contain wedges. Thus both the gravitational effects will act to reduce observed heights of rise to increasing effect as the pore section is enlarged.

CHAPTER 9

Investigations under perfectly wetting conditions

9.1 INTRODUCTION

When the contact angle is zero the MS-P theory is generally easier to apply than is the case if partially wetting conditions are incorporated. In addition, the experiments are both comparatively simpler to perform and much less time consuming. It is for these reasons that most of the past investigations and many of the experiments reported in this study are conducted under perfectly wetting conditions.

In this chapter the theory and experiments for four different pore shapes are discussed in order of ascending geometric complexity. This was unfortunately not the same order in which experiments were conducted. For each pore shape the theory will be derived in terms of the chosen variable and experiments performed to confirm the predictions in variously shaped and sized pores. The results will then be discussed in the light of likely errors arising from the experiments.

9.2 RECTANGULAR DUCTS

One of the simplest imaginable geometries for a capillary that exhibits arc menisci is that of a square or rectangular tube. This is the logical place to start an examination of the MS-P theory. The simple geometry results in a very straightforward solution of the MS-P equation that, as with other n -gon tubes (section 6.4.1), affords an analytical solution.

Experimental verification of the theory is far however from simple. Fabrication of small rectangular tubes to precise dimensions proved difficult. Pores made up from rods have the advantage of being made up from elements considerably larger than the pore itself. Rectangular ducts must either be directly machined or, as here, be made up from contacting plates of the same dimensions as the pore itself. These methods of fabrication result in dimensional errors significantly larger than those in rod pores. However, some meaningful results can still be obtained.

The MS-P theory for rectangular tubes was recently used by Lenormand *et al.* (1983), whilst Legait (1983) utilised the theory with square tubes (section 5.4). Rectangular ducts were also the subject of a undergraduate project at Loughborough University by Clough & Daniels (1986). The latter study sadly provided little assistance as both theory and experiments were wildly in error.

9.2.1 Theory

Figure 9.1 shows the shape adopted by a MTM of a perfectly wetting liquid in a rectangular duct. Four DCAMs, one in each corner, merge to form the MTM. Assuming this meniscus shape the expressions for effective perimeter and area of the meniscus can be found. The nomenclature follows that of chapter 6 except for those parameters defined on Figure 9.2.

Two characteristic dimensions are required to define the pore size, selected to be half the tube depth, R , and half its width, d . The pore shape can be defined by the aspect ratio, d/R . The curvature may be normalised against either dimension, R/r was chosen here. Since the MS-P equation requires only the ratio of meniscus area to perimeter, only one of the four quadrants of the tube needs to be considered.

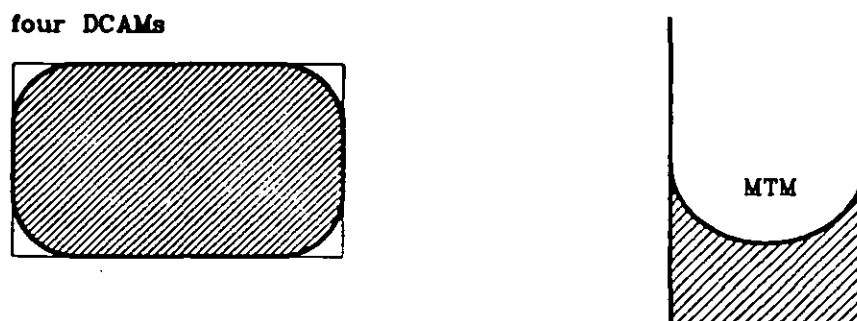


Figure 9.1 - Arrangement of arc menisci (AMs) for a main terminal meniscus (MTM) in a rectangular duct. The effective area of the MTM is shown hatched and the effective perimeter outlined. A schematic representation of the capillary rise profile seen through the glass plate is also shown.

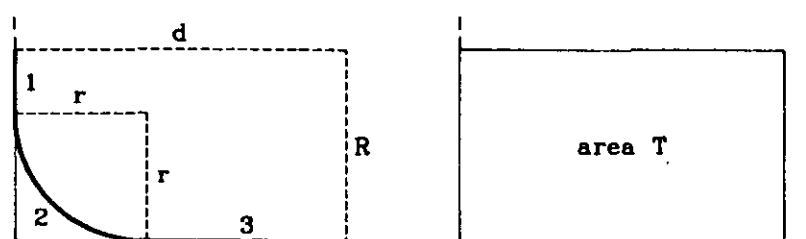


Figure 9.2 - Diagram showing the choice of regions and terminology used in the calculation of effective area and perimeter for the meniscus in a rectangular duct. Note that only a quarter of the duct need be considered owing to the symmetry of the duct.

a) Perimeters

From Figure 9.2:

$$P_1 = R - r \quad \text{Equations}$$

$$P_2 = \pi r / 2$$

$$P_3 = d - r \quad 9.1$$

b) Areas

$$A_T = dR \quad \text{Equations}$$

$$A_2 = (1 - \pi/4)r^2 \quad 9.2$$

c) Effective area and perimeter

The effective perimeter, shown bold on Figure 9.2, is given by:

$$P_{eff} = \sum P_S + \sum P_L \quad (6.11)$$

but $\sum P_S = P_1 + P_3$ and $\sum P_L = P_2$, hence

$$P_{eff} = (d + R) + (\pi/2 - 2)r \quad (9.3)$$

The effective area, shown hatched on Figure 9.2, is simply given by;

$$A_{eff} = A_T - A_2 = dR - (1 - \pi/4)r^2 \quad (9.4)$$

d) Solution of equations

The MS-P equation relates area and perimeter to the radius of the arc menisci, r ,

$$P_{eff}r - A_{eff} = 0 \quad (6.12)$$

substituting for P_{eff} and A_{eff} and normalising with respect to R yields,

$$\left(1 - \frac{\pi}{4}\right)\left(\frac{r}{R}\right)^2 - \left(\frac{d}{R} + 1\right)\left(\frac{r}{R}\right) + \frac{d}{R} = 0 \quad (9.5)$$

a simple quadratic in r/R which can be solved to give

$$\frac{r}{R} = \frac{\left(\frac{d}{R} + 1\right) \pm \sqrt{\frac{d}{R}\left(\frac{d}{R} - 2 + \pi\right) + 1}}{2 - \pi/2} \quad (9.6)$$

Both roots are positive, but only one is physically realistic. This can be simply illustrated by setting $d = R$, a square tube. Equation 9.5 reduces to;

$$\frac{R}{r} = 1 \pm \sqrt{\pi/4}$$

yielding results of $R/r = 0.1138$ or $R/r = 1.8862$. A normalised curvature of 0.1138 implies $r > R$ which is a physical impossibility. Thus the normalised curvature in rectangular tubes is given by:

$$C_{rect} = \frac{R}{r} = \frac{(2 - \pi/2)}{\left(\frac{d}{R} + 1\right) - \sqrt{\frac{d}{R}\left(\frac{d}{R} - 2 + \pi\right) + 1}} \quad (9.6)$$

In section 5.4 Lenormand *et al's* (1983) force balance gave an expression for the capillary pressure in rectangular tubes;

$$P_c^* = F(\epsilon)2\sigma\left(\frac{1}{x} + \frac{1}{y}\right) \quad (5.9)$$

where

$$F(\epsilon) = \frac{\epsilon(4 - \pi)}{2(1 + \epsilon)\{(1 + \epsilon) - \sqrt{(1 + \epsilon)^2 - \epsilon(4 - \pi)}\}} \quad (5.10)$$

and $\epsilon = x/y$ - the aspect ratio of the tube

Incorporation of the Laplace equation in the above and adapting the notation yields an expression for C_{rect} ;

$$\frac{R}{r} = 2F(\epsilon)\left(\frac{1}{d} + \frac{1}{R}\right)R, \quad \epsilon = \frac{d}{R} \quad (9.7)$$

At first glance the above expression bears scant resemblance to equation 9.6. However Lenormand has merely solved the quadratic in terms of $r(1/d + 1/R)$ instead of R/r . Multiplication of 9.5 by the factor;

$$2\frac{d}{R}\left(\frac{1}{d} + \frac{1}{R}\right)^2 R^2$$

yields

$$\frac{d}{2R}(4-\pi)\left(r\left(\frac{1}{d}+\frac{1}{R}\right)\right)^2 - 2\left(\frac{d}{R}+1\right)^2\left(r\left(\frac{1}{d}+\frac{1}{R}\right)\right) + 2\left(\frac{d}{R}+1\right)^2 = 0 \quad (9.8)$$

which solves to give Lenormand's result.

Equation 9.6 was inserted into a very simple computer program and values of R/r calculated in terms of the aspect ratio, d/R . Figure 9.3 shows the results as a continuous relationship on a graph of normalised curvature versus aspect ratio, the numerical results are detailed in Appendix C.

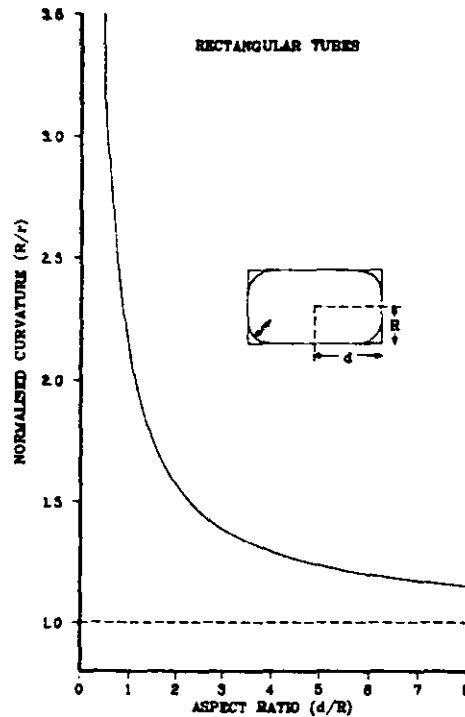


Figure 9.3 - Theoretical results of curvature for menisci in rectangular ducts. The curvature is normalised with respect to R , half the tube depth, and plotted as a continuous relationship against the tube aspect ratio.

9.2.2 Experimental

Three adjustable depth (i.e. variable in R) rectangular ducts were investigated with nominal widths of $3/64$ ", $1/16$ " and $3/32$ ". The aspect ratios covered ranged from 0.5 to 7.5 and were expected to give heights of rise in the range 5 to 25 mm, the entire range for which the comparative method has been validated. Isooctane, the wetting liquid, was used as the test liquid. In general, the experimental procedures followed those laid out in section 7.4. However there are some particulars specific to this configuration; these are discussed below.

9.2.2.1 Cell design

A specially designed cell was used for these experiments, the usual cell blank size being of inadequate size to accommodate the construction components. Figure 9.4 shows the design. All three ducts are accommodated in the cell. The cell is taller and thicker than the standard cell blanks, measuring 3" by 1" by 1 1/2". A 1/2" square channel was machined from the front face of the aluminium alloy cell. The ducts are made up from steel plates in contact. Three precision width plates form the back walls of the tubes. They are separated by four notched steel spacers that also form the side walls of the ducts. The glass plate forms the front wall of the tubes.

The spacers are of equal depth to the machined channel and remain static when aspect ratios are adjusted. Near either end of the spacers are 1/8" deep notches that hold the precision shimstock. Brass or steel shims separate the tubes' back wall from the glass plate and enable the aspect ratios to be adjusted.

The rectangular plates are pushed from behind against the shims by two sets of clamping screws (semi threaded pins), positioned level with the shims as shown in Figure 9.4. All seven plates are also pushed horizontally together against the left-hand wall of the machined channel by three additional clamping screws entering through the right-hand wall as shown in Figure 9.4.

The cell design also has some finer points. The pins at the back were sealed in one of two plastic housings fitted with rubber "O" rings to prevent excessive evaporation /leakage along their threads. The three clamping screws were fitted with plastic nuts for the same reason. Once fabricated, the plates were assembled in the cell in the absence of shims; the rectangular plates clamped level with the front face. The glass plate was then removed so that a few thou could be skimmed from the entire front face, thereby ensuring all the plates married up with each other and the front face. The design of the spacers meant that it was difficult to reassemble them wrongly, whilst the plates were marked to ensure their skimmed faces always faced forward and were the right way up.

It is likely that, despite the above precautions, there will be small gaps between the spacers and glass plate and perhaps between the rectangular plates at some points. These will be in the order of thousandths of an inch. The presence of the gaps will not matter provided the overall dimensions of the tube remain those specified by its aspect ratio. The reason is that the AMs bound the corners and it does not matter what the geometry is behind them as this effects neither the shape of the AMs nor the MTM.

The design described above is cumbersome and, in practice, difficult to set up correctly. A total of nine screws enter the channel and another twelve are needed to clamp on the glass plate and to seal the threaded pins. During assembly great care is required to ensure that no dust or dirt gets in-between the plates as this will distort the geometry greatly. Also the clamping pins must be tightened gradually and evenly so that

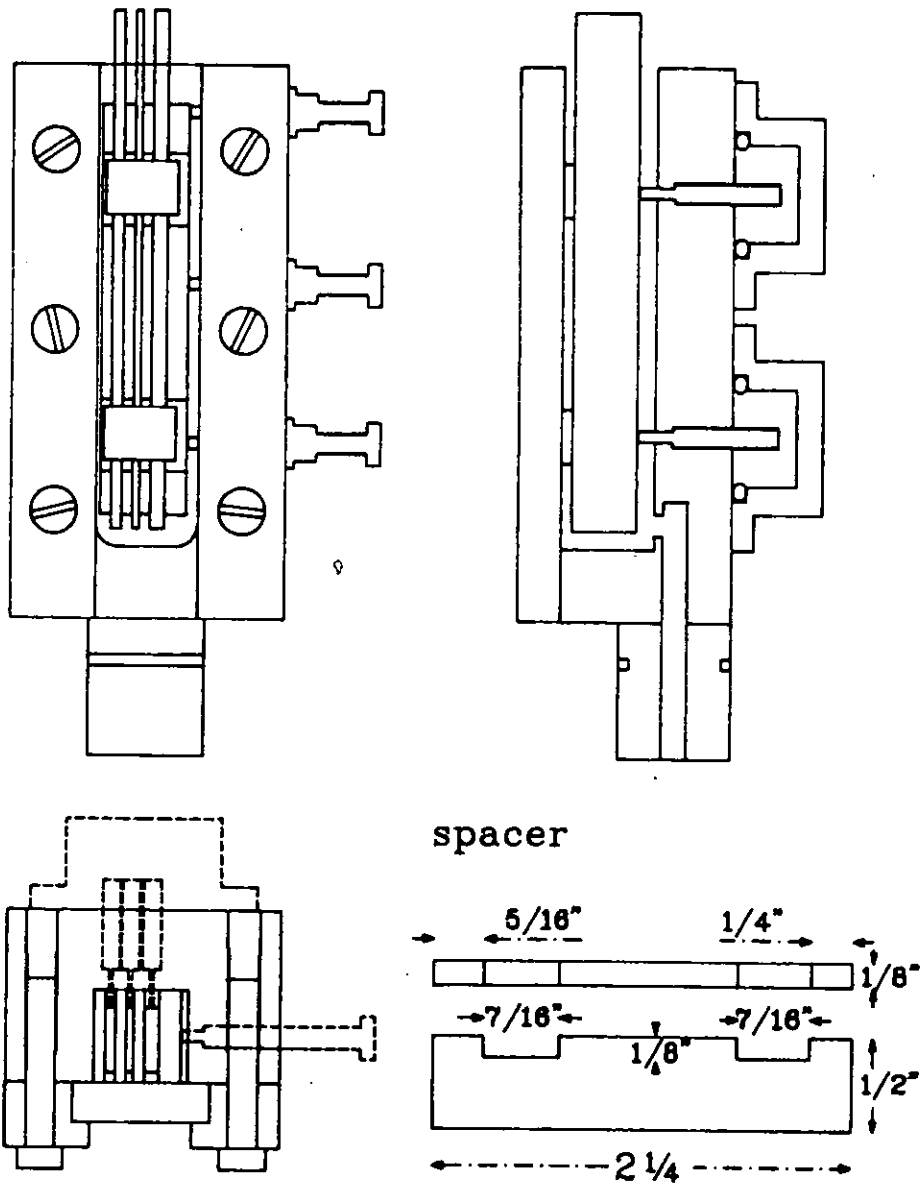


Figure 9.4 - Diagram of the cell used for the experiments with rectangular ducts. Three ducts are held in a single channel. Clamping screws entering through the rear of the cell push three plates against shims held in position against a glass plate by 'spacers'. The entire plate/spacer assembly is pushed against a channel wall by further clamping screws that pass through the opposite wall.

the plates are set square to the glass plate. However short of making a new cell for each aspect ratio I can think of no better design. Aspect ratio is adjustable and reasonable confidence is held in pore dimensions.

9.2.2.2 Determination of aspect ratio.

The aspect ratio of a given rectangular tube is the ratio of its depth, $2R$, to its width, $2d$. The width of the ducts were obtained from micrometer measurements on the rectangular plates. Several measurements were taken along the plate length with the micrometer jaws close to the leading edge of each plate. Table 9.1 shows the average measurement and the tolerances. Table 9.2 shows the mean thicknesses of the five sizes of shimstock used. The 100 thou shims were made from machined steel block, whilst the remainder were made of standard brass engineering shimstock. The shims show a somewhat better tolerance than the steel plates.

Table 9.1 Micrometer measured widths and tolerances for the rectangular duct plates.

Nominal Plate Width (in.)	Mean Plate Width (mm)	Tolerance Range
3/32	2.372	0.010
1/16	1.630	0.170
3/64	1.220	0.023

Table 9.2 Micrometer measured thicknesses and tolerance ranges of the shimstock spacers.

Nominal Shim Size (thou.)	Mean Shim Size (mm)	Tolerance Range
12	0.317	0.003
15	0.401	0.002
20	0.541	0.003
40	0.942	0.002
100	2.540	0.001

9.2.3 Results

Figure 9.5 shows the results compared to the MS-P predictions on a graph of normalised curvature, R/r , versus aspect ratio, d/R . Compared to results from pores made up from rods the agreement is not very good. However the trend of the theory is followed closely by all the experimental data.

Curvatures were calculated from averaged observed heights of rise using the simplified comparative method; equation 7.7. Five different shim sizes (R 's) were used yielding a total of fifteen aspect ratios. Notice some of the data are plotted twice as the same aspect ratio may be regarded as greater or less than unity (R/r vs d/R is equivalent to d/r vs R/d). Appendix C contains the detailed breakdown of results.

Almost all the observed curvatures fall below the MS-P curve. Errors from the predicted values are within 4% except in one case where the error is 5.9%. This latter curvature was obtained from heights of rise in the vicinity of 4 mm - outside the validated range of the simplified comparative method.

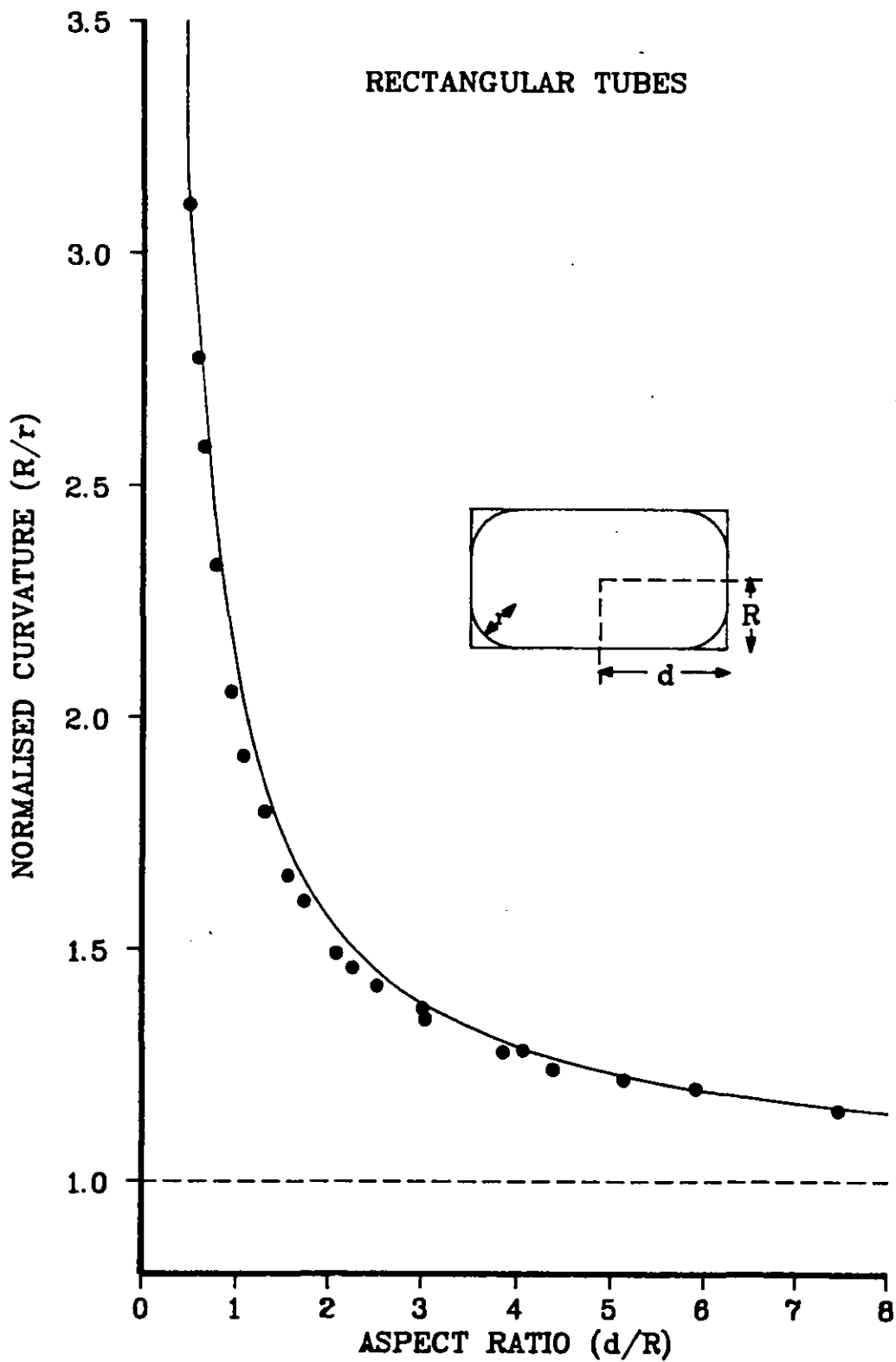


Figure 9.5 Experimental results for normalised curvatures obtained from the heights of rise of menisci in the rectangular ducts. There is a systematic error in the results arising from difficulties encountered in assembling the ducts with the specified aspect ratios.

It is probable that most of these errors arise from dimensional inaccuracies in the tube cross-sections. Unlike pores made up from contacting rods, the pore construction components are of similar size to the pores themselves. The same small dimensional variations found in rods will cause significantly greater errors in the aspect ratios of the rectangular tubes than they would to the sections of rod pores.

For each of the three tubes the magnitude of error from predicted curvatures rises as aspect ratio falls. The rate of change of curvature also increases dramatically with decreasing d/R so identical errors in pore section will result in larger errors in curvature. As with rod pores, dimensional variation in pore construction elements leads to pores of greater size than specified by the mean component size, as components will contact at their largest widths. That observed curvatures fall below theoretical predictions is consistent with tubes of greater section than specified. From the tolerances of the pore components (Table 9.1) it is likely that most of the error is in the tube width, d , but any flecks of dust or dirt caught in-between the plates and/or shims will have similar effects. That the magnitude of dimensional error is so much larger than in other experiments can be attributed to the difficulties with the cell.

Also reducing the observed curvatures from the ideal, but by much less significant amounts, is the distortion of the menisci. The comparative method partially corrects for gravitational effects. In fact many curvatures here have inadvertently been slightly over-corrected. These experiments were conducted prior to those on the standard configuration and the lessons of the latter had yet to be appreciated. In many cases the height of rise in the standard pore (2 x 1/16" diameter rods) was significantly higher than that in the test pore. Thus, when using equation 7.7, with the 0.5 mm correction applied to heights of rise, the rise in the standard pore will be over-corrected in comparison to that in the test pore. The result is curvatures slightly higher than would have been the case had the heights been roughly equivalent (as explained in chapter 8). This has only resulted in errors of a few tenths of a percent however.

With near hemispherical menisci the above discrepancy could have been avoided by applying the Jurin correction. However it is inappropriate here as most of the menisci are far from hemispherical in shape and become less so as aspect ratio increases. A more realistic correction would be to consider the TM as a semicircle and to add the height of a plane positioned such that the sectional area of liquid above it equalled the area of space below it. The AMs considered as a solid boundary. This correction to the minimum curvature that is measured in practice is significantly less than the, $R_T/3$, used by Jurin's correction. However considering the much larger dimensional errors it was not considered appropriate to correct for distortion.

Overall the results are as good as could be expected bearing in mind the difficulties of fabricating rectangular tubes.

9.3 ONE ROD AWAY FROM A PLATE

The meniscus curvature in a pore formed by a single cylindrical rod spaced from a plate was first calculated with the MS-P method by Princen himself (1969a), but he made only one measurement to confirm the theory, finding an error of 3% (see section 5.3.1). Later Mason & Morrow (1987) made a few measurements for the arrangement, but the agreement with the theory was poor, being as much as 15% in error.

The aim of these experiments was to re-examine the arrangement and to take measurements over a wide range of rod spacings. The *open* profile of a meniscus between a rod and plate is unlike those already discussed in that a TAM is formed. This is saddle-shaped and the profile of the MTM when viewed through the plate is thus convex. The majority of previously published results for menisci in asymmetrical uniform pores deal with wholly concave clastic menisci. It was hoped that the MS-P method could be shown to also work well with anticlastic menisci.

9.3.1 Theory

Figure 9.6 shows the shape of meniscus between a rod and a plate in profile and section. Two WOAMs, one at each side of the rod, merge to form a TAM. Note that while the TAM appears convex when viewed through the plate, it appears concave when viewed at right angles to the plate (Figs 9.6 (i) and (ii)), i.e. the TAM is anticlastic.

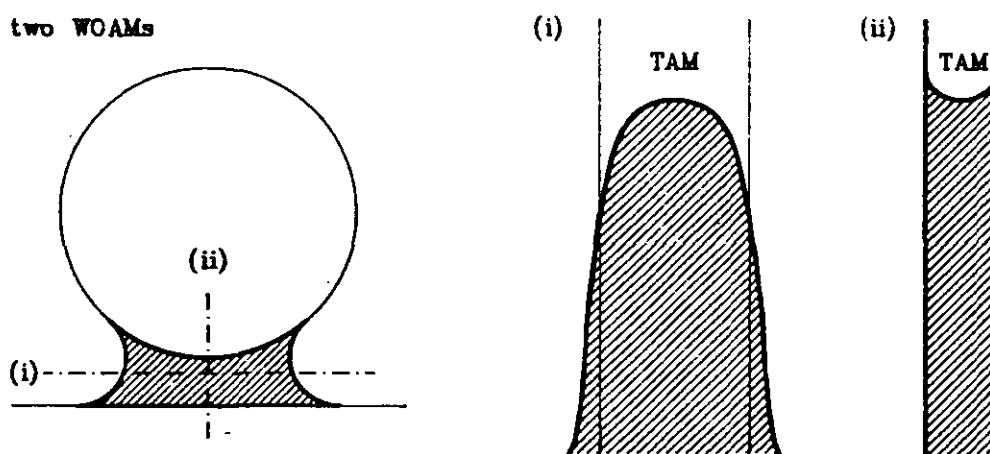


Figure 9.6 - Arrangement of the AMs for the Terminal arc meniscus (TAM) formed in the gap between a rod and a plate. The effective area is shown hatched and the effective perimeter outlined. Schematic representations of capillary rise profiles seen through the plate (i) and at right angles to it (ii) are also shown. Note the anticlastic form of the saddle-shaped TAM.

The arrangement again requires two characteristic dimensions to define the pore; the rod radius, R , and as a measure of the gap between the rod and plate half the total gap, d , was chosen. The curvature may be normalised with respect to either dimension. The rate of change of curvature with rod spacing is expected to be large so normalising with respect to d will yield a more useful, flatter curve when curvature is plotted against the normalised spacing, d/R .

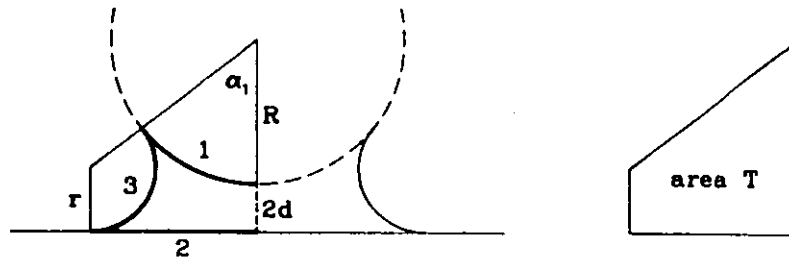


Figure 9.7 - Sketch showing the definition of the angle, the choice of regions and the associated terminology used in the calculation of effective area and perimeter for the one-rod-away-from-a-plate arrangement.

The meniscus cross-section has a plane of symmetry so, as with the analysis of rectangular ducts, only part of the section needs to be considered. Figure 9.7 defines the particular notation for this arrangement which otherwise follows that of chapter 6. Application of simple geometry on Figure 9.7 yields the following expressions.

a) Subtended angle

$$\alpha_1 = \arccos\left(\frac{R + 2d - r}{R + r}\right) \quad (9.9)$$

b) Perimeters

$$\begin{aligned} P_1 &= \alpha_1 R \\ P_2 &= (R + r) \sin \alpha_1 \\ P_3 &= (\pi - \alpha_1) r \end{aligned} \quad \text{Equations 9.10}$$

c) Areas

$$\begin{aligned} A_1 &= \alpha_1 R^2 / 2 \\ A_3 &= (\pi - \alpha_1) r^2 / 2 \\ A_T &= \frac{1}{2} (R + 2d + r) (R + r) \sin \alpha_1 \end{aligned} \quad \text{Equations 9.11}$$

d) Effective area and perimeter

The effective perimeter, shown bold in Figure 9.7, is given by:

$$P_{eff} = \Sigma P_S + \Sigma P_L \quad (6.11)$$

and from Figure 9.7;

$$\Sigma P_S = P_1 + P_2 \quad \text{and} \quad \Sigma P_L = -P_3$$

Note the negative sign for the liquid perimeter, present because the AM is open, and hence,

$$P_{eff} = P_1 + P_2 - P_3 \quad (9.12)$$

The effective area, shown hatched in Figure 9.7, is simply given by,

$$A_{eff} = A_T - A_1 - A_3 \quad (9.13)$$

e) Solution of equations

In addition to equations 9.9 to 9.13 the MS-P equation,

$$P_{eff}r - A_{eff} = 0 \quad (6.12)$$

also applies. With this arrangement it is not possible to solve the equations explicitly for r as both A_{eff} and P_{eff} are functions of α_1 which is, in turn, a function of r . Consequently the standard computer program (section 6.4.2.1) was used to solve the equations. The program was modified to calculate values of normalised curvature, d/r , in terms of the normalised rod spacing, R/r .

The results are shown on Figure 9.8 as a continuous relationship between curvature and spacing. The normalised spacing ranges from 0 to 0.5, this being the range encompassed by the experiments. The curvature of the TAM falls continuously as the gap is increased, rapidly at first and then more slowly. Overall the function is roughly hyperbolic, approaching each axis asymptotically. The results agree with the tabulated values given by Princen (1969a) when they are adjusted to his method of normalisation.

9.3.2 Experimental

Three rod spacings, nominally of 8, 12 and 15 thou, were investigated with drill blanks of various sizes in the range 1/32" to 1/4". Recorded heights of rise were in the range 5 to 22 mm, within the validated scope of the comparative method. The wetting liquid isooctane was used for the experiments. Particulars specific to this arrangement are given below. With these exceptions the general procedure detailed in section 7.4 was followed.

9.3.2.1 Cell design

Any cell employed for experiments with a single rod away from a plate has to satisfy four requirements:

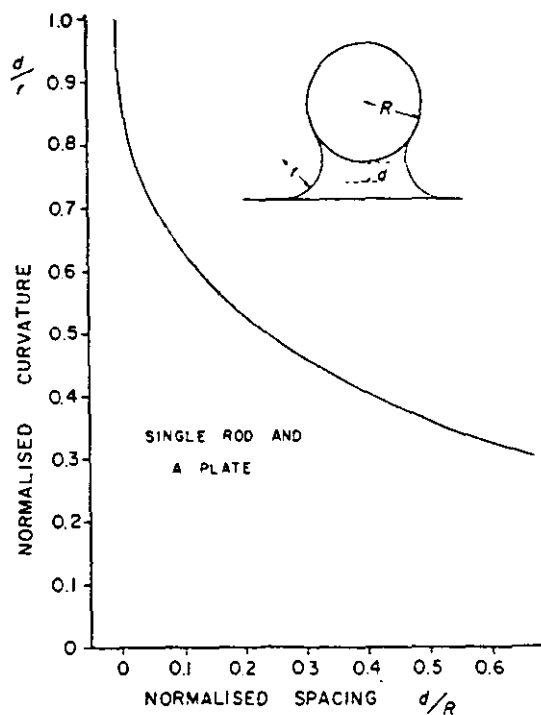


Figure 9.8 - Theoretical results of curvature for menisci between a rod and plate. The curvature is normalised with respect to the gap and plotted as a continuous relationship against the normalised spacing.

- i)* The channel in which the rod is held must be of sufficient width to ensure that the rod, when in position, is isolated from the channel walls. Failure in this respect will result in distortion of the WOAMs caused by the influence of the walls.
- ii)* The rod must be held vertically in the cell thereby yielding a symmetrical meniscus.
- iii)* The two shims that act as the rod-plate spacers, must be accommodated far enough apart to allow capillary rise in-between and in such a way as to facilitate easy cell assembly.
- iv)* The rod must be pushed firmly against the shims, but in a manner that does not cause any bending of the-rod.

Figure 9.9 shows the cell design chosen after consideration of the above points. The cell was fabricated from a standard cell blank and had a 3/8" square channel machined in the front face. Pairs of "shim-holders", measuring 1/4" by 1/8" and 1/16" deep, were cut either side of the channel, one each at the top and bottom of the channel. The rod is pushed against the shims by two clamping screws entering through the back wall of the channel, directly behind the shims. The threads were ground off the last 1/8" of the screws to leave a 1/16" diameter pin. The pins fit into holes in two steel blocks

that act as both vertical aligners and supports. The blocks are identical and have a small "V" shaped groove, $1/32$ " deep, machined in their front face to hold the rod vertically in position in the centre of the channel.

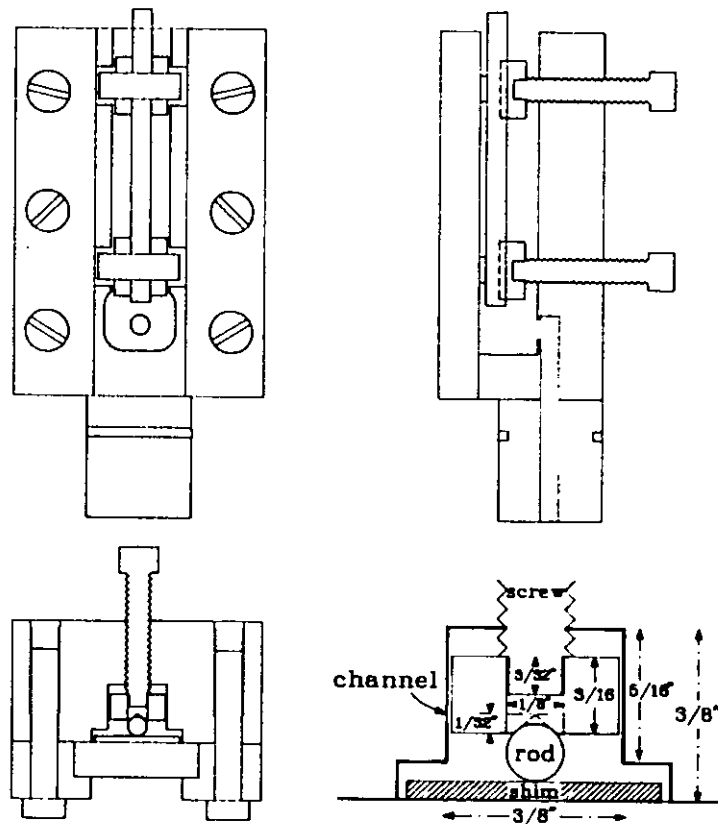


Figure 9.9 - Diagram of the cell used for the capillary rise experiment on the one-rod-away-from-a-plate arrangement. The rod is pushed against the shims by two clamping screws headed with grooved blocks. The blocks ensure that the rod is held in a vertical position in the middle of the channel.

9.3.2.2 Cell assembly

The above design proved easy to assemble, but care was required when pushing the rod against the brass shims. Too tight and the brass deforms, becoming indented, particularly when smaller rod sizes are used. Too loose and rod-shim-plate contact is not achieved. Either way the spacing will not be that specified. Unfortunately there is no way of directly checking the rod spacing once the cell is assembled, so it is all the more important that the screws are properly tightened. This problem was aggravated by difficulties in making shims of the required size that were not somewhat bent after preparation by the method described in section 7.2.5.4. Hence some pressure had to be applied to flatten the flexible shim against the plate.

Through practice a technique was found to check the rod-shim-plate contact. The cell would first be loosely assembled and then immersed briefly in isoctane. With the shims now wet the required tightness of the screws could be judged. When the small menisci between the shim and plate disappeared they were in contact and, by implication, the rod must also be contacting the shim.

The usual practice of attaching plastic nuts to clamping screws to prevent leakage was not followed in order that changes in resistance to screw tightening could be felt. However to prevent excessive leakage along the threads PTFE tape was wrapped around the screws. They were then "exercised" by screwing them in and out of the cell a few times so that in operation they could be moved freely until the point of mutual contact.

9.3.2.3 Point of measurement of height of rise

As viewed through the plate the meniscus profiles appear convex, so the usual criterion of measuring the height of rise to the apex of a meniscus no longer applies. To measure to the apex of the TAM is to measure the maximum curvature. Meaningful experiments require a definable point to measure the heights of menisci. The definable point closest to the minimum curvature of a TAM is that to the bottom of the concave part (see Figure 9.6 (ii)). This point can be made out immediately beneath the profile appearing against the glass.

9.3.3. Results

The mean curvatures obtained from fourteen different rod-gap arrangements are shown compared with the MS-P theory as a graph of normalised curvature, d/r , versus normalised spacing, d/R , on Figure 9.10. The results are generally in excellent agreement with the theory; most to within 1% and all within 2.5%. Further details are given in Appendix D.

Observed heights of rise were used to calculate curvatures with equation 7.7, without correcting for gravity distortion. The Jurin correction is clearly inappropriate as the menisci are partly convex. Indeed, the average curvature of a TAM (which is closest to the constant curvature assumed by the MS-P theory) will correspond to a height less than that measured. This is consistent with most of the experimental curvatures being slightly higher than the theoretical values. The actual correction required to be subtracted for gravity distortion is difficult to quantify, but it will not correspond to the Jurin correction. The menisci are nowhere near the hemispherical shape assumed by this correction, in fact, the two principal radii of curvature are of opposite sign.

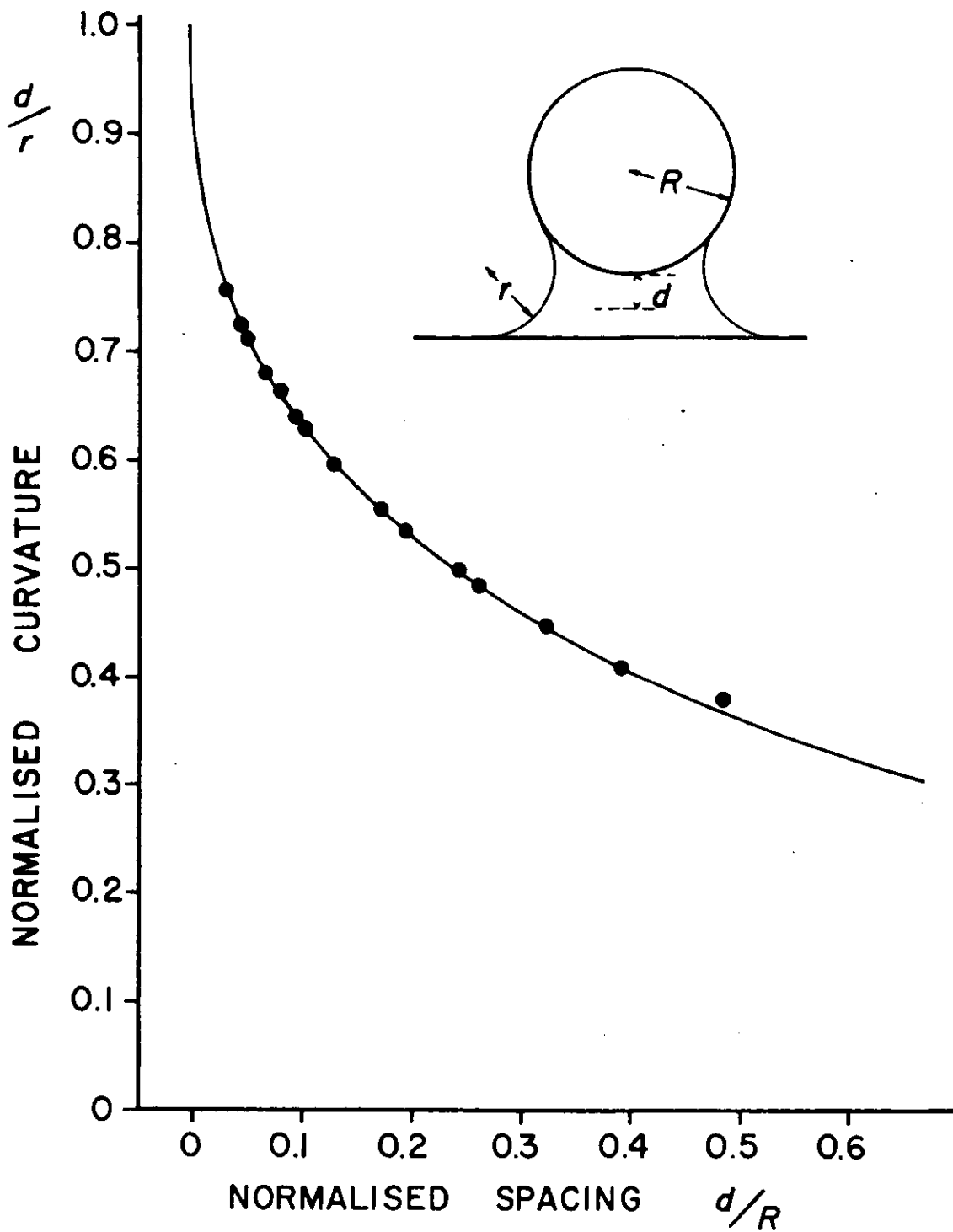


Figure 9.10 - Experimental results of curvatures obtained from heights of rise for the TAM formed in the gap between a rod and plate.

There is little doubt that gravity will act to suppress the curvature, the physics demand it. However, the effect will be largely offset by the measurement of the higher than average curvature. Also it may be that the sloping of the wedges compensate for the effect somewhat. OAMs, unlike CAMs, act to pull down a TM. The fact that they were sloping (observed in practice as well as predicted from the variation of curvature with height) means that they no longer pull the TAM vertically downwards. Only the vertical component will suppress the height obtained by the TAM, leading to higher than expected heights of rise.

Dimensional variations will again account for most of the scatter in the data. Here dimensional errors may make the pore either larger or smaller than that specified. Rods will contact the shims and the shims the plate at their thickest points when the cell is correctly assembled so lowering the curvature. However, if the rod were over-clamped and the rod indented the shim then the spacing will be less than expected, thereby increasing the curvature. This is consistent with results using the smallest rod, 1/32" diameter, giving larger positive errors. Any bending of the rod towards the plate, an effect difficult to avoid with the small diameter rods, will have a similar effect.

9.4 ONE ROD IN A CORNER

The case of a single rod in a corner of known angle is one of the simplest imaginable pore geometries to which the MS-P method can be applied. This arrangement has been considered before. Firstly by Mason & Morrow (1984a), who limited their analysis and experiments to right-angled corners. The theory was derived to show the effect of changing contact angle on meniscus curvature. Their experiments used the full comparative method described in the preceding chapter and were limited to zero contact angle.

Later the arrangement was studied as part of an undergraduate project at Loughborough University by Nibbs & Baynes (1986) with supervision by Mason. Their study extended the theory and experiments to cover acute corner angles of 30° , 50° , and 70° under perfectly wetting conditions.

The object of the study presented below was to confirm, and hopefully improve on, the previous results and extend the analysis and experiments to obtuse corner angles.

9.4.1 Theory

Under perfectly wetting conditions a meniscus in a corner bounded by a rod and plate adopts the shape shown in Figure 9.11. Three DCAMs, two where the rod contacts the plates and one in the angled corner, merge to form the MTM. Knowing this arrangement enables the relationships between the radius of curvature of the AMs and the effective area and perimeter to be defined. The terminology used below follows that proscribed in chapter 6 and Figure 9.12.

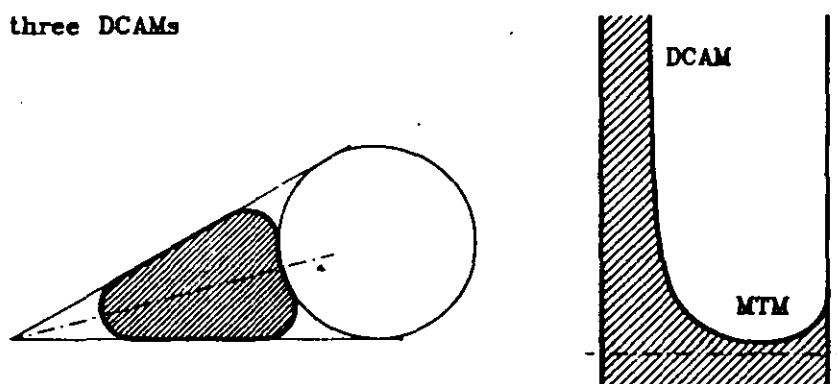


Figure 9.11 - Arrangement of arc menisci for the main terminal meniscus in the pore formed by a rod in a corner. The effective area is shown hatched and the perimeter outlined. A schematic representative of the capillary rise profile seen through the plate is also shown.

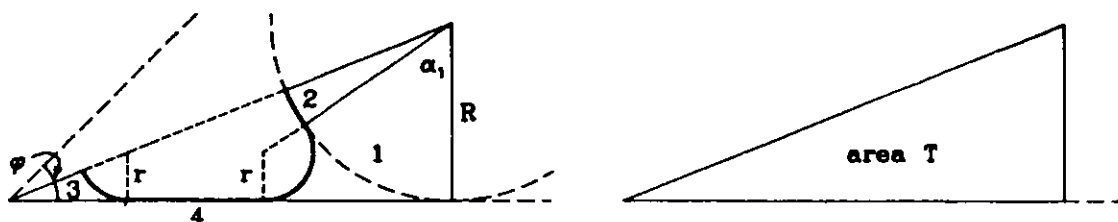


Figure 9.12 - Sketch showing the definition of angles, the choice of regions and associated terminology required for the calculation of effective area and perimeter for the rod-in-a-corner arrangement.

a) Angles

The corner angle, ϕ , is assumed to be known, and since the geometry is symmetrical about the plane AO we need only consider half the cross-section. Only one further angle needs to be defined; α_1 ,

$$\alpha_1 = \arccos\left(\frac{(R-r)}{(R+r)}\right) \quad (9.14)$$

b) Perimeters

From Figure 9.12:

$$\begin{aligned} P_1 &= (\pi - \alpha_1)r \\ P_2 &= (\pi - 2\alpha_1 - \phi)R/2 \\ P_3 &= (\pi - \phi)r/2 \\ P_4 &= (R-r)\cos(\phi/2) - (R+r)\sin\alpha_1 \end{aligned} \quad \begin{array}{l} \text{Equations} \\ 9.15 \end{array}$$

c) Areas

$$\begin{aligned} A_T &= R^2(\cot(\phi/2))/2 \\ A_1 &= ((R+r)^2 \sin\alpha_1 + (\pi - \alpha_1)r^2)/2 \\ A_2 &= (\pi/2 - \alpha_1 - \phi/2)R^2/2 \\ A_3 &= r^2(\cot(\phi/2) - (\pi - \phi))/2 \end{aligned} \quad \begin{array}{l} \text{Equations} \\ 9.16 \end{array}$$

d) Effective area and perimeter

The total effective perimeter, shown bold on Figure 9.12, is given by;

$$P_{eff} = \sum P_S + \sum P_L \quad (6.11)$$

and from Figure 9.12 $\sum P_S = P_2 + P_4$ and $\sum P_L = P_1 + P_3$ hence

$$P_{eff} = P_1 + P_2 + P_3 + P_4 \quad (9.17)$$

The effective area, shown hatched in Figure 9.12, is given by;

$$A_{eff} = A_T - A_1 - A_2 - A_3 \quad (9.18)$$

e) Solution of equations

The equations derived above were entered into the standard solution program together with the MS-P equation,

$$P_{eff}r - A_{eff} = 0 \quad (6.12)$$

The program was modified to give values of normalised meniscus curvatures, R/r , in terms of the corner angle, ϕ , for corners between 0° and 180° (see Appendix E). The results are shown in graphical form as a continuous relationship between R/r and ϕ on Figure 9.13. As expected the curvature increases with increasing corner angle (decreasing pore section). Note however the odd behaviour of the curve near $\phi = 0$.

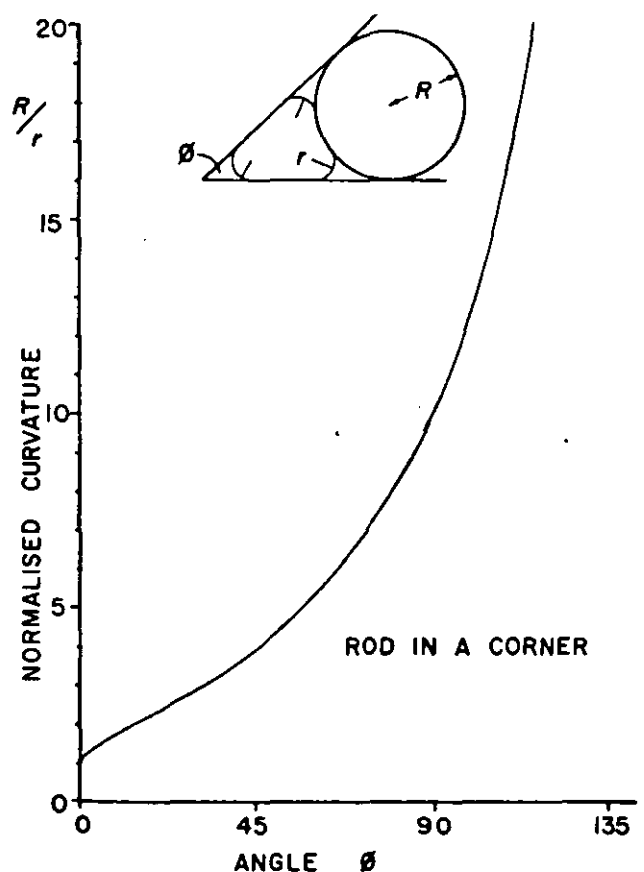


Figure 9.13 - Theoretical results of curvature for the MTM in the rod-in-a-corner arrangement. The normalised curvature is plotted as a continuous relationship against the corner angle.

9.4.3 Experimental

Three corner angles were investigated with nominal angles of 30° , 90° and 110° ; the 50° and 70° cells from the previous study being unavailable. The theory indicates that, for corner angles much greater than 110° , the curvature is so large as to make heights of rise too large to be accommodated in the cells.

Experiments to measure capillary rise, and hence determine the normalised meniscus curvatures for the rod-in-a-corner system were conducted using the simplified comparative method (see section 7.4).

Several different rod sizes were used in each corner so as to confirm the observed curvatures of a range of different heights of rise. For the 30° corner a total of ten sizes were utilized, ranging from 1.8 to 3.2 mm diameter. With rod sizes smaller than this range difficulties were experienced in properly clamping the rod in the corner. The points of pressure from the clamping screws were too far from the test rod. Rods in the ranges 2.1 to 6.3 mm and 3.2 to 6.3 mm were used in the 90° and 110° corners respectively. The higher size ranges reflecting the greater heights of rise expected. All the rod sizes yielded heights of rise within the range 5 - 25 mm for which the experimental method has been validated.

9.4.3.1 Cell design

The cell design for the corner arrangement is straightforward. Standard aluminium alloy cell blanks simply had channels with a specified corner angle machined in the front face. Figure 9.14 shows diagrams of the 30° and 110° cells used for the experiments, the latter designed and commissioned as part of this study. The test rod was clamped in the corner by a combination of other rods and threaded pins ensuring contact of the rod with the cell wall and the glass plate. Plastic nuts were added to the pins against the outer wall of the cells to prevent leakage of isooctane along the screw threads.

9.4.3.2 Measurement of corner angle

The cells used in these experiments were fabricated by a professional machinist, but the accuracy of the machinery does not guarantee the corner angles exactly. The experiments require a direct measurement of these angles.

Each cells corner angle was measured with a rotating microscope, equipped with a vernier scale accurate to 0.05°. Measurement with the microscope could only be done at the top of a cell due to the design. Any variation in the cross-section of the cells remains undetected. It proved difficult to measure the angles reproducibly in practice, resulting in quite large deviations.

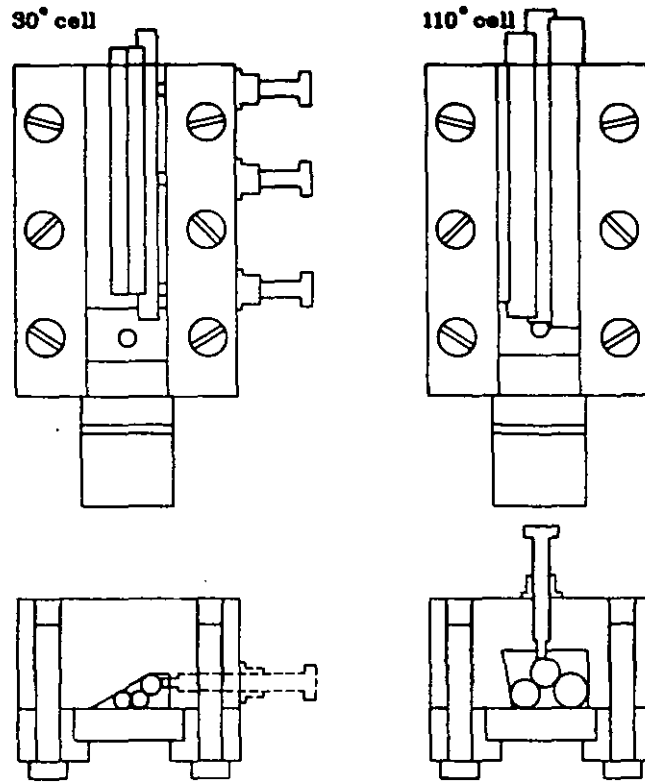


Figure 9.14 - Sketch illustrating the design of cells to hold rods in 30° and 110° corners. Both employ clamping screws to push the test rod into the corner. Other rods may be used to direct the pressure from the screws.

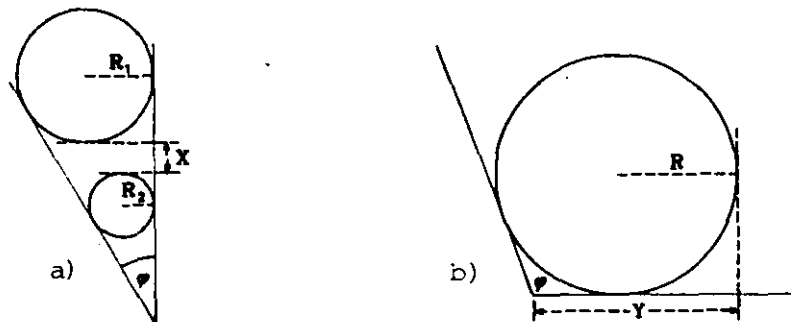


Figure 9.15 - Sketches illustrating the methods used to confirm corner angles.
 (a) For acute corner angles the distance between two rods resting in the corner is measured.
 (b) With obtuse angles an alternative method based on a single rod is used.

A further physical measurement of the corner angles was obtained using a rod or rods in the corner. For acute angles two rods of known diameter were placed in the corner as shown in Figure 9.15. The distance between the rods, X , was measured with a

travelling microscope accurate to 0.01 mm. The corner angle was then calculated using trigonometry,

$$\phi = 2 \tan^{-1} \left(\frac{(R_1 - R_2)}{(R_1 + R_2 + X)} \right) \quad (9.18)$$

For obtuse angles the above method is inappropriate and another technique was required. A single rod of known diameter, the largest possible, was clamped in the corner as shown in Figure 9.15. The distance of the outermost point on the circumference to the apex of the corner, Y, was measured with the travelling microscope. This method, although not as accurate as that for the acute angles, provides a check on the directly measured angle. The corner angle is obtained by calculation from;

$$\phi = 2 \tan^{-1} \left(\frac{R}{Y - R} \right) \quad (9.19)$$

With right angled corners neither of the above methods are appropriate and only rotating microscope measurements were taken. However, the accuracy of the machining appeared better with right angled corners.

Averaging the angles obtained from direct measurements with the rotating microscope and from the other methods (where appropriate) gave a mean corner angle. For the three corners investigated here mean corner angles of 30.17°, 90.06° and 109.83° were found. Table E.2, Appendix E gives the details.

9.4.4 Results

The experimental results are shown on Figure 9.16 compared to the theoretical curve of normalised curvature versus corner angle. As can be seen, the results are in excellent agreement with the theory. The points plotted represent the mean corner curvatures.

In addition to the results found here the findings of Nibbs and Baynes (1986) ^{are shown} for 50° and 70° corners. The students used neither the full or simplified comparative methods. They compared gradients of straight lines of graphs of height of rise versus reciprocal rod radius with that of a similar line they obtained, at a different time, for two rods and a plate. The curvatures were found from,

$$C_{corner} = 6.970 \times \frac{G_{corner}}{G_{2rods}}$$

The value of curvature in the two rod pore, 6.970, is that obtained from the MS-P theory. In other words they have used a result of the theory to test the said theory. Also the heights of rise used for their graphs were obtained at different times, making the gradients of the lines sensitive to temperature changes. Furthermore no attempt was made to confirm corner angles by measurement.

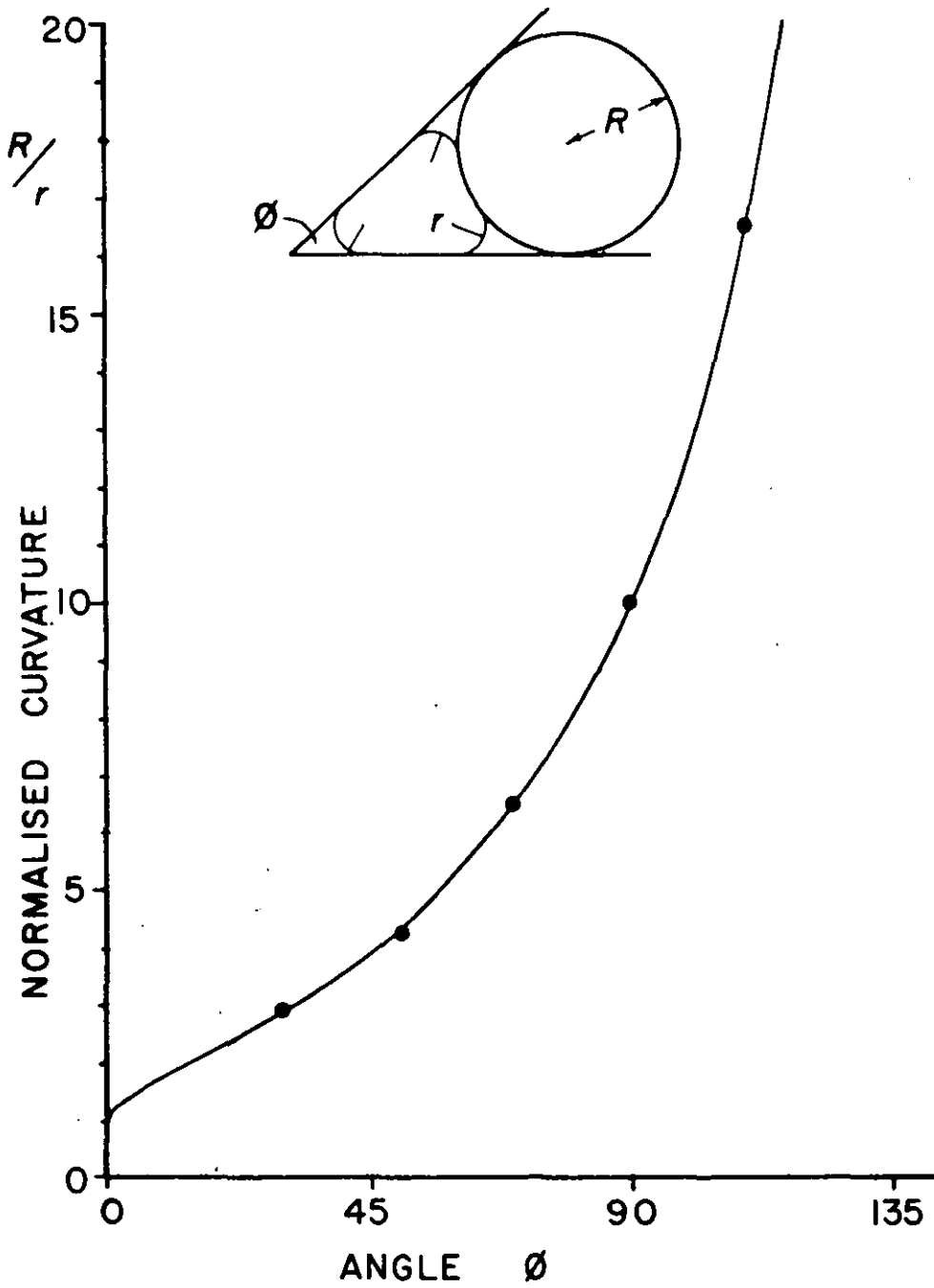


Figure 9.16 - Experimental results for curvatures obtained from capillary rise experiments on the rod-in-a-corner system. The 50° and 70° results only are taken from an earlier study by Nibbs & Baynes (1986).

The above factors explain the relative inaccuracy of the results for the 50° and 70° corners. The improved experiment techniques used here in the same 30° cell resulted in the error from theory improving from +2.3% (Nibbs and Baynes 1986) to only -0.56%. I would expect similar improvements for their other results had the experiments been conducted.

Since the menisci are concave and near-hemispherical the Jurin correction was applied to observed heights of rise. The gravity corrected equation, 7.8, was used to calculate curvatures. Detailed experimental results are given in Appendix E. Table 9.3 summarizes the data and gives estimates of the error. Two entries are accorded for the 30° corner, once for the results of Nibbs and Baynes and once for this study.

Table 9.3 Summary of experimental results for the rod-in-a-corner arrangement. A comparison between the results of Nibbs & Baynes (N&B) and those found here (W) is shown where applicable.

Nominal Angle (deg.)	Mean Angle (deg.)	Expt. Curvature C_{EXPT}	MS-P Curvature C_{MS-P}	% Deviation	Standard Deviation	Study
30	30.17°	2.875	2.891	-0.56	0.008	W
30		2.947	2.881	+2.30		N&B
50		4.243	4.329	-2.03		N&B
70		6.423	6.469	-0.72		N&B
90	90.06°	9.973	9.996	-0.23	0.020	W
110	109.83°	16.346	16.479	-0.81	0.084	W

All the results of this study fall within 1% of the theoretical values. This agreement is very good in the light of possible dimensional errors, which have the effect of reducing the observed curvatures. As the corner angle increases the effect of fabrication errors are likely to increase due to the much greater rate of change of curvature with corner angle.

9.5 TWO UNEQUAL RODS AND A PLATE

The curvature of the meniscus formed between two rods of equal diameter and a plate, all in mutual contact, has been studied with the MS-P method on several occasions. Mason & Morrow (1983, 1984a) have studied the arrangement twice, undergraduate students Ashton & Cable (1985) and Nibbs & Baynes (1986) have also looked at the configuration and finally experiments on the system conducted as part of this study were discussed in chapter 8. However, nowhere in these studies are there meaningful results for the case of unequal rods.

None of the previous studies enjoyed the benefits of the simplified comparative method in their experiments. Mason & Morrow used the full comparative method, as described and employed in chapter 8, but with outdated apparatus. Ashton & Cable were more concerned with contact angle variations. Their few results were obtained by assuming the physical properties of test liquids (density and surface tension) and also ignoring any effects of temperature variation. Nibbs & Baynes did extend the study beyond equal rods, but their experimental method was in error (as described in section 9.4.4).

The configuration of two unequal rods and a plate, although bearing no particular special features, was expected to yield very accurate results as it takes maximum advantage of the experimental technique. The menisci formed are of almost identical shape to those of the standard arrangement and so experimental errors due to dimensional variation and gravity distortion will almost entirely cancel when curvatures are calculated. In addition, the shape of a two-rod pore is entirely defined by the ratio of the rod radii. No secondary measurement, such as shim thickness or corner angle, is required. The likely experimental errors are therefore minimised.

The analysis and results presented in this section formed the basis of a paper I wrote that was presented at the International Union of Pure and Applied Chemistry (IUPAC) conference on the Characterisation of Porous Solids (COPS I) (see Unger *et al.* 1988). The two unequal rod arrangement was selected as an example of the geometric analysis required when using the MS-P method. The configuration does this well without being over complex, whilst it is also capable of illustrating the power of the MS-P method to workers in the field of porous materials. A copy of the paper (Mason, Morrow & Walsh 1988) is given in Appendix A. The experimental results have been updated here in the light of the new standard configuration curvature determination.

9.5.1. Theory

The arrangement of arc menisci between two unequal rods and a plate and the capillary rise profile as viewed through the glass plate are shown in Figure 9.17. Three dryside CAMs merge to form the MTM. The geometrical expressions for the effective area and perimeter of the meniscus are now more complex than discussed previously. The basic principal remains unchanged; application of simple geometric relations. The analysis presented below differs from that presented to IUPAC, but only in method, not result. The standard technique for analysing wedging systems had not been developed at the time of publication.

three DCAMs

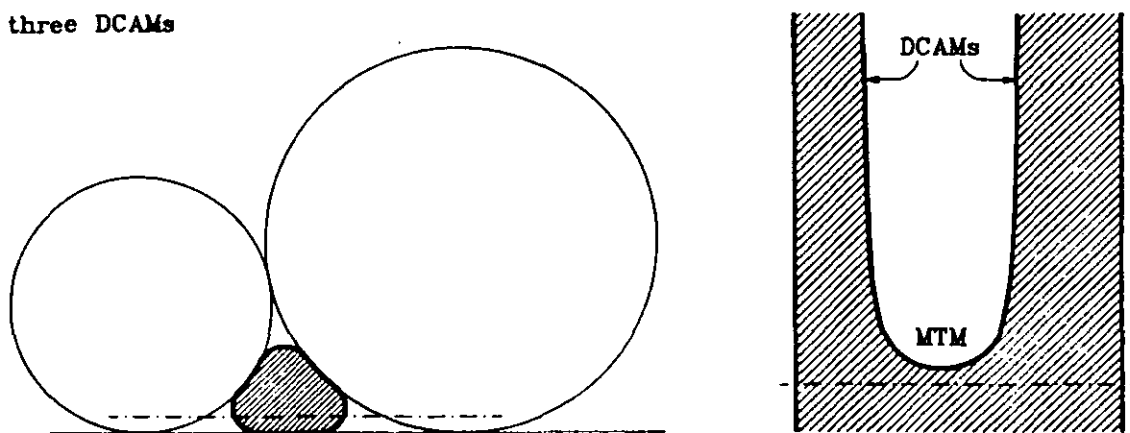


Figure 9.17 - Arrangement of the AMs for the MTM between two unequal rods and a plate. The effective area is shown hatched and the effective perimeter outlined. A schematic representation of the capillary rise profile, as viewed through the plate, is also shown.

Figure 9.18 shows the definition of terms and regions used to calculate the effective area and perimeter. Other nomenclature used follows that of chapter 6.

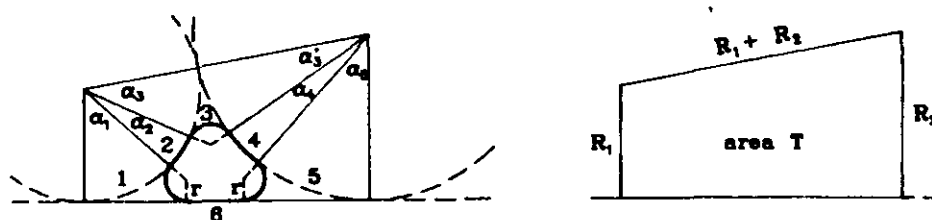


Figure 9.18 - Diagram showing the definition of angles, choice of regions and associated terminology used in the calculation of effective area and perimeter of a MTM in the two-unequal-rods-and-plate arrangement.

a) Angles

From Figure 9.18:

$$\alpha_1 = \arccos\left(\frac{R_1 - r}{R_1 + r}\right)$$

$$\alpha_2 = \gamma_1 - \alpha_1 - \alpha_3$$

$$\alpha_3 = \arccos\left(\frac{(R_1 + r)^2 + (R_1 + R_2)^2 - (R_2 + r)^2}{2(R_1 + R_2)(R_1 + r)}\right)$$

$$\alpha_3 = \arccos\left(\frac{(R_2 + r)^2 + (R_1 + R_2)^2 - (R_1 + r)^2}{2(R_1 + R_2)(R_2 + r)}\right)$$

Equations

$$\alpha_4 = \gamma_2 - \alpha_3 - \alpha_5$$

$$\alpha_5 = \arccos\left(\frac{R_2 - r}{R_2 + r}\right)$$

9.21

$$\gamma_1 = \arcsin\left(\frac{R_2 - R_1}{R_1 + R_2}\right)$$

$$\gamma_2 = \arccos\left(\frac{R_2 - R_1}{R_1 + R_2}\right)$$

b) Perimeters

$$P_1 = (\pi - \alpha_1)r$$

$$P_2 = \alpha_2 R_1$$

$$P_3 = (\pi - \alpha_3 - \alpha_3)r$$

Equations

$$P_4 = \alpha_4 R_2$$

9.23

$$P_5 = (\pi - \alpha_5)r$$

$$P_6 = (R_1 + R_2) \sin \gamma_2 - (R_1 + r) \sin \alpha_1 - (R_2 + r) \sin \alpha_5$$

c) Area

$$A_T = \frac{1}{2}(R_1 + R_2)^2 \sin \gamma_2$$

$$\begin{aligned}
 A_1 &= \frac{1}{2}((R_1 + r)^2 \sin \alpha_1 + (\pi - \alpha_1)r^2) \\
 A_2 &= \frac{1}{2}\alpha_2 R_1^2 \\
 A_3 &= \frac{1}{2}((R_1 + R_2)(R_1 + r) \sin \alpha_3 - (\pi - \alpha_3 - \alpha_3')r^2) \\
 A_4 &= \frac{1}{2}\alpha_4 R_2^2 \\
 A_5 &= \frac{1}{2}((R_2 + r)^2 \sin \alpha_5 + (\pi - \alpha_5)r^2)
 \end{aligned}
 \tag{9.23}$$

d) Effective Area and Perimeter

The effective perimeter, shown bold in Figure 9.18, is given by:

$$P_{eff} = \sum P_S + \sum P_L \tag{6.11}$$

and from Figure 9.18 $\sum P_S = P_2 + P_4 + P_6$ and $\sum P_L = P_1 + P_3 + P_5$. Hence,

$$P_{eff} = P_1 + P_2 + P_3 + P_4 + P_5 + P_6 \tag{9.24}$$

The effective area, shown hatched in Figure 9.18, is simply given by,

$$A_{eff} = A_T - A_1 - A_2 - A_3 - A_4 - A_5 \tag{9.25}$$

Equations 9.20 to 9.25 were written into the usual solution program together with the MS-P equation,

$$P_{eff}r - A_{eff} = 0 \tag{6.12}$$

Results were obtained as values of the normalised curvature, R_1/r , in terms of the rod radius ratio, R_1/R_2 . These are shown in graphical form as a continuous relationship on Figure 9.19 for rod radius ratios up to 11; the range for which experimental results were obtained.

9.5.2 Experimental

The experiments used the full range of rod sizes then available to give rod radius ratios up to eleven. Rods of nominal diameters, 1/32", 1/16", 5/64", 3/32", 1/8", 5/32", 1/4" and 5/16" were employed in pairs chosen to give heights of rise in the range 10 to 20 mm, the optimum range for the comparative method when isooctane is the test liquid. The experimental procedure closely followed that described in section 7.4, this arrangement presenting few specific problems in its own right.

9.5.2.1 Cell assembly

No new cells needed to be designed for this configuration, the existing cells (those made for the rod-in-a-corner) proved capable of accommodating the rods in position. The 30° and 110° cells proved particularly adaptable. Figure 9.14 showed a typical set up, with the rods in the 30° cell. The two test rods are pushed into the corner and against the plate by the larger rod positioned between the test rods and tightened clamping screws.

9.5.3 Results

As expected the results show exceptionally good agreement with the theory. The mean curvatures from twelve different rod radius ratios are shown compared to the theory on Figure 9.19. The results shown on the graph were obtained with gravity corrected heights of rise with equation 7.8, but they only show slight improvement over the uncorrected curvatures (a detailed breakdown is given in Appendix F). There is only a small improvement as heights of rise in the standard cells were always kept close to those in the test cells. All the experimental curvatures are slightly less than their theoretical counterparts, but most are within 1% and all within 1.5%. Note that some points have been plotted twice on Figure 9.19 as the radius ratio can be read as greater or less than unity.

That the experimental curvatures are lower than those obtained from the theory is consistent with dimensional errors in the pores, which always act to increase the size of the pores and so decrease the observed curvatures.

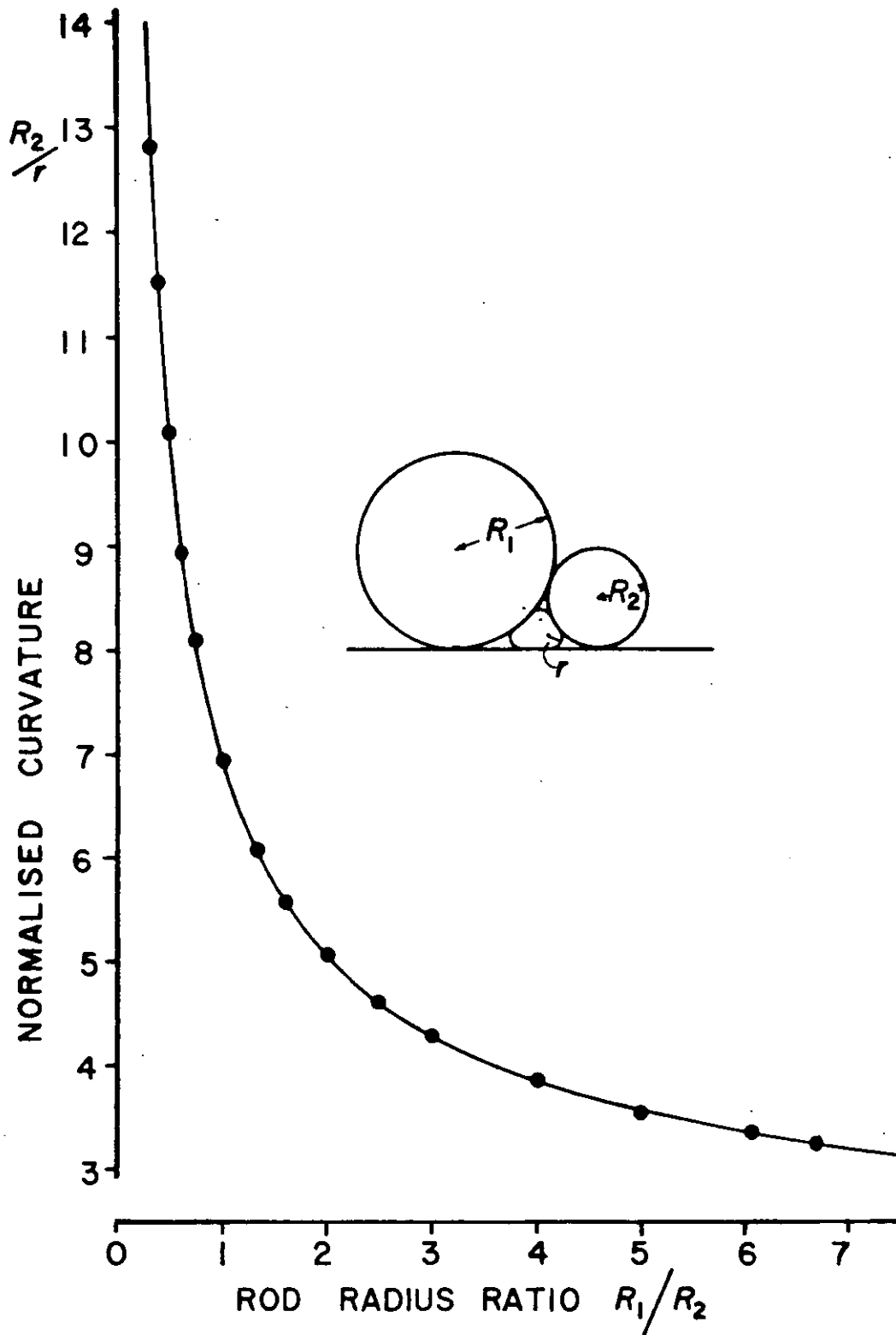


Figure 9.19 - Comparison of theoretical and experimental curvatures for the menisci formed in the pore space between two contacting unequal rods and a plate. The theoretical normalised curvature is shown as a continuous relationship in the rod radius ratio. The experimental results have been corrected for effects of gravity distortion.

CHAPTER 10

Investigations with non-zero contact angle

10.1 INTRODUCTION

The MS-P method has shown an impressive ability to predict meniscus curvatures in uniform pores containing a perfectly wetting liquid. In many real situations where the method may find application the liquid will not wet the solid surface. The future of the MS-P analysis therefore depends on it being shown to also predict curvatures when the liquid(s) only partially wets the solid.

Over the following pages a limited number of cases in which the effect of contact angle was investigated are presented. Allowing for the variation of contact angle increases the complexity of the theory as the AMs do not now meet the construction components tangentially. However, it is the complications in the experiments that present most difficulties for the MS-P method in these cases. The well known irreproducibility of contact angle makes the experiments considerably less precise, but there is no superior measure of wettability. The advantages of the metal construction components must be abandoned in favour of PTFE components which cannot be made as accurately and deform easily. Many of the benefits of the wetting liquid isooctane are also lost.

Previously published work involving the MS-P method and non-zero contact angle is limited to a study of the two equal rods and a plate arrangement (Nguyen 1980, see also Mason, Nguyen & Morrow 1983).

10.2 ONE ROD AWAY FROM A PLATE

The arrangement of a single rod spaced from a plate was studied under perfectly wetting conditions, the results of which were presented in section 9.3. It is difficult to think of a simpler geometry, but the wetting behaviour is far from simple. The capillary action of this arrangement when the contact angle of the liquid with the solid is varied shows a fascinating insight into the complex behaviour that can be expected in such systems, whilst the theory is kept simple.

10.2.1 Theory

The configuration of the AMs and most of the capillary profiles seen through the plate remain largely similar to that shown in Figure 9.6. Two back-to-back OAMs merge to form a TAM. The meniscus curvature between the rod and plate is still primarily decided by the size of the gap. At very small spacings the geometry resembles that of two parallel plates and the meniscus curvature is large. As the gap is enlarged the curvature falls off.

When the contact angle is increased from zero it would be expected that the curvature will decrease until, at 90° the curvature will be zero. The effects of spacing and contact angle should interact in an intriguing fashion. There is also the likelihood that the two back-to-back OAMs will contact, and so rupture, at some spacings and wettabilities.

The TAM possesses a plane of symmetry so only half the section needs to be considered. Figure 10.1 shows the definition of terms and regions used to obtain expressions for effective area and perimeter for the case where rod and plate are wetted with the same contact angle, θ . Other terminology follows that of chapter 6. Due to the complex trigonometry some of the analysis is afforded rather more detail than usual.

a) Subtended angle

Unfortunately the half angle subtended at the centre of the rod by the AMs can no longer be found from a simple trigonometric function. It can however be obtained from difference formula. Equating length A to length B (Fig. 10.1) yields;

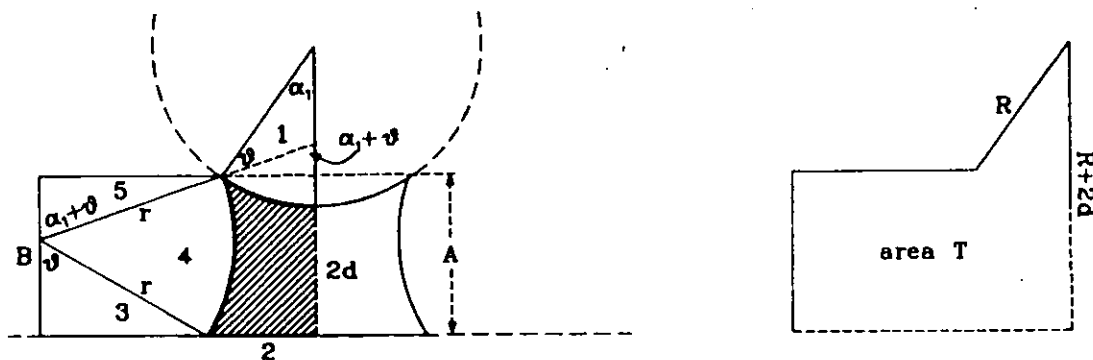


Figure 10.1 - Diagram showing the definition of angles, choice of regions and associated terminology used in calculating the effective area and perimeter of a meniscus in the gap between a rod and a plate when the contact angle is non-zero.

$$\frac{r}{R} = \frac{1 - \cos \alpha_1 + 2d/R}{\cos \theta + \cos(\theta + \alpha_1)} \quad 10.1$$

which can be rearranged to give;

$$(1 + r/R \cos \theta) \cos \alpha_1 - (r/R) \sin \theta \sin \alpha_1 = 1 + 2d/R - r/R \cos \theta$$

an equation of the form $A \cos x - B \sin x = C$, which may be written;

$$\sin(y - x) = \frac{C}{\sqrt{A^2 + B^2}} \quad \text{where} \quad \sin y = \frac{A}{\sqrt{A^2 + B^2}}$$

Inserting the relevant terms from 10.1 in the above yields;

$$\alpha_1 = \arcsin \left(\frac{(1 + r/R \cos \theta)}{\sqrt{(1 + r/R \cos \theta)^2 + (r/R \sin \theta)^2}} \right) - \arcsin \left(\frac{(1 + 2d/R - r/R \cos \theta)}{\sqrt{(1 + r/R \cos \theta)^2 + (r/R \sin \theta)^2}} \right) \quad (10.2)$$

b) Perimeters

The perimeters of the regions bordering on the meniscus section are as follows:

$$P_1 = \alpha_1 R$$

$$P_2 = R \sin \alpha_1 + (\sin(\alpha_1 + \theta) - \sin \theta) r \quad \text{Equations 10.3}$$

$$P_4 = (\pi - \alpha_1 - 2\theta) r$$

c) Areas

The areas of the regions required to define the effective area given below.

$$\begin{aligned}
 A_T &= \frac{r^2}{4} \sin 2\alpha_1 + (r \sin(\alpha_1 + \theta) + R \sin \alpha_1)(R(1 - \cos \alpha_1) + 2d) \\
 A_1 &= \alpha_1 R^2 / 2 \\
 A_3 &= (\sin 2\theta)r^2 / 4 && \text{Equations 10.4} \\
 A_4 &= (\pi - \alpha_1 - 2\theta)r^2 / 2 \\
 A_5 &= (\sin(2(\alpha_1 + \theta)))r^2 / 4
 \end{aligned}$$

d) Effective area and perimeter

Using equations 10.2 to 10.4 the area and perimeter of the TAM may be defined. The effective perimeter, shown bold in Figure 10.1, is given by;

$$P_{eff} = \sum P_S \cos \theta + \sum P_L \quad (6.11)$$

Note the modified solid perimeter term. Hence from Figure 10.1;

$$\sum P_S = (P_1 + P_2) \cos \theta \quad \text{and} \quad \sum P_L = -P_4$$

Note the negative sign due to the open AMs, hence;

$$P_{eff} = (P_1 + P_2) \cos \theta - P_4 \quad (10.5)$$

The effective area, shown hatched in Figure 10.1, is simply given by;

$$A_{eff} = A_T - A_1 - A_3 - A_4 - A_5 \quad (10.6)$$

e) Solution of equations

In addition to equations 10.1 through 10.5 the MS-P equation,

$$P_{eff}r - A_{eff} = 0 \quad (6.12)$$

also applies. These equations were entered into the solution program. Curvature and spacing were normalised, as under wetting conditions, by the half the rod-plate gap, d . The program was modified to give results as normalised curvature, R/r , in terms of either the normalised spacing, d/R , or the contact angle, θ . It is capable of generating curvatures for the full range of d/R at a specified θ or the full range of θ at a specified d/R . The point at which the OAMs meet back-to-back is also given by the program.

The extra variable leads to the need for a three dimensional graph to show all the results. For a fixed rod spacing the curvature varies approximately as the cosine of the contact angle leading to the surface shown on Figure 10.2. At large spacings and/or contact angles the AMs interfere back-to-back and the surface cuts off abruptly (dotted lines). Note that for contact angles greater than 90° exactly the same shape of surface

will be seen. However, it will be the mirror image of that on Figure 10.2 with the curvatures negative, reflecting the capillary depressions that would be seen in practice.

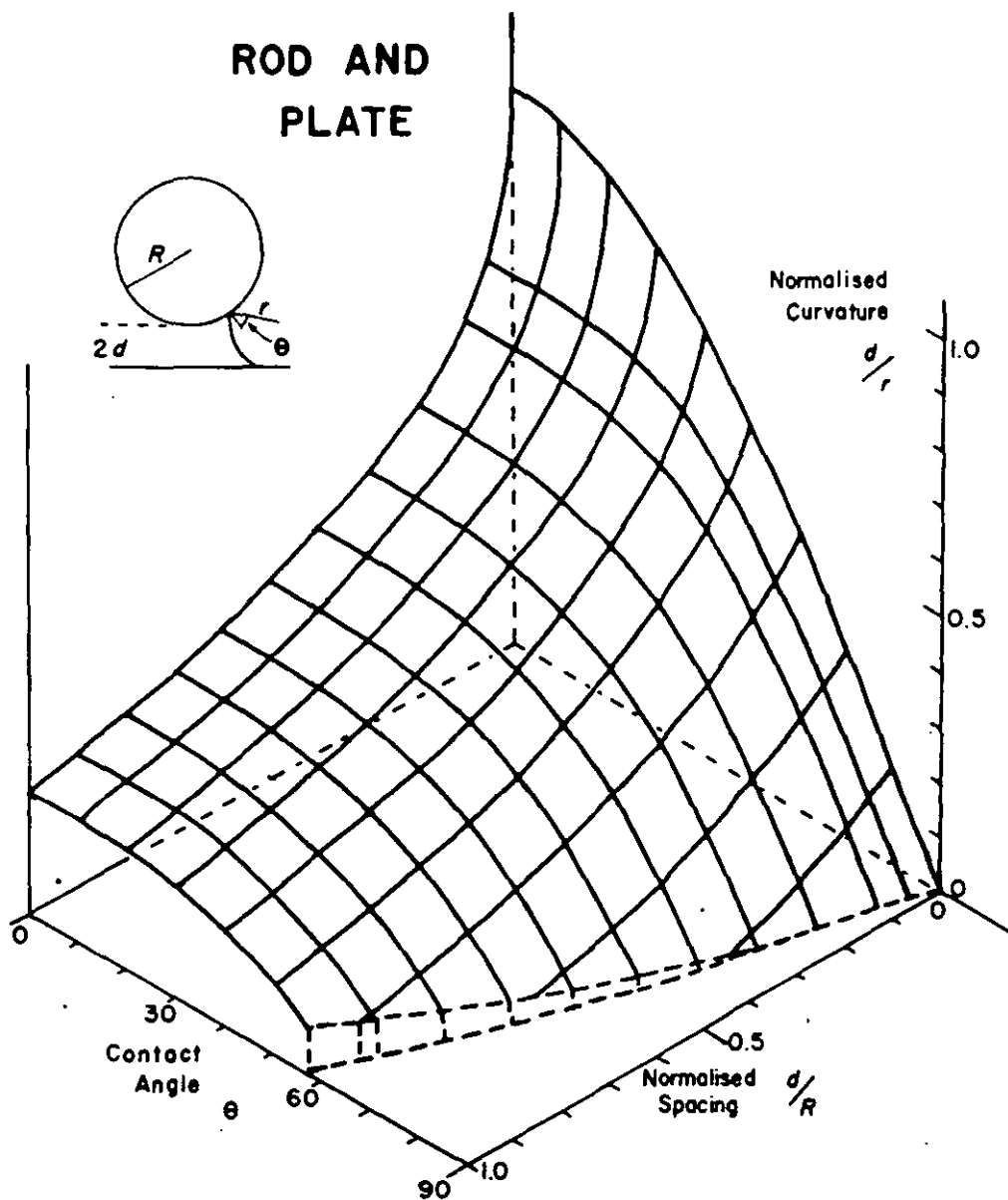


Figure 10.2 A three-dimensional graph showing the effect on the TAM's theoretical curvature of changes in rod-plate spacing and contact angle. The dotted lines mark the points beyond which the TAM cannot exist as the WOAMs meet back-to-back.

10.2.2 Experimental

Capillary rise experiments at non-zero contact angle are much more time consuming than the wetting experiments. For this reason verification of the theory over the entire surface shown on Figure 10.2 could not be justified. In the end the time allowed just one

rod spacing to be investigated at $d/R = 0.1$. An 1/8" diameter teflon rod was used with 12.5 thou shims as spacers. Various liquids were used to vary the contact angle. Heights of rise were in the range 5 to 15 mm depending on the test liquid. The physical properties of the test liquids were given in Table 7.1, section 7.3.2. The apparatus employed for the wetting experiments was re-used for this examination (see section 9.3). The experimental procedures had to be altered considerably for the non-wetting tests and are detailed below.

10.2.2.1 Cell assembly

The cell designed specifically for the single-rod-and-plate arrangement proved a satisfactory design for these experiments (see Fig. 9.8). The components differed only in respect of the steel rod, which was exchanged for a teflon rod. A piece of fully fluorinated transparent plastic sheeting was inserted between the glass plate and the front face of the cell to make the pore one of uniform wettability.

The sheet needed to be stretched flat over the front face. With the cell dismantled double-sided sticky tape was stuck to the front face around the machined channel. The transparent sheet was then stuck over the tape. Ensuring that sheet stuck on properly, with no sagging or wrinkling, was a delicate operation. The New Mexico Institute of Technology, who supplied the sheet, had also sent the sheet in self-adhesive form. However problems were encountered owing to the thickness of the adhesive. Under the pressure of the clamping screws the "flat" surface slowly became indented at points of contact between shims and plate, leading to spacings less than specified.

The above points aside, the cell was assembled according to the procedure detailed in section 9.3, but now extra care was required when clamping the rod in position. Teflon rods are flexible and easily deformed which made the task of assembling a pore of uniform geometry very difficult. Inevitable wrinkling of the sheet and bending of the rod contributing most heavily to the non-uniformity.

10.2.2.2 Measurement of capillary rise

Initial experiments with the pore showed considerable variation in height of rise along the pore length. There being no way of directly checking the pore geometry once the cell had been assembled an indirect method of ensuring correct geometry was required. A satisfactory method was arrived at by a process of intuitive trial-and-error. It amounts to a "fixing" of the pore geometry.

For the purposes of the experiments it was assumed that isooctane wets the teflon surfaces perfectly under receding conditions. The MS-P theory predicts virtually identical curvatures (equal to four decimal places) for contact angles of 0° and at isooctane's receding angle of 4.6° . Now, with the rod held only loosely against the plate with hardly any pressure on the rod, measurements of the height of rise of the TAM were

taken at 2 mm intervals between the shims. If calculated curvatures were mostly falling below the theoretical value the implication was that the spacing was too large and the screws would be tightened accordingly. Any gradual shift from top to bottom implied one clamping screw required more tightening than the other.

Heights of rise were re-measured and the process repeated until at least a 1.5 cm section of the pore gave curvatures within 1% of the theoretical value. This prediction has been validated by the wetting experiment. If no satisfactory section was found the cell was dismantled and the rod and sheet replaced. In practice this technique worked well, although it could be tiresome.

Having at least a section of pore authenticated was not the end of the problems. Before a test^{of} one of the liquids could be conducted the residual isooctane in the cells, left behind in wedges in the corners etc. after the pore validation, had to be removed. The cell obviously could not be dismantled or roughly handled. A suitable method was to pass compressed air (with the dust and dirt removed by a compact inline filter) through the fluid system. The main reservoir was removed and the air line connected to the system tubing. After a few minutes all the isooctane evaporates.

The procedure developed for the measurement of "recently advancing" and "recently receding" heights of rise for each test liquid is as follows.

(i) The main reservoir laboratory jack is lowered well below the cells. The test liquid is poured into the reservoir which is then raised by hand until the TAM rises to a level just below that of the authenticated section. The height of the jack is adjusted to maintain the meniscus in roughly this position and the system left to stabilise. The time taken increased with the liquids' viscosities. The more viscous liquids taking up to 1/2 an hour to equilibrate.

(ii) The main reservoir is removed from the jack and held below the level of the cells until the TAM has receded by about 1 cm when it is replaced on the jack. Which is raised a couple of millimetres so that the TAM settles at the bottom of the test section.

(iii) Once the system has come to equilibrium the heights of rise of the advanced TAM and of the meniscus in the standard are measured. These levels are checked several times over a five minute period to confirm the equilibrium.

(iv) The lab jack is raised by about 2 mm and the level of the TAM lowered well below the test section by hand.

(v) Steps (iii) and (iv) are repeated until the top of the authenticated section is reached.

(vi) The reservoir is now held aloft forcing the TAM to rise well above the authenticated section and the main reservoir lab jack is lowered a few mm so that the TAM will still settle around the top of the test section despite its greater height of rise when receding.

(vii) Once the system has settled the heights of rise of the receded menisci are measured.

(viii) The jack is lowered by about 2 mm and the level of the TAM raised well above the test section by hand.

(ix) Steps (vii) and (viii) are repeated until the bottom of the authenticated section is reached.

It is important to measure advancing height first while the rod and plate above the TAM are dry. When wet they encourage the liquid to spread resulting in lower contact angles.

Unlike isooctane the other test liquids are not highly volatile and thus cannot easily be evaporated from the system. So the cells had to be dismantled, cleaned, reassembled and re-authenticated before the next liquid could be investigated. The sheeting and rod were replaced for each liquid.

These experiments also required additional safety precautions as most of the liquids are classified as either "harmful" or "toxic". Leakage was more of a problem as the liquids no longer evaporated from cell joins, but collected in puddles around the cell blocks. The Sellotape and transparent sheet acted as a seal on the front face of the test cell. The other cells were equipped with strips of PTFE tape in-between their front faces and glass plates.

10.2.3 Results

The experimental results are shown compared to the MS-P theory predictions on a graph of normalised curvature, d/r , against the contact angle, θ (Figure 10.3). When compared to the corresponding results for the arrangement under perfectly wetting conditions, Figure 9.10, the agreement with the theory is poor. However if the problems with pore geometry and the well known irreproducibility of contact angle are taken into account the results are not as bad as they at first appear. The general trend predicted by the theory is followed. A detailed breakdown of the results can be found in Appendix G. The curvatures were calculated using both the simplified comparative method (equation 7.7) and from the physical properties of the test liquids (units in mm);

$$C_p = \frac{2(h + 0.5)d}{a^2} \quad (10.7)$$

The results from both equations were generally in close agreement (within 2%), indicating the validity of the comparative method.

Generally the value of the capillary constant, a^2 , obtained from the height of rise in the standard cell was slightly greater than that obtained from physical constants. Exceptions were the two liquids with the highest contact angles, hexachlorobutadiene and α -bromonaphthalene, which gave lower values of a^2 than those from the liquid properties. The implication is that wetting conditions do not prevail in the standard cell. The results from equation 10.7 are plotted on Figure 10.3 for these liquids, others were obtained from the comparative method.

The points displayed on Figure 10.3 represent the mean curvatures, obtained from measurements taken at, at least, four levels in the pore. The range of curvatures obtained is shown by the vertical limits. Most of these come close to or intercept the theoretical curve. The variation found, up to ± 0.2 around the mean curvature, can be explained by contact angle variations. Dimensional errors were predetermined by the method of testing with isooctane and set within ± 0.05 ($\pm 1\%$) of the theory.

The magnitude of the advancing and receding angles used for the analysis were determined from Morrow's (1974) empirical equations. For three of the test liquids Morrow published the raw data used to calculate the arithmetic average contact angles that were in turn, employed to determine the empirical equations. The standard deviations of his results are also shown by the horizontal limits on Figure 10.3 (if maximum and minimum angles were shown the limits would be almost twice the width apart). Morrow's data (obtained from capillary rise in cylindrical tubes) shows mostly similar variations to those encountered here. Generally, it is the advancing angles that are the more reproducible.

Bearing the above limits in mind, it appears that much of the data confirms the MS-P theory rather well for the single-rod-and-plate arrangement at non-zero contact angle. Notable exceptions are for n-dodecane receding ($\theta = 22.8^\circ$) and α -bromonaphthalene advancing ($\theta = 83.2^\circ$) which both give large errors from their theoretical curvatures. The non-attainment of the specified contact angles that these results imply may have arisen from contamination of the test liquids or pore surfaces.

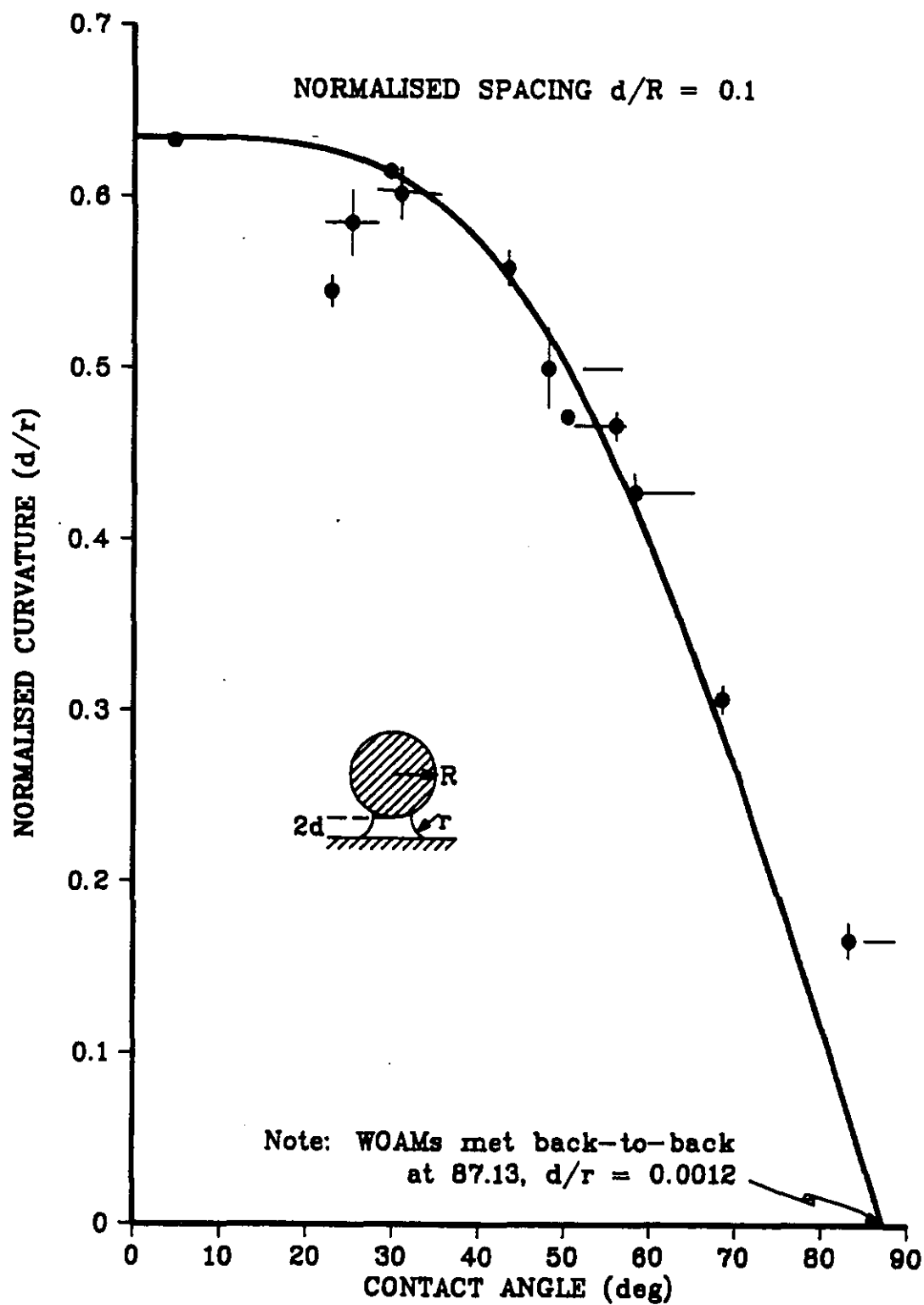


Figure 10.3 - Experimental results for curvature obtained from capillary rise experiments with a partially wetting rod and plate. The results, at a normalised space of 0.1, are not as good as those obtained under perfectly wetting conditions due to the irreproducibility of contact angles (shown by the horizontal limits). Variations in curvature found by the experiments are shown by the vertical limits.

10.3 TWO EQUAL RODS AND A PLATE

The arrangement of two rods and a plate containing a perfectly wetting liquid has been extensively investigated, and is discussed elsewhere (see chapter 8, section 9.5 and Appendix A). A MS-P study of the case of two equal rods and a plate with only partially wetting liquids has been studied by Nguyen (1980) (see also Mason, Nyugen & Morrow 1983) This formed the starting point for this present work. The arrangement was re-investigated with the dual aims of developing a procedure for the analysis of partially wetted systems and to hopefully improve upon Nyugen's results. The experiments presented below were conducted before those on the geometrically simpler, single rod and plate arrangement discussed in the preceding section.

The arrangement can also be assembled with mixed wettability by making either (or both) of the rods or plate wetted. The mixed wettability system was subject to a tentative investigation by Ashton and Cable (1985), but only a portion of the theory was derived and very little experimental data collected. The study of mixed wettability systems extends the bounds of the MS-P method further and enlarges the range of applications to which the method can be applied.

The theory for all cases of mixed wettability is presented below and later experiments are discussed for the cases of two partially wetted rods and one and two perfectly wetted rods against a partially wetted plate.

10.3.1 Theory

The arrangement of AMs and the general shape of the capillary profiles seen through the transparent plate remain largely unchanged from those shown earlier; Figure 9.17. The AMs will not now meet partially wetted solid surfaces tangentially, but at an angle, θ ; the contact angle. As wettability of the pore decreases the profile becomes noticeably flatter (curvature will fall), until at $\theta = 90^\circ$ the AMs can no longer form in partially wetted corners.

Since mixed wettability systems were to be studied the expressions for effective area and perimeter were derived to allow for different contact angles on each pore construction component surface. Figure 10.4 shows the definition of terms and regions used in the analysis. The theory is now considerably more complex than that of the wetted system. Solution of the equations requires two iterations, one as before, for the radius of curvature and a second for the angle subtended by the AM between the two rods.

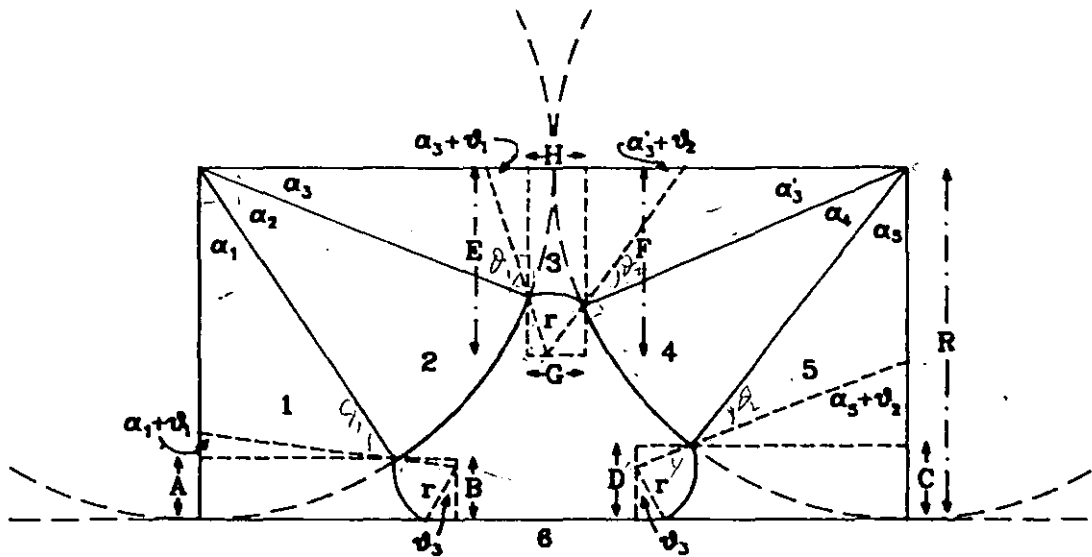


Figure 10.4 - Diagram showing the definition of lengths and angles, choice of regions and associated terminology used in calculating the effective area and perimeter of MTM in the pore space formed between two equal rods and a plate. The rods and plate all exhibit different contact angles allowing the study of mixed wettability arrangements.

a) Lengths

$$A = B \Rightarrow \frac{r}{R} = \left(\frac{1 - \cos \alpha_1}{\cos \theta_3 + \cos(\alpha_1 + \theta_1)} \right) \quad (10.8)$$

$$C = D \Rightarrow \frac{r}{R} = \left(\frac{1 - \cos \alpha_5}{\cos \theta_3 + \cos(\alpha_5 + \theta_2)} \right) \quad (10.9)$$

$$E = F \Rightarrow \frac{r}{R} = \left(\frac{\sin \alpha_3' - \sin \alpha_3}{\sin(\alpha_3 + \theta_1) + \sin(\alpha_3' + \theta_2)} \right) \quad (10.10)$$

$$G = H \Rightarrow \frac{r}{R} = \left(\frac{2 - \cos \alpha_3 - \cos \alpha_3'}{\cos(\alpha_3 + \theta_1) + \cos(\alpha_3' + \theta_2)} \right) \quad (10.11)$$

b) Angles

From equations 10.8 to 10.11 combined with difference formula:

$$\alpha_1 = \arctan \left(\frac{(1 + (r/R) \cos \theta_1)}{(r/R) \sin \theta_1} \right) - \arcsin \left(\frac{(1 - (r/R) \cos \theta_3)}{\sqrt{(1 + (r/R) \cos \theta_1)^2 + ((r/R) \sin \theta_1)^2}} \right) \quad (10.12)$$

$$\alpha_5 = \arctan\left(\frac{(1 + (r/R)\cos\theta_2)}{(r/R)\sin\theta_2}\right) - \arcsin\left(\frac{(1 - (r/R)\cos\theta_3)}{\sqrt{(1 + (r/R)\cos\theta_2)^2 + ((r/R)\sin\theta_2)^2}}\right) \quad (10.13)$$

$$\alpha_3 = -\arctan\left(\frac{(r/R)\sin\theta_1}{(1 + (r/R)\cos\theta_1)}\right) + \arcsin\left(\frac{(\sin\alpha_3 + (r/R)\sin(\alpha_3 + \theta_2))}{\sqrt{(1 + (r/R)\cos\theta_1)^2 + ((r/R)\sin\theta_1)^2}}\right) \quad (10.14)$$

α_3 and α_3' must be found by iteration from equations 10.11 and 10.14.

$$\alpha_2 = \pi/2 - \alpha_1 - \alpha_3 \quad (10.15)$$

$$\alpha_4 = \pi/2 - \alpha_5 - \alpha_3' \quad (10.16)$$

c) Perimeters

$$P_1 = \pi - (\alpha_1 + \theta_1) - \theta_3$$

$$P_2 = \alpha_2 R$$

$$P_3 = \pi - (\alpha_3 + \theta_1) - (\alpha_3' + \theta_2)$$

Equations

$$P_4 = \alpha_4 R$$

10.17

$$P_5 = \pi - (\alpha_5 + \theta_2) - \theta_3$$

$$P_6 = (2 - \sin\alpha_1 - \sin\alpha_5)R + \{\sin(\alpha_1 + \theta_1) + \sin(\alpha_5 + \theta_2) - 2\sin\theta_3\}r$$

d) Areas

$$A_T = 2R^2$$

$$A_1 = \frac{R^2}{4}\sin 2\alpha_1 + r\{\cos(\alpha_1) + \theta_1 + \cos\theta_3\}\{R\sin\alpha_1 + r\sin(\alpha_1 + \theta_1)\}$$

$$- \frac{r^2}{4}\{\sin 2(\alpha_1 + \theta_1) + \sin 2\theta_3 + 2(\pi - (\alpha_1 + \theta_1) - \theta_3)\}$$

$$A_2 = \frac{R^2}{2}\alpha_2$$

Equations

$$A_3 = \frac{R^2}{4}(\sin 2\alpha_3 + \sin 2\alpha_3') + R\{2 - \cos\alpha_3 - \cos\alpha_3'\}\{R\sin\alpha_3 + r\sin(\alpha_3 + \theta_1)\}$$

$$- \frac{r^2}{4}\{\sin 2(\alpha_3 + \theta_1) + \sin 2(\alpha_3' + \theta_2) + 2(\pi - (\alpha_3 + \theta_1) - (\alpha_3' + \theta_2))\}$$

$$A_4 = \frac{R^2}{2} \alpha_4 \quad (10.18)$$

$$A_5 = \frac{R^2}{4} \sin 2\alpha_5 + r \{ \cos(\alpha_5 + \theta_2) + \cos \theta_3 \} \{ R \sin \alpha_5 + r \sin(\alpha_5 + \theta_2) \} \\ - \frac{r^2}{4} \{ \sin 2(\alpha_5 + \theta_2) + \sin 2\theta_3 + 2(\pi - (\alpha_5 + \theta_2) - \theta_3) \}$$

e) Effective area and perimeter

The effective perimeter, shown outlined on Figure 10.4, of the mixed wettability system is given by;

$$P_{eff} = \sum_{i=3}^{i=1} P_S \cos \theta_i + \sum P_L \quad (6.11)$$

and from Figure 10.4;

$$P_{eff} = P_2 \cos \theta_1 + P_4 \cos \theta_2 + P_6 \cos \theta_3 + P_1 + P_3 + P_5 \quad (10.19)$$

The effective area, shown hatched, is simply the area of the whole rectangle formed by the rod centres and the plate less the area of the regions it contains:

$$A_{eff} = A_T - A_1 - A_2 - A_3 - A_4 - A_5 \quad (10.20)$$

f) Solution of equations

The above expressions for the effective area and perimeter were written into the standard solution program together with the MS-P equation,

$$P_{eff} r - A_{eff} = 0 \quad (6.12)$$

Alterations were made to enable normalised meniscus curvature, R/r , to be iterated in terms of the pore components' contact angles, θ 's (see Appendix H). The second iteration, for α_3 and α_5 , was also achieved by successive bisection; the equations showing rapid convergence.

The effect of contact angle on the two equal rods and plate arrangement when all, some or none of the perimeter is perfectly wetted is illustrated by the curves shown on Figure 10.5. A total of six curves are shown. As the number of partially wetted components increases the curvature at a given contact angle decreases. The curves show that a partially wetted plate contributes more to the reduction in curvature than does a partially wetted rod, reflecting the larger meniscus perimeter against the plate.

10.3.2 Experimental

Experiments were conducted on three of the systems shown on Figure 10.5, all with a partially wetted plate. The instances where both, one or neither of the rods are partially wetted were investigated. Steel drill blanks of 1/8" diameter were employed as wetted elements, whilst 1/8" diameter teflon rods were used for the partially wetted rods.

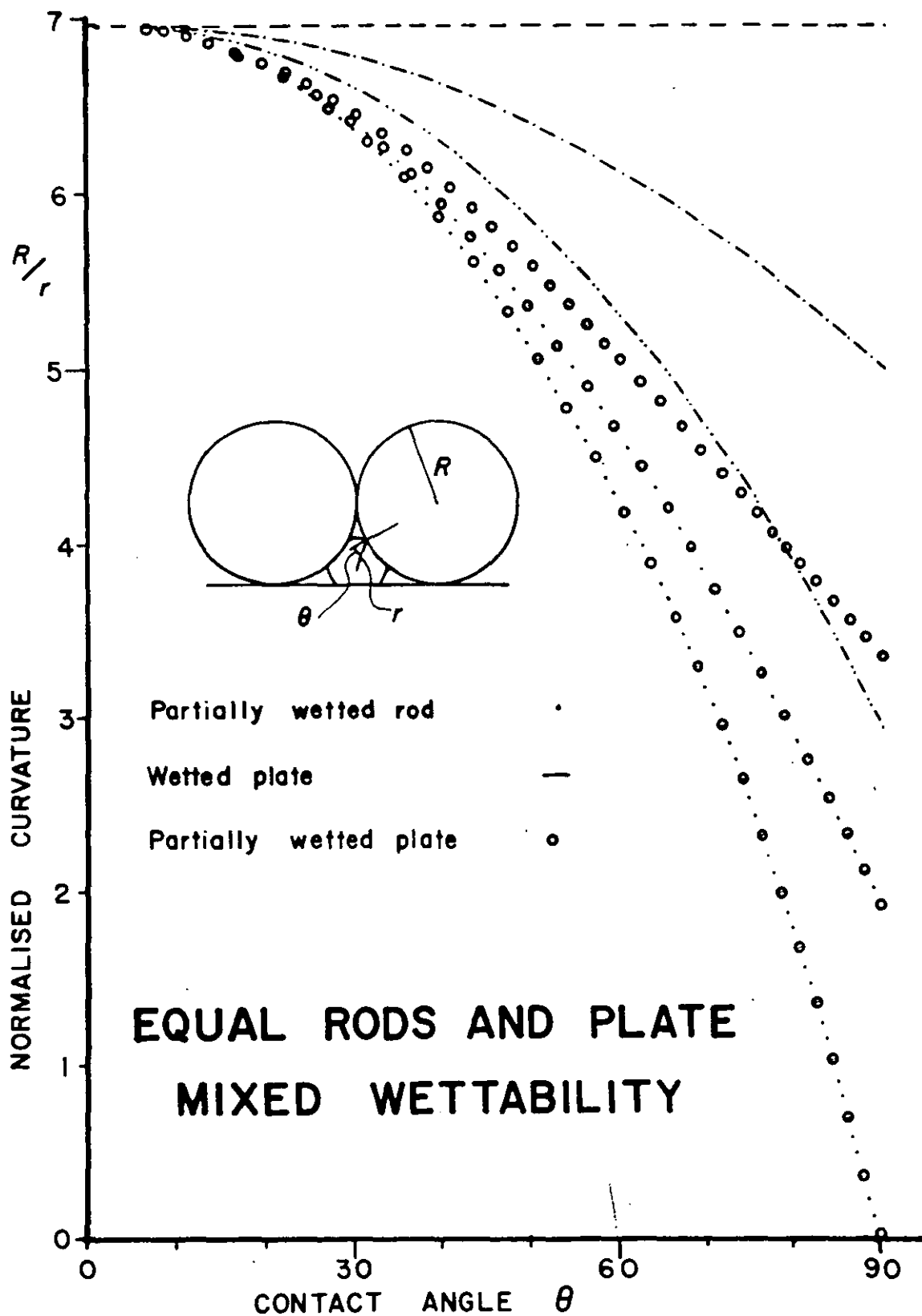


Figure 10.5 - Graph illustrating the effect of contact angle on theoretical curvature in the two-equal-rods-and-plate arrangement when all, some or none of the perimeter is wetted by the liquid. Each of the six curves refers to a different combination of wetted and partially wetted components. Note that the effect of a partially wetted plate is greater than that of a partially wetted rod owing to its larger wetted perimeter

The rods partially supported one another which made assembling this apparatus easier than that of the rod separated from a plate. The test liquids used for the single-rod-and-plate arrangement (see Table 7.1) were used.

The apparatus was identical to that used for the wetted system; described in section 9.5. The rods were clamped against the plate in rectangular channels. A fluorinated transparent sheet was inserted between the rods and glass plate as described in section 10.2. Greater care had to be taken when clamping the screws to avoid deformation of the geometry. The procedures described in section 10.2 were followed when validating the geometry of the pore and for measuring the heights of rise of advancing and receding menisci.

Readings for the two mixed wettability arrangements were taken together. The dual cell blocks then contained the two test cells, a standard cell and only one reservoir indicator cell. The confidence in the experimental technique was sufficient by this time.

10.3.3 Results

The data obtained from the experiments on the three arrangements are displayed on Figures 10.6 through 10.8. The scatter of points is markedly worse than that for the perfectly wetted system, but the general trend predicted by the theory is followed. Together the sets of results are encouraging as they show remarkably similar errors from the theory, indicating that the contact angles were reproduced quite well from arrangement to arrangement. The single-rod-away-from-a-plate results also largely confirm this finding.

A detailed breakdown of the results can be found in Appendix H. Curvatures shown on the figures are arithmetic averages of results for the most part determined from the simplified comparative method. Exceptions were those readings pertaining to the viscous liquids hexachlorobutadiene and α -bromonaphthalene where the steel rods were not thought to be perfectly wetted. These curvatures were obtained from equation 10.7, using the physical constants of the liquids.

All the heights of rise were corrected for the height of rise in the indicator cell. The value used was that obtained for isooctane in pores made up from two wetted rods and a plate. The 0.5 mm correction is unlikely to be numerically correct for the other liquids, particularly the more viscous ones. Strictly speaking the experiments of chapter 8 should have been repeated for each of the liquids in each of the partially wetted systems under both advancing and receding conditions. However, bearing in mind the large variation in contact angles this would not have dramatically improved results. Indeed experiments conducted with hexachlorobutadiene receding in differently sized pores made up from two steel rods and a plate produced a value for the rise in the indicator cell of 0.3 mm

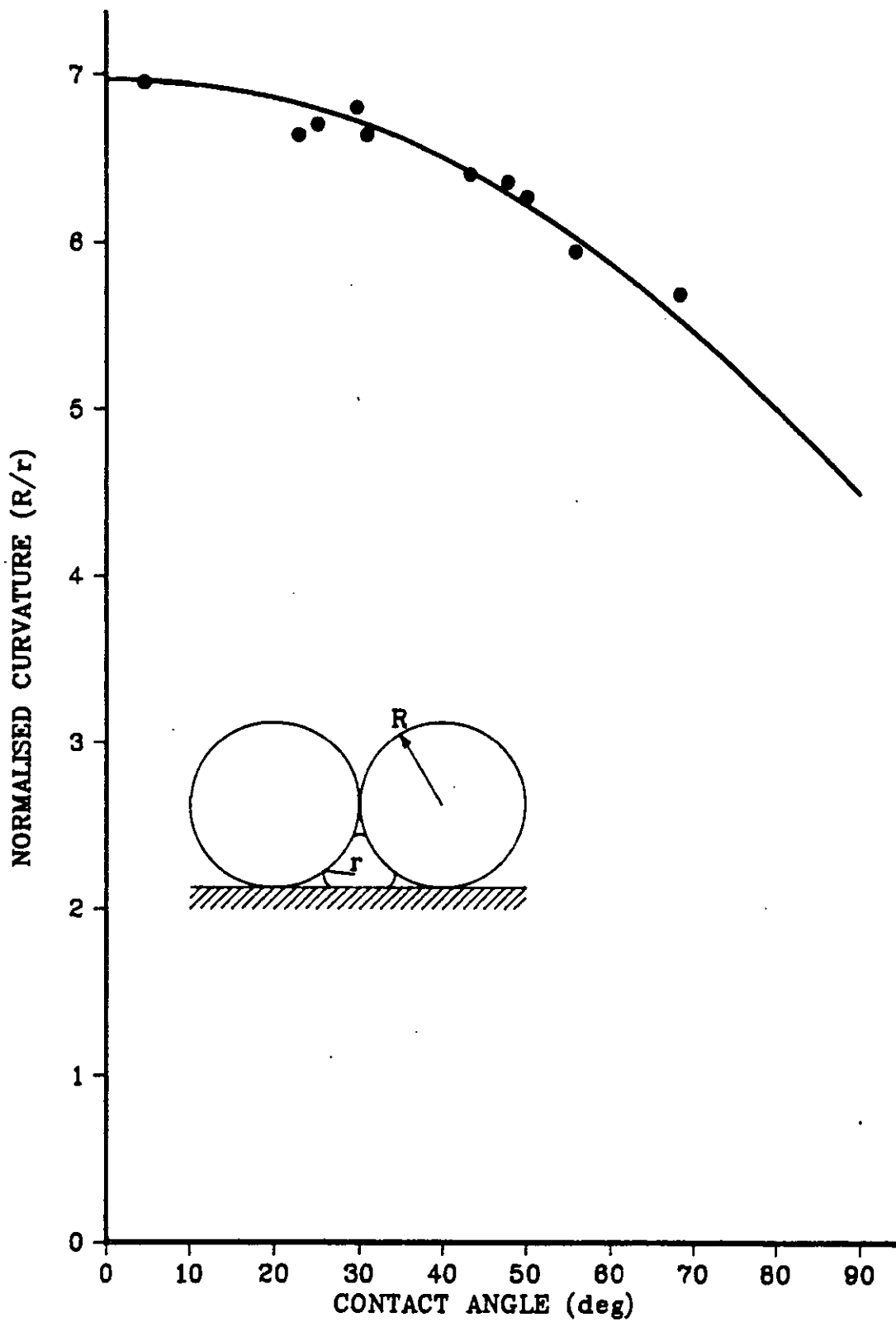


Figure 10.6 - Experimental results for curvatures in terms of the solid/liquid contact angle in a mixed wettability arrangement of two perfectly wetted rods and a partially wetted plated.

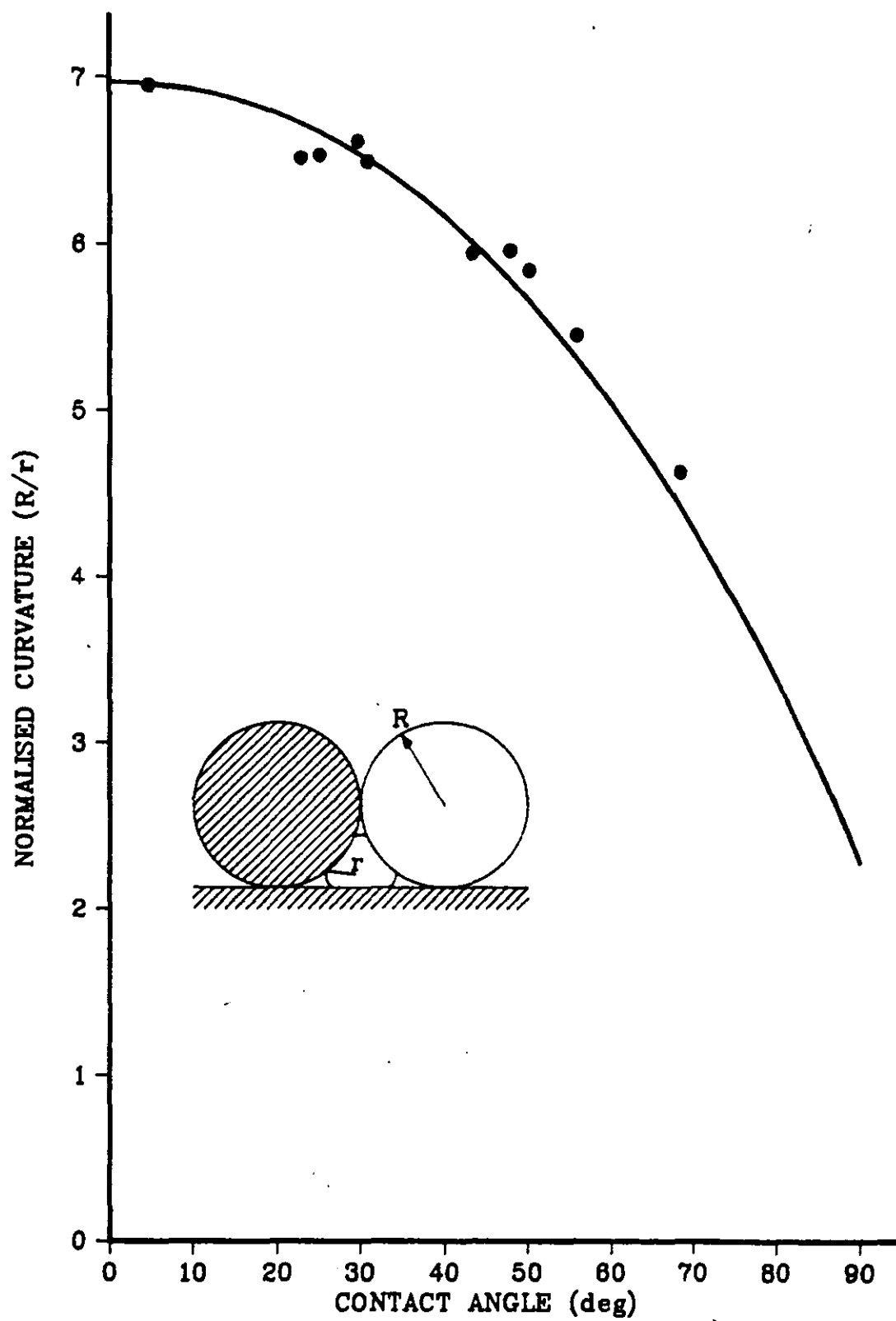


Figure 10.7 - Experimental results for curvatures in terms of the contact angle in a mixed wettability arrangement of one perfectly wetted rod and a partially wetted rod and plate.

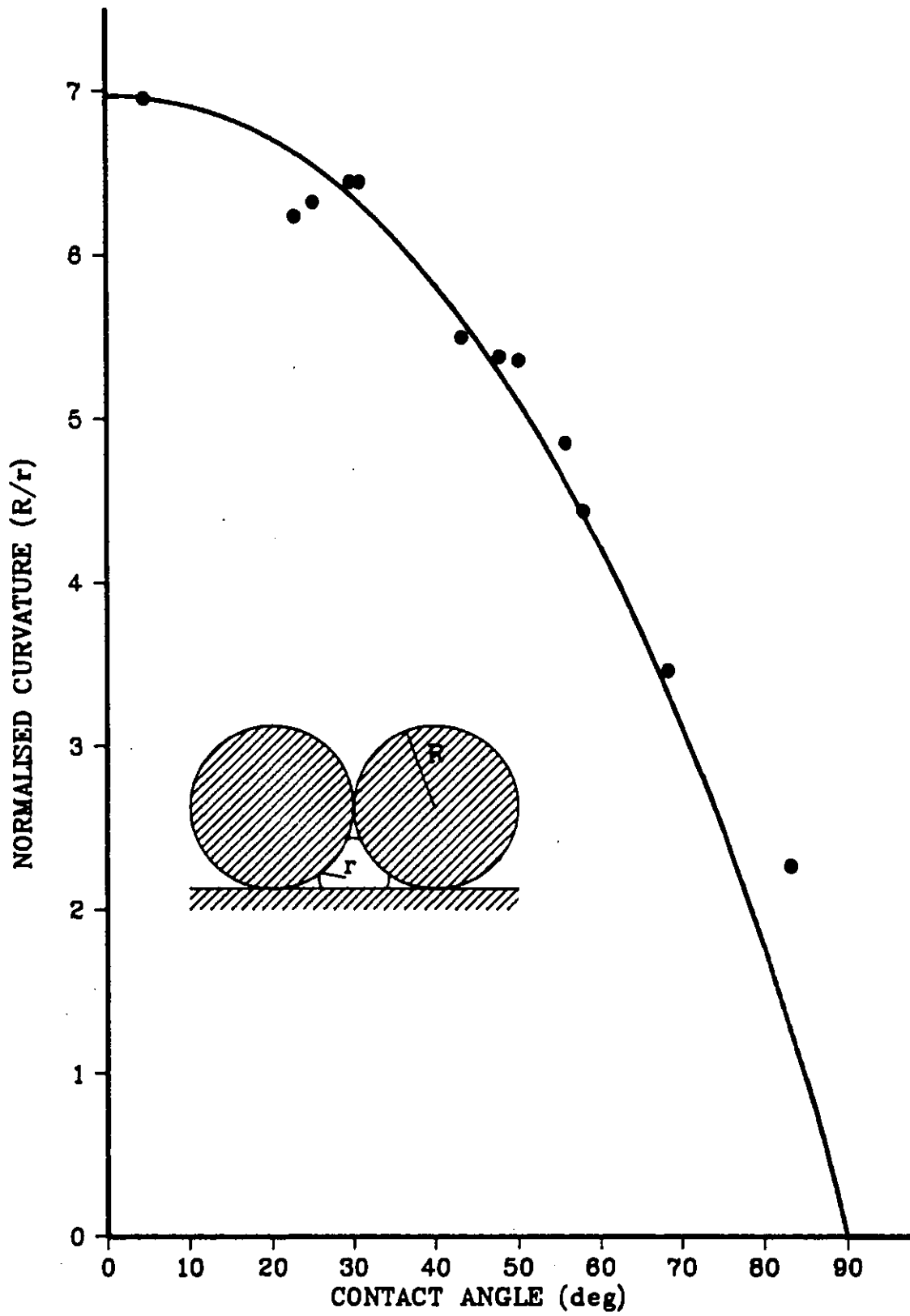


Figure 10.8 - Experimental results for curvatures in terms of the contact angle in a fixed wettability arrangement of two partially wetted equal rods and a plate.

(Ashton and Cable 1985; the only partially wetting liquid they studied). Under advancing conditions this is likely to be even lower. Application of this result changes the curvature by less than the experimental error.

The deviations of the observed curvatures from the theory are consistent with the majority of the experimental error arising from contact angles, the geometrical error having been preset by testing with wetting isooctane. The two wetted rod arrangement, with the smallest partially wetted perimeter, shows better agreement than does the two partially wetted rod system. The spread of curvatures observed at each contact angle is also noticeably less with the wetted rod arrangement.

CHAPTER 11

Investigations with neighbours: three rods and a plate

11.1 INTRODUCTION

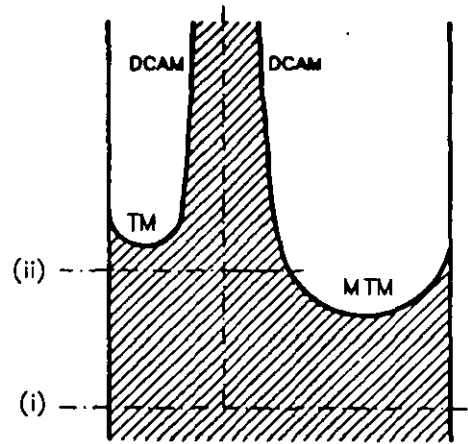
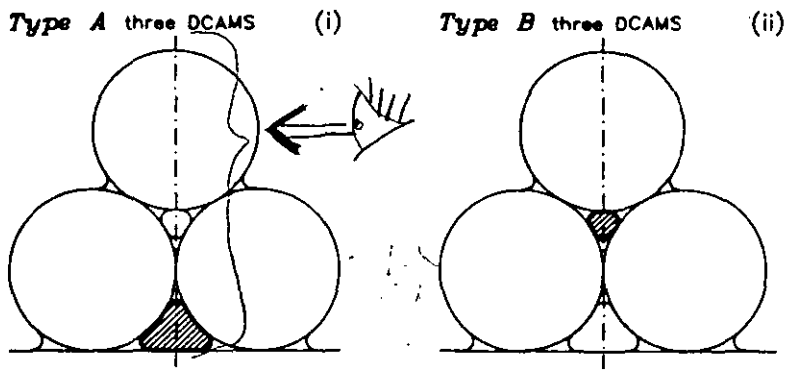
Two separate tubular pores, each bound by two rods and a plate, are formed when three rods are aligned touching a plate. If the outer rods are pushed together so that only the middle rod loses contact with the plate, the two pores become interconnected, giving a pore doublet. Upon further pushing together of the rods a capillary surface in the system will eventually come to regard the geometry as a single pore. As the rods are moved still closer together the system again becomes a pore doublet, until when the outer rods touch, two entirely independent pores are formed, one bounded by three rods and the other by two rods and a plate. When the geometry gives rise to pore doublets the properties of each pore are interrelated and the meniscus behaviour in one neighbouring pore may be dependent on the behaviour in the other. This system yields not one, but a whole family of different terminal menisci. In addition to the described variation in the outer rod separation the rods can be of equal or unequal sizes. All the above possibilities are examined with the MS-P method. It is this analysis of the different menisci and their interaction together, combined with extensive experimental confirmation, that has been the greatest test, to date, of the MS-P method.

Some of the terminal menisci that may exist between three rods and a plate have been partially studied in the past (and some already in this study) by authors such as Mayer & Stowe (MS-), Princen (P), Dodds (1978) and Mason & Morrow (1987). Over the following pages the MS-P analyses and experimental results from four different rod size arrangements are presented and discussed.

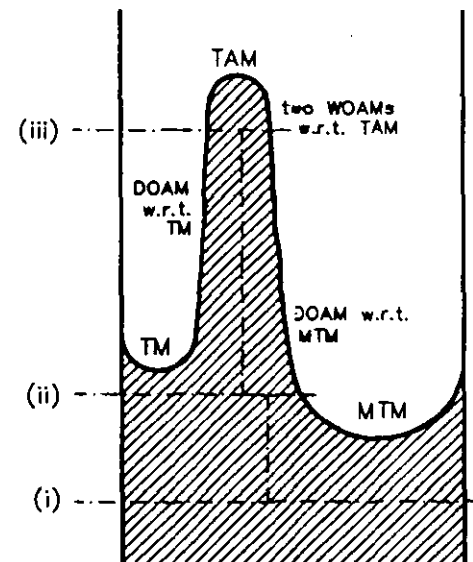
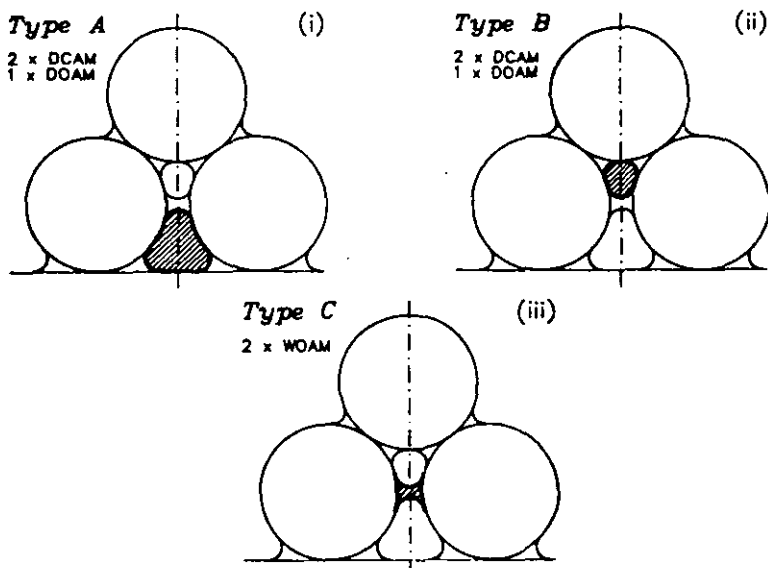
11.2 THEORY

The three rod and plate arrangement can exhibit eight different terminal menisci depending on the rod positioning. Some coexist together, while others are only formed with particular rod sizes and centre rod spacings from the plate. The basic assumption throughout the analysis is that the liquid vapour interface will always adopt the configuration that has the minimum surface energy, or maximum meniscus curvature, for the given geometry. Figures 11.1 to 11.3 show all the possible positions that the AMs can adopt, the appearance of some of the resulting capillary rise profiles together with the approximate arrangement of the rods.

a)



b)



c)

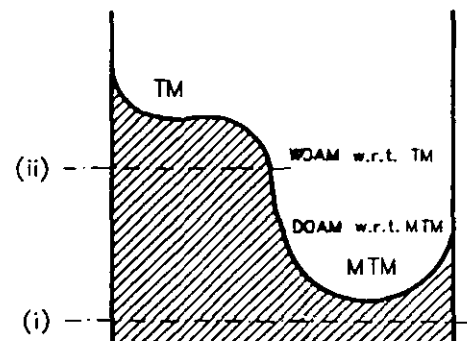
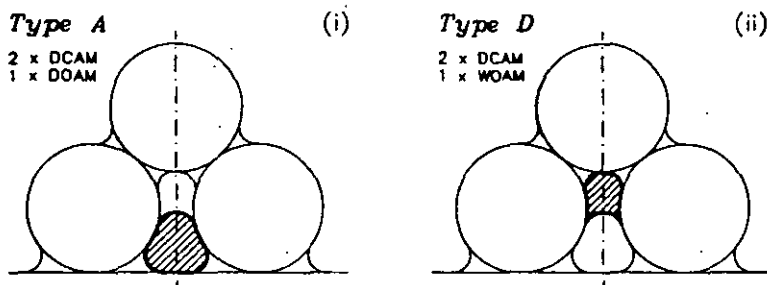


Figure 11.1 - Arrangements of arc menisci for the terminal menisci formed between three rods and a plate at low side rod separation. The effective area of each terminal meniscus is shown hatched and its effective perimeter outlined. In each case the capillary rise profile is shown as envisaged through the indicated section. Three different situations are shown, separation gradually increasing from the minimum

Figure 11.1 (a) shows the two side rods touching each other (the minimum rod separation) and the arrangement shows two pores each containing an isolated terminal meniscus. Both comprise three DCAMs that merge to form separate MTMs, one between two rods and a plate, termed *type A*, and the other between three contacting rods, henceforth called a *type B* TM.

If the side rods are moved even very slightly apart the back-to-back AMs in the corners formed by the contacting rods are no longer closed, but open. At some height, dependant on the rod separation, the now back-to-back OAMs will merge to form a TAM, a *type C* TM, as shown in Figure 11.1 (b).

Figure 11.1 (c) shows the situation when the rod separation has been increased, so decreasing the curvature of the *type C* TAM, to a point where the curvature of the TAM is less than that of the *type B* TM. The TAM and the its rearmost associated OAM (Fig. 11.1 (b)) cannot now form. The minimum surface energy criterion results in the formation of a *type D* TM, comprising two CAMs at the back and one OAM towards the front of the arrangement as shown in the figure.

If the rod separation is increased still further the curvature of the *type D* TM eventually becomes equal to that of the *type A* TM. The TMs can no longer coexist and they merge to form a fifth TM, *type E*, shown in Figure 11.2. The OAM disappears leaving four CAMs in the corners. The *type E* MTM exists by itself for a large range of intermediate rod spacings, its profile becoming progressively flatter as separation is increased.

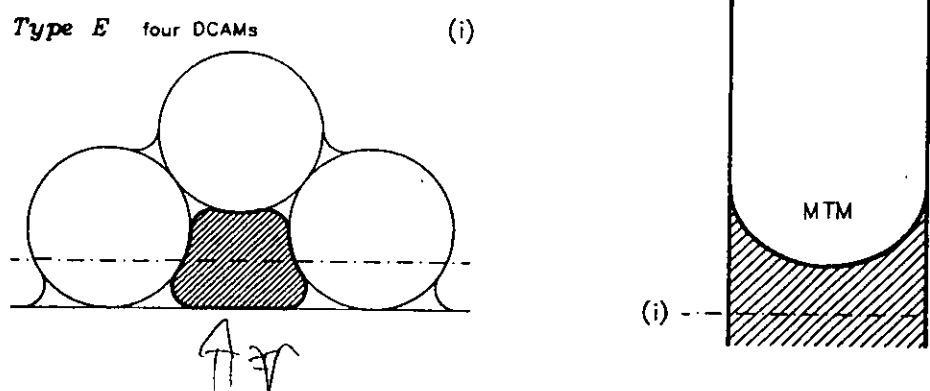


Figure 11.2 - Arrangement of AMs for the MTM formed between three rods and a plate at intermediate side rod spacings. The effective area of the MTM is shown hatched and its effective perimeter outlined. An example of the capillary rise profile seen through the plate is also shown.

Figure 11.3 (a) shows the situation at maximum rod separation with all three rods in a row touching the plate. Here there are two isolated pores of two rods against a plate. When the rod separation is decreased slightly the centre rod becomes separated from the plate resulting in the formation of two back-to-back OAMs. The two side pores now contain TMs comprising two CAMs and one OAM, termed *type F*; Figure 11.3 (b). *Type F* menisci are similar to *type A* TMs, but the OAM is now between the middle rod and

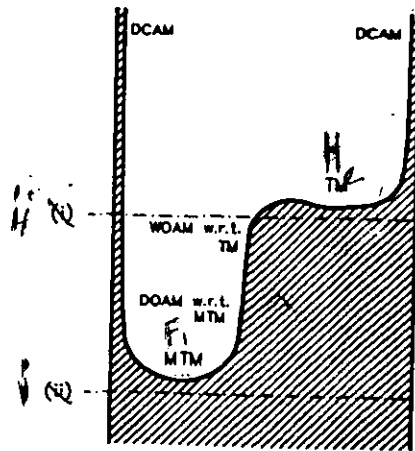
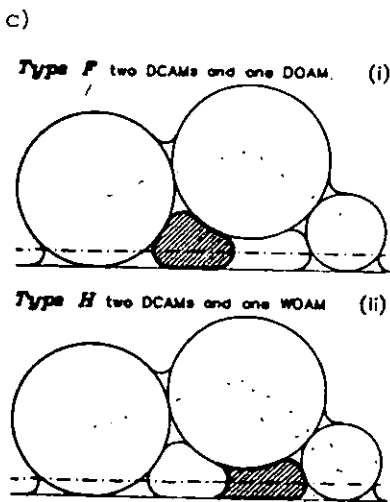
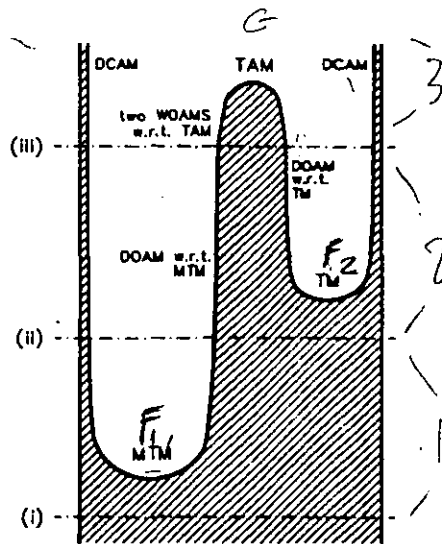
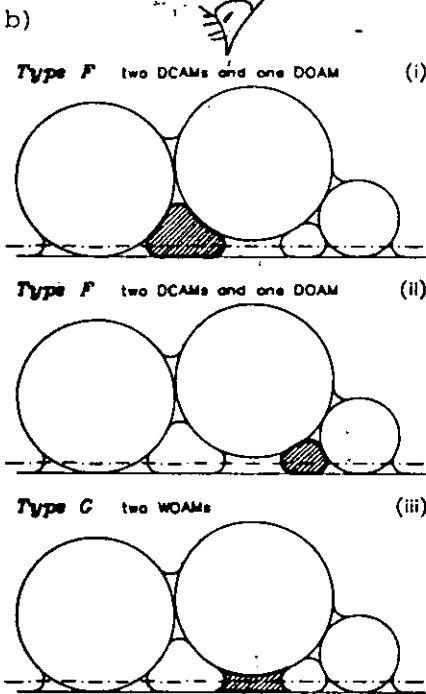
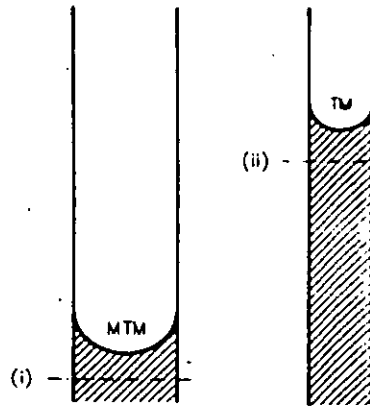
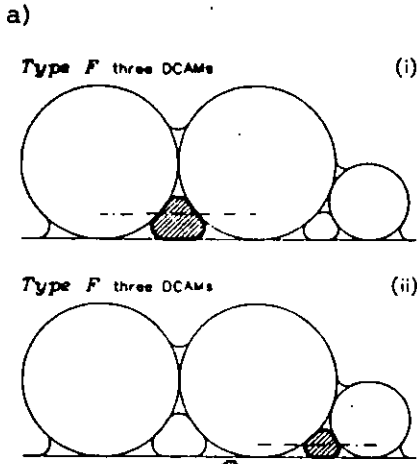


Figure 11.3 - Arrangements of AMs for the terminal menisci formed between three rods and a plate at high side rod separations. The effective area of each TM is shown hatched and its perimeter outlined. In each case the capillary rise profile is shown as viewed through the glass plate. The situation is shown at three different rod separations ranging from the maximum intermediate side rod spacings.

the plate not between the two side rods. Associated with the back-to-back OAMs will be a TAM, *type G*, with identical properties to that discussed in the single rod away from a plate arrangement (see section 9.3).

As the rod separation is decreased further the curvature of the *type G* TAM in the gap in-between the centre rod and plate falls until a point is reached where it is less than one of the *type F* TMs in the side pores. This gives rise to a *type H* TM, Figure 11.3 (c). *Type H* is similar to the *type D* TM in that it is in part bound by two DCAMs and a WOAM, but it is also bounded by the flat glass plate. Further reductions in the rod separation eventually leads to destabilisation of the OAM and a reversion to the *type E* MTM of Figure 11.2.

11.2.1 Analysis for effective areas and perimeters

On Figures 11.1 to 11.3 each terminal meniscus' effective area is shown hatched and its effective perimeter outlined. Due to the greater complexity of the geometry and the larger number of AMs the analysis required to find expressions for the area and perimeter is much more elaborate than so far encountered with perfectly wetting conditions. However, it is still simply the application of geometrical relationships.

As usual there is a need for easily measurable characteristic dimensions to define the exact tube shape. A rod radius, R_r , is used to normalise curvatures. To define the rod separation the half angle, ϕ , subtended at the centre of the middle rod by the side rods is employed. The analysis that follows allows for the rods to be of any sizes, but assumes that TMs are formed as shown in the Figures.

The analysis follows the usual method, the five sided figure formed by joining the centres of the rods to each other or the plate is divided into different regions. Each region has a perimeter adjoining the pore. The effective area and perimeter of a particular TM can be obtained from the areas and perimeters of the relevant regions. The analysis is given without explanation other than that provided by diagrams that define the nomenclature. Extensive use is made of simple geometrical relationships such as the Cosine, Sine and Trapezium rules.

a) *Type E* TM

From Figure 11.4 the required lengths, angles, perimeters and areas for the *type E* TM can be defined:

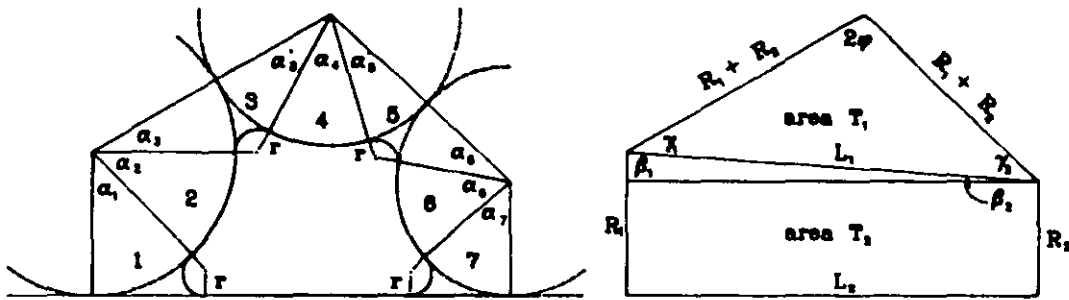


Figure 11.4 - Diagram showing the definition of angles, choice of regions and associated terminology required in the calculation of effective area and perimeter for the type *E* TM.

i) Lengths

$$L_1 = \sqrt{((R_1 + R_2)^2 + (R_2 + R_3)^2 - 2((R_1 + R_2)(R_2 + R_3) \sin 2\phi))} \quad \text{Equations}$$

$$L_2 = \sqrt{(L_1^2 - (R_1 - R_3)^2)} \quad 11.1$$

ii) Angles

$$\alpha_1 = \arccos\left(\frac{R_1 - r}{R_1 + r}\right)$$

$$\alpha_2 = \beta_1 + \gamma_1 - \alpha_1 - \alpha_3$$

$$\alpha_3 = \arccos\left(\frac{(R_1 + r)^2 + (R_1 + R_2)^2 - (R_2 + r)^2}{2(R_1 + R_2)(R_1 + r)}\right)$$

$$\alpha_3 = \arccos\left(\frac{(R_2 + r)^2 + (R_1 + R_2)^2 - (R_1 + r)^2}{2(R_1 + R_2)(R_2 + r)}\right)$$

$$\alpha_4 = 2\phi - \alpha_3 - \alpha_5$$

$$\alpha_5 = \arccos\left(\frac{(R_3 + r)^2 + (R_3 + R_2)^2 - (R_2 + r)^2}{2(R_3 + R_2)(R_3 + r)}\right)$$

$$\alpha_5 = \arccos\left(\frac{(R_2 + r)^2 + (R_3 + R_2)^2 - (R_3 + r)^2}{2(R_3 + R_2)(R_2 + r)}\right)$$

Equations 11.2

$$\alpha_6 = \beta_2 + \gamma_2 - \alpha_5 - \alpha_7$$

$$\alpha_7 = \arccos\left(\frac{R_3 - r}{R_3 + r}\right)$$

$$\beta_1 = \arccos\left(\frac{(R_1 - R_3)}{L_1}\right)$$

$$\beta_2 = \pi - \beta_1$$

$$\gamma_1 = \arccos \left(\frac{(R_1 + R_2)^2 + L_1^2 - (R_3 + R_2)^2}{2(R_1 + R_2)L_1} \right)$$

$$\gamma_2 = \pi - \gamma_1 - 2\phi$$

iii) Perimeters

$$P_1 = (\pi - \alpha_1)r$$

$$P_2 = \alpha_2 R_1$$

$$P_3 = (\pi - \alpha_3 - \alpha_3')r$$

$$P_4 = \alpha_4 R_2$$

$$P_5 = (\pi - \alpha_5 - \alpha_5')r$$

$$P_6 = \alpha_6 R_3$$

$$P_7 = (\pi - \alpha_7)r$$

$$P_8 = L_2 - (R_1 + r) \sin \alpha_1 - (R_2 + r) \sin \alpha_7$$

Equations

11.3

iv) Areas

$$A_{T_1} = \frac{1}{2}(R_1 + R_2)(R_2 + R_3) \sin 2\phi$$

$$A_{T_2} = \frac{1}{2}(R_1 + R_3)L_2$$

$$A_1 = \frac{1}{2}((R_1 + r)^2 \sin \alpha_1 + (\pi - \alpha_1)r^2)$$

$$A_2 = \frac{1}{2}\alpha_2 R_1^2$$

$$A_3 = \frac{1}{2}((R_1 + R_2)(R_1 + r) \sin \alpha_3 - (\pi - \alpha_3 - \alpha_3')r^2)$$

Equations 11.4

$$A_4 = \frac{1}{2}\alpha_4 R_2^2$$

$$A_5 = \frac{1}{2}((R_3 + R_2)(R_3 + r) \sin \alpha_5 - (\pi - \alpha_5 - \alpha_5')r^2)$$

$$A_6 = \frac{1}{2}\alpha_6 R_3^2$$

$$A_7 = \frac{1}{2}((R_3 + r)^2 \sin \alpha_7 + (\pi - \alpha_7)r^2)$$

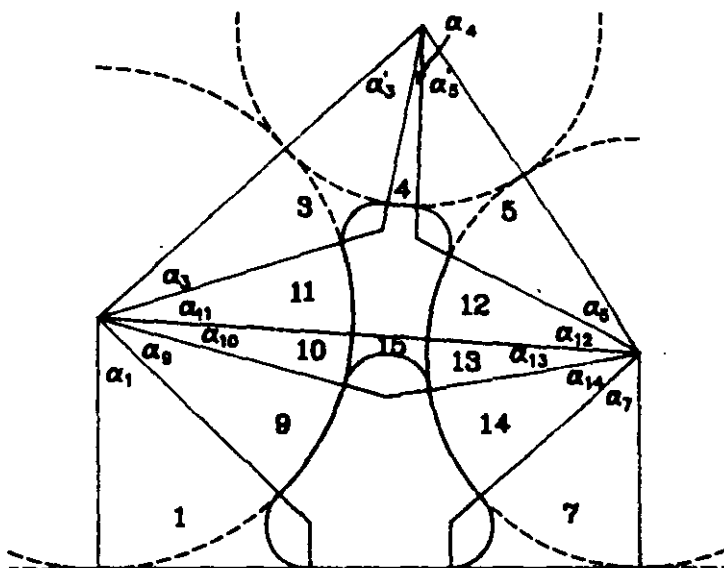


Figure 11.5 - Diagram showing the definition of angles, choice of regions and associated terminology required in the calculation of effective area and perimeter for the *types A and D* TMs.

b) *Types A and D* TMs

The analysis given above for the *type E* TM applies, but with the exception that regions 2 and 6 which no longer apply. In addition, the regions 9 to 15 must be defined. From Figure 11.5:

i) Angles

$$\alpha_9 = \beta_1 - \alpha_{10} - \alpha_1$$

$$\alpha_{10} = \arccos \left(\frac{(R_1 + r)^2 + L_1^2 - (R_3 + r)^2}{2(R_1 + r)L_1} \right)$$

$$\alpha_{11} = \gamma_1 - \alpha_3$$

$$\alpha_{12} = \gamma_2 - \alpha_5$$

$$\alpha_{13} = \arccos \left(\frac{(R_3 + r)^2 + L_1^2 - (R_1 + r)^2}{2(R_3 + r)L_1} \right)$$

$$\alpha_{14} = \beta_2 - \alpha_{13} - \alpha_7$$

Equations

11.5

ii) Perimeters

$$P_9 = \alpha_9 R_1$$

$$P_{10} = \alpha_{10} R_1$$

$$P_{11} = \alpha_{11} R_1$$

$$P_{12} = \alpha_{12} R_3$$

$$P_{13} = \alpha_{13} R_3$$

$$P_{14} = \alpha_{14} R_3$$

$$P_{15} = (\pi - \alpha_{10} - \alpha_{13})r$$

Equations 11.6

iii) Areas

$$A_9 = \frac{1}{2} \alpha_9 R_1^2$$

$$A_{10} = \frac{1}{2} \alpha_{10} R_1^2$$

$$A_{11} = \frac{1}{2} \alpha_{11} R_1^2$$

$$A_{12} = \frac{1}{2} \alpha_{12} R_3^2$$

$$A_{13} = \frac{1}{2} \alpha_{13} R_3^2$$

$$A_{14} = \frac{1}{2} \alpha_{14} R_3^2$$

$$A_{15} = \frac{1}{2} (L_1(R_1 + r) \sin \alpha_{10} - (\pi - \alpha_{10} - \alpha_{13})r^2)$$

Equations 11.7

c) Types A, B and C TMs

The analysis for these menisci follows that for *types A* and *D* except that regions 11 and 12 no longer apply (see Figure 11.6) and:

i) Angles

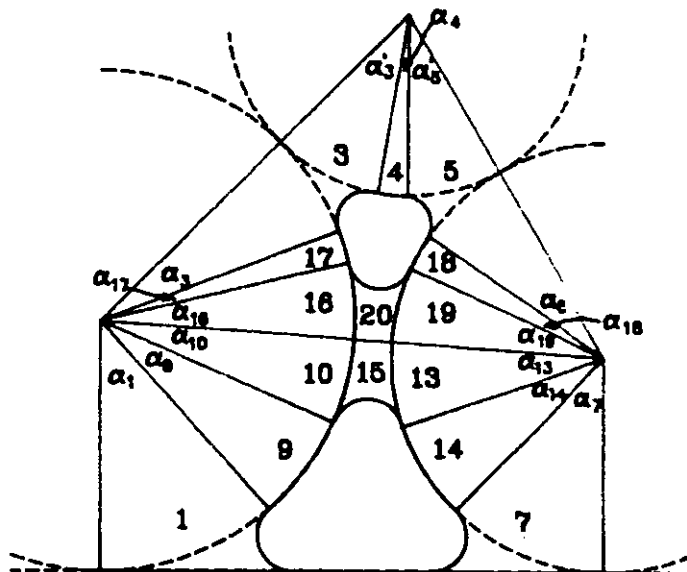


Figure 11.6 - Diagram showing the definition of angles, choice of regions and associated terminology required in the calculation of effective area and perimeter for the types A, B and C TMs.

$$\alpha_{16} = \arccos\left(\frac{(R_1 + r)^2 + L_1^2 - (R_3 + r)^2}{2(R_1 + r)L_1}\right) = \alpha_{10}$$

$$\alpha_{17} = \gamma_1 - \alpha_3 - \alpha_{16}$$

$$\alpha_{18} = \gamma_2 - \alpha_5 - \alpha_{19}$$

$$\alpha_{19} = \arccos\left(\frac{(R_3 + r)^2 + L_1^2 - (R_1 + r)^2}{2(R_3 + r)L_1}\right) = \alpha_{13}$$

Equations

11.8

ii) Perimeters

$$P_{16} = P_{10}$$

$$P_{17} = \alpha_{17}R_1$$

$$P_{18} = \alpha_{18}R_3$$

$$P_{19} = P_{13}$$

$$P_{20} = P_{15}$$

Equations 11.9

iii) Areas

$$A_{16} = A_{10}$$

$$A_{17} = \frac{1}{2} \alpha_{17} R_1^2$$

$$A_{18} = \frac{1}{2} \alpha_{18} R_3^2$$

Equations 11.10

$$A_{19} = A_{13}$$

$$A_{20} = A_{15}$$

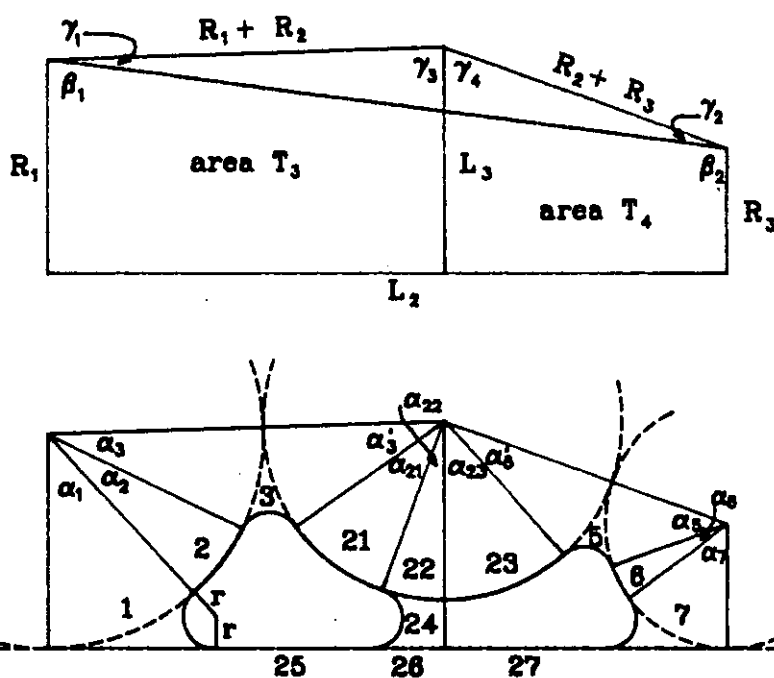


Figure 11.7 - Diagram showing the definition of angles, choice of regions and associated terminology required in the calculation of effective area and perimeter for the types *F* and *H* TMs.

d) Types *F* and *H* TMs

The analysis now reverts to that of the type *E* TM except that sections 4 and 8 no longer apply as shown in Figure 11.7 and:

i) Lengths

$$L_3 = R_1 + (R_1 + R_2) \sin(\gamma_1 + \beta_1 - \pi/2) \quad (11.11)$$

ii) Angles

$$\alpha_{21} = \gamma_3 - \alpha_3 - \alpha_{22}$$

$$\alpha_{22} = \arccos\left(\frac{L_3 - r}{R_2 + r}\right)$$

$$\alpha_{23} = \gamma_4 - \alpha_5$$

$$\gamma_3 = \pi - \gamma_1 - \beta_1$$

$$\gamma_4 = 2\phi - \gamma_1$$

Equations 11.12

iii) Perimeters

$$P_{21} = \alpha_{21}R_2$$

$$P_{22} = \alpha_{22}R_2$$

$$P_{23} = \alpha_{23}R_2$$

$$P_{24} = (\pi - \alpha_{22})r$$

Equations 11.13

$$P_{25} = (R_1 + R_2) \sin \gamma_3 - (R_1 + r) \sin \alpha_1 - (R_2 + r) \sin \alpha_{22}$$

$$P_{26} = (R_2 + r) \sin \alpha_{22}$$

$$P_{27} = (R_3 + R_2) \sin \gamma_4 - (R_3 + r) \sin \alpha_7$$

iv) Areas

$$A_{T_3} = \frac{1}{2}(R_1 + L_3)(R_1 + R_2) \sin \gamma_3$$

$$A_{T_4} = \frac{1}{2}(R_3 + L_3)(R_3 + R_2) \sin \gamma_4$$

$$A_{21} = \frac{1}{2}\alpha_{21}R_2^2$$

Equations

$$A_{22} = \frac{1}{2}\alpha_{22}R_2^2$$

11.14

$$A_{23} = \frac{1}{2}\alpha_{23}R_2^2$$

$$A_{24} = \frac{1}{2}((L_3 + r)(R_2 + r) \sin \alpha_{22} - \alpha_{22}R_2^2 - (\pi - \alpha_{22})r^2)$$

e) Types F and G TMs

The analysis of the final rod arrangement follows that given for *types F and H TMs*, but regions 23 and 27 do not apply, Figure 11.8, and:

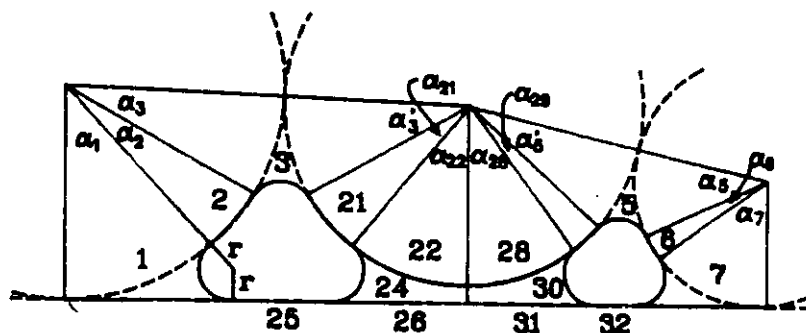


Figure 11.8 - Diagram showing the definition of angles, choice of regions and associated terminology required in the calculation of effective area and perimeter for the types *F* and *G* TMs.

i) Angles

$$\alpha_{28} = \alpha_{22} \quad \text{Equations}$$

$$\alpha_{29} = \gamma_4 - \alpha_5 - \alpha_{28} \quad 11.15$$

ii) Perimeters

$$P_{28} = P_{22}$$

$$P_{28} = \alpha_{29} R_2$$

$$P_{30} = P_{24}$$

Equations 11.16

$$P_{31} = P_{26}$$

$$P_{32} = (R_3 + R_2) \sin \gamma_4 - (R_3 + r) \sin \alpha_7 - (R_2 + r) \sin \alpha_{28}$$

iii) Areas

$$A_{28} = A_{22}$$

$$A_{29} = \frac{1}{2} \alpha_{29} R_2^2$$

Equations 11.17

$$A_{30} = A_{24}$$

Having now determined the areas and perimeters of all the regions, the effective area and perimeter of each TM may be defined in terms of the pore characteristic dimensions of ϕ , R_1 , R_2 , R_3 , and the radius of curvature, r .

a) Type A - two DCAMs and one DOAM

Figures 11.1 (a), (b) and (c) show the effective area, hatched, and the effective perimeter, outlined, of the *type A* TM at various rod separations. Using the relationships

defined from Figure 11.5, equations 11.1 to 11.4 and 11.5 to 11.7, these may be defined as follows:

$$P_{eff} = \sum P_S + \sum P_L \quad (6.11)$$

$$= (P_8 + P_9 + P_{14}) + (P_1 + P_7 + P_{15}) \quad (11.18)$$

and
$$A_{eff} = A_{T_2} - A_1 - A_7 - A_9 - A_{10} - A_{13} - A_{14} - A_{15} \quad (11.19)$$

b) Type B - two DCAMs and one DOAM

Figures 11.1 (a) and (b) show the required effective area and perimeter (hatched and outlined respectively) of the *type B* TM and using the analysis derived from Figure 11.6 they may be defined as follows:

$$P_{eff} = (P_{17} + P_4 + P_{18}) + (P_3 + P_5 + P_{20}) \quad (11.20)$$

and
$$A_{eff} = A_{T_1} - A_{16} - A_{17} - A_3 - A_4 - A_5 - A_{18} - A_{19} - A_{20} \quad (11.21)$$

c) Type C - two WOAMs

Figure 11.1 (c) shows the effective area and perimeter of this TAM. From the relationships derived from Figure 11.6:

$$P_{eff} = (P_{10} + P_{16} + P_{19} + P_{13}) + (-P_{15} - P_{20}) \quad (11.22)$$

Note the negative contribution to the liquid perimeter from the two back-to-back WOAMs.

Also
$$A_{eff} = A_{15} + A_{20} \quad (11.23)$$

d) Type D - two DCAMs and one WOAM

Refer to Figures 11.1 (c) and 11.5

$$P_{eff} = (P_{10} + P_{11} + P_4 + P_{12} + P_{13}) + (P_3 + P_5 - P_{15}) \quad (11.24)$$

Note the negative contribution to the perimeter from the WOAM.

Also
$$A_{eff} = A_{T_1} - A_{11} - A_3 - A_4 - A_5 - A_{12} + A_{15} \quad (11.25)$$

e) Type E - four DCAMs

The effective area and perimeter of the *type E* TM are shown on Figure 11.2 and defined by relationships derived from Figure 11.4.

$$P_{eff} = (P_2 + P_4 + P_6 + P_8) + (P_1 + P_3 + P_5 + P_7) \quad (11.26)$$

and
$$A_{eff} = A_{T_1} + A_{T_2} - A_1 - A_2 - A_3 - A_4 - A_5 - A_6 - A_7 \quad (11.27)$$

f) Type F - two DCAMs and one DOAM

Refer to Figures 11.3 (a), (b) and (c) for examples of the effective areas and perimeters of this type of TM at various rod separations. Figure 11.7 shows the regions used to derive the relations that yield:

$$P_{eff} = (P_2 + P_{21} + P_{25}) + (P_1 + P_3 - P_{24}) \quad (11.28)$$

and
$$A_{eff} = A_{T_3} - A_1 - A_2 - A_3 - A_{21} - A_{22} + A_{24} \quad (11.29)$$

g) Type G - two WOAMs

Figure 11.3 (b) shows the effective area and perimeter of the *type G* TAM. From the relationships derived from Figure 11.8:

$$P_{eff} = (P_{22} + P_{28} + P_{26} + P_{30}) + (-P_{26} - P_{31}) \quad (11.30)$$

and
$$A_{eff} = A_{24} + A_{30} \quad (11.31)$$

h) Type H - two DCAMs and one WOAM

Refer to Figures 11.3 (c) and 11.7.

$$P_{eff} = (P_{22} + P_{23} + P_6 + P_{27} + P_{26}) + (P_5 + P_7 - P_{24}) \quad (11.32)$$

Note the negative contribution to the perimeter from the WOAM.

Also
$$A_{eff} = A_{T_4} - A_{23} - A_5 - A_6 - A_7 + A_{24} \quad (11.33)$$

11.2.2 Solution of equations

The equations for effective areas and perimeters derived above were written into the standard computer program. Some modifications to the workings of the program were required to enable selection of the type of TM and to incorporate the half angle, ϕ (see Appendix I for a program listing).

The resulting program is capable of solving the equations for rods of unequal sizes with varying rod separation. Results are given as normalised meniscus curvature, R/r , in terms of the half angle, ϕ . With the likely stable positions of the AMs already determined in the analysis and with the computer generated results for each of the TMs it is now possible to determine which type of TM or TMs exist at which rod separations. The minimum surface energy criteria must be employed. The TM with the highest normalised curvature for each particular portion of geometry is always formed. Figures 11.9 and 11.10 show such graphs obtained for the arrangements where $R_1 = R_2 = R_3$ at low ϕ and where $R_1 = R_2 = 2R_3$ at intermediate and high ϕ . These graphs illustrate the behaviour of the eight TMs. Each is represented by a different portion of the graph, as shown.

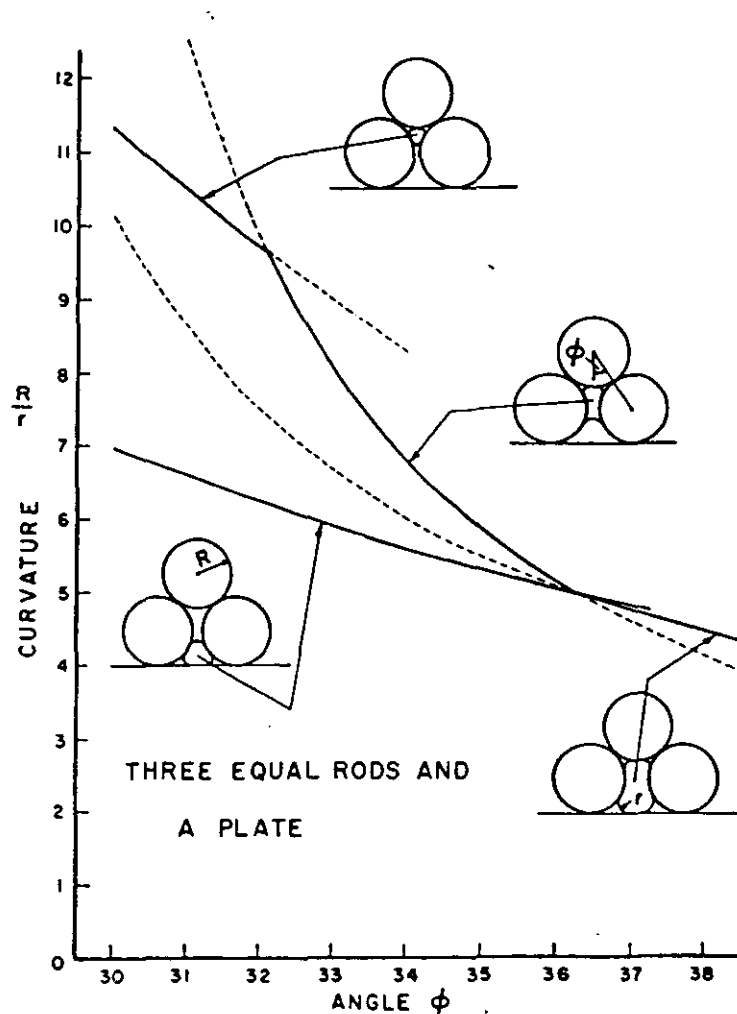


Figure 11.9 - Graph showing the theoretical results for curvatures of the various terminal menisci formed in the three equal rods and plate system at low and intermediate half angles. Curvatures of types A, B, C, D and E TMs are shown in terms of the half angle by the curves indicated.

Validation of the program against previously published results was possible at specific separations for the case of equal rods. TM types A and F, between two rods and a plate, have been discussed elsewhere for the case when all components are in mutual contact, see section 9.5, and the type G TM was covered in section 9.3. Mayer & Stowe (1965), Princen (1969b) and Dodds (1978) have published results that were used to validate the equations for type B when all three rods are in contact. Princen (1969a) covered type C and Dodds also recorded some results for the type D TM. Finally Mason & Morrow's (1987) study provided comparison for results obtained for the type H TM. The program cannot determine which of the TMs is formed and will calculate theoretical curvatures for menisci that do not exist in the real system (the dotted lines on Figures 11.9 and 11.10). It is left up to the user to determine which TMs are formed where.

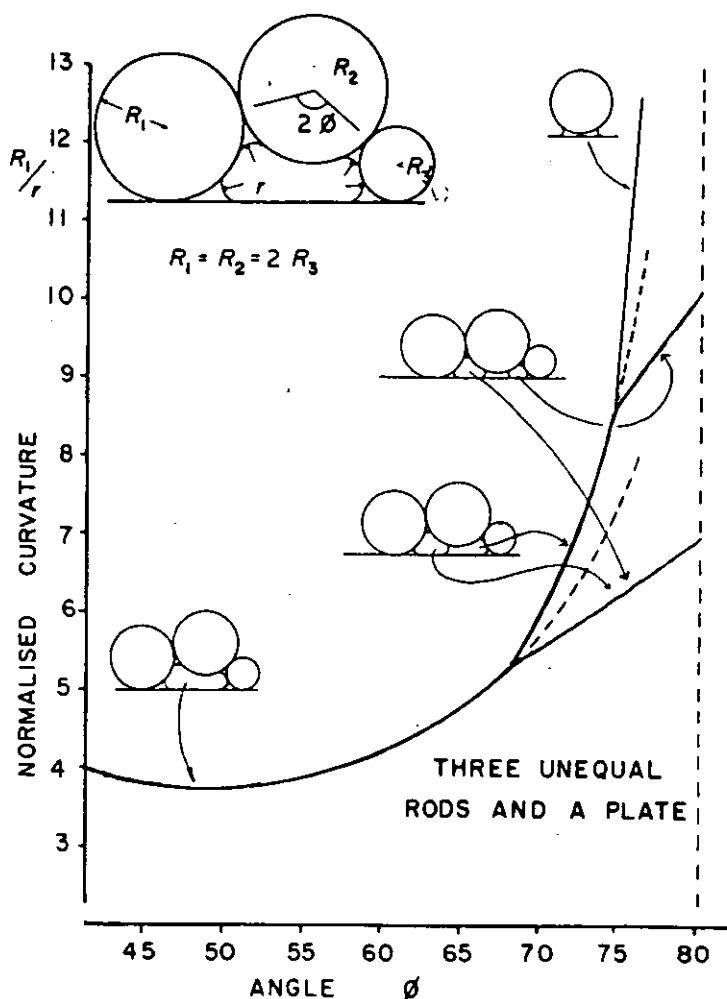


Figure 11.10 - Graph showing the theoretical results for curvatures of the various terminal menisci formed in the three unequal rods, non-symmetrically arranged ($R_1 = R_2 = 2R_3$) system at intermediate and high half angles. Curvatures of types E, F, G, and H TMs are shown in terms of the half angle by the curves indicated.

11.3 EXPERIMENTAL

The experiments for the three rod system sought to confirm the transition points between the different menisci in addition to the usual objective of confirming theoretical curvatures. Also some "neighbouring pore" effects were expected.

Four rod size arrangements were investigated beginning with the comparatively simple case of three equal rods ($R_1 = R_2 = R_3$). The study of this arrangement is relatively straightforward and set the pattern for the more complicated cases. As a step to increasing the complexity of the system the centre rod was replaced by a rod twice the size ($R_1 = 1/2R_2 = R_3$), and then by a rod half the size of those at the side ($R_1 = 2R_2 = R_3$). Finally

non-symmetrically arranged unequal rods were investigated, with a side rod and the centre rod of equal size and the remaining rod half the size of the other two ($R_1 = R_2 = 2R_3$). This last arrangement demonstrates the entire range of menisci.

The experimental procedures again closely followed those described in chapter 7, but new cells had to be designed and fabricated and a suitable method for measuring the half angle determined. Also uncertainties over exactly where to measure some menisci's heights of rise needed to be addressed.

11.3.1 Cell design

In order to realise all of the possible rod separations for the various rod sizes several different cell designs were needed. At many rod separations, notably at low and intermediate half angles, it was possible to utilise the existing cells with clamping screws at the rear. The centre rod was simply pushed forward against the side rods which were supported by the channel walls and glass plate. By varying the rod sizes many different separations could be obtained.

At large values of ϕ the above method fails as small changes in the rod sizes result in very large changes in ϕ . The available range of cells and rod sizes was not fine enough to provide adequate variation. Two new cell designs were devised and four cells commissioned during the course of the experiments.

11.3.1.1 Intermediate and low ϕ design

Whilst conducting some early experiments for the three equal rod arrangement it became apparent that a more versatile cell was required if the full range of intermediate and low ϕ values were to be covered. The resulting cell design is shown in Figure 11.11. A stepped channel designed to hold 3 x 3/32" rods was machined to the front face of a standard cell blank. Three 1/8" diameter screws, with the end 1/4" ground down to 1/16" diameter pins, enter through the rear face of the channel. As it stands the cell can accommodate three 3/32" rods in a row against the plate.

The half angle, ϕ , is altered by inserting equal thicknesses of shimstock between the side rods and the walls of the channel. The centre rod is then forced against the side rods by the clamping action of the screws as shown in Figure 11.11. The rod size of 3/32" diameter was selected as initial experiments had shown this sized rod gave heights of rise within the limits of the comparative method over the whole range of ϕ values. Brass shims were used and were prepared in 2" long strips about 1/16" wide.

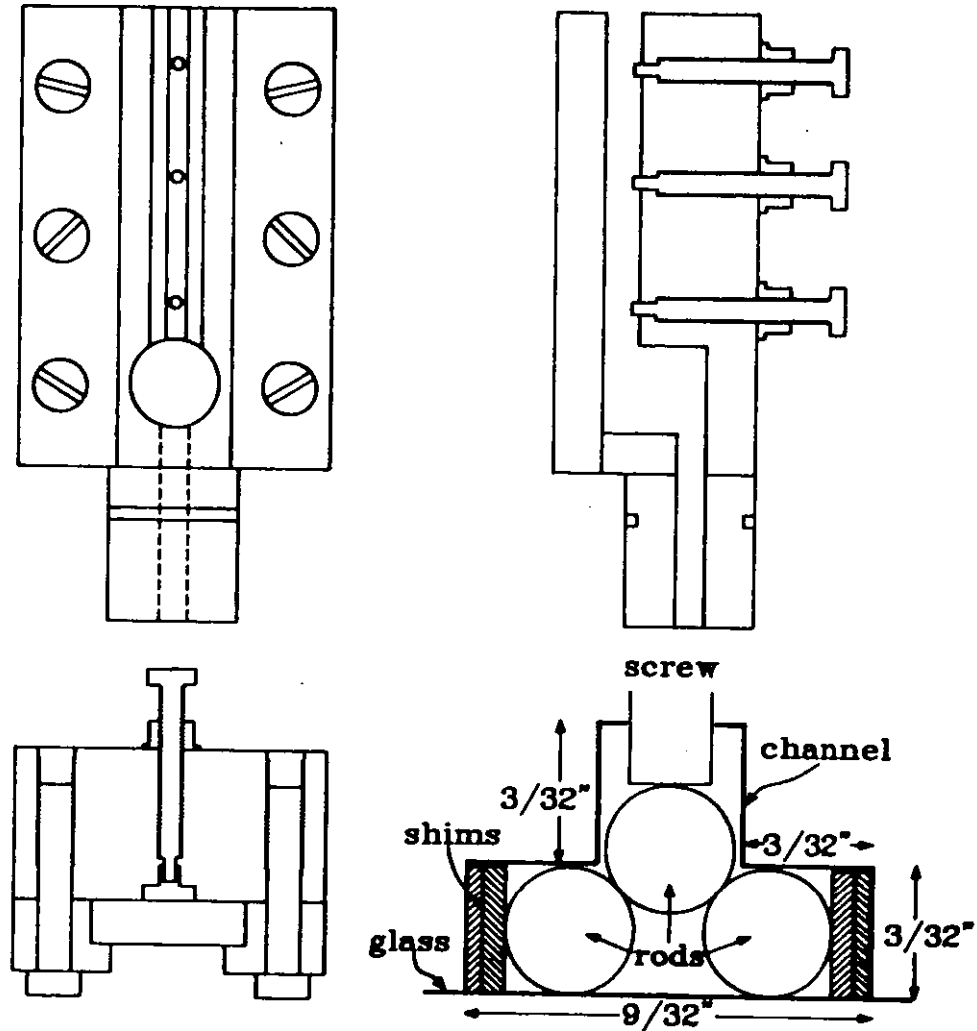


Figure 11.11 - Diagram showing the design of the cell employed in the capillary rise experiments for the three-rods-and-a-plate arrangement at low and intermediate ϕ .

The cell proved to be easily assembled and very useful for low and intermediate values of ϕ with the equal rods and also with the symmetrically arranged unequal rods. At high ϕ the cell did not work so well as even changing the shim size by as little as one thou resulted in excessive changes in ϕ .

11.3.1.2 High ϕ design

As a result of the failure at high ϕ of the cell described above a new cell was commissioned, designed specifically for the three equal rods at high rod separations. The cell is shown in Figure 11.12, as is its operation (schematically). The principals of the

design remain the same, but now the rod separation is altered by changing the depth, not width, of the cell enabling much finer control of ϕ at high separations.

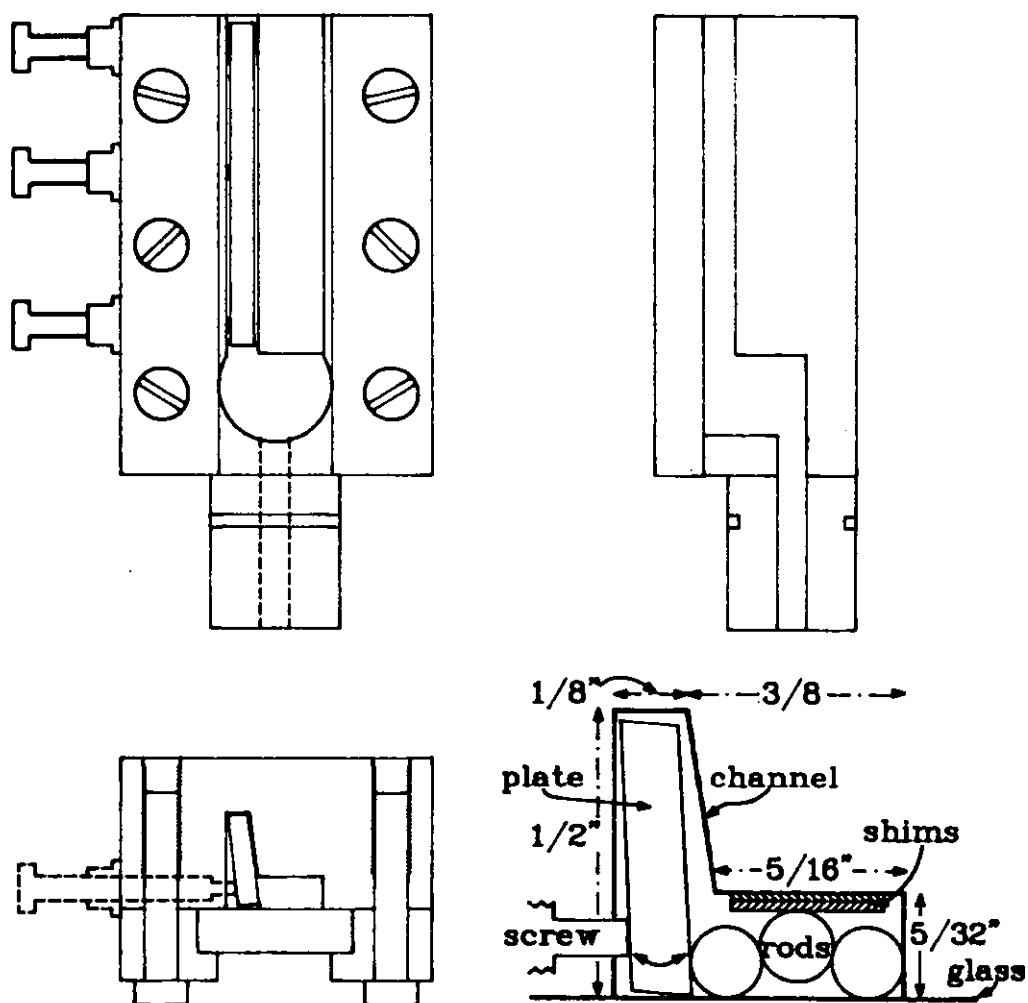


Figure 11.12 - Diagram showing the design of the cell employed in the capillary rise experiments for the three-rods-and-a-plate arrangement at high ϕ .

The heights of rise encountered at high ϕ are significantly greater than those at intermediate ϕ enabling 1/8" rods to be used. Larger rods lead to pores of greater dimensional accuracy. The three rods are clamped in position by a 3/32" thick steel plate that is pushed onto a side rod by three clamping screws entering through the channel wall. The plate's section was that of a parallelogram enabling it to swing without catching the glass plate, yet still contact the rod properly.

In practice this cell was not so easy to assemble and often required a lot of patience, but worked well in the end and an improved simpler design could not be conceived. Two further cells of similar design, but with different specifications were later commissioned for the investigations with unequal rods.

11.3.2 Measurement of half angle

Direct measurement of the half angle, ϕ , was never really a realistic possibility. The only place that the angle can be measured with a rotating microscope is looking down onto the top of a cell and positioning the cross-hairs on the outer edges of the rods. Any variation in tube section caused by mistakes in assembling the cell would go undetected. Furthermore the cells were difficult enough to assemble without having to ensure that all the tops of the rods would be in focus at the same time.

Indirect measurements of ϕ involve the measurement of the rod-rod, termed L , or rod-plate, D , separations (see Figure 11.13). Measurement of L is more desirable as it may be checked along the length of the pore. This method worked well at low and intermediate ϕ , but at high ϕ small errors in L lead to large variation in the observed value for ϕ . A sine function must be used to obtain ϕ from L . The same small errors in a measurement of D lead to much less variation as ϕ is obtained from a cosine relationship. Similarly a low rod separation use of D was less accurate than L .

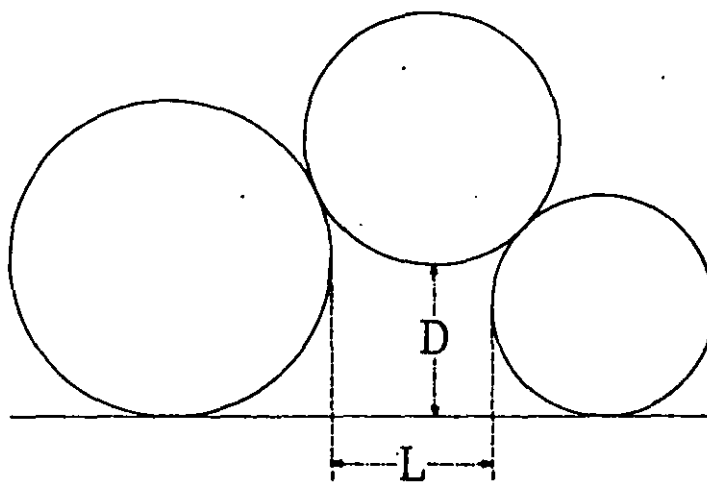


Figure 11.13 - Illustration of the parameters measured for the determination of the half angle, ϕ .

Table 11.1 shows the simple trigonometric functions employed to calculate ϕ from L and D for each of the rod arrangements investigated. Variation in gap measurements over several readings could be as much as 10 thou (0.25 mm). This arose from difficulties in illuminating the shiny steel rods so that their edges were clearly defined. Table 11.2 shows the effect of a 10 thou variation on ϕ for three equal 1/8" rods at different nominal ϕ values.

Table 11.1 Determination of half angle, ϕ , from measured gap sizes: L , the rod-rod spacing and D , the rod-plate spacing.

Rod Arrangement	$\phi(L)$	Gap	$\phi(D)$
Equal Rods	$\sin^{-1}\left(\frac{R+L/2}{2R}\right)$		$\cos^{-1}\left(\frac{d}{2R}\right)$
Unequal Rods - Symmetrical	$\sin^{-1}\left(\frac{R_1+L/2}{R_1+R_2}\right)$		$\cos^{-1}\left(\frac{D+R_2-R_1}{R_1+R_2}\right)$
Unequal Rods - Non-Symmetrical	$\frac{1}{2}\cos^{-1}\left(\frac{(R_1+R_2)^2+(R_2+R_3)^2-(R_1+R_3+L)^2}{2(R_1+R_2)(R_2+R_3)}\right)$		$\frac{1}{2}\left(\cos^{-1}\left(\frac{D+R_2-R_1}{R_1+R_2}\right)+\cos^{-1}\left(\frac{D+R_2-R_3}{R_2+R_3}\right)\right)$

At intermediate separations these errors in ϕ are not a major problem as curvature changes only slightly with ϕ , but at high and low separations, where the rate of change of curvature with ϕ is greatest, these variations in ϕ can cause significant errors. In practice L measurements were used at low and intermediate separations, and D measurements only at high ϕ , where having only the top of the cell to make measurements is preferable to the large errors incurred with L .

Table 11.2 Range of possible ϕ values given a 10 thou (0.25mm) uncertainty in L or D with $3 \times 1/8$ " diameter rods.

Nominal ϕ	$L/2$ (mm)	Maximum range of ϕ	D (mm)	Maximum range of ϕ
40°	0.4515	40 ± 0.15°	2.3975	40 ± 0.35°
60°	1.1575	60 ± 0.25°	1.5562	60 ± 0.25°
80°	1.5331	80 ± 0.70°	0.5241	80 ± 0.20°

11.3.3 Point of measurement of height of rise

The three rod system gives rise to eight different TMs and thus several different capillary profiles which must undergo transitions from one shape to the next. With some profiles a definable point or points for the measurement of heights is not obvious. At rod separations near to transition points between menisci it is sometimes difficult to know which menisci you are looking at. Figures 11.14 and 11.15 show examples of these profiles, and the points selected for measurement of heights, as viewed through the glass plate when ϕ is increased.

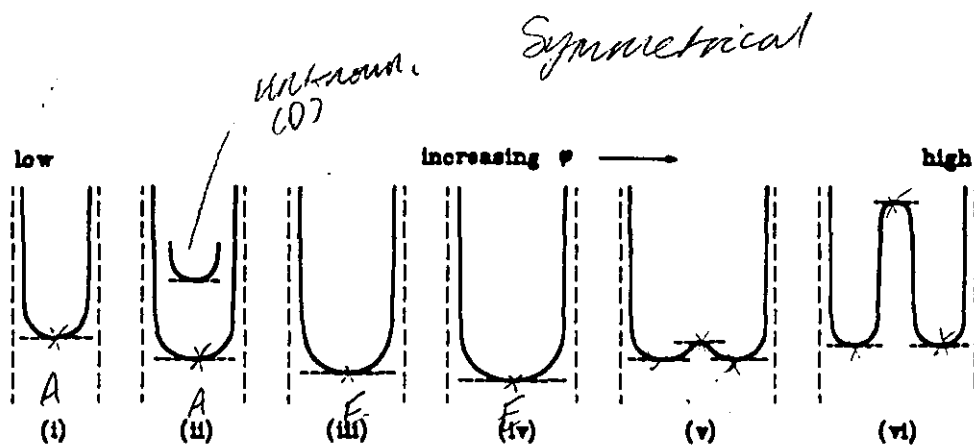


Figure 11.14 - Schematic illustration of some of the capillary profiles seen through the glass plate with the three-rods-and plate, symmetrically arranged system. The points at which heights of rise were measured are indicated by the dotted lines.

Figure 11.14 shows profiles seen with symmetrically arranged rods. At low ϕ the *type A* TM, akin to that shown by the two rods and a plate arrangement, gives a well defined point for measurement. At some small separations it was possible to see a meniscus behind the *type A* TM (Fig. 11.14 (ii)), but at the time of measurement it was impossible to tell which from observation alone. These turned out to be *type D* menisci and measurements were taken at the lowest visible point. TMs of *type C* and *B* were not seen.

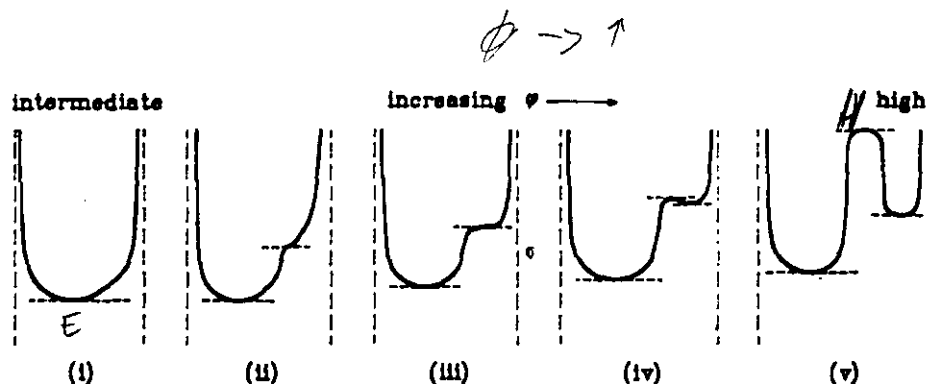


Figure 11.15 - Schematic illustration of some of the capillary profiles seen through the glass plate with the three-rods-and plate, non-symmetrically arranged system. The points at which heights of rise were measured are indicated by the dotted lines.

Taking readings from *type E* TMs is simple for most of the separations for which it exists (Figs 11.14 (iii) and (iv)). As ϕ increases the profile becomes progressively "flatter", the TM more cubic, until at higher ϕ values there arises a slight "hump" in the centre of the profile (Fig 11.14 (v)). This was seen at values of ϕ significantly less than would be associated with the formation of a *type H* TAM and so the height of the lowest part of the TM was used to determine curvature. At high ϕ all menisci give discernible points for measurement.

With non-symmetrically arranged rods there are additional problems arising from the formation of the *type G* TM. Figure 11.15 shows the changes in profile from intermediate to very high separations. The *type E* TM initially becomes more asymmetric

(Fig 11.15 (i)), before a slight kink, like a point of inflection, is seen near the smaller rod (Fig 11.15 (ii)). The position of the "kink" is difficult to ascertain exactly, but a measurement could usually be taken. The "kink" appears at ϕ values less than those associated with the development of the *type G* TM. Further increases in ϕ flatten out the region near the "kink" (Fig. 11.15 (iii)) until a slight "hump" appears (Fig. 11.15 (iv)) before the *type H* TAM is properly formed (Fig. 11.15 (v)).

11.4 RESULTS

Over the following pages the theoretical and experimental results for each rod arrangement are given and examined. All experimental curvatures were obtained from observed heights of rise using the simplified comparative method equation 7.7. No corrections were added for gravity distortion. Appendix I shows the detailed experimental results.

11.4.1 Three equal rods

Figure 11.16 shows the MS-P generated curves of normalised meniscus curvature, R/r , in terms of the half angle, ϕ . The half angle varies between a minimum of 30° , the rods mutually touching, to a maximum of 90° , all three rods in a row. The arrangement behaves as either one or two pores depending on the rod separation. For the majority of ϕ values (from about 36.5° to 84°) the arrangement behaves as a single pore bound by three rods and a plate and exhibits a *type E* TM with a curvature between 3 and 5. The experimentally determined curvatures for intermediate ϕ are also shown on Figure 11.16 and are generally in excellent agreement with the theory.

At high ϕ , Figure 11.17, the arrangement behaves as two identical mirror image pores of two rods and a plate. Only the *types F and G* TMs are seen. It is not possible for a *type H* TM (two DCAMs and one WOAM) to form with equal rods. When the curvature of the TAM, *type G*, equals that of one *type F* TM it will also equal that of the other resulting in a transition directly to the *type E* TM. The experimental results for this region are shown on the expanded scale of Figure 11.17 so that they may be better compared with the theory. The agreement is again excellent.

At low ϕ the arrangement also behaves as two separate pores, but now all four possible TM types are exhibited depending on the exact value of ϕ . However in practice, it was only possible to measure the curvature of the *type A* TM and a few points for the *type D* TM. At these small values of ϕ the gap between the side rods is too small to allow the other TMs to be seen properly. Figure 11.18 shows the experimental results on an expanded scale.

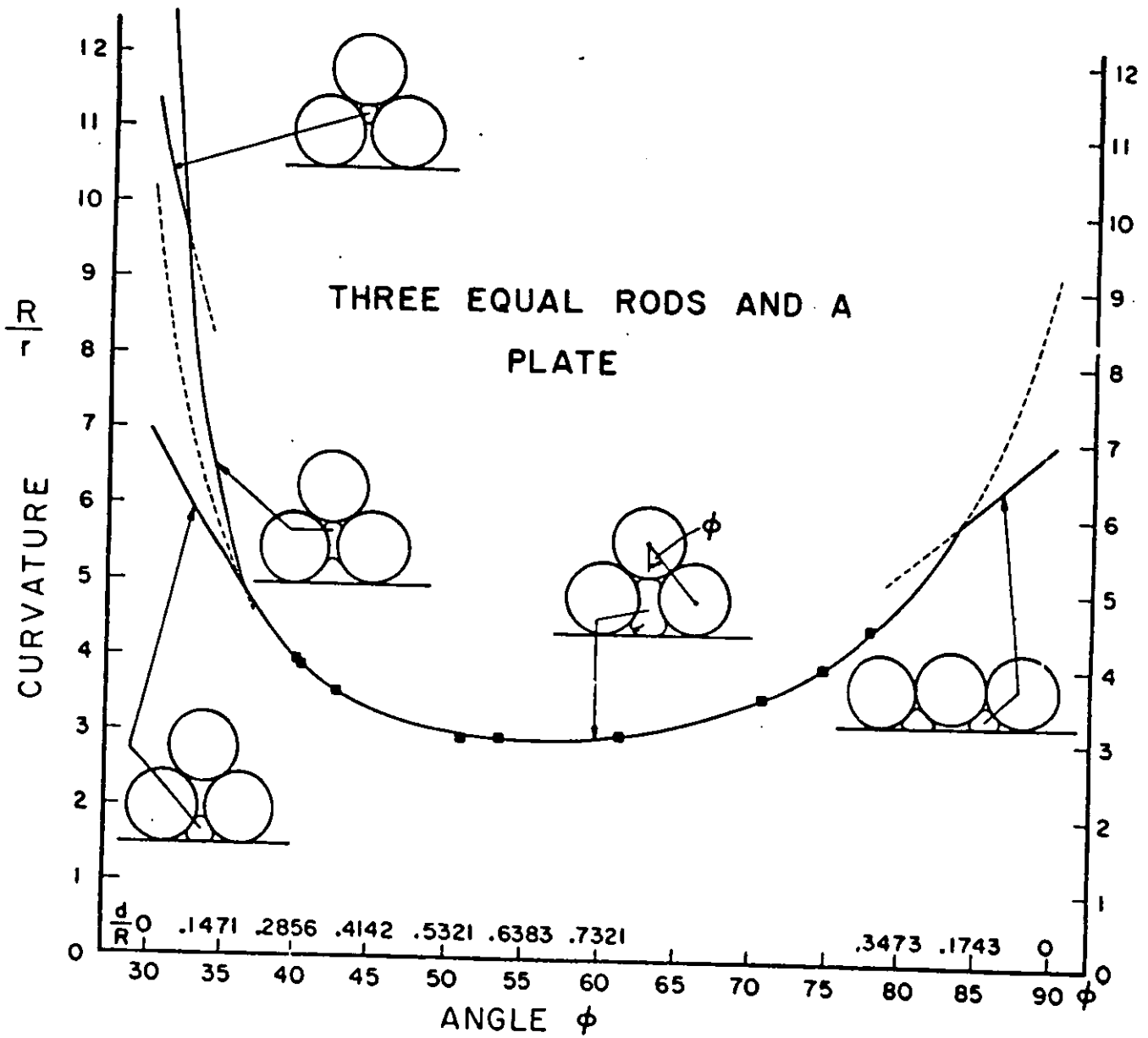


Figure 11.16 - Graph showing the experimentally determined curvatures at intermediate ϕ compared with the MS-P predictions for the case of three equal rods and a plate.

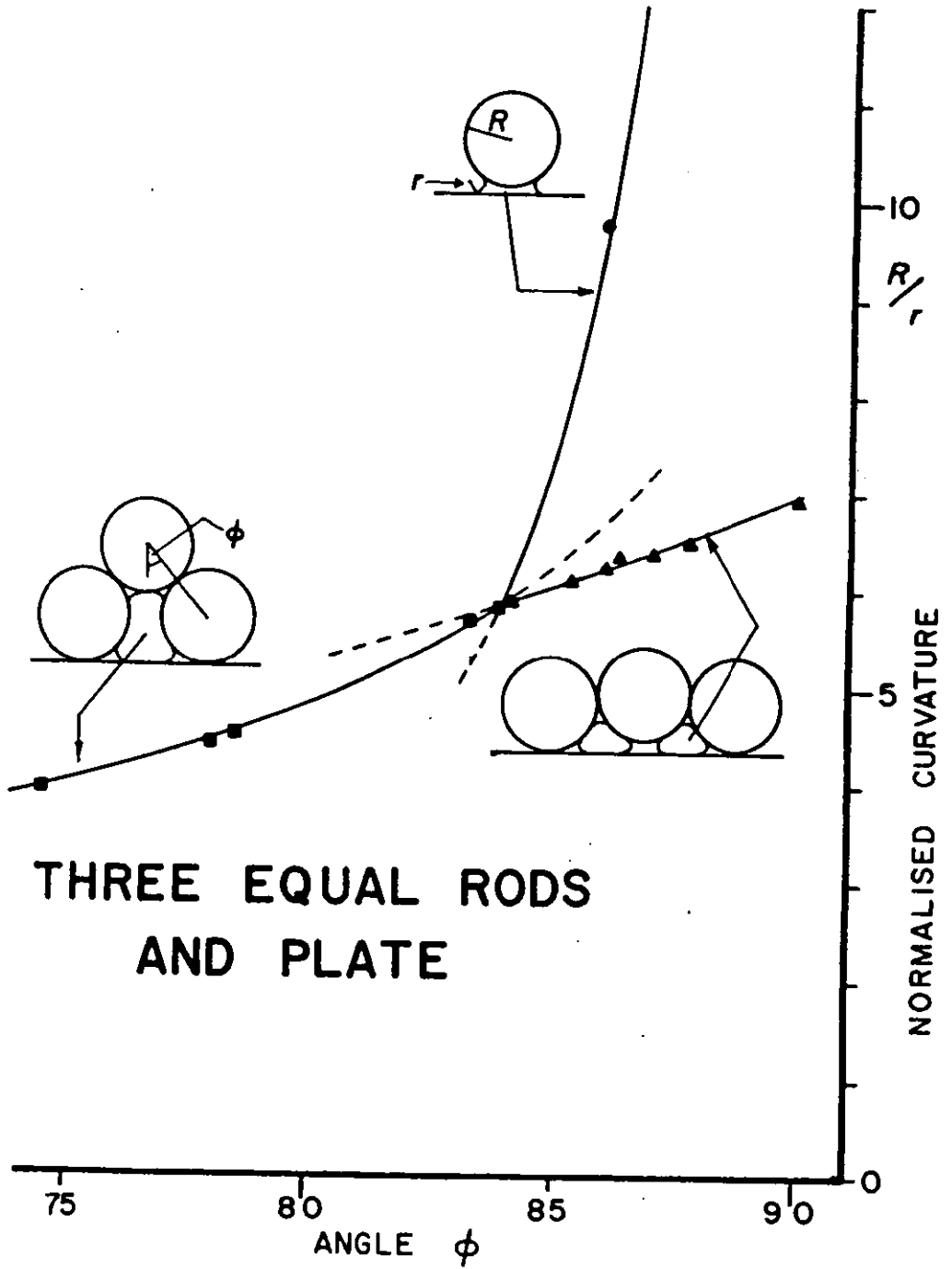


Figure 11.17 - Graph showing the comparison of experimental and theoretical curvatures for the three-equal-rods-and-a-plate system on an expanded scale at high ϕ .

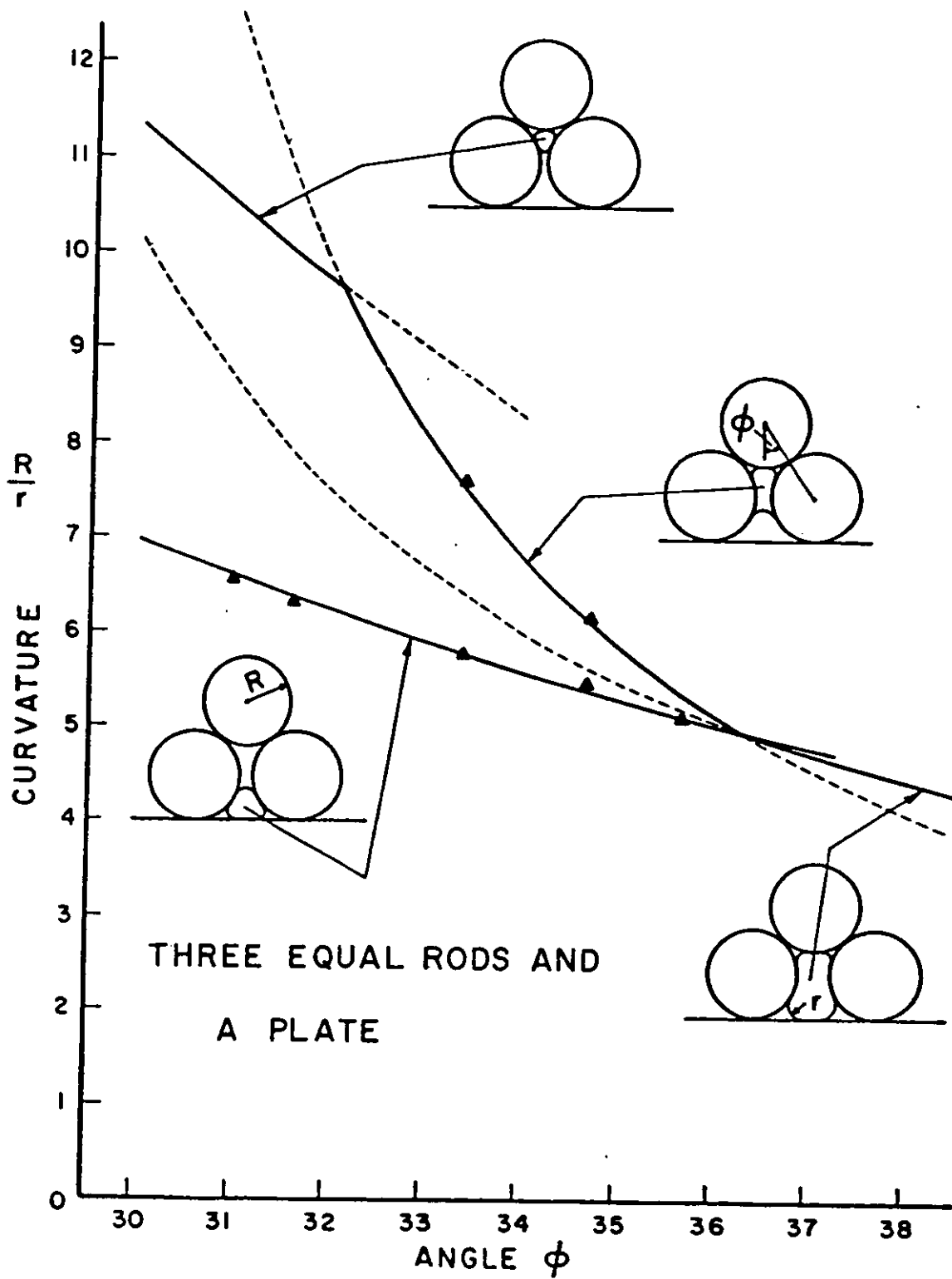


Figure 11.18 - Graph showing the comparison of experimental and theoretical curvatures for the three-equal-rods-and-a-plate system on an expanded scale at low ϕ .

The Figures show that the experimental results agree very well with the theory. The points show errors either side of their theoretical values. These errors are mostly within 1%, notable exceptions being the results for the *type H* TM, two WOAMs, where the rate of change of curvature with ϕ is greatest.

It was whilst these experiments were being performed that the idea of using the three rod arrangement as a standard arose. For a relatively large range of ϕ the curvature of the *type E* TM hardly changes. (For $52^\circ \leq \phi \leq 60^\circ$, $2.95 \leq R/r \leq 3.00$). Errors in the manufacture of the pore construction components and the measurement of ϕ will have a very small effect on the resulting curvature making the arrangement a suitable standard (see chapter 8)

11.4.2 Unequal rods symmetrically arranged

With the centre rod replaced by a rod of different size the complexity of the system is increased and different relationships between curvature and ϕ result. Two arrangements were investigated, one with the centre rod twice the size and the other with the centre rod half the size of the side rods.

a) $R_1 = 1/2R_2 = R_3$

Figure 11.19 shows both the theoretical and experimental results for this arrangement. The half angle, ϕ , varies between a minimum of about 19.5° to a maximum of 70.5° . The overall appearance of the theoretical curves change little from those for equal rods but the relative proportion of ϕ values for which *types A, B, C* and *D* TMs exist, is smaller and that where *types F* and *G* are seen, significantly greater. It was in this latter area in which the investigation centred. It was thought that the larger middle rod would particularly benefit readings on the *type G* TAM and this was borne out in practice. Experimental results are mostly within 1% of their theoretical values, all within 2%.

b) $R_1 = 2R_2 = R_3$

With the centre rod now half the size of the side rods the curves shown by Figure 11.20 are found. The minimum value of ϕ is 41.8° and its maximum 109.5° . It is now the region for which *types A, B, C* and *D* TMs exist that is the most fully developed area of the graph. It was hoped that the larger gaps obtainable between the side rods (rod-rod separation) when these menisci are present would facilitate better observation of the rearmost menisci. The experiments did not prove successful in this respect. The greater rod-plate separations resulted in increased difficulties in illuminating the back menisci and poorer, not better visibility.

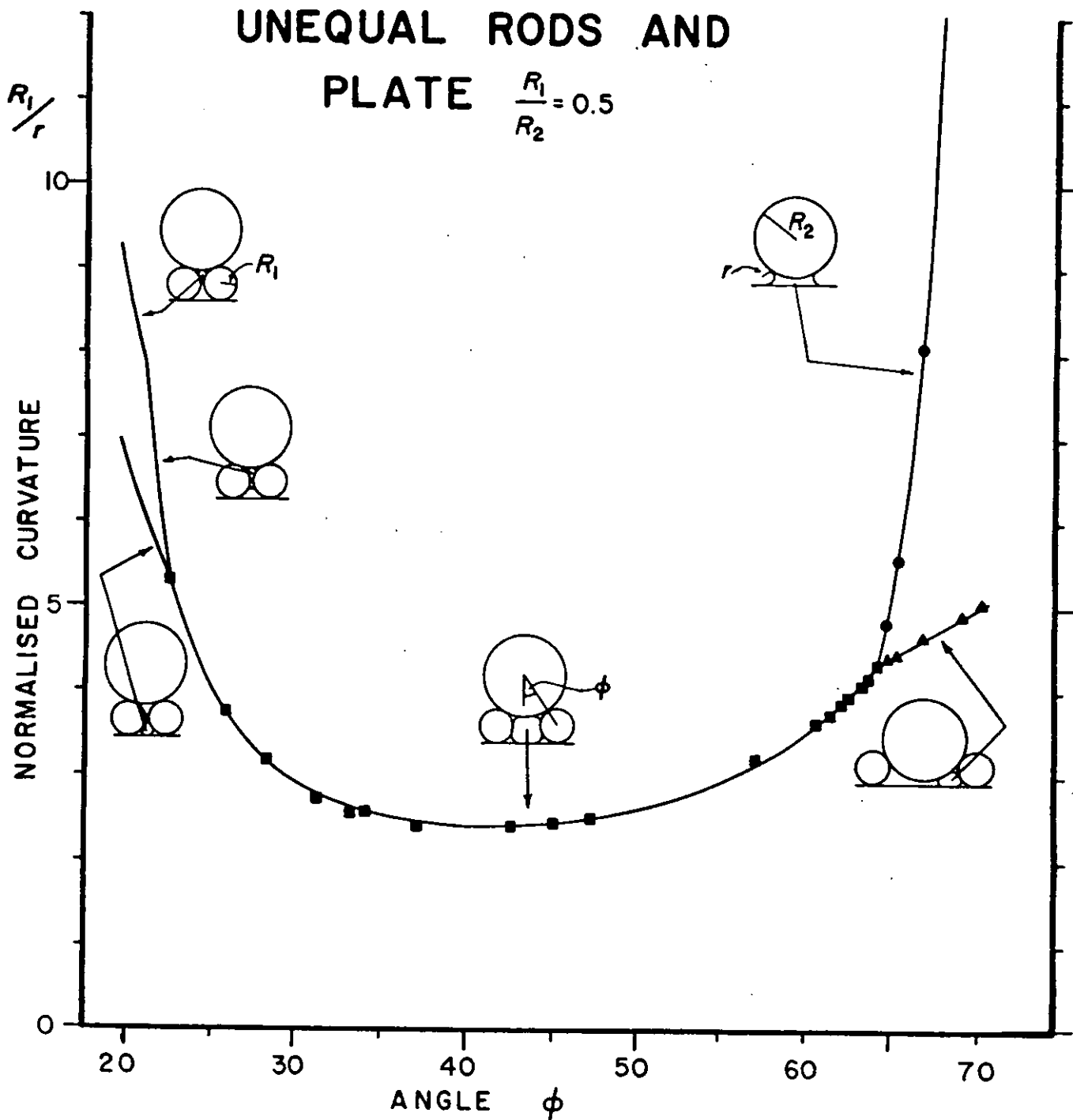


Figure 11.19 - Graph showing the comparison of experimental and theoretical curvatures for the case of three unequal rods, symmetrically arranged ($R_1 = 1/2 R_2 = R_3$)

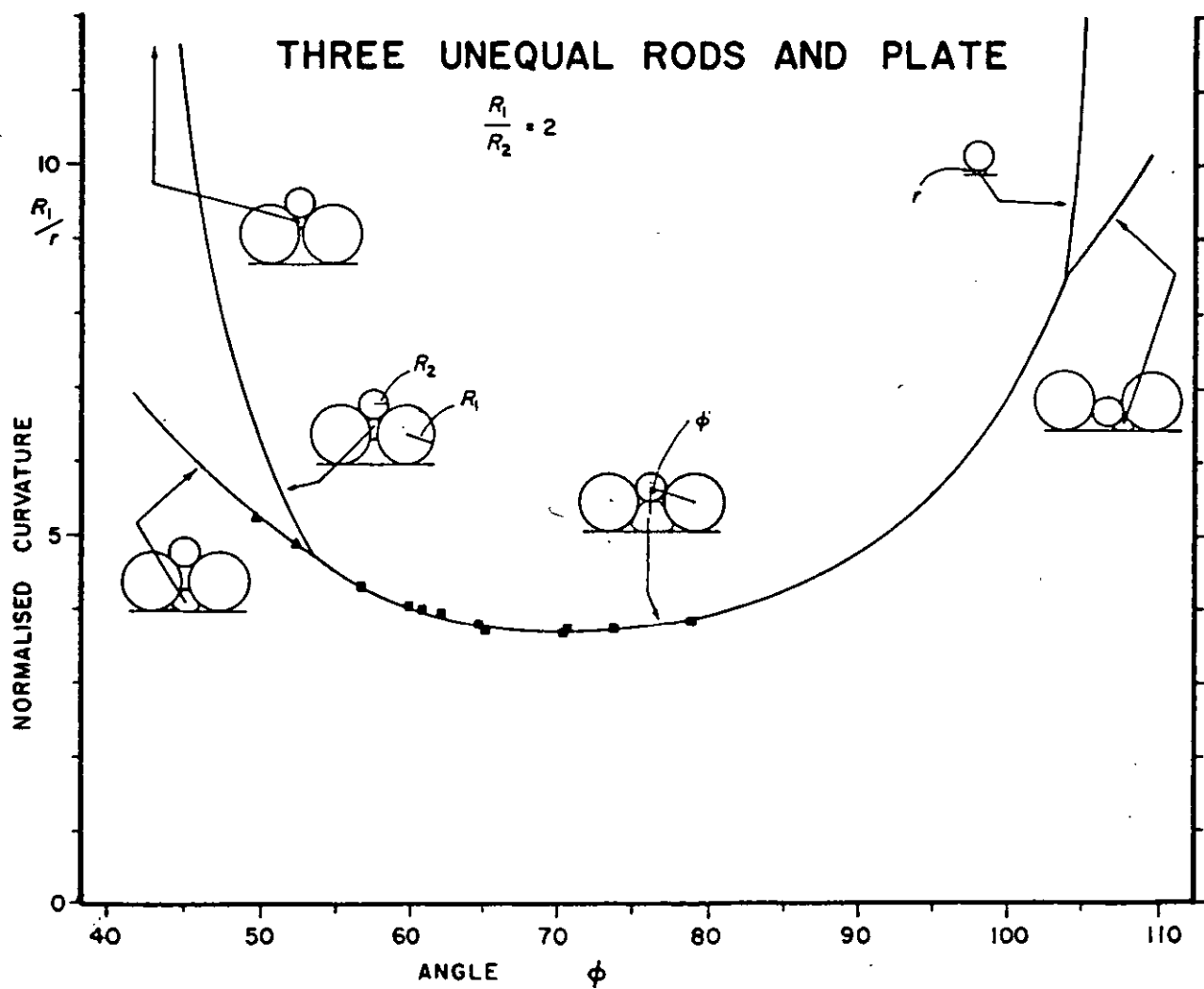


Figure 11.20 - Graph showing the comparison of experimental and theoretical curvatures for the case of three unequal rods, symmetrically arranged ($R_1 = 2R_2 = R_3$)

The assembly of cells at high ϕ was not possible with the existing cell designs. For $\phi > 90^\circ$ the centre rod is no longer held by the larger side rods and falls against the plate. The region for which *types F* and *G* are formed is, in any case, not well developed and would further increase the complexity of experiments at high ϕ . The comparatively few measurements that were obtained showed good agreement with theory, almost all within $\pm 1\%$.

11.4.3 Unequal rods non-symmetrically arranged

In this arrangement it is one of the side rods that is of a different size to the other two equal rods. The arrangement is by far the most interesting example of the three rod systems studied as it shows the full range of behaviour and all eight TMs are exhibited.

Only the arrangement for which $R_1 = R_2 = 2R_3$ was investigated. Now, with the three rods all in a row, the two separate pores hold menisci with different curvatures. As the separation is decreased there are two stages to the behaviour before the two pores become one. First the two back-to-back WOAMs give rise to a *type H* TAM between the two *type F* TMs. The second stage occurs when the curvature of the TAM falls below that of the *type F* TM in the smaller of the two pores. A *type G* TM, comprising two DCAMs and one WOAM, is now formed before reversion to a *type E* TM.

Experimentally the arrangement is of most interest at high rod separations where five TMs can be observed through the glass plate (a distinct advantage). To have assembled the rods at low separations would require complex cell designs and not reveal anything new.

Figure 11.21 shows the experimental results compared to the theoretical predictions. Referring to the figure, at low ϕ the arrangement behaves as a single pore exhibiting a *type E* TM. At high ϕ the system behaves as two separate pores each holding *type F* TMs and at intermediate values of ϕ the effect of one neighbouring pore on the other becomes important.

The curves of Figure 11.21 show a wonderful illustration of the effect of one two-rod-pore on another. At intermediate separations the curvature is not set by the two-rods-and-a-plate arrangement, but depends on how the third rod is positioned.

The experimental results show excellent agreement with the theory (mostly within $\pm 1\%$), both in terms of the curvature and in the change in meniscus types. These results show the power possessed by the MS-P method to predict the effects of one pore on another in addition to its now well proven abilities at predicting curvatures in uniform pores.

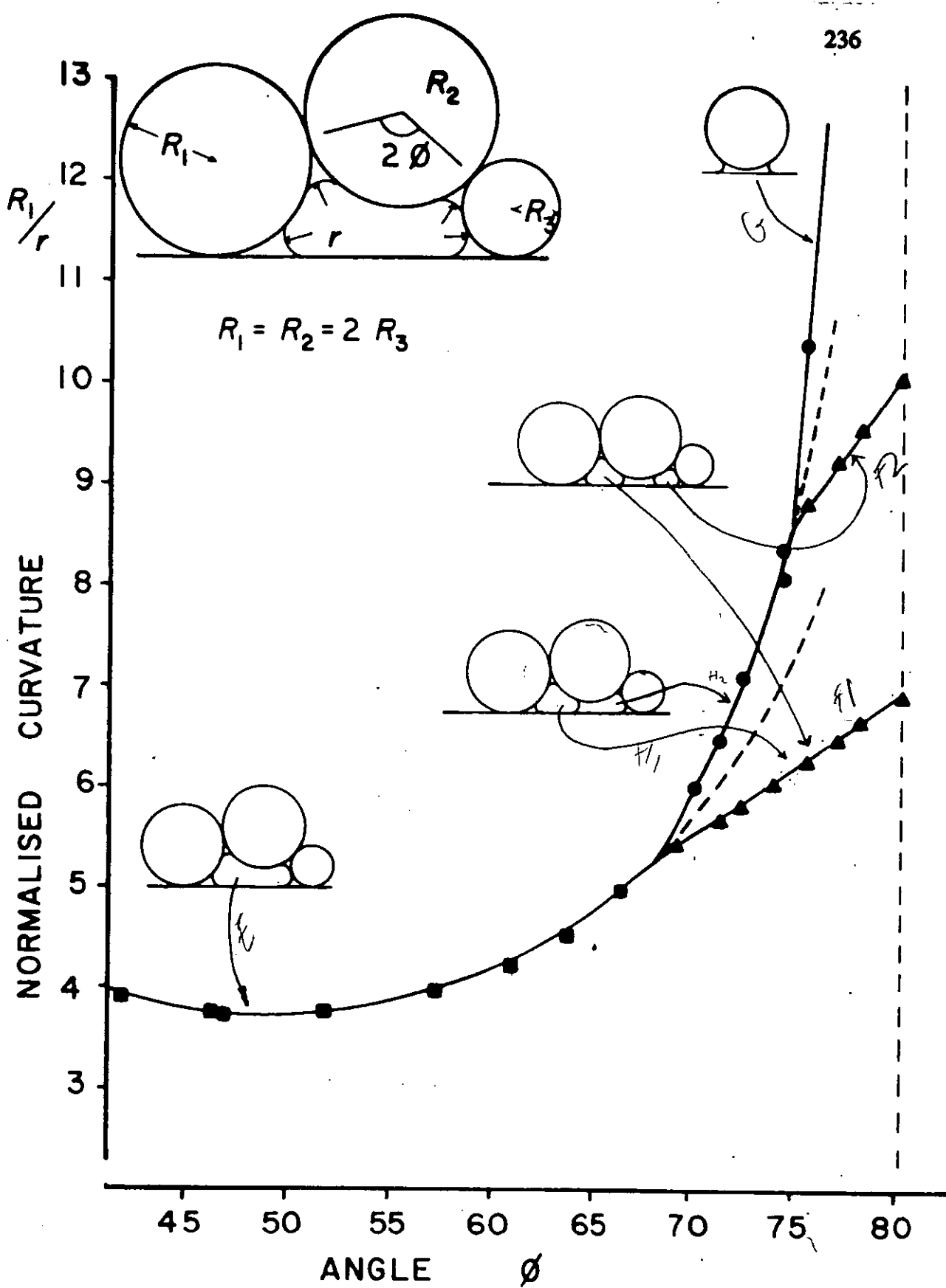


Figure 11.21 - Graph showing the comparison of experimental and theoretical curvatures for the case of three unequal rods, non-symmetrically arranged ($R_1 = R_2 = 2R_3$). Note that now a type C TM is formed before the reversion to a type E TM.

11.4.4 General observations

The results just presented for the various three rod arrangements all exhibit excellent agreement with the theory. If the error inherent to the measurement of the half angle, ϕ , is taken into consideration then almost all the data could be made to fit the theoretical curves. Even the points showing the worst error, those for the *type H* TM where curvature changes rapidly with ϕ , would come into close agreement with theory. When the *type H* TM was studied in its own right, section 9.3, the agreement with theory was excellent. The conclusion that the best way to measure an arrangement's half angle is to measure the curvature of the meniscus it holds and then compare it with the theory is inescapable!

The general trend of the experimental data is for curvatures to be slightly less than those predicted by the theory which is consistent with previously discussed dimensional variations in the pore construction components and distortion of menisci by gravity.

Beyond the use of the comparative method no attempt has been made to correct the data for gravitational distortion. Application of the Jurin correction would be wholly inappropriate to many of the menisci formed as they bear no resemblance to the hemispherical shape assumed in equation 7.8. Estimation of the actual corrections, required to be applied to each meniscus to adjust heights of rise to those corresponding to average curvatures, would present difficulties unjustified by the magnitude of the errors. Incidentally, for menisci with flatter profiles the heights actually measured will correspond quite closely to the average curvature when compared with the more spherical menisci. Hence, errors in these curvatures arising from gravity will be significantly less.

In section 11.2 it was noted that at higher values of ϕ associated with the *type E* TM a small "hump" arose in the middle gap with symmetrically arranged rods. This occurs before the theory predicts a transition to *types F* and *G* TMs. Shown on Figure 11.22 are the maximum and minimum observed curvatures for a meniscus in this region. The minimum heights of rise yield curvatures that agree well with predictions for a *type E* TM, implying that it is this TM and not *types F* and *G* that is seen. However the shape of the profile suggests that back-to-back OAMs exist, if only partially developed. A possible explanation for this seeming paradoxical situation may be attributed to the capillary rise method. The method depends on, and suffers from, the changing curvature of the liquid vapour interface with height above the free liquid surface.

Figure 11.22 also shows a plot of normalised centre rod spacing from the plate, R_2/D , versus the half angle, ϕ . The point at which this crosses the curve for the *type F* TM (marked X) represents the point at which the two back-to-back OAMs would meet and so rupture had one of the side rods been removed. The point where this curve crosses the *type E* TM curve (marked Y) represents the separation at which a pair of back-to-back OAMs would rupture had both side rods been removed.

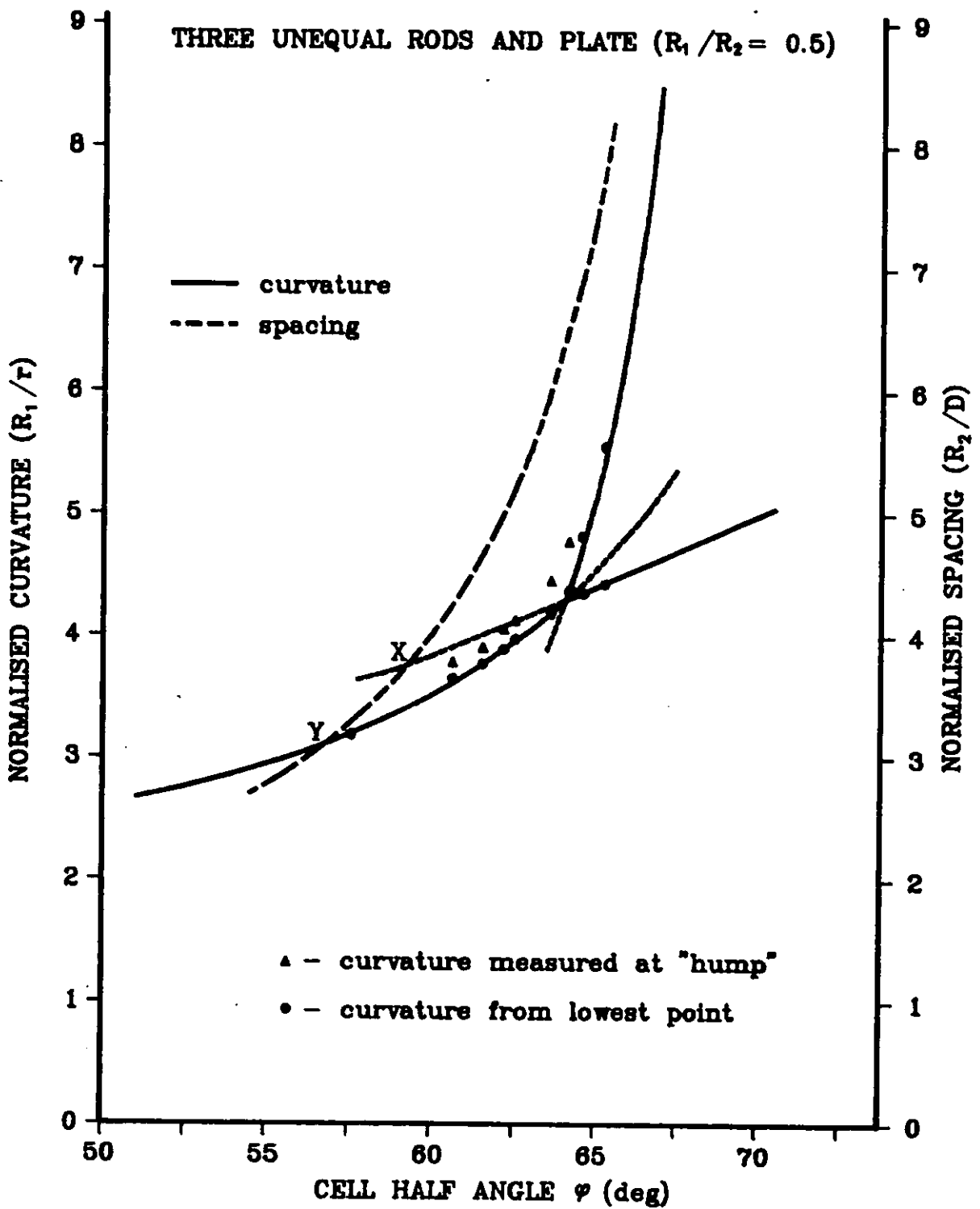


Figure 11.22 - Graph showing the maximum and minimum observed curvatures in the "hump" region between TMs of types *E* and *F*. Also shown is a plot of normalised centre rod spacing from the plate versus the half angle.

As the liquid/vapour interface in a capillary is able to alter its curvature depending on its height, it may be possible for the OAMs to exist at ϕ values greater than X . The small "hump" probably arises from capillary rise from the flatish surface of the *type E* TM. Results show the effect occurs without causing excessive distortion of the remainder of the surface.

CHAPTER 12

Principal findings, further work, and conclusions

Over the previous chapters the investigative procedures and experimental results have been presented and discussed. From the results a general conclusion may be drawn:

The experiments performed show that the curvatures of non-axisymmetric menisci in uniform tubes can, when gravity effects are small, be predicted by the MS-P method.

Here, by way of a summary of the preceding chapters, the main findings of the study are chronicled before suggestions for further work are made and the conclusions of the work detailed.

12.1 APPLICATION OF THE MS-P THEORY

The study has brought together existing ideas and methods of calculating the curvature of menisci in tubes of arbitrary, but uniform, cross-section. When arc menisci do *not* form the hydraulic radius method may be used, but when AMs exist the MS-P method must be used if significant errors are not to be introduced. The main problem in applying the MS-P theory is the determination of exactly where the AMs form.

The MS-P equation (eq. 6.12) may be derived via consideration of the energies or forces involved or directly from the Gauss equation of capillarity. The theory is exact only for menisci of constant mean curvature, as the respective derivations assume. It may be necessary, as with the three rod pores or if the AM arrangement is uncertain, to calculate the meniscus curvature for several possible configurations and assume that the actual curvature adopted will be the one with the lowest curvature.

The effect of changing wettability in a system of fixed geometry has been discussed. In these cases there can be a contact angle at which the AMs cease to exist, and this must be reflected in the analysis. The effect was illustrated by the analysis of the n-sided polygonal tubes which have particular contact angles at which the arc menisci disappear (section 6.4.1.2). In principle, the MS-P theory may be applied to estimate the meniscus curvature of any particular pore geometry and at any particular contact angle, the limitation being the tractability of the resulting equations. It may be applied to menisci having either open or closed capillary rise profiles.

In this study a standardised method was developed for the application of the theory to arbitrary-sectioned uniform tubes. The method's basis is the division of the pore cross-section into a number of simple geometric regions, each having a perimeter bordering the section of the particular terminal meniscus, and usually an area and angle. The division into such regions enables simpler calculation of the effective area to perimeter ratio. It also has the advantage that in pore shapes where more than one stable TM can exist the expressions for the angle, area and perimeter of particular regions may be re-used as required.

A standard computational routine was developed in conjunction with the above application method that enables re-use *en-block* of major procedures. The relevant equations for region areas and perimeters of any TM need only be inserted into an iteration program based on a successive bisection and interpolation technique. With only minor adjustments of input and output procedures sets of solutions for curvature in terms of either a geometric or wetting variable are given.

The tubes investigated are all made up of simple geometric components. Solving the equations for the radius of curvature when the contact angle is zero was relatively straightforward, only one numerical iteration is required. However, even with the simple geometrical units the analysis can become quite involved, particularly when the contact angle is also a variable. With the two-equal-rods-and-plate arrangement under mixed wetting conditions two iterations were required. It must be expected that when the method is applied to more irregular shapes more powerful computing techniques than those employed here will be needed in order that the resulting multiple iterations can be performed speedily.

12.2 EXPERIMENTAL APPARATUS AND PROCEDURES

The apparatus utilised for the experiments had evolved during investigations conducted before this study by Mason and co-workers. However during the course of the experiments some further development and several modifications to the apparatus and procedures were required. These have significantly contributed to the increased accuracy of the results presented here.

- a) The new Gaertner cathetometer (section 7.2.3) undoubtedly improved the ease and the accuracy of the capillary rise measurements compared to those taken with the older instrument.
- b) The better tolerance of the needle rollers provides an advantage over the HSS drill blanks, significantly reducing the dimensional errors in the constructed pores. However, drill blanks are still required for their extensive size range and greater length, particularly with the smaller rod sizes.

c) Developments needed to be made in the area of cell design to enable the observation of curvatures of menisci in awkward arrangements. Of particular advantage was the practice of clamping together the pore construction components. The use of the clamping technique contributed to the reduction in dimensional errors and represents a significant improvement on the "precisely" machined channels previously employed.

d) A new procedure was developed for experiments using partially and mixed wetting conditions in order that due account could be made of contact angle hysteresis between advancing and receding menisci.

12.3 STANDARD CONFIGURATIONS AND THE FULL COMPARATIVE METHOD

In chapter 8 the experiments performed to determine the curvatures in selected standard configurations were reported. A repeat of Mason & Morrow's (1984a) experiments using the full comparative method with the two-equal-rods-and-plate arrangement provided an improved value for the normalised curvature, the error from the predicted curvature rising from - 1.3% to only - 0.4%. A further set of experiments investigated the potential use of the three-rods-and-a-plate system as a standard; with advantage being taken of particular rod arrangements where the MS-P theory predicts a curvature that is virtually independent of the geometry. Uncorrected results from the full comparative method were not so encouraging, giving a error of + 1.3% from the predicted value. However the results were distorted by the use of capillary tubes giving heights of rise in a different range to the assembled pores.

Using the results obtained from these standard configurations a detailed account was made of the likely experimental errors - principally the opposing effects arising from gravitational distortion of menisci and dimensional variations in pore geometry. The near-hemispherical shape of the menisci in both standard configurations enabled an approximate application of the Jurin correction for gravity distortion. This led to improved estimates of the meniscus curvatures; errors from the predicted values were only - 0.3% for both systems. The Jurin correction seemingly giving an excellent correction for the different levels of distortion in the rod pores and cylindrical tubes when heights of rise are dissimilar. Its validity was confirmed by its agreement with a calculated value for the height of rise in the reservoir indicator cell.

Furthermore, it has been shown that the Jurin correction can provide a satisfactory correction for gravity distortion in cylindrical tubes for heights of rise down to as little as 3 mm. This result, if also applicable to the assembled pores, implies that both comparative methods may be used for heights of rise greater than 3mm and significantly enlarges the "window of opportunity" in the scale of the apparatus that enables the

effective use of capillary rise methods. Some further experimental work is required to show that these results for the tubes are approximately correct for the menisci in the rod assemblies. The work with the Jurin correction also produced an alternative relationship for the calculation of observed curvatures measured with the simplified comparative method. This expression is only applicable in cases where menisci are near-hemispherical and when heights of rise are within the validated range of 7 to 25 mm.

A rough quantitative account was also made of the effect on the observed height of rise, of the slope of the liquid wedges which are held behind arc menisci. The wedges slope owing to the direct relationship between curvature and height that is the basis of capillary rise methods. The effects were found to be small across the height ranges investigated. Without application of corrections the validity of the comparative method was confirmed for heights of rise in the range 7 to 25 mm with the optimum range, where the opposing effects of gravity and dimensional variation give minimum errors, is between 10 and 15mm.

When combined with a quantitative investigation into dimensional errors the above analyses allow the conclusion that differences between observed and predicted curvatures can be accounted for by the experimental error. Either standard should afford adequate comparison for the simplified method provided the rods are correctly assembled. Small dimensional errors incurred by incorrect assembly and/or rod tolerances will have a significantly larger effect on the curvature in the two rod system, thereby favouring the use of the three rod standard. However, the latter system requires much smaller rods to produce a pore giving the same height of rise as a two-rod pore, inevitably leading to relatively larger dimensional variations as these increase with decreasing pore size.

Overall the full comparative method experiments provided the information necessary to optimise the experimental procedures and it is difficult to imagine a more exact method utilizing capillary rise.

12.4 INVESTIGATIONS WITH THE SIMPLIFIED COMPARATIVE METHOD

12.4.1 Perfectly wetting conditions

In chapter 9 the results of experiments conducted in four different pore shapes with a perfectly wetting liquid were compared with the theoretical predictions of meniscus behaviour. Results, obtained with the simplified comparative method were generally in excellent agreement with the theory and all within the determined experimental error.

a) Rectangular tubes

The theory for this geometry can be obtained analytically. Experiments proved much more difficult. The other pore shapes are made up from rods where the pore size is much smaller than the rod size. When a rectangular pore is made it is difficult to fabricate small square corners to the same degree of accuracy as the rod pores. Eventually a cell design based upon a stack of precisely machined plates was adopted. Reasonably successful results were found over a range of tube sizes and aspect ratios. Almost all the observed curvatures fell within 4% of the predicted values.

b) One rod away from a plate

The meniscus formed in the space in-between a rod and plate is anticlastic and has an open capillary profile. The meniscus behaviour is however relatively straightforward and no particular problems were encountered with the theory or experiments. Measured curvatures are in good agreement with the theory, most within 1% and all within 2.5%. These results represent a significant improvement over the limited (and secondary) observations made by Mason & Morrow (1987) who found errors as great as 15%.

c) One rod in a corner

Previous studies had involved rods in right-angled and acute corners. That work was confirmed and extended to cover the general angle. Experiments showed less than 1% deviation from the theory once a correction for gravitational distortion was added to the measured heights of rise (a significant improvement in accuracy).

d) Two unequal rods and a plate

The meniscus behaviour in this arrangement is again relatively straightforward, although application of the theory is more involved. Results agree excellently with the theory - generally within 1% of predicted curvatures. This arrangement was selected as the basis for a short paper to demonstrate the use of the MS-P method which was presented at the IUPAC conference on the characterisation of porous solids (Mason, Morrow & Walsh 1988 - see Appendix A).

12.4.2 Non-zero contact angle

For a limited number of cases the effect of contact angle variation was studied to determine whether the MS-P method is still accurate (see chapter 10). The theory becomes much harder to apply for non-zero contact angle; in some cases a second iteration being required for solution. More problematic however was the irreproducibility of contact angle which made the experiments much less precise than those with zero contact angle. In addition the use of less accurate PTFE components meant that pore geometry was not as precisely known.

a) One rod away from a plate

The capillary behaviour of the meniscus in the varying space between a rod and a plate when the contact angle of the liquid with the solid is also varied provides an insight into the complex behaviour that can be expected with mixed wettability systems. The geometry is straightforward, but the behaviour produced is far from simple.

The investigation of the system under perfectly wetting conditions had shown that the meniscus curvature between the rod and the plate is primarily determined by the size of the gap, gradually increasing to approach that between two parallel plates as the gap is decreased. As the contact angle is increased from zero at a given spacing the curvature decreases until at 90° the curvature is zero. There is also a region where the two WOAMs meet back-to-back and no stable terminal meniscus is possible. The interactions between the above effects were displayed on a three dimensional diagram (Fig. 10.2)

Experiments were performed using a homologous series of liquids for both advancing and receding contact angles in pores of uniform wettability. In so far as the experiments were precise enough the theory was confirmed by the experiments.

b) Two equal rods and a plate

This arrangement has the advantage that it can be assembled with mixed wettability by making either or both the rods or plate partially wetted. The totally partially wetted system was the subject of an early investigation by Mason, Nguyen & Morrow (1983) which originally gave rise to this present work. Application of the theory when the contact angles on the three surfaces are all different is very involved. It predicts that making the rods partially wetted does not make as much difference as making the plate partially wetted. A consequence of the wetted perimeter of the plate being larger than that of the rods.

Experiments were performed on three arrangements, all with a partially wetted plate. The instances where both, one or neither of the rods are partially wetted were investigated. The data obtained was again much less precise than that for the perfectly wetted system. Results for the totally partially wetted system showed a slight improvement over those of Mason *et al.*'s study.

Perhaps more important was the confirmation of the theory in the mixed wettability systems. As explained in section 3.5.1 surface heterogeneity, and hence mixed wettability, is almost the norm for oil bearing rocks. The presence of individual rock grains in a pore structure that may or may not be wetted by the oil makes the capillary behaviour very curious. There is currently a large interest in these mixed wettability rocks (see Anderson 1987a) and the results presented here may shed some light on the oil behaviour and could contribute significant advances to enhanced oil recovery techniques.

12.4.3 Investigations with neighbours

As described in chapter 11 the space enclosed by three parallel rods and a plate gives rise to a complex family of interacting terminal menisci as the cell half angle is varied. Depending on the rod geometry the arrangement may yield two separated pores, two interconnected pores or a single pore. When the two pores are interconnected the effect of the meniscus behaviour in one neighbouring pore on the behaviour in the other becomes important.

The theory applied to this arrangement is involved, but yields the curvatures of the eight possible terminal menisci. Determination of which type of TM exists in the particular geometry was effected with the minimum energy criterion. The particular half angles where one meniscus gives way to another can be determined with the theory.

Experiments, covering the entire range of behaviour, were performed on four systems; three equal rods, two systems of unequal rods symmetrically arranged and a system of non-symmetrically arranged unequal rods. All observed curvatures were for zero contact angle. That the predictions of the MS-P theory have been so closely confirmed by experiment (mostly to within 1%), both in terms of the meniscus curvatures and for the transitions from one type of TM to another, is indicative of the true power and exactness of the theory and represents the finest achievement, to date, of the MS-P method.

It is expected that the properties of these model pores will be able to illuminate the behaviour of adjacent pores in a porous medium undergoing drainage or desorption. For example, at certain half angles the unequal rods, non-symmetrical arrangement gives rise to the *type H* TM. The curvature of this TM in the interconnected pores is not set by the geometry of a particular two-rods-and-plate arrangement, but depends on how the third rod is positioned. Extended to a porous material this means that a particular geometry cannot be unambiguously deduced from a capillary pressure or meniscus curvature measurement. This result has obvious bearing on pore sizing methods such as mercury porosimetry, thermoporometry and Kelvin analysis.

12.5 FURTHER WORK

The work reported in this thesis does not complete the validation of the MS-P method, but rather serves as a comprehensive introduction to it. There are an almost limitless number of pore shapes to which the method might be applied, but for future investigations it would be prudent to keep potential applications in mind.

A further step is the application of the method to model uniform pores that are more like real systems. Some work is now proceeding in this area. During the course of this study Mason & Morrow (1989) have applied the theory to triangular pores resembling real pores observed in some rocks. Some success was noted as regards the modelling of some aspects of capillary pressure hysteresis (see section 3.5.2). At the time of writing an undergraduate project supervised by Mason is investigating a two rod arrangement where the rods have had precise flats ground on (such that the rod sections are circle segments). These model pores resemble some consolidated oil reservoir rocks where grains are dissolved away at points of contact. Initial results are promising. If the work is extended to mixed wettability, situations will arise where the arc menisci in the corners will not necessarily exist.

It would also be desirable to apply the flats and/or mixed wettability to the three rod arrangement. These systems could be used as models for hysteresis in drainage and imbibition capillary pressure. They would possess some realistic properties; neighbouring pore effects, an irreducible wetting phase saturation, and with certain geometries the configurations of a receding (draining) meniscus will differ (having a higher curvature) from that of the advancing (imbibing) meniscus. Furthermore, if the above hysteresis models were combined with percolation theory (section 3.5.3) network effects could be incorporated; pore connectivity and pore blocking effects. Validatory experiments could be performed on small scale networked models in the manner of Lenormand (1983). A truly realistic and versatile model could result.

Unfortunately there is probably a limit to the complexity of uniform pore shapes that can be conveniently analysed with the method. Even with some relatively straightforward configurations studied here under variable wetting conditions (such as the two rod system) the theory becomes quite complex. It would be advantageous to investigate more complicated shapes and ascertain these limits.

12.6 CONCLUSIONS

- 1) A general routine has been developed for the application of the MS-P theory based on the division of pore sections into simple geometric regions. This technique has proved successful in the analysis of the behaviour of even quite complex capillary surfaces in non-axisymmetric uniform tubes.
- 2) Previously developed experimental procedures for the validation of the MS-P theory have been modified and extended. Investigations with either the full or simplified comparative method have yielded results of improved accuracy in excellent agreement with predictions.

- 3) A particular three rod and plate arrangement has been investigated and is proposed as a new general standard, advantage being taken of a meniscus with a curvature that is virtually independent of the particular geometry.
- 4) The experiments reported in this study lead to the conclusion that the behaviour of non-axisymmetric menisci in uniform tubes can, when gravitational effects are small, be predicted by the MS-P method. This statement applies to both open and closed capillary profiles in tubes of perfect, partial or mixed wettability.
- 5) The results presented indicate that the MS-P method can enjoy a wider usage in research and development concerning the measurement of liquid properties; interfacial tension, contact angle and solderability; the behaviour of fluids in partially saturated porous media; characterisation methods and in the modeling of capillary pressure hysteresis, two phase fluid flow and enhanced oil recovery operations. These are in addition to a now proven ability to predict interfacial configurations of the particular class of capillary surfaces that are bounded by uniform non-axisymmetric tubes.

BIBLIOGRAPHY

-
- Adam, N.K. 1958 *Endeavour* Jan., 37.
- Adamson, A. W. 1976 *Physical Chemistry of Surfaces* (Wiley-Interscience, New York), 3rd ed.
- Anderson, W. G. 1986a *J. Pet Technol.* Oct. 1125.
- Anderson, W. G. 1986b *J. Pet Technol.* Nov. 1246.
- Anderson, W. G. 1986c *J. Pet Technol.* Dec. 1371.
- Anderson, W. G. 1987a *J. Pet Technol.* Oct. 1283.
- Anderson, W. G. 1987b *J. Pet Technol.* Nov. 1125.
- Arriola, A., Willhite, G. P. & Green, D. W. 1980 *55th Ann. Fall Conf. of SPE-AIME*, Dallas, Texas, Preprint No. 9404.
- Ashton, P. T. & Cable, A. S. 1985 *The Study of Meniscus Curvatures in Capillaries of Various Cross Section* Final yr. Project (Dept. of Chem. Engng., LUT, Loughborough).
- Bakker, G. 1928 - quoted in Paddy 1971 p266.
- Barker, J. A. 1958 *The Structure and Properties of Porous Materials* eds. D. H. Everett & F. S. Stone *Colston Papers* No. 10 (Butterworth, London) p125.
- Bashforth, F. & Adams, J. C. 1883 *An Attempt to Test the Theory of Capillary Action* (Cambridge University Press).
- Bell, W. K., van Brackel, J. & Heertjes, P. M. 1981 *Powder Technol.* 29, 75.
- Benjamin, J. B. & Cocker, A. D. 1984 *Proc. Roy. Soc. Lond.* A 394, 19.
- Bikerman, J. J. 1970 *Physical Surfaces* (Academic Press, New York).
- Boucher, E. A. 1978 *Proc. Roy. Soc. Lond.* A 338, 519.
- Boucher, E. A. 1980 *Rep. Prog. Phys.* 43, 497.
- Boucher, E. A. & Kent, H.J. 1977a *Proc. Roy. Soc. Lond.* A 356, 61.
- Boucher, E. A. & Kent, H.J. 1977b *J. Chem. Soc. Faraday Trans. I* 73, 1882.
- Boucher, E. A. & Kent, H.J. 1978 *J. Chem. Soc. Faraday Trans. I* 74, 846.
- Boucher, E. A. & Evans, M. J. B. 1980 *J. Colloid Interface Sci.* 75, 2, 409.
- Boucher, E. A. & Jones, T. G. J. 1982 *J. Chem. Soc. Faraday Trans. I* 78, 2643.
- Boucher, E. A., Evans, M. J. B. & Jones, T. G. J. 1987 *Adv. Colloid Interface Sci.* 27, 43.
- Brown, R. A. 1979 *J. Comput. Phys.* 33, 217.
- Brown, R. A., Orr, F. M. Jr. & Scriven, L. E. 1977 *J. Colloid Interface Sci.* 73, 1, 76.
- van Brackel, J. 1975 *Powder Technol.* 11, 205.
- van Brackel, J. & Heertjes, P. M. 1978 *Physico-chemical Hydrodynamics* vol 1, ed. D. B. Spalding p119.
- Brunauer, S. 1945 *The Adsorption of Gases and Vapours* (Oxford University Press and Princeton University Press, Princeton, New Jersey, USA).
- Brunauer, S., Emmett, P. H. & Teller, E. 1938 *J. Amer. Chem. Soc.* 60, 309.
- Carli, F. & Motta, A. 1984 *J. Pharm. Sci.* 73, 197.
- Carman, P.C. 1941 *Soil Sci.* 52, 1.
- Carman, P.C. 1953 *J. Phys. Chem.* 57, 56.
- Carroll, B. J. 1976 *J. Colloid Interface Sci.* 57, 488.
- Carroll, B. J. 1984 *J. Colloid Interface Sci.* 97, 195.

- Cassie, A. B. D. 1948 *Discussions Faraday Soc.* 3, 11.
- Chatzis, I & Dullien, F. A. L. 1977 *J. Can. Pet. Technol.* 16, 97.
- Clark, W. C., Haynes, J. M., Mason, G. 1968 *Chem. Eng. Sci.* 23, 810.
- Clark, W. C. & Mason, G. 1967 *Nature* 216, 826.
- Clark, W. C. & Mason, G. 1968 *J. Appl. Chem.* 18, 240.
- Clough, A. P. & Daniels, P.I. 1986 *"The Analysis and Prediction of Capillary Rise in Different Pore Shapes"* Final Yr. Project (Dept. of Chem. Engng., LUT, Loughborough).
- Cohan, L. H. 1938 - quoted in Adamson 1976 p637.
- Concus, P. 1974 *Preprints, 48th National Colloid Symposium* Austin, Texas (Amer. Chem. Soc., Washington D. C.) p12.
- Concus, P. & Finn, R. 1969 *Proc. Nat. Acad. Sci.* 63, 292.
- Concus, P. & Finn, R. 1970 *J. Analyse Math.* 23, 65.
- Concus, P. & Finn, R. 1974 *Acta. Math.* 132, 179.
- Dodds, J. A. 1978 *Powder Technol.* 20, 61.
- Dullien, F. A. L. & Batra, V. K. 1970 *Ind. Eng. Chem.* 62, 25.
- Dupre, A. 1869 - quoted in Adamson 1976 p353.
- Eick, J. D., Good, R.J. & Neumann, J. 1975 *J. Colloid Interface Sci.* 53, 235.
- Emmerson, W. W., Bond, R. D. & Dexter, A. R. 1978 *"Modification of Soil Structure"* (Wiley-Interscience, New York).
- Erle, M. A., Dyson, D.C. & Morrow, N. R. 1971 *AIChEJ* 17, 115.
- European Space Agency (ESA) 1976 *Special Publ.* 114.
- Everett, D. H. 1958 *"The Structure and Properties of Porous Materials"* eds. D. H. Everett & F. S. Stone *Colston Papers* No. 10 (Butterworth, London) p95.
- Everett, D. H. & Haynes, J. M. 1972 *Z. Phys. Chem. Neue Folge* 82, 36.
- Everett, D. H. & Haynes, J. M. 1975 *Z. Phys. Chem. Neue Folge* 97, 301.
- Everett, D. H. (ed) 1975 *"Colloid Science"* vol. 2 (Chemical Soc., London.).
- Everett, D. H. 1988 *"Characterisation of Porous Solids"* eds. K. K. Unger, J. Rouquerol, K. S. W. Sing & H. Kral *Studies in Surface Science and Catalysis* vol. 39 (Elsevier, Amsterdam) p243.
- Fisher, R. A. 1926 *J. Agric. Sci.* 16, 492.
- Fisher, R. A. 1928 *J. Agric. Sci.* 18, 406.
- Fisher, L. R. & Isrealachvili, J. N. 1981 *J. Colloid Interface Sci.* 80, 528.
- Fowkes, F.M. 1965 *"Chemistry and Physics of Interfaces"* (Amer. Chem. Soc., Washington D. C.) p1.
- Fox, H. W. & Zisman, W. A. 1950 *J. Colloid Interface Sci.* 5, 514.
- Frevel, L. K. & Kressley, L. J. 1963 *J. Anal. Chem.* 35, 1492.
- Fricke, G. H., Rosenthal, D. & Welford, G. A. 1973 *AIChEJ* 19, 991.
- Furmidge, C. G. L. 1962 *J. Colloid Interface Sci.* 17, 309.
- Gauss, C. F. 1830 (Ger. Trans. 1903) - quoted in Hwang 1977 p226.
- Gibbs, J. W. 1872 - quoted in Jaycock & Parfitt 1987 p11.
- Gillette, R. D & Dyson, D. C. 1971 *Chem. Engng. J.* 2, 44.
- Good, R. J. 1979 *"Surface and Colloid Science"* vol. 11, eds. R. J. Good & R. R. Stromberg (Plenum Press, New York) p1.
- Graham, C. & Griffith, P. 1973 *Int. J. Heat Mass Trans.* 16, 337.

- Greenkorn, R. A. 1983 *"Flow phenomena in Porous Media"* (Marcel Dekker, New York).
- Gregg, S. J. & Sing, K. S. W. 1982 *"Adsorption, Surface Area and Porosity"* (Academic Press, London) 2nd ed.
- Guggenheim, E. A. 1967 *"Thermodynamics"* (North Holland, Amsterdam) 5th ed.
- Hackett, F. E. & Strettan, J. S. 1938 *J. Agric. Sci.* **18**, 671.
- Haines, W. B. 1925 *J. Agric. Sci.* **15**, 529.
- Haines, W. B. 1927 *J. Agric. Sci.* **17**, 264.
- Haines, W. B. 1928 *Nature* **122**, 607.
- Haines, W. B. 1930 *J. Agric. Sci.* **20**, 97.
- Hartland, S. Gapan, P. & Ramakrishnan, S. 1982 *Proc. R. Soc. Lond. A* **379**, 345.
- Hartland, S. & Hartley, R. 1976 *"Axisymmetric Fluid/Liquid Interfaces"* (Elsevier, Amsterdam).
- Haynes, J. M. 1975 *"Porous Media: Structures and Models"* ed. D. H. Everett *"Colloid Science"* vol. 2 (Chemical Society, London) p101.
- Haynes, J. M. 1989 *Private communication*.
- Heady, R. B. & Cahn, J. W. 1970 *Met. Trans.* **1**, 185.
- Herb, C. A., Buckner, J. L. & Overton, J. R. 1983 *J. Colloid Interface Sci.* **94**, 14.
- Higuti, I. & Utsugi, L. 1952 *J. phys. Chem.* **20**, 1180.
- Hosking, R. J. 1978 *"First Steps in Numerical Analysis"* (Hodder and Stroughton).
- Hotta, K., Takeda, K. & Iinoya, K. 1974 *Powder Technol.* **10**, 231.
- Huh, C. & Scriven, L. E. 1969 *J. Colloid Interface Sci.* **30**, 323.
- Hwang, S-T. 1977 *Z. Physik. Chem. Neue Folge* **105**, 15.
- Iczkowski, R. P. 1972 *AICHEJ* **18**, 864
- Jaycock, M. J. & Parfitt, G. D. 1987 *"Chemistry of Interfaces"* (Ellis Horwood, Chichester).
- Jenkins, R. G. & Rao, M. B. 1984 *Powder Technol.* **38**, 177.
- Johnson, R. E. Jr. & Dettre, R. H. 1964a *Advan. Chem. Ser.* **43**, 112.
- Johnson, R. E. Jr. & Dettre, R. H. 1964b *J. Phys. Chem.* **68**, 1744.
- Jurin, J. 1718 *Phil. Trans.* **29-30**, 739.
- Katan, T. & Grens, E. A. 1971 *J. Electrochem. Soc.* **18**, 1881.
- Keey, R. B. 1972 *"Drying Principles and Practice"* (Pergamon Press, Oxford).
- Kelvin, Lord (Thomson, W.) 1871 - quoted in Jaycock & Parfitt 1987 p28.
- Kitchener, J. A. 1977 *Chem. Britain* **13**, 105.
- Kruyer, S 1958 *Trans Faraday Soc.* **54**, 1758.
- Lai, F. S. Y., MacDonald, I. F., Dullien, F. A. L. & Chatzis, I. 1981 *J. Colloid Interface Sci.* **84**, 362.
- Laplace, de, P. S. 1805 - quoted in Jaycock & Parfitt 1987 p41.
- Langmuir, I. - quoted in Jaycock & Parfitt 1987 p190.
- Larkin, B 1967 *J. Colloid Interface Sci.* **23**, 350.
- Larson, R.G. & Morrow, N. R. 1981 *Powder Technol.* **30**, 123.
- Larson, R.G., Scriven, L. E. & Davis, H. T. 1981 *Chem. Eng. Sci.* **36**, 57.
- Latil, M. 1980 *"Enhanced Oil Recovery"* (Editions Technip, Paris).
- Lawal, A. & Brown, R. A. 1982a *J. Colloid Interface Sci.* **89**, 332.

- Lawal, A. & Brown, R. A. 1982b *J. Colloid Interface Sci.* **89**, 346.
- Legait, B. 1983 *J. Colloid Interface Sci.* **96**, 28.
- Legait, B. & Jacquin, C. 1982 *C. R. Acad. Sci. Paris B* **294**, 1111.
- Lenormand, R. 1981 *These Doctorat d'Etat* (I.N.P. Toulouse, France).
- Lenormand, R., Zarcone, C. & Sarr, A. 1983 *J. Fluid. Mech.* **135**, 337.
- Lester, G. R. 1967 - quoted in Morrow 1970 p37.
- Leverett, M. C. 1941 *Trans. AIME* **142**, 152.
- Lisgarten, N. D., Sambles, J. R. & Skinner, L. M. 1971 *Contemp. Phys.* **12**, 575.
- Livine, S., Reed, P., Shutts, G. & Neale, G. 1977 *Powder Technol.* **17**, 163.
- Mandelbrot, B. B. 1977 *"Fractals, Form, Chance and Dimension"* (Freeman and Co., San Francisco).
- Mason, G. 1970 *J. Colloid Interface Sci.* **32**, 172.
- Mason, G. 1971 *J. Colloid Interface Sci.* **35**, 279.
- Mason, G. 1972 *Trans. Brit. Ceram. Soc.* **71**, 93.
- Mason, G. 1973 *Br. Polym. J.* **5**, 101.
- Mason, G. 1974 *Building Sci.* **9**, 227.
- Mason, G. 1988a *"Characterisation of Porous Solids"* eds. K. K. Unger, J. Rouquerol, K. S. W. Sing & H. Kral *Studies in Surface Science and Catalysis* vol. 39 (Elsevier, Amsterdam) p323.
- Mason, G. 1988b *Proc. R. Soc. Lond. A* **415**, 453.
- Mason, G. & Clark, W. C. 1965 *Brit. Chem. Engng.* **10**, 327.
- Mason, G. & Morrow, N. R. 1984a *J. Chem. Soc., Faraday Trans. 1* **80**, 2375.
- Mason, G. & Morrow, N. R. 1984b *J. Colloid Interface Sci.* **100**, 519.
- Mason, G. & Morrow, N. R. 1986 *J. Colloid Interface Sci.* **109**, 46.
- Mason, G. & Morrow, N. R. 1987 *Proc. R. Soc. Lond. A* **414**, 111.
- Mason, G. & Morrow, N. R. 1989 *in press*.
- Mason, G. & Morrow, N. R. & Walsh, T. J. 1988 *"Characterisation of Porous Solids"* eds. K. K. Unger, J. Rouquerol, K. S. W. Sing & H. Kral *Studies in Surface Science and Catalysis* vol. 39 (Elsevier, Amsterdam) p243.
- Mason, G. Nguyen, M. D. & Morrow, N. R. 1983 *J. Colloid Interface Sci.* **95**, 494.
- Mason, G. & Yadav, G. D. 1983 *Proc. R. Soc. Lond. A* **390**, 47.
- Mast, R. F. 1972 *47th Ann. Fall Meet. of the SPE-AIME San Antonio* (SPE) Preprint No. 3997.
- Mayer, R. P. & Stowe, R. A. 1965 *J. Colloid Interface Sci.* **20**, 893.
- Mayer, R. P. & Stowe, R. A. 1966 *J. Phys. Chem.* **70**, 12.
- Melrose, J. C. 1965a *J. Colloid Interface Sci.* **20**, 911.
- Melrose, J. C. 1965b *Soc. Petrol. Eng. J.* **5**, 259.
- Melrose, J. C. 1966 *AIChEJ* **12**, 986.
- Melrose, J. C. & Brandner, C. F. 1974 *J. Canad. Pet. Technol.* **13**, 54.
- Michael, D. H. & Williams, P. G. 1976 *Proc. R. Soc. Lond. A* **351**, 117.
- Michael, D. H. & Williams, P. G. 1981 *Annu. Rev. Fluid Mech.* **13**, 189.
- Michaels, A. S. & Dean, S.W. Jr. 1962 - quoted in Adamson 1976 p363.
- Modry, S. & Svata M. (eds.) 1973 *"Pore Structure and Properties of Materials"* (Academia, Prague) 6 vols.
- Morrow, N. R. 1970 *Ind. Eng. Chem.* **62**, 32.
- Morrow, N. R. 1974 *J. Canad. Pet. Technol.* **14**, 42.
- Morrow, N. R. 1976 *J. Canad. Pet. Technol.* **15**, 49.

- Morrow, N. R. & Nguyen, M. D. 1982 *J. Colloid Interface Sci.* **89**, 523.
- Neumann, A. W. & Good, R. J. 1979 "*Surface and Colloid Science*" vol. 11, eds. R. J. Good & R. R. Stromberg (Plenum Press, New York) p31.
- Nguyen, M. D. 1980 *M.S. Thesis* (New Mexico Institute of Mining and Technology, Socorro, New Mexico).
- Nguyen, H. V., Padmanabhan, S., Desisto, W. J. & Bose, A. 1987 *J. Colloid Interface Sci.* **115**, 410.
- Nibbs, M. D. & Baynes, P. 1986 "*Capillary Rise in Irregular Pores*" Second Yr. Project (Dept. of Chem. Engng., LUT, Loughborough).
- Orr, C. 1970 *Powder Technol.* **3**, 117.
- Orr, F. M. Jr. 1976 *Ph.D. Thesis* (University of Minnesota).
- Orr, F. M. Jr., Brown, R. A. & Scriven, L. E. 1977 *J. Colloid Interface Sci.* **60**, 137.
- Orr, F. M. Jr., Scriven, L. E. & Chu, T. Y. 1977 *J. Colloid Interface Sci.* **52**, 402.
- Orr, F. M. Jr., Scriven, L. E. & Rivas, A. P. 1975a *J. Colloid Interface Sci.* **52**, 602.
- Orr, F. M. Jr., Scriven, L. E. & Rivas, A. P. 1975b *J. Fluid Mech.* **67**, 723.
- Padday, J. F. 1971 *Phil. Trans. R. Soc. A* **269**, 265.
- Petrash, D. A. & Otto, E. W. 1964 *Astro. & Aero. Eng.* Mar., 56.
- Petrov, V. M. & Chernous'ko, F. L. 1966 *Fluid Dynamics* **1**, 109.
- Pickard, W. 1981 *Prog. Biophys. Molec. Biol.* **37**, 181.
- Pitts, E. 1974 *J. Fluid Mech.* **63**, 487.
- Polanyi, M. 1914 - quoted in Jaycock & Parfitt 1987 p204.
- Poulavassilis, A. 1962 *Soil Sci.* **93**, 405.
- Princen, H. M. 1969a *J. Colloid Interface Sci.* **30**, 69.
- Princen, H. M. 1969b *J. Colloid Interface Sci.* **30**, 359.
- Princen, H. M. 1970a *J. Colloid Interface Sci.* **34**, 171.
- Princen, H. M. 1970b *Aust. J. Chem.* **23**, 1789.
- Purcell, W. R. 1949 *Trans AIME* **186**, 39.
- Quinson, J. F. & Brun, M. 1988 "*Characterisation of Porous Solids*" eds. K. K. Unger, J. Rouquerol, K. S. W. Sing & H. Kral *Studies in Surface Science and Catalysis* vol. 39 (Elsevier, Amsterdam) p307.
- Ransohoff, T. C., Gauglitz, P. A. & Radke, C. J. 1987 *AIChEJ* **33**, 753.
- Rayleigh, Lord (Strutt, J. W.) 1915 *Proc. R. Soc. Lond. A* **92**, 184.
- Ritter, H. L. & Drake, L. C. 1945a & b - quoted in Adamson (1976) p546.
- Rottenberg, Y., Boruvka, L & Neumann, A. W. 1984 *J. Colloid Interface Sci.* **102**, 424.
- Schofield, R. K. 1935 *Trans. 3rd Int. Congr. Soil Sci.* No. 2, 37.
- Schultze, K. 1925a & b - quoted by Carman 1941 p3.
- Schumacher, E. E., Bouton, G. M. & Phipps, G. S. 1945 *Materials and Methods* **22**, 1407.
- Schwartz, A. M. 1969 *Ind. Eng. Chem.* **61**, 10.
- Sheetz, D. P. 1965 *J. Polym. Sci.* **9**, 3759.
- Shepard, J. W. & Bartell, F. E. 1953 *J. Phys. Chem.* **57**, 458.
- Shipley, J. F. 1975 *Welding Res. Suppl.* 357.

- Shuttleworth, R. & Bailey, G. L. J. 1948 *Discussions Faraday Soc.* 3, 16.
- Singhal, A.K. & Somerton, W. H. 1970 *J. Canad. Pet. Technol.* 9, 197.
- Slicher, C. S. 1897 - quoted in Haynes 1975 p113.
- Smith, D. M., Gallegos, D. P. & Stermer D. L. 1987a *Powder Technol.* 53, 11.
- Smith, D. M. & Stermer D. L. 1987b *Powder Technol.* 53, 23.
- Stacy, M. H. 1988 "*Characterisation of Porous Solids*" eds. K. K. Unger, J. Rouquerol, K. S. W. Sing & H. Kral *Studies in Surface Science and Catalysis* vol. 39 (Elsevier, Amsterdam) p55.
- Stanley-Wood, N. G. 1979 *Analyst* 104, 97.
- Sugden, S. 1921 *J. Chem. Soc.* 129, 1483.
- Svata, M. 1971 *Powder Technol.* 5, 345.
- Svata, M. & Zabransky, Z. 1970 *Powder Technol.* 3, 296.
- Tamai, Y. & Aratani, K. 1972 *J. Phys. Chem.* 76, 3267.
- Tatarchenko, V. A. 1977 *J. Crystal Growth.* 37, 272.
- Topp, G. C. & Miller E. E. 1966 *Soil Sci. Soc. Amer. Proc.* 30, 156.
- Topp, G. C. 1969 *Soil Sci. Soc. Amer. Proc.* 33, 645.
- Tuskada, T., Hozawa, M., Imaishi, N. & Fujinawa, K. 1982 *J. Chem. Eng., Japan* 15, 421.
- Unger, K. K., Rouquerol, J., Sing, K. S. W. & Kral, H. (eds) 1988 "*Characterisation of Porous Solids*" IUPAC, *Studies in Surface Science and Catalysis* vol. 39 (Elsevier, Amsterdam)
- Washburn, E. W. 1921 *Proc. Nat. Acad. Sci.* 7, 115.
- Wenzel, R. N. 1936 *Ind. Eng. Chem.* 28, 988.
- Young, T. 1805 - quoted in Jaycock & Parfitt 1987 p235.
- Youngquist, G. R. 1970 *Ind. Eng. Chem.* 62, 52.
- Zimon, J. 1969 "*Adhesion of Dust and Powder*" (Plenum Press, Ney York).
- Zsigmondy, R. 1911 - quoted in Jaycock & Parfitt 1987 p223.

NOMENCLATURE

English

A	interfacial area
a	capillary constant $a^2 = 2\sigma/\rho g$ (mm ²)
A_{eff}	effective area (cross-sectional) of a meniscus
A_i	area of region i in the MS-P analysis
A_{SL}	area of solid/liquid interface
A_{SLG}	adhesion tension
A_T	area of a sector in the MS-P analysis
B	dimensionless Bond number $= gL^2\rho/\sigma$
b	radius of curvature at apex of drop (<i>c.f.</i> eq. 2.52)
C	normalised meniscus curvature
C_{R_i}	normalised curvature of menisci in i th-rod standard arrangement (<i>c.f.</i> chap 8)
$C_{R_i}^*$	reduced normalised curvature of menisci in i th-rod standard arrangement (<i>c.f.</i> chap 8)
C_S	normalised curvature in a standard cell
C_T	normalised curvature of a meniscus in a cylindrical capillary tube (= 2)
D	rod-plate spacing (<i>c.f.</i> chap. 11)
d	half depth of rectangular duct (<i>c.f.</i> sect. 9.2), half rod-plate spacing (<i>c.f.</i> sect. 9.3)
F	Free (available) energy
$F(\epsilon)$	function of aspect ratio (<i>c.f.</i> sect. 9.2)
$F(r)$	functional relationship for radius of curvature
$f(r)$	function of radius of curvature
$F(RR)$	function describing variation of r with parameter RR
G	Gibbs free energy
g	acceleration due to gravity
G_{R_i}	gradient of rod line (<i>c.f.</i> chap. 8)
G_T	gradient of tube line (<i>c.f.</i> chap. 8)
G_{T_c}	gradient of tube line with heights of rise corrected for gravity distortion (<i>c.f.</i> chap. 8)
H	enthalpy
H_θ	contact angle hysteresis $= \theta_s - \theta_r$
h	height of rise from a planar liquid surface to the bottom of a meniscus
h_j	Jurin correction to height of rise

h_o	extrapolated height of rise in reservoir indicator cell (<i>c.f.</i> chap. 8)
h_{∞}	extrapolated height of rise in reservoir indicator cell corrected for gravity distortion (<i>c.f.</i> chap. 8)
h_{R_i}	height of rise in <i>i</i> th-rod standard (<i>c.f.</i> chap. 8)
Δh_s	height of rise in standard cell
Δh_t	height of rise in test cell
J	meniscus curvature = $(1/r_1 + 1/r_2)$
$j(S_w)$	Leverett <i>j</i> -function (<i>c.f.</i> eq. 3.13)
k	permeability
L_i	lengths in MS-P analysis
l	length
N_{L_i}	dimensionless Leverett number (<i>c.f.</i> eq. 3.14)
\mathbf{n}	unit normal vector
n_i	number of moles of the <i>i</i> th component
P	pressure (<i>c.f.</i> chap. 2)
P	perimeter (not chap. 2)
P^o	saturated vapour pressure
P_c	capillary pressure
P_c^*	breakthrough pressure
P_{eff}	effective perimeter of a meniscus
P_L, P_S	liquid and solid perimeters
P_{NW}, P_W	non-wetted and wetted perimeters
P_{nw}, P_w	non-wetting and wetting phase pressures
$Q_{reversible}$	recoverable heat = TdS
R	radius
R	width of rectangular tube (<i>c.f.</i> sect. 9.2)
R_h	hydraulic radius of tube = A/P
R_i	rod radius in <i>i</i> th-rod standard (<i>c.f.</i> chap. 8)
R_n	thermoporometric radius
R_p	pore radius
R_s, R_t	standard and test rod radii
R_T	tube radius
R_{Te}	equivalent tube radius (<i>c.f.</i> chap. 8)
RR	variable parameter for computational interpolation in MS-P calculations
r	mean radius of curvature
r_1, r_2	principle radii of curvature
r_k	Kelvin radius

r_w	roughness factor
S	entropy
S_w	fractional saturation of wetting fluid
T	temperature
T_c	critical temperature of adsorbate
t	adsorbed film thickness
U	internal energy
V	volume
V_b	bulk volume of a porous sample
V_w	volume of wetting phase
v_i	partial molar volume of the i th component
W	work
W_{SLG}	work of adhesion
x, y, z	distances along axes

Greek

α_i	angles in MS-P analysis
β	corner angle of polygon (<i>c.f.</i> chap. 6)
β	angle of slope of liquid wedges (<i>c.f.</i> chap. 8)
γ_i	angles in MS-P analysis
ε	aspect ratio of rectangular tube = d/R (<i>c.f.</i> sect 9.2)
θ	contact angle
θ_a, θ_r	advancing and receding contact angles
θ_{app}	apparent contact angle
θ_c	composite surface contact angle
θ_1	contact angle on a single fibre
θ_i	intrinsic contact angle
θ^*	contact angle observed at a rough surface
μ_i	chemical potential of the i th component
π	film pressure
ρ	density
σ	interfacial tension
τ	height (<i>c.f.</i> chap. 2)
ϕ	corner angle (<i>c.f.</i> sect. 9.4), half angle of three rod arrangements (<i>c.f.</i> chap. 11)

Appendices

APPENDIX A

Two unequal rods contacting a plate

The following paper was presented at a poster session at the International Union of Pure and Applied Chemistry conference on the characterisation of porous solids. The particular geometry has no particularly special features and the motive for presenting the paper was to make workers in the field of porous materials more aware of the power of the MS-P method.

The paper gives an idea of the geometric analysis required to use the MS-P method and the experimental results confirm the analysis.

CAPILLARY PROPERTIES OF PORES FORMED BY TWO UNEQUAL PARALLEL RODS AND A PLATE

Geoffrey Mason, Norman R. Morrow (*) and Tim Walsh.

Dept. Chemical Engineering, Loughborough University of Technology,
Loughborough, Leicestershire, England.

* New Mexico Petroleum Recovery Research Centre, New Mexico
Institute of Mining and Technology, Socorro,
New Mexico 87801, U.S.A.

It is sometimes necessary to calculate the curvature of liquid menisci in non-axisymmetric pores. The method attributable to Mayer and Stowe - Princen can often be used successfully. The meniscus curvature of a wetting liquid in the space between two unequal contacting rods and a plate is calculated by this method. Experiments with accurately assembled model systems verify the theoretical predictions for rod radius ratios of up to 7:1.

INTRODUCTION

Liquid interfaces in porous materials produce a significant pressure difference. This pressure can be measured and used to determine pore sizes. If the interfacial tension is known, the key step in the process is obtaining the curvature of the meniscus in an average pore shape as the meniscus curvature depends upon the shape of the pore as well as on its size. Frequently it is assumed that the pore has a circular cross-section which has a normalised curvature of two. In the pore space of a sphere packing however, the pores are nearer triangular in shape and this affects their normalised curvature. Pores in a porous material are also converging-diverging and it is the pressure required to force the meniscus through the neck of the pore that is usually measured in some way.

There is no exact analysis of meniscus curvature in non-axisymmetric converging-diverging geometries. There is however an analysis of menisci in uniform non-axisymmetric geometries which approximates to the constrictions and widenings in an actual pore space. The technique is known as the Mayer and Stowe-Princen (MS-P) method. It was put forward by Mayer and Stowe { 1 } and

later developed by Princen { 2 }. The theory will be demonstrated and then experimentally validated using the case of a pore formed by two unequal parallel rods and a flat plate.

FUNDAMENTALS

In a simple cylindrical capillary tube the liquid surface will, in the absence of gravitational effects, form part of a sphere. This surface has constant mean curvature and gives the minimum surface energy. The liquid usually meets a solid boundary with a particular contact angle but, in order to keep the analysis simple, only perfectly wetting systems are considered here.

Liquid menisci in pores of complex configurations are generally complex themselves. In describing the basic form of these menisci the terms arc menisci and terminal menisci are used. Arc menisci occur in the wedge like spaces or corners formed by two rods in contact (Fig. 1a), by two flat plates contacting at an angle (Fig. 1b) or by two contacting rods against a plate (Fig. 1c). Arc menisci are, in mathematical terms, infinitely long and of constant volume per unit length. The terminal meniscus

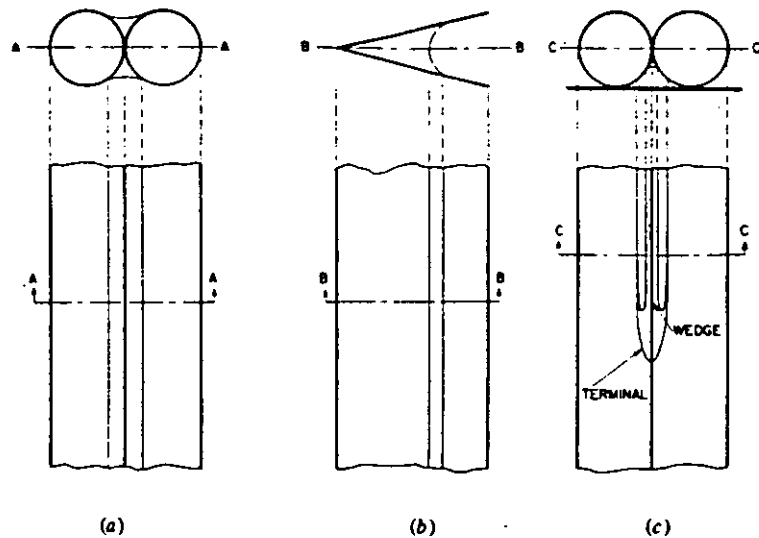


Fig. 1. (a) Arc meniscus formation between two contacting rods. (b) Arc meniscus formation in the angle between two flat plates. (c) Arc menisci and the terminal meniscus in the space between two contacting rods and a plate.

spans the tubular pore space unoccupied by the liquid wedges. With a cylindrical capillary tube there are no arc menisci, so a terminal meniscus will occupy the entire tube cross-section. With a pore formed by two rods against a plate (Fig. 1c) the terminal meniscus merges into three arc menisci. As mentioned earlier, the arc and terminal menisci are surfaces of constant mean curvature in the absence of gravitational effects (so they must have identical curvatures). Thus the curvature of the arc menisci, and hence the total curvature, is set by the terminal meniscus.

The basis of the MS-P method is the equating of the curvature of the arc menisci to the curvature of the terminal meniscus. Put together with a virtual work (or force balance) equation the curvature of the terminal meniscus can be found.

THEORY

The objective of the theory is to find the curvature of the terminal meniscus. Consider the meniscus formed between two unequal rods and a flat plate (Fig 2).

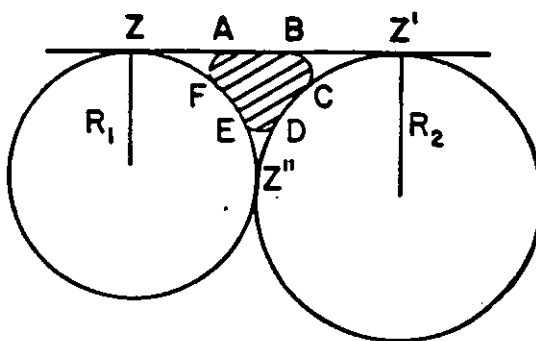


Fig. 2. Cross-section of a uniform tube formed by two rods and a plate with a perfectly wetting liquid, it contains three arc menisci of radius r , in the corners Z , Z' and Z'' . The shaded area represents the terminal meniscus.

Let area $ABCDEF$ be A , and perimeter $ABCDEF$ be P . A virtual work balance for a displacement dx along the tube axis gives

$$P_c A dx = \sigma P dx \quad (1)$$

where P_c is the capillary pressure, σ is the interfacial

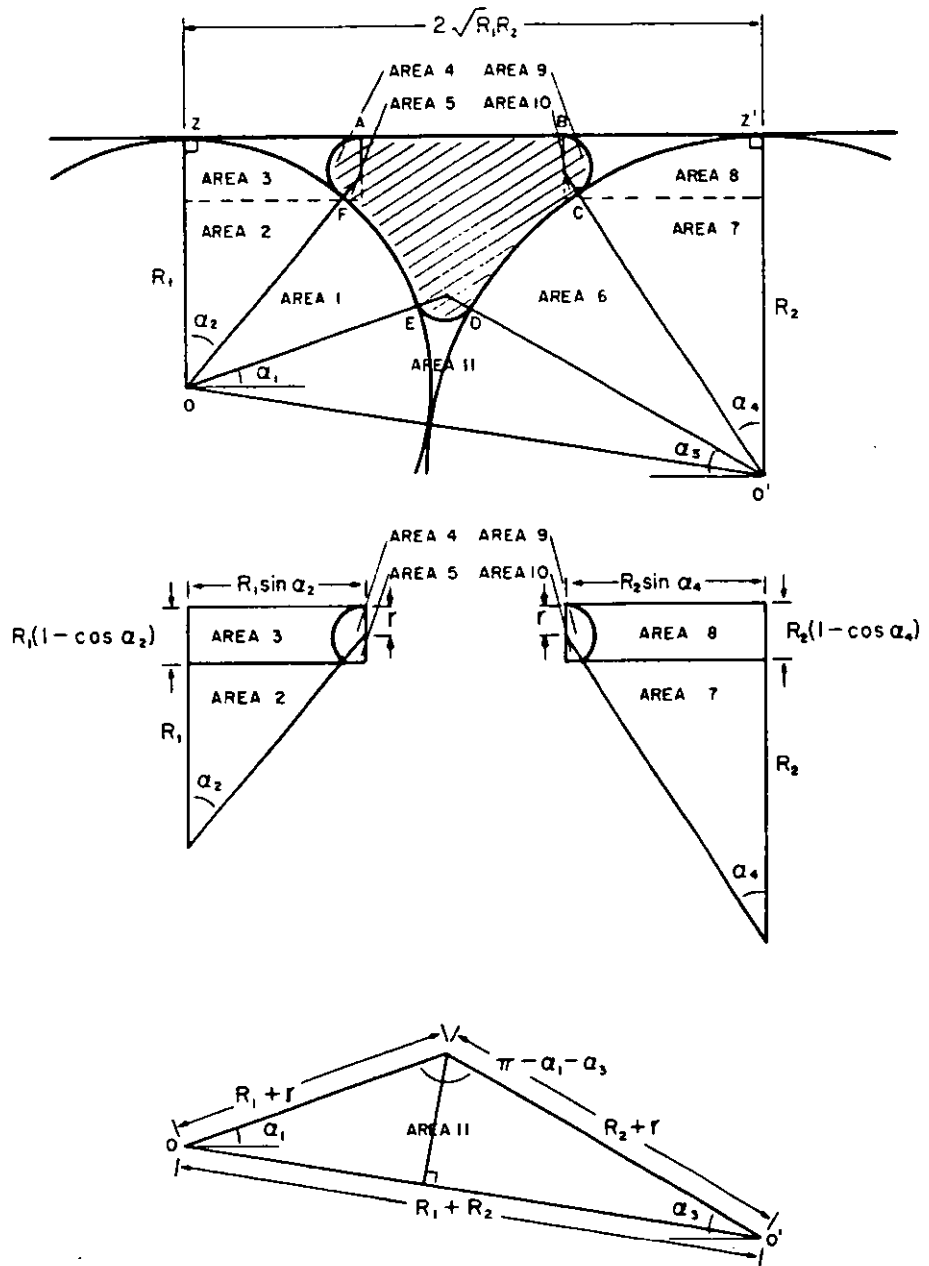


Fig. 3. Cross-section of the pore formed by two rods against a plate showing how expressions for area and perimeter are generated in the curvature calculation. The sections through the wedge menisci are arcs of circles of the same radius r .

tension. The curvature C , is given by

$$C = P_c / \sigma \quad (2)$$

so (1) reduces to

$$AC = P \quad (3)$$

Normalising the curvature with respect to R_1 we obtain

$$\frac{A}{R_1 P} = \frac{r}{R_1} \quad (4)$$

Which is the normalised MAYER AND STOWE - PRINCEN equation.

Both P and A independently depend on r in a simple geometrical manner. The lengths and areas in equation (4) are given by arcs of circles or straight lines, and straight forward but tedious geometry gives the following equations for the perimeter and area in terms of the angles α_1 , α_2 , α_3 and α_4 (see Fig. 3).

ANGLES

$$\alpha_1 = \arccos \left\{ \frac{((R_1 - r)^2 + (R_1 + R_2)^2 - (R_2 + r)^2)}{2(R_1 + R_2)(R_1 + r)} \right\} \\ - \arcsin \left\{ \frac{(R_2 - R_1)}{(R_1 + R_2)} \right\} \quad (5)$$

$$\alpha_2 = \arccos \left\{ \frac{(R_1 - r)}{(R_1 + r)} \right\} \quad (6)$$

$$\alpha_3 = \arccos \left\{ \frac{((R_2 - r)^2 + (R_1 + R_2)^2 - (R_1 + r)^2)}{2(R_1 + R_2)(R_2 + r)} \right\} \\ - \arcsin \left\{ \frac{(R_2 - R_1)}{(R_1 + R_2)} \right\} \quad (7)$$

$$\alpha_4 = \arccos \left\{ \frac{(R_2 - r)}{(R_2 + r)} \right\} \quad (8)$$

PERIMETER

$$P = FA + BC + DE + FE + DC + AB \\ = r \left\{ (\pi - \alpha_2) + (\pi - \alpha_4) + (\pi - \alpha_1 - \alpha_3) \right\} + R_1 (\pi/2 - \alpha_1 - \alpha_2) \\ + R_2 (\pi/2 - \alpha_3 - \alpha_4) + 2\sqrt{R_1 R_2} - (R_1 + r) \sin \alpha_2 - (R_2 + r) \sin \alpha_4 \quad (9)$$

AREA

$$A = \text{areaZZ'O'O} + A_4 + A_5 + A_9 + A_{10} + A_{12} - A_1 - A_2 - A_3 - A_6 - A_7 - A_8 - A_{11}$$

$$\begin{aligned} &= (R_1 + R_2)\sqrt{R_1 R_2} + r^2/2 \{(\pi - \alpha_2) + \cos \alpha_2 \sin \alpha_2 + (\pi - \alpha_4) \\ &\quad + \cos \alpha_4 \sin \alpha_4 + (\pi - \alpha_1 - \alpha_3)\} + R_1^2/2 \{(\pi - \alpha_1 - \alpha_2) + \cos \alpha_2 \sin \alpha_2\} \\ &\quad - R_1(1 - \cos \alpha_2)(R_1 + r) \sin \alpha_2 - R_2^2/2 \{(\pi - \alpha_3 - \alpha_4) + \cos \alpha_4 \sin \alpha_4\} \\ &\quad - R_2(1 - \cos \alpha_4)(R_2 + r) \sin \alpha_4 - 1/2 \{(R_1 + r)(R_2 + r) \sin(\alpha_1 + \alpha_3)\} \quad (10) \end{aligned}$$

These simultaneous equations can be solved either numerically or by graphical solution as in Fig. 4. A graph of $y = A/R_1 P$ against $y = r/R_1$ can be plotted. The intersection of the line $y = r/R_1$ with $y = A/R_1 P$ gives the value of r/R_1 which is

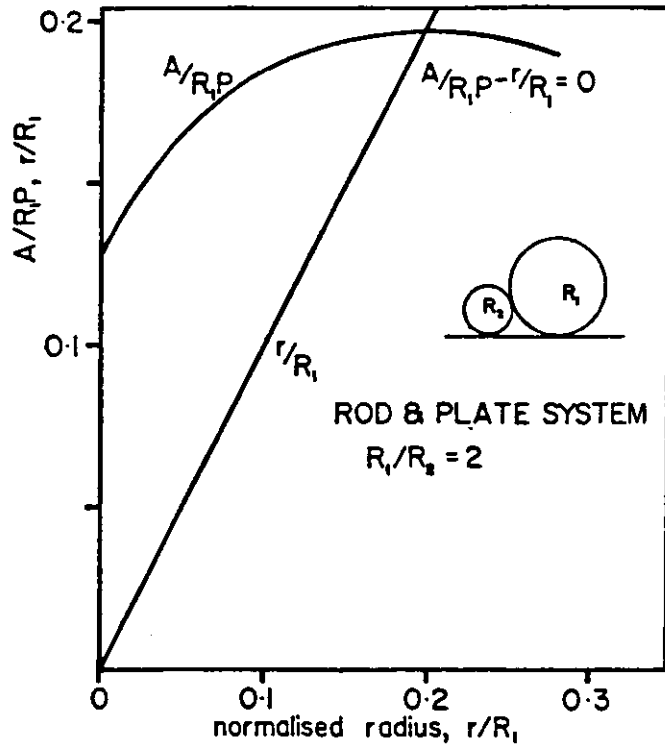


Fig. 4. Example of the graphical solution for R_1/r for a perfectly wetting liquid. The solution is where the $y = R_1/r$ line cuts the $y = A/R_1 P$ line. This occurs at maximum $A/R_1 P$.

the solution to the equations. The intersection value of $A/R P$ is also its maximum possible (and thus the maximum value of r). So as might be expected at equilibrium the meniscus has minimum curvature (maximum radius of curvature) for the particular boundary conditions. This is always true, irrespective of the tube section.

EXPERIMENT

The experiments to validate the theory principally involved measuring the heights of capillary rise in capillaries of constant cross-section made up of two rods and a plate. The apparatus was a compromise between using small rods which maximise capillary rise but leave the geometry affected by dimensional errors, and large rods which minimise the dimensional errors but introduce errors because menisci become distorted by gravity. Previous work { 3 } had shown that capillary rise greater than about 10 mm (equivalent to a rod diameter less than 10 mm or 3/8") made gravitational effects negligible and that dimensional errors only became apparent with rod sizes less than about 1 mm (1/32").

The apparatus consisted of precisely machined cells or channels into which ground steel rods were placed such that they just touched a glass plate. Four cells were used, the test cell, a standard cell with two equal contacting rods and a plate (whose characteristics were known) and two reservoir cells, 1/2" square. All the cells were connected via PTFE tubing to a main reservoir containing isooctane, the test liquid for the zero

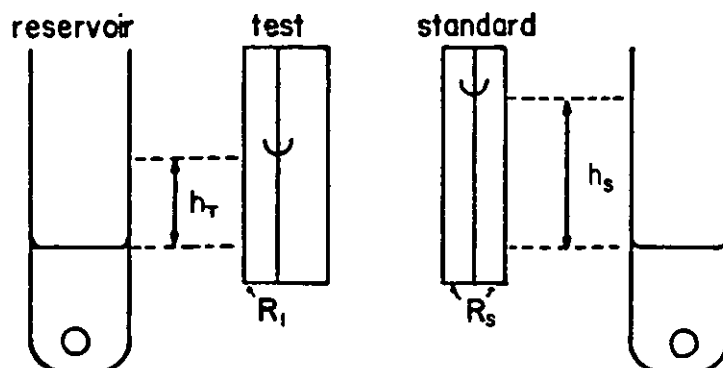


Fig. 5. Diagram of the various heights which were used in the analysis of the results.

contact angle experiments. The reservoir was raised or lowered to give appropriate heights in the cells. After the liquid levels had settled heights of rise were measured with a cathetometer accurate to 0.01 cm.

For any shaped capillaries

$$h_T \rho g = C \sigma / R_1 \quad (11)$$

$$h_S \rho g = C_S \sigma / R_S \quad (12)$$

Combining (11) and (12) gives

$$\frac{h_T}{h_S} = \frac{C}{R_1} \frac{R_S}{C_S} \quad (13)$$

So with the characteristics of the standard cell known C/R_1 can be found. R_1 is measured to give C . The standard cell used two 1/16" rods against a plate. A previous study by Mason, Nguyen, and Morrow { 3 } had determined the normalised curvature of this system as 6.88 ± 0.02 . By conducting the experiments in this way the effects of atmospheric conditions on interfacial tension and density were avoided.

Rod radius ratios from 1 to about 7 were used. The rods had diameters of ca. 3/64, 1/16, 5/64, 3/32, 1/8, 5/32, 5/16, 1/4, and 5/16 inches while their actual diameters were 1.184, 1.585, 1.971, 2.377, 3.167, 3.950, 4.755, 6.342 and 7.932 mm respectively.

RESULTS

The experimental results are given as a graph of meniscus curvature vs rod radius ratio (Fig. 6). All the results show excellent agreement with the theoretical curve, most to within 1%, and all within 2%. These errors arise from fabrication and measurement. The results provide excellent evidence of the accuracy of the MS-P method. Other studies have shown that the MS-P method works well for pores formed by two equal rods and a plate with liquids of finite contact angle { 3 }, so long as due attention is given to contact angle hysteresis. It is relatively simple to extend the theory to include variation of contact angle. The method has also been successfully applied to rectangular ducts by Lenormand { 4 }, and rod in a corner systems { 5 }, capillary

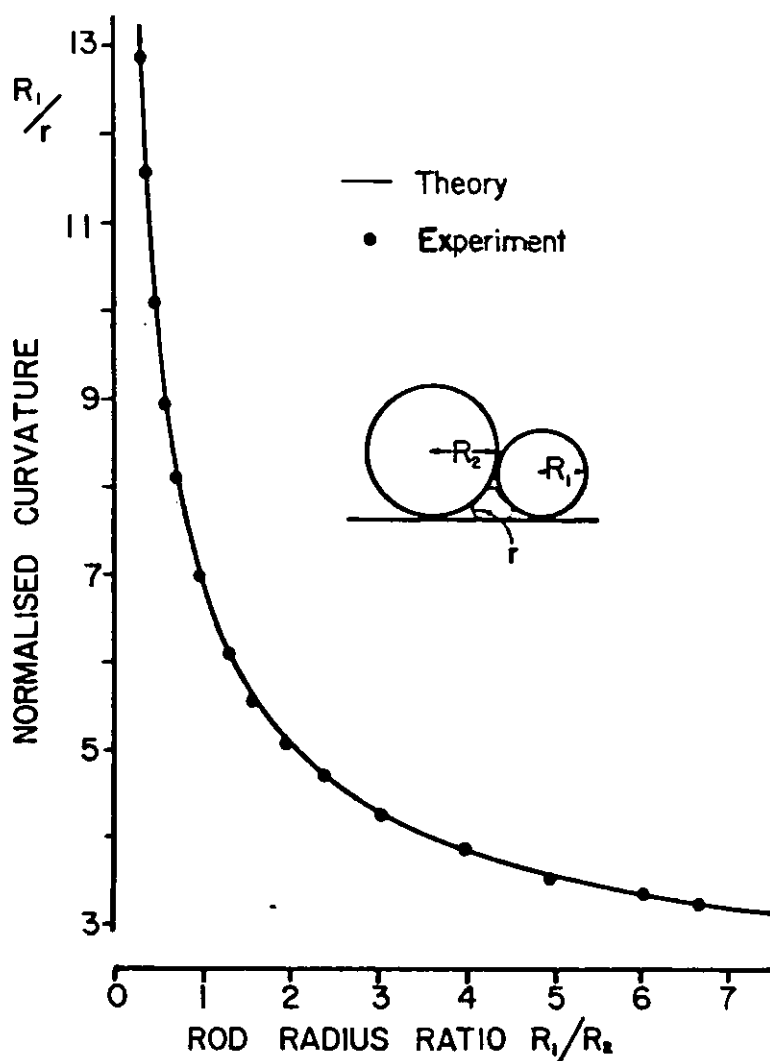


Fig. 6. Graph of normalised curvature against rod radius ratio for the two rods and plate menisci. The small scatter of points is caused by dimensional variations in the machining of the cells.

pore throats formed by spheres { 6 } and various other rod - plate systems by Mason et al.

SUMMARY

The MS-P method of calculating meniscus properties was used to calculate meniscus curvatures in capillaries formed by two

unequal parallel rods and a flat plate. For completely wetting systems theoretical results were in excellent agreement with measured values of capillary rise.

ACKNOWLEDGEMENTS

We thank Jack Burton for precisely machining the cells and R. Nibbs and P. Baynes for their contribution to the analysis and experiments. This work was funded by a SERC grant.

REFERENCES

1. Mayer, R. P. and Stowe, R. A., J. Colloid Interface Sci. 20 (1965) 893.
2. Princen, H. M., J. Colloid Interface Sci. 30 (1969) 69.
3. Mason, G., Nguyen, M. D. and Morrow N. R., J. Colloid Interface Sci., 95 (1983) 494.
4. Lenormand, R., Zarcone, C. and Sarr, A., J. Fluid Mechanics. 195 (1983) 337.
5. Mason, G. and Morrow, N. R., J. Chem. Soc., Faraday Trans. 80 (1984) 2375.
6. Mason, G. and Morrow, N. R., J. Colloid Interface Sci. 109 (1986) 46.

APPENDIX B

Standard configurations

Table B.1 Mercury thread sizes of capillary tubes

Nominal diameter (mm)	Weight empty (g)	Weight with mercury (g)	Weight of mercury W (g)	First point (mm)	Second point (mm)	Length of thread L (mm)	Tube radius mean R_T (mm)
0.50	3.683	3.901	0.218	13.069	6.232	6.837	0.274
		3.893	0.210	13.293	6.539	6.754	0.270
		3.909	0.226	13.289	6.062	7.227	0.271
							0.272
0.60	5.900	6.287	0.387	14.802	5.466	9.336	0.312
		6.373	0.473	14.958	3.382	11.576	0.310
		6.369	0.469	14.211	2.806	11.405	0.311
							0.311
0.78	6.734	7.240	0.506	14.451	6.676	7.775	0.391
		7.198	0.464	13.763	6.704	7.059	0.393
		6.987	0.253	10.533	6.600	3.933	0.389
							0.391
0.80	5.209	5.623	0.414	10.704	5.435	5.269	0.430
		5.622	0.413	10.857	5.613	5.244	0.430
		5.655	0.446	10.850	5.207	5.643	0.431
							0.430
1.20	8.615	10.193	1.578	13.373	2.791	10.582	0.592
		10.194	1.579	13.379	2.791	10.588	0.592
		9.643	1.028	9.522	2.678	6.844	0.594
							0.593

$$R_T = W/2\rho\pi L \quad \text{where} \quad \rho = 0.13546 \text{ g/mm}^3$$

Table B.2 Experimental results for the two rod standard. Heights of rise and curvatures are shown both with and without application of the Jurin correction.

Run no.	Rod rise Δh_R (bold), Δh_{R_j} (mm)							Tube rise Δh_T (bold), Δh_{T_j} (mm)					Linear Regressions				Curv.
Tube size	1/16	2	2.5	3	3.5	4	5	0.5	0.6	0.78	0.80	1.20	Rod line		Tube line		C
R_i (mm)	0.791	0.999	1.249	1.498	1.749	1.999	2.498	0.272	0.311	0.391	0.430	0.593	Grad.	Int.	Grad.	Int.	C_j
h_j (mm)	0.08	0.01	0.12	0.14	0.17	0.19	0.24	0.09	0.10	0.13	0.14	0.20	G_{R_2}	h_0	G_T	h_0	
1	23.75	18.68	14.96	12.37	10.52	9.10	7.13	19.88	17.28	13.68	12.37	8.82	19.18	-0.48	5.54	-0.51	6.93
	23.83	18.78	15.08	12.51	10.69	9.29	7.37	19.97	17.38	13.81	12.51	9.02	19.01	-0.21	5.48	-0.23	6.93
2	23.78	18.70	14.96	12.38	10.55	9.12	7.14	19.87	17.29	13.75	12.35	8.80	19.20	-0.47	5.54	-0.52	6.93
	23.86	18.80	15.08	12.52	10.72	9.31	7.38	19.96	17.39	13.88	12.49	9.02	19.03	-0.20	5.48	-0.21	6.94
3	23.66	18.61	14.84	12.30	10.48	9.02	7.09	19.80	17.24	13.67	12.36	8.78	19.14	-0.52	5.51	-0.48	6.94
	23.74	18.71	14.96	12.44	10.65	9.21	7.33	19.89	17.34	13.80	12.50	8.98	18.97	-0.24	5.46	-0.21	6.95
4	23.72	18.72	14.91	12.35	10.54	9.04	7.10	19.82	17.25	13.68	12.37	8.79	19.21	-0.52	5.52	-0.48	6.96
	23.80	18.82	15.03	12.49	10.71	9.23	7.34	19.91	17.35	13.81	12.51	8.99	19.04	-0.24	5.47	-0.21	6.97
5	23.69	18.70	14.95	12.33	10.54	9.09	7.10	19.80	17.27	13.66	12.32	8.83	19.16	-0.48	5.51	-0.46	6.96
	23.77	18.80	15.07	12.47	10.71	9.28	7.34	19.89	17.37	13.79	12.46	9.03	18.99	-0.20	5.45	-0.19	6.96
Mean	23.72	18.68	14.92	12.35	10.52	9.07	7.11	19.83	17.27	13.69	12.35	8.80	19.18	-0.49	5.53	-0.49	6.94
	23.80	18.78	15.04	12.51	10.70	9.26	7.35	19.92	17.37	13.82	12.49	9.00	19.02	-0.24	5.47	-0.22	6.95
All points													19.18	-0.49	5.52	-0.49	6.94
													19.01	-0.22	5.47	-0.21	6.95

$$C = 2G_R/G_T, C_j = 2G_{R_j}/G_{T_j}, \Delta h_{i_j} = \Delta h_i + h_x, h_j = a^2/(\Delta h_i + 0.5)/3 \text{ and } a^2 = 5.511 \text{ mm}^2.$$

Table B.3 Experimental results for the three rod standard.

Run no.	Rod rise Δh_R (bold), Δh_{R_j} (mm)							Tube rise Δh_T (bold), Δh_{T_j} (mm)					Linear Regressions				Curv.
Tube size	62	56	1/16	2	2.5	3	3.5	0.5	0.6	0.78	0.80	1.20	Rod line		Tube line		C
R_i (mm)	0.480	0.588	0.791	0.999	1.249	1.498	1.749	0.272	0.311	0.391	0.430	0.593	Grad.	Int.	Grad.	Int.	C_j
h_j (mm)	0.11	0.13	0.18	0.23	0.29	0.35	0.40	0.09	0.10	0.13	0.14	0.20	G_{R_3}	h_0	G_T	h_0	
1	16.70	13.60	9.94	7.68	6.10	4.86	4.19	19.90	17.27	13.80	12.35	8.80	8.330	-0.62	5.548	-0.52	3.003
	16.81	13.73	10.12	7.91	6.39	5.21	4.59	19.99	17.38	13.93	15.50	9.00	8.146	-0.16	5.496	-0.24	2.964
2	16.59	13.57	9.92	7.64	6.04	4.84	4.14	19.80	17.24	13.76	12.29	8.78	8.302	-0.63	5.521	-0.49	3.007
	16.70	13.70	10.10	7.87	6.33	5.19	4.54	19.89	17.35	13.89	12.44	8.98	8.117	-0.18	5.468	-0.21	2.969
3	16.74	13.51	10.01	7.68	6.10	4.85	4.21	19.92	17.32	13.78	12.33	8.85	8.324	-0.60	5.551	-0.51	2.999
	16.85	13.64	10.19	7.91	6.39	5.20	4.61	20.01	17.43	13.91	12.48	9.05	8.140	-0.15	5.498	-0.23	2.961
4	16.64	13.47	9.93	7.66	6.07	4.90	4.19	19.90	17.32	13.68	12.38	8.83	8.260	-0.56	5.549	-0.52	2.977
	16.75	13.60	10.11	7.89	6.36	5.25	4.59	19.99	17.43	13.81	12.53	9.03	8.075	-0.11	5.496	-0.24	2.939
5	16.64	13.60	9.95	7.76	6.08	4.83	4.18	19.86	17.28	13.72	12.36	8.84	8.309	-0.60	5.520	-0.45	3.010
	16.75	13.73	10.13	7.99	6.37	5.18	4.58	19.95	17.39	13.85	12.51	9.04	8.125	-0.14	5.468	-0.18	2.972
Mean	16.66	13.55	9.95	7.68	6.08	4.86	4.18	19.88	17.29	13.65	12.34	8.82	8.304	-0.60	5.541	-0.50	2.997
	16.77	13.68	10.13	7.91	6.37	5.21	4.58	19.97	17.40	13.88	12.49	9.02	8.119	-0.15	5.488	-0.23	2.959
All points													8.305	-0.60	5.538	-0.50	2.999
													8.121	-0.15	5.485	-0.22	2.961

$$C = 2G_R/G_T, \quad C_j = 2G_{R_j}/G_{T_j}, \quad \Delta h_{ij} = \Delta h_i + h_j, \quad h_j = a^2/(\Delta h_i + 0.5)/3 \quad \text{and} \quad a^2 = 5.511 \text{ mm}^2$$

APPENDIX C

Rectangular ducts

Table C.1 details the MS-P predictions, the solutions of the quadratic equation 9.6) shown were used to draw the graph shown in section 9.2. Table C.2 shows the experimental results.

Table C.1 MS-P predictions for the rectangular tubes covering the range of aspect ratios investigated.

Aspect Ratio d/R	Curvature C_{MS-P}	Aspect Ratio d/R	Curvature C_{MS-P}	Aspect Ratio d/R	Curvature C_{MS-P}
8.00	1.148	4.50	1.260	1.50	1.748
7.50	1.158	4.00	1.292	1.25	1.891
7.00	1.169	3.50	1.332	1.00	2.102
6.50	1.182	3.00	1.385	0.75	2.450
6.00	1.196	2.50	1.459	0.50	3.137
5.50	1.124	2.00	1.568	0.25	5.166
5.00	1.235	1.75	1.646	0.00	∞

Table C.2 Experimental results for rectangular ducts. Observed curvatures are shown in terms of the tube aspect ratio and compared to the MS-P predictions.

Half width d (mm)	Half depth R (mm)	Aspect ratio d/R (R/d)	Standard rise $\Delta h_{s,c}$ (mm)	Test rise $\Delta h_{t,c}$ (mm)	Expt. curvature C_{exp}	MS-P curvature C_{MS-P}	% dev. (%)
1.186	0.158	7.483	24.55	20.59	1.153	1.159	-0.50
0.815		5.142		21.78	1.220	1.229	-0.75
0.610		3.849		22.85	1.280	1.303	-1.82
1.186	0.200	5.915	24.57	16.97	1.201	1.199	+0.17
0.815		4.065		18.14	1.284	1.287	-0.25
0.610		3.042		19.08	1.350	1.380	-2.20
1.186	0.270	4.385	24.57	13.01	1.242	1.267	-1.99
0.815		3.013		14.39	1.374	1.383	-0.66
0.610		2.255		15.30	1.461	1.507	-3.16
1.186	0.471	2.518	24.48	8.52	1.422	1.456	-2.39
0.815		1.730		9.61	1.604	1.653	-3.06
0.610		(0.578) 1.295 (0.772)		10.77	2.775 1.798 2.329	2.859 1.861 2.409	-3.53
1.186	1.270	0.934	24.50	4.57	2.055	2.176	-5.91
0.815		(1.071) 0.642 (1.558)		5.75	1.917 2.585 1.659	2.032 2.683 1.722	-3.79
0.610		0.480 (2.083)		6.91	3.106 1.492	3.221 1.547	-3.69

Experimental curvatures calculated from $C_{exp} = 6.94 (\Delta h_{t,c} R / \Delta h_{s,c} R_s)$ where $R_s = 0.800 \text{ mm}$, $\Delta h_{s,c} = \Delta h_s + 0.5$ and $\Delta h_{t,c} = \Delta h_t + 0.5$

APPENDIX D

One rod away from a plate

Table D.1 MS-P predictions for the single-rod-and-plate arrangement in terms of the normalised spacing.

Normalised Spacing d/R	Subtended Angle α_1 (deg.)	Effective Area A_{eff} (rod units ²)	Effective Perimeter P_{eff} (rod units)	Curvature C_{MS-P}
0.01	4.89	0.003	0.270	0.8401
0.02	8.04	0.010	0.416	0.7956
0.03	10.76	0.021	0.532	0.7637
0.04	13.25	0.034	0.630	0.7380
0.05	15.47	0.050	0.717	0.7160
0.07	19.86	0.089	0.866	0.6792
0.10	25.68	0.165	1.051	0.6349
0.15	34.27	0.336	1.293	0.5773
0.20	41.85	0.558	1.483	0.5316
0.25	48.68	0.831	1.639	0.4934
0.30	54.95	1.159	1.778	0.4604
0.35	60.60	1.533	1.891	0.4316
0.40	65.70	1.952	1.981	0.4059
0.45	70.46	2.428	2.066	0.3828
0.50	74.94	2.969	2.149	0.3620
0.55	79.01	3.554	2.216	0.3430
0.60	82.77	4.194	2.276	0.3256

Table D.2 Experimental results for the single-rod-and-plate arrangement.

Half Spacing d (mm)	Rod Radius R (mm)	Norm. Spacing d/R (R/d)	Standard Rise Δh_{1c} (mm)	Test Rise Δh_{1c} (mm)	Expt. Curvature C_{exp}	MS-P Curvature C_{MS-P}	% Dev. (%)
0.102	3.175	0.032	16.59	21.35	0.764	0.758	+0.79
0.102	1.992	0.051	16.49	19.93	0.717	0.714	+0.42
0.102	1.468	0.069	16.50	19.1	0.687	0.681	+0.87
0.102	1.243	0.082	16.54	18.65	0.669	0.660	+1.35
0.152	1.581	0.096	16.56	12.01	0.646	0.640	+0.93
0.102	0.983	0.103	16.41	17.57	0.635	0.631	+0.63
0.102	0.790	0.129	16.43	16.67	0.602	0.600	+0.33
0.102	0.591	0.172	16.47	15.47	0.557	0.556	+0.18
0.152	0.790	0.193	16.46	9.96	0.539	0.538	+0.19
0.190	0.790	0.241	16.39	7.37	0.500	0.500	+0.00
0.102	0.391	0.260	16.45	13.73	0.495	0.486	+1.82
0.190	0.592	0.322	16.39	6.57	0.446	0.447	-0.22
0.152	0.390	0.391	16.41	7.54	0.409	0.410	-0.24
0.190	0.395	0.485	16.43	5.57	0.377	0.368	+2.39

Experimental curvatures calculated from $C_{exp} = 6.94 (\Delta h_{1c} R / \Delta h_{1c} R_s)$ where $R_s = 1.188$ mm, $\Delta h_{1c} = \Delta h_s + 0.5$ and $\Delta h_{1c} = \Delta h_s + 0.5$

APPENDIX E

One rod in a corner

Table E.1 MS-P curvature predictions in terms of the corner angle for the rod-in-a-corner arrangement.

Corner Angle ϕ (deg.)	Curvature C_{MS-P}	Corner Angle ϕ (deg.)	Curvature C_{MS-P}	Corner Angle ϕ (deg.)	Curvature C_{MS-P}
5	1.478	65	5.841	125	26.435
10	1.762	70	6.469	130	31.703
15	2.030	75	7.179	135	38.711
20	2.301	80	7.987	140	48.430
25	2.583	85	8.914	145	62.144
30	2.881	90	9.986	150	83.002
35	3.200	95	11.235	155	116.883
40	3.544	100	12.705	160	177.750
45	3.919	105	14.459	165	305.749
50	4.329	110	16.572	170	659.365
55	4.781	115	19.156	180	∞
60	5.282	120	22.367		

Table E.2 Corner angle measurements by rotating microscope and rod methods, as described in section 9.4.

Nominal Corner Angle (deg.)	Rotating Microscope Average (deg.)	Standard Deviation	Rod(s) Method Average (deg.)	Standard Deviation	Mean Corner Angle (deg.)
30°	30.23	0.172	30.11	0.084	30.17
90°	90.06	0.153	-	-	90.06
110°	109.72	0.221	109.95	0.313	109.83

Table E.3 Experimental results for the rod-in-a-corner arrangement.

Corner Angle (deg)	Stand. Rod Radius R_s (mm)	Stand. Jurin Corr. h_{js} (mm)	Stand. Rise Δh_{rc} (mm)	Test Rod Radius R_t (mm)	Test Jurin Corr. h_{jt} (mm)	Test Rise Δh_{rc} (mm)	Expt. Curv. Mean C_{expt}	MS-P Curv. $C_{\text{MS-P}}$	% Dev. Stand. Dev.
30.17	1.188	0.11	16.30	0.864	0.21	8.95	2.872		-0.66
			16.35	0.947	0.22	8.49	2.877		-0.49
			16.40	0.995	0.23	8.06	2.864		-0.94
			16.20	1.049	0.24	7.93	2.890		-0.00
			16.35	1.098	0.25	7.32	2.876		-0.52
			16.20	1.185	0.27	6.71	2.873		-0.62
			16.18	1.298	0.30	6.10	2.863		-0.98
			16.20	1.398	0.32	5.69	2.873		-0.62
			16.14	1.582	0.37	5.02	2.878		-0.45
			16.17	1.594	0.37	5.00	2.884		-0.24
						2.875	2.891	0.008	
90.06	1.188	0.11	16.20	1.046	0.07	26.34	9.954		-0.42
			16.34	1.578	0.10	17.69	9.994		-0.00
			16.23	3.169	0.21	8.73	9.972		-0.24
						9.973	9.996	0.020	
109.83	0.792	0.08	24.13	1.586	0.06	28.79	16.408		-0.43
			24.10	2.370	0.09	19.21	16.380		-0.60
			24.13	3.169	0.12	14.27	16.250		-1.40
						16.346	16.479	0.084	

$$C_{\text{expt}} = 6.95 \Delta h_{rc} R_t / \Delta h_{rc} R_s \quad \text{where} \quad \Delta h_{rc} = \Delta h_s + h_{js} + 0.21 \quad \text{and} \quad \Delta h_{rc} = \Delta h_t + h_{jt} + 0.21$$

APPENDIX F

Two unequal rods and a plate

Table F.1. MS-P predictions in terms of the rod radius ratios for the unequal-rods-and-plate arrangement.

Rod Radius Ratio R_1/R_2	Effective Area A_{eff} (rod units ²)	Effective Perimeter P_{eff} (rod units)	Curvature C_{MS-P}
11.00	2.059	5.778	2.806
10.50	2.001	5.688	2.842
10.00	1.942	5.595	2.881
9.50	1.881	5.498	2.923
9.00	1.818	5.397	2.968
8.50	1.753	5.291	3.018
8.00	1.686	5.180	3.073
7.50	1.616	5.063	3.132
7.00	1.544	4.940	3.199
6.50	1.469	4.810	3.274
6.00	1.391	4.672	3.358
5.50	1.309	4.524	3.455
5.00	1.223	4.365	3.566
4.50	1.134	4.193	3.697
4.00	1.039	4.006	3.854
3.50	0.939	3.799	4.046
3.00	0.831	3.568	4.289
2.75	0.775	3.442	4.437
2.50	0.717	3.306	4.609
2.25	0.656	3.159	4.812
2.00	0.593	3.000	5.056
1.75	0.527	2.826	5.357
1.50	0.458	2.632	5.740
1.25	0.386	2.415	6.250
1.00	0.310	2.164	6.970
0.80	0.247	1.932	7.813
0.60	0.181	1.658	9.124
0.40	0.114	1.322	11.523
0.20	0.048	0.873	17.832
0.00			∞

Table F.2. Experimental results: curvatures are calculated both with and without the application of the Jurin correction (bold figures are the coordinates of points shown on the graph in section 9.5).

Radius Ratio	Stand. Rise	Test Rod Radius	Test Jurin Corr.	Test Rise	Expt. Curv.	MS-P Curv.	% Dev.
R_1/R_2 (R_2/R_1) (mm)	Δh_{1c} (mm)	R_1 (mm)	h_{j1} (mm)	Δh_{1c} (mm)	C_{exp}	C_{MS-P}	(%)
10.139	16.59	3.966	-	20.74	2.857	2.870	-0.51
	16.41		0.09	20.54	2.863		-0.24
8.107	16.58	3.171	-	21.98	3.029	3.060	-1.01
	16.40		0.08	21.77	3.037		-0.75
6.699	16.54	3.966	-	15.48	3.237	3.243	-0.19
	16.36		0.12	15.31	3.241		-0.06
6.061	16.58	2.377	-	23.99	3.306	3.348	-1.27
	16.40		0.08	23.78	3.318		-0.88
5.004	16.58	3.966	-	12.60	3.518	3.566	-1.33
	16.40		0.15	12.46	3.522		-1.21
4.009 (0.249)	16.61	3.167	-	13.77	3.826	3.851	-0.65
			-		15.388	15.439	
	16.43		0.14	13.62	3.830	3.851	-0.54
3.001 (0.333)					15.354	15.439	
	16.57	2.370	-	15.25	4.247	4.289	-0.99
			-		12.745	12.871	
16.39	0.12		15.08	4.252	4.289	-0.86	
2.500 (0.400)					12.760	12.871	
	16.55	1.975	-	16.43	4.582	4.609	-0.59
			-		11.453	11.522	
16.37	0.11		16.25	4.588	4.609	-0.46	
1.998 (0.500)					11.470	11.522	
	16.51	1.583	-	17.95	5.033	5.058	-0.50
			-		10.057	10.106	
16.33	0.10		17.76	5.043	5.058	-0.29	
1.607 (0.622)					10.076	10.106	
	16.51	1.583	-	15.87	5.534	5.565	-0.56
			-		8.892	8.943	
16.33	0.12		15.70	5.542	5.565	-0.41	
1.000 (1.000)					8.905	8.943	
	16.51	1.583	-	14.35	6.035	6.066	-0.51
			-		8.040	8.080	
16.33	0.13		14.19	6.040	6.066	-0.44	
					8.045	8.080	
	16.51	1.583	-	12.36	6.925	6.970	-0.64
			-		12.22	6.931	6.970
16.33	0.15						

Standard rod radius, $R_s = 1.188$ mm and a Jurin correction, h_{j_s} , of 0.11 mm applies to heights of rise in the standard. Also:

$$C_{exp} = 6.94 \Delta h_{1c} R_1 / \Delta h_{1c} R_s \quad \text{where} \quad \Delta h_{1c} = \Delta h_s + 0.50 \quad \text{and} \quad \Delta h_{1c} = \Delta h_s + 0.50$$

$$C_{exp} = 6.95 \Delta h_{1c} R_1 / \Delta h_{1c} R_s \quad \text{where} \quad \Delta h_{1c} = \Delta h_s + h_{j_s} + 0.21 \quad \text{and} \quad \Delta h_{1c} = \Delta h_s + h_{j_s} + 0.21$$

APPENDIX G

One rod away from a plate - non-zero contact angle

Generation of the data for the 3-D graph of section 10.2 required extensive use of the above program, producing over twenty pages of print-out. Hence, the only MS-P predictions given below are those that have a direct bearing on the experiments, i.e. for $d/R = 0.1$. Table G.2 details the experimental results.

Table G.1 MS-P predictions of normalised meniscus curvature in terms of the liquid/solid contact angle for the case of one rod away from a plate.

Contact Angle θ (deg.)	Angle α_1 (deg.)	Effective Area A_{eff} (rod units ²)	Effective Perimeter P_{eff} (rod units)	Curvature C_{MS-P}
0	25.68	0.1655	1.0510	0.6349
5	24.96	0.1650	1.0475	0.6349
10	23.93	0.1607	1.0195	0.6345
15	22.72	0.1540	0.9748	0.6330
20	21.32	0.1453	0.9148	0.6298
25	19.80	0.1351	0.8424	0.6236
30	18.20	0.1240	0.7601	0.6130
35	16.55	0.1125	0.6713	0.5968
40	14.93	0.1011	0.5799	0.5735
45	13.38	0.0904	0.4900	0.5421
50	11.96	0.0807	0.4050	0.5020
55	10.67	0.0721	0.3270	0.4535
60	9.54	0.0647	0.2571	0.3972
65	8.56	0.0585	0.1955	0.3342
70	7.72	0.0533	0.1414	0.2654
75	6.99	0.0490	0.0940	0.1920
80	6.36	0.0454	0.0522	0.1151
85	5.81	0.0425	0.0151	0.0356
86	5.71	0.0419	0.0082	0.0195
87	5.61	0.0414	0.0017	0.0033
87.13	5.60	0.0414	0.0005	0.0012
WOAMs meet back-to-back				

Table G.2 Experimental results for the partially wetted arrangement of one rod away from a plate.

Contact Angle	Standard Rise	Test Rise	Comparative Method Curvature (mean)	Physical Properties Curvature (mean)	MS-P Curvature	% Dev.
θ (deg.)	Δh_{sc} (mm)	Δh_{zc} (mm)	C_{EXPT}	C_P		
Iso.						
4.6	12.97	11.27	0.636			
r	12.91	11.12	0.631			
	13.08	11.30	0.633			
			0.633±.003		0.635	-0.31
29.6	13.08	10.91	0.611			
a	13.10	11.05	0.617			
	13.12	11.09	0.619			
	13.10	11.02	0.615			
			0.615±.004		0.614	+0.11
n-Do.						
22.8	15.98	11.71	0.536	0.541		
r	15.95	12.03	0.552	0.556		
	15.97	11.91	0.545	0.550		
	15.97	11.93	0.547	0.551		
			0.545±.009	0.550±.009	0.626	-12.14
47.9		11.30		0.522		
a		10.96		0.506		
		10.53		0.486		
		10.55		0.487		
				0.500±.022	0.519	-3.66
n-Tet						
25.1	16.38	12.95	0.579	0.583		
r	16.33	13.29	0.597	0.598		
	16.35	13.39	0.599	0.603		
	16.36	12.65	0.566	0.569		
			0.585±.019	0.588±.019	0.623	-5.62
50.2		10.57		0.476		
a		10.53		0.474		
		10.47		0.471		
		10.43		0.469		
				0.472±.004	0.500	-5.60
Dioc.						
30.8	15.99	13.16	0.602	0.658		
r	15.95	13.26	0.608	0.663		
	16.03	13.38	0.611	0.669		
	15.98	12.82	0.587	0.641		
			0.602±.015	0.658±.017	0.610	-1.30

continued...

Table G.2 concluded.

Contact Angle	Standard Rise	Test Rise	Comparative Method Curvature (mean)	Physical Properties Curvature (mean)	MS-P Curvature	% Dev.	
θ (deg.)	Δh_{1c} (mm)	Δh_{2c} (mm)	C_{EXPT}	C_P			
Dioc.							
55.9	Mean of above used	10.37	0.475	0.518			
a		10.09	0.462	0.504			
		10.20	0.467	0.510			
		10.13	0.464	0.507			
				0.467±0.008	0.510±0.021	0.443	+5.41
Hexa.							
43.3	10.03	7.85	0.572	0.569			
r		10.01	7.61	0.557	0.552		
		10.05	7.71	0.568	0.559		
		10.12	7.67	0.555	0.556		
				0.563±0.009	0.559±0.017	0.553	+1.08
68.4		4.13		0.299			
a		4.28		0.310			
		4.30		0.312			
		4.22		0.306			
				0.307±0.008	0.288	+6.63	
α -Br.							
58.1	13.61	8.06	0.450	0.429			
r		13.08	7.91	0.443	0.421		
		13.21	8.26	0.458	0.439		
		13.11	7.98	0.446	0.425		
				0.449±0.009	0.428±0.011	0.419	+2.15
83.2		3.21		0.171			
a		3.04		0.162			
		3.31		0.176			
		2.93		0.156			
				0.166±0.010	0.064	+2.58	

$$C_{EXPT} = 6.94\Delta h_{1c}R_1/\Delta h_{2c}R_2, \text{ and } C_P = 2\Delta h_{1c}R_1/a^2 \text{ where } R_1 = 1.580 \text{ mm and } R_2 = 1.498 \text{ mm.}$$

APPENDIX H

Two equal rods and a plate - non-zero contact angle

H.1 COMPUTER PROGRAM

Listed overleaf is the program used to generate the results for these arrangements and for the two unequal rods and plate arrangement (section 9.5). Essentially the routines are those of the standard solution program discussed in section 6.4.2.1, with the relevant expressions for angles, areas and perimeters added. However the mixed wettability systems creates added complexities and requires a second iteration for an angle in addition to that for the curvature. The program is written in BBC basic.

```

100 REM*****
110 REM***CURV CALC FOR TWO RODS AGAINST A PLATE***
120 REM**VARIABLE IN RADIUS RATIO OR CONTACT ANGLE**
130 REM*****
1000 CLS:A41=0
1010 PROCINIT
1020 J=1
1030 FOR RR = RI TO RX+SS/2 STEP SS
1040 IF A#="A" THEN T=RADRR:IF RR>90 THEN T=RAD(180-RR)
1050 IF A#="R" THEN R2=1:R1=RR
1060 IF J=1 THEN RB=0:GOTO1090
1070 IF J=2 THEN PROCJ2:GOTO1090
1080 PROCJ3
1090 PROCSPLIT
1100 NEXT
1110 END
1120 DEF PROCSPLIT
1130 R=(W1+W2)/2:PROCCURV
1140 IF F>R5 THEN W1=R:R=(W1+W2)/2:PROCCURV:GOTO 1140
1150 IF F<R6 THEN W2=R:R=(W1+W2)/2:PROCCURV:GOTO 1140
1160 RA=RB:RB=R:C=R2/R:C=INT(C*10000+.5)/10000:S=INT(S*10000+.5)/10000:V=INT(V*
10000+.5)/10000:A5=INT(DEG(A4)*100+.5)/100:RR=INT(RR*1000+.5)/1000
1170 VDU2:PRINT TAB(10);RR TAB(20);C TAB(30);S TAB(40);V TAB(50);A5:VDU3
1180 J=J+1:ENDPROC
1190 DEF PROCCURV
1200 REM*****2 rods + plate contact angle T*****
1210 REM*****angles*****
1220 K1=R*COS(T):K2=R*SIN(T):K3=(R1+K1)/(R1-K1):K4=K2/(K1-R1):K5=K3/(K3*K3+4+.
4)^.5:IF K5>.999999 THEN K5=1
1230 A1=ASN(K5)-ASN(1/(K3*K3+K4*K4)^.5)
1240 K3=(R2+K1)/(R2-K1):K4=K2/(K1-R2):IF K5>.999999 THEN K5=1
1250 A3=ASN(K5)-ASN(1/(K3*K3+K4*K4)^.5)
1260 IF A41<>0 THEN 1280
1270 INPUT"A41 (DEG)";A41:INPUT"A42";A42:A41=RAD(A41):A42=RAD(A42)
1280 A43=A41:A4=A41:PROCANGLE:E1=R-RP
1290 A44=A42:A4=A42:PROCANGLE:E2=R-RP
1300 IF E1<0 OR E2>0 THEN PRINT"E1";E1:PRINT"E2";E2:GOTO1270
1310 A4=(A43+A44)/2:PROCANGLE
1320 IF E>R7 THEN A43=A4:A4=(A43+A44)/2:PROCANGLE:GOTO1320
1330 IF E<RB THEN A44=A4:A4=(A43+A44)/2:PROCANGLE:GOTO1320
1340 G=ASN((R1-R2)/(R1+R2))
1350 REM*****area*****
1360 ST=(R1+R2)*COS(G)*R1-.5*(R1-R2)*(R1+R2)*COS(G)
1370 S1=-.5*R1*R1*SIN(A1)*COS(A1)-R1*R1*SIN(A1)*(1-COS(A1))-R*R1*(1-COS(A1))*S
IN(A1+T)+.5*R*R*SIN(T)*COS(T)+.5*R*R*SIN(A1+T)*COS(A1+T)+.5*R*R*(PI-A1-2*T)
1380 S2=-.5*R2*R2*SIN(A3)*COS(A3)-R2*R2*SIN(A3)*(1-COS(A3))-R*R2*(1-COS(A3))*S
IN(A3+T)+.5*R*R*SIN(T)*COS(T)+.5*R*R*SIN(A3+T)*COS(A3+T)+.5*R*R*(PI-A3-2*T)
1390 S3=- (R1+R2-R1*COS(A2)-R2*COS(A4))*(R1*SIN(A2)+R*SIN(A2+T))+R*R*(COS(A2+T)
*SIN(A2+T)+COS(A4+T)*SIN(A4+T)+(PI-2*T-A2-A4))/2-.5*R1*R1*SIN(A2)*COS(A2)-.5*R2*
R2*SIN(A4)*COS(A4)
1400 S4=-.5*R1*R1*(PI/2-G-A1-A2)-.5*R2*R2*(PI/2+G-A3-A4)
1410 S=S1+S2+S3+S4
1420 REM*****Perimeter*****
1430 V1=(R1+R2)*COS(G)-R1*SIN(A1)-R2*SIN(A3)-R*(SIN(T+A1)+SIN(T+A3))+2*
R*SIN(T)
1440 V2=R*(6*(PI/2-T)-A1-A2-A3-A4)
1450 V3=R1*(PI/2-G-A1-A2)+R2*(PI/2+G-A3-A4)
1460 V=(V1+V3)*COS(T)+V2
1470 F=S/V-R:R5=.0001*R:R6=-.0001*R
1480 ENDPROC
1490 DEF PROCANGLE
1500 IF T=0 THEN B=0:GOTO1520
1510 B=ATN(R*SIN(T)/(R1+R*COS(T)))
1520 A2=ASN((R2*SIN(A4)+R*SIN(A4+T))/((R*SIN(T))^2+(R1+R*COS(T))^2)^.5)-B:A2=AB

```

```

S(A2)
1530 RP=(R1*(1-COS(A2))+R2*(1-COS(A4)))/(COS(A2+T)+COS(A4+T))
1540 E=R-RP;R7=.001*R;R8=-.001*R
1550 ENDPROC
1560 DEF PROCJ2
1570 RA=R;Q=.05
1580 REPEAT:Q=Q+.05;W1=RA+Q*RA;W2=RA-Q*RA
1590 IF F1<F2 THEN W1=W2;W2=RA+Q*RA;Q=Q-.05
1600 R=W1;PROCCURV:F1=F
1610 R=W2;PROCCURV:F2=F
1620 UNTIL F1>0 AND F2<0
1630 ENDPROC
1640 DEF PROCJ3
1650 W=R+(R8-RA);R=W;PROCCURV
1660 Q=.02
1670 IFF<0 THEN 1710
1680 REPEAT:Q=Q+.001;W1=W;W2=W+Q*R;R=W2;PROCCURV
1690 UNTIL F<0
1700 GOTO1730
1710 REPEAT:Q=Q+.001;W2=W;W1=W-Q*R;R=W1;PROCCURV
1720 UNTIL F>0
1730 ENDPROC
1740 DEF PROCINIT
1750 PRINT:PRINT:PRINT:INPUT"Do you want RADIUS RATIO or CONTACT ANGLE variatio
n (R/A) ";A$:IF A$="R" THEN 1810
1760 PRINT:INPUT"Radius Ratio R1/R2 ";R1:R2=1
1770 PRINT:INPUT"Min contact angle (deg)";RI
1780 PRINT:INPUT"Max contact angle (deg)";RX
1790 RR=RI:T=RARR:IF RR>90 THEN T=RAD(180-RR)
1800 GOTO1850
1810 PRINT:PRINT:INPUT"CONTACT ANGLE (DEG) ";T:T=RAD(T)
1820 PRINT:INPUT"MIN R1/R2 ";RI
1830 PRINT:INPUT"MAX R1/R2 ";RX
1840 RR=RI:R1=RR:R2=1
1850 PRINT:INPUT"Step size ";SS
1860 CLS:PRINT"*****"
1870 PRINT"*****CURVATURE CALCULATION*****"
1880 PRINT"*****"
1890 PRINT:PRINT:PRINT"GUESS TWO WEDGE RADII (ROD UNITS)"
1900 PRINT:PRINT:INPUT"ONE ABOVE GUESS - ( +ive error ) ";W1
1910 PRINT:INPUT"ONE BELOW GUESS - ( -ive error ) ";W2
1920 R=W1;PROCCURV
1930 F1=F;R=W2;PROCCURV
1940 F2=F:PRINT:PRINT:PRINT"GUESS (1) - ERROR = ";F1
1950 PRINT:PRINT"GUESS (2) - ERROR = ";F2
1960 PRINT:PRINT:F:PRINT"CONTINUE - (Y/N)"
1970 get$=GET$
1980 IF get$="N"THEN 1860
1990 IF get$<>"Y"ANDget$<>"N"THEN1970
2000 CLS:PRINT:PRINT:INPUT"HEADINGS (Y/N) ";B$:IF B$<>"Y"THEN2050
2010 VDU2: PRINT:PRINT:PRINT:PRINT"CURVATURE CALCULATIONS FOR TWO RODS AGAINST
A PLATE":IF A$="R" THEN PRINT:PRINT:PRINT"CONTACT ANGLE = ";DEG(T):PRINT:PRINT:G
OTO 2040
2020 PRINT:PRINT:PRINT"RADIUS RATIO = ";R1:PRINT:PRINT
2030 PRINT" CONTACT ANGLE CURVATURE AREA PERIMETER A4":PRINT:PRINT:VD
U3:GOTO2050
2040 PRINT" RADIUS RATIO CURVATURE AREA PERIMETER A4":PRINT:PRINT:VD
U3
2050 ENDPROC

```


H.2 THEORETICAL RESULTS

Tables H.1 to H.3 show the MS-P predicted curvatures for the three partially wetted systems investigated. The results given by the above program were used to plot the curves shown in section 10.3.

Table H.1 MS-P predictions for the two equal rod arrangement with all components partially wetted ($\theta_1 = \theta_2 = \theta_3$).

Contact Angle $\theta_1, \theta_2, \theta_3$ (deg.)	Angle α_3 (deg.)	Effective Area A_{eff} (rod units ²)	Effective Perimeter P_{eff} (rod units)	Curvature C_{MS-P}
0	29.02	0.3105	2.1641	6.970
5	28.36	0.3113	2.1649	6.956
10	27.69	0.3132	2.1637	6.908
15	26.99	0.3162	2.1586	6.827
20	26.24	0.3202	2.1479	6.708
25	25.46	0.3250	2.1287	6.551
30	25.64	0.3306	2.0993	6.351
35	23.78	0.3368	2.0573	6.108
40	22.84	0.3438	2.0017	5.822
45	21.82	0.3515	1.9303	5.491
50	20.70	0.3598	1.8405	5.116
55	19.46	0.3688	1.7306	4.693
60	18.03	0.3785	1.5980	4.222
65	16.37	0.3888	1.4390	3.701
70	14.38	0.3997	1.2492	3.125
75	11.92	0.4107	1.0217	2.488
80	8.80	0.4207	0.7466	1.775
85	4.81	0.4276	0.4103	0.959
90	0.00	0.0000	0.0000	0.000

Table H.2 Mixed wettability MS-P predictions for the two equal rod arrangement with the plate and one rod partially wetted with the other rod perfectly wetted ($\theta_2 = 0$).

Contact Angle	Angles		Effective Area	Effective Perimeter	Curvature
θ_1, θ_3 (deg.)	α_3	α_3'	A_{eff} (rod units ²)	P_{eff} (rod units)	C_{MS-P}
0	29.02	29.02	0.3105	2.1641	6.970
5	28.39	29.00	0.3111	2.1640	6.960
10	27.77	28.98	0.3124	2.1638	6.927
15	27.17	28.94	0.3145	2.1603	6.869
20	26.59	28.91	0.3172	2.1524	6.785
25	26.01	28.86	0.3205	2.1389	6.674
30	25.45	28.82	0.3242	2.1181	6.533
35	24.91	28.78	0.3283	2.0890	6.363
40	24.38	28.75	0.3327	2.0500	6.161
45	23.87	28.74	0.3374	2.0004	5.929
50	23.37	28.75	0.3423	1.9389	5.665
55	22.89	28.78	0.3472	1.8641	5.368
60	22.44	28.86	0.3522	1.7752	5.040
65	22.01	28.98	0.3571	1.6708	4.679
70	21.61	29.19	0.3617	1.5490	4.283
75	21.25	29.51	0.3655	1.4078	3.851
80	20.95	30.00	0.3682	1.2441	3.379
85	20.74	30.78	0.3687	1.0538	2.858
90	20.69	30.08	0.3656	0.8312	2.274

Table H.3 Mixed wettability MS-P predictions for the two equal rod arrangement with only the plate partially wetted and both rods perfectly wetted ($\theta_1 = \theta_2 = 0$).

Contact Angle	Angle	Effective Area	Effective Perimeter	Curvature
θ_3 (deg.)	α_3 (deg.)	A_{eff} (rod units ²)	P_{eff} (rod units)	C_{MS-P}
0	29.02	0.3105	2.1641	6.970
5	29.03	0.3108	2.1641	6.964
10	29.06	0.3116	2.1639	6.944
15	29.12	0.3128	2.1617	6.911
20	29.21	0.3143	2.1573	6.863
25	29.34	0.3162	2.1494	6.798
30	29.49	0.3182	2.1376	6.717
35	29.68	0.3204	2.1213	6.620
40	29.92	0.3228	2.0996	6.505
45	30.19	0.3252	2.0724	6.373
50	30.51	0.3276	2.0390	6.223
55	30.87	0.3301	1.9995	6.058
60	31.29	0.3325	1.9534	5.876
65	31.76	0.3348	1.9008	5.679
70	32.29	0.3369	1.8415	5.465
75	32.89	0.3389	1.7758	5.240
80	33.55	0.3407	1.7039	5.001
85	34.29	0.3422	1.6260	4.752
90	35.12	0.3433	1.5424	4.492

H.3 EXPERIMENTAL RESULTS

Tables H.4 and H.5 contain the detailed experimental results for the wholly partially wetted system and each of the mixed wettability systems investigated with the two rods and a plate arrangement.

Table H.4 Experimental results for the mixed wettability arrangements. The readings relating to the one and two wetted rod systems were obtained together using a joint standard.

Contact Angle	Standard Rise	Test Rise	Comparative Method Curvature (mean)	Physical Properties Curvature (mean)	MS-P Curvature	% Dev.
θ (deg.)	Δh_{sc} (mm)	Δh_{2c} (mm)	C_{EXPT}	C_p		
Iso.						
4.6	13.09	12.67	6.950			
r	12.87	12.57	6.950			
	12.98	12.60	6.961			
	12.92	12.55	6.959		6.958	-0.4
			6.955±.006			
29.6		11.44		6.412		
a		11.55		6.474		
		11.43		6.407		
		11.59		6.496	6.368	+1.25
				6.447±.049		
n-Do.						
22.8	15.96	13.99	6.287	6.328		
r	15.98	13.74	6.166	6.215		
	15.90	13.65	6.157	6.174		
	15.93	14.06	6.330	6.360	6.625	-5.37
			6.235±.095	6.269±.095		
47.9		11.90		5.383		
a		12.12		5.482		
		11.65		5.270		
		11.87		5.369	5.279	+1.80
				5.376±.106		
n-Tet.						
25.1	16.41	14.41	6.298	6.351		
r	16.39	14.49	6.340	6.386		
	16.37	14.25	6.243	6.281		
	16.34	14.59	6.404	6.430	6.546	-2.81
			6.321±.083	6.362±.081		
50.2		12.13		5.346		
a		12.18		5.368		
		12.20		5.377		
		12.09		5.329	5.010	+6.40
				5.355±.026		
Dioc.						
30.8	15.99	14.36	6.441	7.030		
r	16.03	14.31	6.402	7.006		
	15.98	14.40	6.463	7.050		
	16.01	14.46	6.477	7.079	6.315	+2.07
			6.446±.044	7.041±.038		

continued...

Table H.4 concluded.

Contact Angle	Standard Rise	Test Rise	Comparative Method Curvature (mean)	Physical Properties Curvature (mean)	MS-P Curvature	% Dev.
θ (deg.)	Δh_{s_c} (mm)	Δh_{z_c} (mm)	C_{EXPT}	C_p		
55.9 a	mean of above used	10.80	4.843	5.287	4.611	+5.22
		10.83	4.856	5.302		
		10.77	4.829	5.273		
		10.86	4.870	5.317		
			4.852±.023			
Hexa. 43.3 r	9.98 10.01 9.97 10.05	7.83	5.627	5.556	5.605	-1.88
		7.59	5.438	5.386		
		7.75	5.575	5.500		
		7.83	5.587	5.556		
			5.557±.149	5.496±.117		
68.4 a		4.94		3.506	3.315	+4.31
		4.90		3.477		
		4.77		3.385		
		4.88		3.463		
				3.458±.073		
α -Bro. 58.1 r	13.06 13.09 13.11 13.08	8.51	4.673	4.433	4.406	+0.60
		8.44	4.624	4.396		
		8.49	4.644	4.422		
		8.60	4.715	4.480		
			4.664±.051	4.433±.047		
83.2 a		4.32		2.250	1.267	+78.50
		4.41		2.297		
		4.26		2.219		
		4.37		2.276		
				2.261±.042		

$C_{EXPT} = 6.94\Delta h_{i_c}R_i/\Delta h_{s_c}R_s$ and $C_p = 2\Delta h_{i_c}R_i/a^2$ where $R_i = 1.547$ mm and $R_s = 1.497$ mm.

Table H.5 Experimental results for the mixed wettability arrangements. The readings relating to the one and two wetted rod systems were obtained together using a joint standard.

Contact Angle	Two Rods Wetted					One Rod Wetted				
	Standard Rise	Test Rise	Comp. Method Curvature (mean)	Physical Properties Curvature (mean)	MS-P Curv.	Test Rise	Comp. Method Curvature (mean)	Physical Properties Curvature (mean)	MS-P Curv.	
	θ (deg.)	Δh_{1c} (mm)	Δh_{2c} (mm)	C_{EXPT}	C_P	% Dev.	Δh_{2c} (mm)	C_{EXPT}	C_P	% Dev.
Iso. r 4.6	12.96	12.33	6.968		6.964	12.33	6.968		6.960	
	12.89	12.20	6.932			12.21	6.938			
	12.83	12.16	6.942			12.15	6.936			
	12.87	12.25	6.972			12.23	6.960			
			6.954±.022			-0.14		6.951±0.017		
a 29.6	12.93	12.05	6.826		6.725	11.70	6.628		6.546	
	12.90	12.00	6.814			11.69	6.637			
	12.83	11.89	6.788			11.60	6.622			
	12.93	11.97	6.781			11.61	6.577			
			6.802±.024			+1.14		6.616±.039		
n-do. r 22.8	15.94	14.43	6.631	6.671	6.828	14.13	6.493	6.532	6.726	
	15.93	14.42	6.630	6.666		14.22	6.538	6.574		
	15.95	14.47	6.645	6.689		14.23	6.535	6.578		
	15.90	14.39	6.629	6.652		14.10	6.495	6.518		
			6.634±.016	6.669±.037	-2.84		6.515±.040	6.551±.060		-3.14
a 47.9	15.95	13.84	6.356	6.398	6.288	12.97	5.956	5.996	5.780	
	15.89	13.77	6.347	6.366		12.90	5.946	5.963		
	15.90	13.86	6.385	6.407		12.98	5.979	6.000		
	15.92	13.80	6.349	6.379		12.94	5.953	5.982		
			6.359±.022	6.387±.022	+1.13		5.958±.022	5.985±.022		+3.08
n-tet r 25.1	16.14	14.83	6.730	6.680	6.797	14.39	6.530	6.482	6.672	
	16.27	14.93	6.721	6.725		14.50	6.528	6.531		
	16.25	14.85	6.693	6.689		14.49	6.531	6.527		
	16.33	14.85	6.661	6.689		14.56	6.531	6.558		
			6.701±.040	6.696±.029	-1.41		6.530±.002	6.524±.042		-2.13
a 50.2	16.35	14.01	6.276	6.310	6.217	13.04	5.842	5.874	5.654	
	16.23	13.87	6.260	6.247		12.93	5.835	5.824		
	16.16	13.82	6.264	6.225		12.88	5.838	5.802		
	16.25	13.92	6.274	6.270		12.97	5.846	5.842		
			6.268±.008	6.263±.047	+0.82		5.840±.006	5.836±.040		+3.29
Dioc. r 30.8	16.02	14.52	6.639		6.703	14.15	6.469		6.508	
	16.03	14.60	6.671			14.40	6.580			
	16.03	14.40	6.580			14.11	6.447			
	16.04	14.61	6.672			14.20	6.484			
			6.640±.060			-0.94		6.495±.085		

continued...

Table H.5 Concluded.

Contact Angle	Standard Rise	Two Rods Wetted				One Rod Wetted			
		Test Rise	Comp. Method Curvature (mean)	Physical Properties Curvature (mean)	MS-P Curv.	Test Rise	Comp. Method Curvature (mean)	Physical Properties Curvature (mean)	MS-P Curv.
θ (deg.)	Δh_{1c} (mm)	Δh_{2c} (mm)	C_{EXPT}	C_P	% Dev.	Δh_{2c} (mm)	C_{EXPT}	C_P	% Dev.
a 55.9	16.06	13.02	5.938		6.026	11.88	5.418		5.312
	16.03	12.94	5.912			11.79	5.387		
	16.06	13.12	5.984			12.18	5.555		
	16.06	13.02	5.938			11.93	5.441		
			5.943±.041		-1.38		5.450±.063		+2.60
Hexa. r 43.3	10.10	8.85	6.418	6.418	6.419	8.19	5.939	5.940	6.012
	10.04	8.80	6.420	6.382		8.15	5.946	5.911	
	10.06	8.79	6.400	6.375		8.11	5.905	5.882	
	10.01	8.72	6.381	6.324		8.18	5.985	5.932	
			6.405±.024	6.375±.051	-2.18		5.944±.041	5.916±.034	-1.13
a 68.4	9.77	7.78		5.642	5.535	6.28		4.554	4.414
	9.67	7.87		5.708		6.47		4.692	
	9.64	7.83		5.679		6.35		4.605	
	9.63	7.90		5.729		6.42		4.656	
				5.689±.048	+2.78			4.627±.065	+4.82

$C_{EXPT} = 6.94\Delta h_{1c}R_1/\Delta h_{2c}R_2$, and $C_P = 2\Delta h_{1c}R_1/a^2$ where $R_1 = 1.581$ mm and $R_2 = 1.498$ mm.

APPENDIX I

Three rods and a plate

I.1 COMPUTER PROGRAM

The solution program for this system differs somewhat from those for the other arrangements. The system was investigated early in the study period and a Commodore PET was used for the programming; the procedures of section 6.4.2.1 being replaced by broadly similar subroutines. The program, which is listed overleaf, is also more involved as there are eight possible TM configurations, each with its own set of equations. The initialisation routine enables the user to select a configuration for given rod sizes. Maximum and minimum possible values of the half angle, ϕ , and outer rod spacing, L_2 , are given to guide the user when selecting limits for the interpolation. Single predictions may also be obtained. All inputted information in addition to the curvatures of menisci at selected ϕ values are given on a hard printout.

READY.

```
1000 REM*****
1010 REM** CAPILLARY RISE/CURVATURE **
1020 REM** THREE UNEQUAL RODS+PLATE **
1030 REM** TIM WALSH - AUG 1986 **
1040 REM*****
1050 GOTO2760
1060 IFX>.99999THEN Y=0:GOTO 1090
1070 IF X<-.99999 THEN Y=π:GOTO1090
1080 Y=-ATN(X/SQR(-X*X+1))+π/2
1090 RETURN
1095 REM****SUCCESSIVE BISECTION****
1100 DEF FNAC(Y)=-ATN(X/SQR(-X*X+1))+π/2:GOTO2760
1110 W1=R:R=(W1+W2)/2:ONNNHGOSUB1220,1480,1770,1950,2070,2310,2620:RETURN
1120 W2=R:R=(W1+W2)/2:ONNNHGOSUB1220,1480,1770,1950,2070,2310,2620:RETURN
1130 R=(W1+W2)/2:ON NN GOSUB 1220,1480,1770,1950,2070,2310,2620
1140 IFF>R5THEN GOSUB1110:GOTO1140
1150 IFF<R6THEN GOSUB1120:GOTO1140
1160 RA=RB:RB=R:REM PRINT FIRST*****
1170 RR=R1/R:TH=INT(TH*100+.5)/100:RR=INT(RR*10000+.5)/10000:L=INT(L*1000+.5)
1180 L=L/1000:PRINT#2,TH;L;RR;S;Y
1190 J=J+1:GOTO4180
1200 REM****FOUR WEDGES - TYPE E****
1210 REM****ANGLES****
1220 A=R1+R2:B=R2+R:C=R1+R:X=(A*A+B*B-C*C)/2/A/B:GOSUB1060:A4=Y
1230 B=R1+R:C=R2+R:X=(A*A+B*B-C*C)/2/A/B:GOSUB1060:A3=Y
1240 A=R2+R3:B=R2+R:C=R3+R:X=(A*A+B*B-C*C)/2/A/B:GOSUB1060:A6=Y
1250 A=R2+R3:B=R3+R:C=R2+R:X=(A*A+B*B-C*C)/2/A/B:GOSUB1060:A7=Y
1260 A=R1-R:B=R1+R:X=A/B:GOSUB1060:A1=Y
1270 A=R3-R:B=R3+R:X=A/B:GOSUB1060:A9=Y:K=(R1-R3)/L:T=ATN(K)
1280 A=R1+R2:B=R2+R3:C=L/COS(T):X=(A*A+B*B-C*C)/2/A/B:GOSUB1060:P=Y:G=π/2-T
1290 B=R1+R2:C=R2+R3:A=L/COS(T):X=(A*A+B*B-C*C)/2/A/B:GOSUB1060:G1=Y:G2=π-P-G1
1300 A2=G+G1-A3-A1:A8=π/2+T+G2-A9-A7:A5=P-A4-A6
1310 IF HT=π THENA2=π/2-T-G1-A3-A1:A5=2*π-P-A4-A6:A8=π/2-(G2-T)-A7-A9
1320 REM****AREA OF POLYGON
1330 A=.5*(R1+R3)*L:B=.5*(R1+R2)*(R2+R3)*SIN(P):S9=A+B:IF HT=πTHENS9=A-B
1340 A=.5*(R1+R)*(R1-R)*SIN(A1):B=R*(R1+R)*SIN(A1):C=(π-A1)*.5*R*R:S1=A+B-C
1350 S2=R1*R1*A2/2
1360 A=.5*(R1+R2)*(R1+R)*SIN(A3):B=.5*R*R*(π-A3-A4):S3=A-B
1370 S4=.5*R2*R2*A5
1380 A=.5*(R2+R3)*(R3+R)*SIN(A7):B=.5*R*R*(π-A6-A7):S5=A-B
1390 S6=.5*R3*R3*A8
1400 A=.5*(R3+R)*(R3-R)*SIN(A9):C=.5*R*R*(π-A9):B=R*(R3+R)*SIN(A9):S7=A+B-C
1410 A=S1+S2+S3+S4+S5+S6+S7:S=S9-A
1420 REM****PERIMETER***
1430 V1=R1*A2:V2=R2*A5:V3=R3*A8:A=(R3+R)*SIN(A9):B=(R1+R)*SIN(A1)
1440 V4=L-A-B:V5=R*(π-A1):V6=R*(π-A3-A4):V7=R*(π-A6-A7):V8=R*(π-A9)
1450 V=V1+V2+V3+V4+V5+V6+V7+V8
1460 F=(S/Y)-R:R5=.0001*R:R6=-.0001*R
1470 RETURN
1480 REM****BACK 2 UP 1 DOWN-LOW THI ~ TYPE D****
1490 REM*** ANGLES ***
1500 L1=SQR((R1-R3)^2+L*L)
1510 A=R1+R2:B=R1+R:C=R2+R:X=(A*A+B*B-C*C)/2/A/B:GOSUB1060:A3=Y
1520 A=R1+R2:B=R2+R:C=R1+R:X=(A*A+B*B-C*C)/2/A/B:GOSUB1060:A4=Y
1530 A=R3+R2:B=R2+R:C=R3+R:X=(A*A+B*B-C*C)/2/A/B:GOSUB1060:A6=Y
1540 A=R3+R2:B=R3+R:C=R2+R:X=(A*A+B*B-C*C)/2/A/B:GOSUB1060:A7=Y
1550 A5=HT-A6-A4
1560 A=R1+R:B=L1:C=R3+R:X=(A*A+B*B-C*C)/2/A/B:GOSUB1060:A1=Y
1570 A=R3+R:B=L1:C=R1+R:X=(A*A+B*B-C*C)/2/A/B:GOSUB1060:A9=Y
1580 A=R1+R2:B=L1:C=R2+R3:X=(A*A+B*B-C*C)/2/A/B:GOSUB1060:G1=Y:G2=π-HT-G1
```



```

1590 A2=G1-A3:A8=G2-A7
1600 REM***AREA OF POLYGON***
1610 S9=L1*SIN(G1)*(R1+R2)/2+L1*SIN(A1)*(R1+R)/2
1620 S1=(A1*R1*R1+A9*R3*R3+(PI-A1-A9)*R*R)/2
1630 S2=A2*R1*R1/2
1640 S3=((R1+R2)*(R1+R)*SIN(A3)-(PI-A3-A4)*R*R)/2
1650 S4=A5*R2*R2/2
1660 S5=((R2+R3)*(R3+R)*SIN(A7)-(PI-A7-A6)*R*R)/2
1670 S6=A8*R3*R3/2
1680 S=S9-S1-S2-S3-S4-S5-S6
1690 REM***PERIMETER***
1700 V1=(A1+A2)*R1+(A9+A8)*R3+A5*R2
1710 V2=R*((PI-A3-A4)+(PI-A7-A6)-(PI-A1-A9))
1720 V=V1+V2
1730 F=(S/V)-R:R5=.0001*R:R6=-.0001*R
1740 RETURN
1750 REM***UP IN FRONT-LOW THI - TYPE A***
1760 REM*** ANGLES ***
1770 X=(R1-R)/(R1+R):GOSUB1060:A1=Y
1780 X=(R3-R)/(R3+R):GOSUB1060:A6=Y
1790 A=SQR(L*L+(R1-R3)^2):X=(A^2+(R1+R)^2-(R3+R)^2)/2/A/(R1+R):GOSUB1060:A3=Y
1800 B=(R3+R):X=(A*A+B*B-(R1+R)^2)/2/A/B:GOSUB1060:A4=Y
1810 T=ATN((R1-R3)/L):L1=L/COS(T):A=R1+R2:B=R2+R3:X=(A*A+B*B-L1^2)/2/A/B
1820 A2=PI/2-A3-A1-T:A5=PI/2+T-A4-A6
1830 REM***AREA OF POLYGON***
1840 S1=R*(R1+R)*SIN(A1)+.5*(R1+R)*(R1-R)*SIN(A1)-(PI-A1)*R*R/2
1850 S2=.5*A2*R1*R1
1860 S3=.5*L1*(R1+R)*SIN(A3)-.5*R*R*(PI-A3-A4)
1870 S4=.5*A5*R3*R3
1880 S5=R*(R3+R)*SIN(A6)+.5*(R3+R)*(R3-R)*SIN(A6)-(PI-A6)*R*R/2
1890 S=L*R1-.5*(R1-R3)*L-S1-S2-S3-S4-S5
1900 REM***PERIMETER***
1910 V1=(3*PI-A1-A3-A4-A6)*R
1920 V2=A2*R1+A5*R3+L-(R3+R)*SIN(A6)-(R1+R)*SIN(A1):V=V1+V2
1930 F=(S/V)-R:R5=.0001*R:R6=-.0001*R
1940 RETURN
1950 REM***BACK 1 UP 1 UP-LOW THI - TYPE C***
1960 REM*** ANGLES ***
1970 A=SQR(L*L+(R1-R3)^2):X=(A^2+(R1+R)^2-(R3+R)^2)/2/A/(R1+R):GOSUB1060:A1=Y
1980 A2=A1:B=(R3+R):X=(A*A+B*B-(R1+R)^2)/2/A/B:GOSUB1060:A3=Y:A4=A3
1990 REM***AREA OF POLYGON***
2000 S=A*(R1+R)*SIN(A1)-R*R*(PI-A1-A4)-A4*R3-A1*R1
2010 REM***PERIMETER***
2020 V1=(A1+A2)*R1+(A3+A4)*R3
2030 V2=-R*((PI-A2-A3)+(PI-A1-A4))
2040 V=V1+V2
2050 F=(S/V)-R:R5=.0001*R:R6=-.0001*R
2060 RETURN
2070 REM***BACK 3 UP-LOW THI - TYPE B***
2080 REM***ANGLES***
2090 L1=SQR((R1-R3)+L*L)
2100 A=L1:B=R1+R:C=R3+R:X=(A*A+B*B-C*C)/2/A/B:GOSUB1060:A1=Y
2110 A=L1:B=R3+R:C=R1+R:X=(A*A+B*B-C*C)/2/A/B:GOSUB1060:A9=Y
2120 A=R1+R2:B=R1+R:C=R2+R:X=(A*A+B*B-C*C)/2/A/B:GOSUB1060:A3=Y
2130 A=R1+R2:B=R2+R:C=R1+R:X=(A*A+B*B-C*C)/2/A/B:GOSUB1060:A4=Y
2140 A=R3+R2:B=R2+R:C=R3+R:X=(A*A+B*B-C*C)/2/A/B:GOSUB1060:A6=Y
2150 A=R3+R2:B=R3+R:C=R2+R:X=(A*A+B*B-C*C)/2/A/B:GOSUB1060:A7=Y
2160 A=R1+R2:B=L1:C=R3+R2:X=(A*A+B*B-C*C)/2/A/B:GOSUB1060:G1=Y:G2=PI-HT-G1
2170 A5=HT-A4-A6:A2=G1-A1-A3:A8=G2-A7-A9
2180 REM***AREAS***
2190 S9=L1*(R1+R2)*SIN(G1)/2
2200 S1=L1*(R1+R)*SIN(A1)/2-(PI-A1-A9)*R*R/2
2210 S3=(R1+R2)*(R1+R)*SIN(A3)/2-(PI-A3-A4)*R*R/2
2220 S5=(R3+R2)*(R3+R)*SIN(A7)/2-(PI-A6-A7)*R*R/2
2230 S2=A2*R1*R1/2:S4=A5*R2*R2/2:S6=A8*R3*R3/2
2240 S=S9-S1-S2-S3-S4-S5-S6

```

```

2250 REM***PERIMETER***
2250 V1=A2*R1+A5*R2+A8*R3
2270 V2=R*((PI-A1-A9)+(PI-A3-A4)+(PI-A6-A7))
2280 V=V1+V2
2290 F=(S/V)-R;R5=.0001*R;R6=-.0001*R
2300 RETURN
2310 REM***UP IN SIDE PORES-HIGH THI - TYPE F***
2320 REM***ALSO SIDE 2 UP MID 1 DOWN - TYPE H***
2330 REM*** ANGLES ***
2340 X=(R8-R)/(R8+R);GOSUB1060:A1=Y
2350 A=R8+R2;B=R8+R;C=R2+R;X=(A*A+B*B-C*C)/2/A/B;GOSUB1060:A3=Y
2360 A=R8+R2;B=R2+R;C=R8+R;X=(A*A+B*B-C*C)/2/A/B;GOSUB1060:A4=Y
2370 L1=SQR((R8-R9)^2+L*L);B1=ATN((R8-R9)/L)
2380 B=L1;C=R2+R9;X=(A*A+B*B-C*C)/2/A/B;GOSUB1060;G1=Y
2390 B2=G1-B1;B3=PI/2-B2;IF HT>=PI THEN B2=G1+B1;B3=PI/2+B2
2400 DG=SIN(B2)*(R8+R2);DF=R8+DG;D=DF-R2;IF HT>=PI THEN DF=R8-DG;D=DF-R2
2410 X=(DF-R)/(R2+R);GOSUB1060:A6=Y
2420 A2=B2+PI/2-A1-A3;IF HT>=PI THEN A2=PI/2-B2-A1-A3
2430 A5=B3-A4-A6;IF NI=1 THEN A5=B3-A4
2440 REM***AREA OF POLYGON***
2450 S9=(R8+R2)*COS(B2)*(DG/2+R8);IF HT>=PI THEN S9=(R8+R2)*COS(B2)*(R8-DG/2)
2460 A=R8+R;S1=R*A*SIN(A1)+A*(R8-R)*SIN(A1)/2-(PI-A1)*R*R/2
2470 S2=A2*R8*R8/2
2480 S3=A*(R8+R2)*SIN(A3)/2-R*R*(PI-A4-A3)/2
2490 S4=A5*R2*R2/2
2500 A=R2+R;S5=A*SIN(A6)*(R+(R2+D-R)/2)-(PI-A6)*R*R/2
2510 IF NI=1 THEN S9=S9+(R2+R)*SIN(A6)*(R+(DF-R)/2);S5=A6*R2*R2/2+(PI-A6)*R*R/2
2520 S=S9-S1-S2-S3-S4-S5
2530 REM***PERIMETER***
2540 IF NI=1 THEN 2570
2550 V1=A2*R8+A5*R2+(R8+R2)*COS(B2)-(R8+R)*SIN(A1)-(R2+R)*SIN(A6)
2560 V2=R*((PI-A1)+(PI-A3-A4)+(PI-A6));GOTO2590
2570 V1=A2*R8+A5*R2+A6*R2+(R2+R)*SIN(A6)+(R8+R2)*COS(B2)-(R8+R)*SIN(A1)
2580 V2=R*((PI-A1)+(PI-A3-A4)-(PI-A6))
2590 V=V1+V2
2600 F=(S/V)-R;R5=.0001*R;R6=-.0001*R
2610 RETURN
2620 REM***UP IN MIDDLE-HIGH THI - TYPE G***
2630 REM***ANGLES***
2640 L1=SQR((R1-R3)^2+L*L);B1=ATN((R1-R3)/L)
2650 A=R1+R2;B=L1;C=R2+R3;X=(A*A+B*B-C*C)/2/A/B;GOSUB1060;G1=Y
2660 B2=G1-B1;B3=PI/2-B2;IF HT>=PI THEN B2=G1+B1;B3=PI/2+B2
2670 DG=SIN(B2)*(R1+R2);DF=R1+DG;D=DF-R2;IF HT>=PI THEN DF=R1-DG;D=DF-R2
2680 X=(DF-R)/(R2+R);GOSUB1060:A1=Y
2690 REM***AREA***
2700 S=2*(R2+R)*SIN(A1)*(R+(R2+D-R)/2)-(PI-A1)*R*R-A1*R2*R2
2710 REM***PERIMETER***
2720 V1=2*A1*R2+2*(R2+R)*SIN(A1);V2=-2*(PI-A1)*R
2730 V=V1+V2
2740 F=(S/V)-R;R5=.0001*R;R6=-.0001*R
2750 RETURN
2755 REM***INITIALISATION***
2760 OPEN1,4:OPEN2,4,1:OPEN3,4,2:OPEN4,4,4:PRINT#4
2770 F#="|1999.99 |199.999 |1999.999 |1 9.999 |1 99.999 |1|":PRINT#3,F#
2780 POKE59468,14
2790 PRINT"
2800 PRINT"
2810 PRINT"
2820 PRINT" *ELECT MENISCUS SHAPE"
2830 PRINT" 1) 2OUR WEDGES (TYPE E) INTERMEDIATE |HI"
2840 PRINT" 2) JACK 2 UP 1 DOWN (TYPE D) LOW |HI"
2850 PRINT" 3) P IN FRONT (TYPE A) LOW |HI"
2860 PRINT" 4) P IN MIDDLE GAP (TYPE C) LOW |HI"
2870 PRINT" 5) JACK 3 UP (TYPE B) LOW |HI"
2880 PRINT" 6) P IN SIDE PORES (TYPE F) HIGH |HI"
2890 PRINT" 7) *IDE 2 UP MIDDLE 1 DOWN (TYPE H) HIGH |HI"

```



```

3560 C#=" 3) UP IN FRONT          LOW THI":GOTO3620
3570 C#=" 4) UP IN MIDDLE GAP     LOW THI":GOTO3620
3580 C#=" 5) BACK 3 UP           LOW THI":GOTO3620
3590 C#=" 6) UP IN SIDE PORES     HIGH THI":GOTO3620
3600 C#=" 7) SIDE 2 UP MIDDLE 1 DOWN HIGH THI":GOTO3620
3610 C#=" 8) UP IN MIDDLE GAP     HIGH THI"
3620 PRINT#1,"CAPILLARY SHAPE -";
3630 PRINT#1,C#
3640 IF VAL(A#)=1THENPRINT#1,"ROD RADII          R1=";R1;" R2=";R2;" F3=";R3
3650 IF VAL(A#)=2THENPRINT#1,"RADIUS RATIOS" - R1/R2 =";R2;" R1/R3 =";R3
3660 PRINT#1,"PHYSICAL LIMITS - ; MIN THI =" ;T8;" MAX THI =" ;T9
3670 PRINT#1," MIN L =" ;L8;" MAX L =" ;L9
3680 PRINT#1:PRINT#1:PRINT#1
3690 PRINT#1," THI L CURVATURE AREA PERIMETER "
3700 PRINT"J"
3710 PRINT" "
3720 PRINT" "
3730 PRINT" (GUESS) OF WEDGE RADII (ROD UNITS), AT MINIMUM I.R. (OR MIN L)"
3740 INPUT" (GUESS) OF THE ABOVE GUESS (+IVE ERROR)";W1
3750 INPUT" (GUESS) OF THE BELOW GUESS (-IVE ERROR)";W2
3760 R=W1
3770 R=W1:ON NN GOSUB 1220,1480,1770,1950,2070,2310,2620
3780 F1=F:R=W2:ON NN GOSUB 1220,1480,1770,1950,2070,2310,2620
3790 F2=F
3800 PRINT" (GUESS) (1) - ERROR =" ;F1
3810 PRINT" (GUESS) (2) - ERROR =" ;F2
3820 PRINT" (Y/N) "
3830 GET G#
3840 IF G#<>"Y"AND G#<>"N"THEN3830
3850 IF G#="N"THEN3700
3860 IF F1<0 OR F2>0 THEN3700
3870 PRINT" "
3880 PRINT" "
3890 PRINT" "
3900 J=1
3910 REM****INTERPOLATION LOOP****
3920 FOR TH=T1 TO T2 STEPSS
3930 HT=2*TH:HT=HT*PI/360:GOTO3940
3940 LC=SQR((R1+R2)^2+(R2+R3)^2-2*COS(HT)*(R1+R2)*(R2+R3))
3950 L=SQR(LC*LC-(R1-R3)^2)
3960 IF J>2THEN 4030
3970 IF J=2THEN 3990
3980 GOTO 1130
3990 RA=R:Q=.1
4000 W1=RA+Q*RA:W2=RA-Q*RA
4010 IF F1<F2THEN W1=W2:W2=RA+Q*RA
4020 R= W1:ON NN GOSUB 1220,1480,1770,1950,2070,2310,2620:F1=F
4030 R= W2:ON NN GOSUB 1220,1480,1770,1950,2070,2310,2620:F2=F
4040 IF F1<F2THEN W1=W2:W2=RA+Q*RA
4050 IF F1>0 AND F2>0 THEN Q=Q+.05:GOTO4000
4060 IF F1<0 AND F2<0 THEN Q=Q+.05:GOTO4000
4070 GOTO 1130
4080 W=R+(R6-RA):R=W:ON NN GOSUB1220,1480,1770,1950,2070,2310,2620
4090 IF F<0THEN4140
4100 Q=.01
4110 W1=W:W2=W+Q*R:R=W2:ON NN GOSUB1220,1480,1770,1950,2070,2310,2620
4120 F1=F:IF F>0 THEN Q=Q+.001:GOTO4110
4130 GOTO 1130
4140 Q=.01
4150 W2=W:W1=W-Q*R:R=W1:ON NN GOSUB1220,1480,1770,1950,2070,2310,2620
4160 F2=F:IF F<0 THEN Q=Q+.001:GOTO4150
4170 GOTO 1130
4180 NEXT TH
4190 FORI=1TO5:PRINT#1:NEXTI
READY.

```

I.2 THEORETICAL RESULTS

Tables I.1 through I.23 detail the MS-P predicted curvatures for each of the four systems studied. The results, obtained from the computer program above, were used to plot the graphs of chapter 11.

I.2.1 Three equal rods and a plate - $R_1 = R_2 = R_3$

Table I.1 MS-P predictions for the three equal rod arrangement containing a type E TM.

Half Angle ϕ (deg)	Outer Rod spacing L_2 (rod units)	Effective Area A_{eff} (rod units)	Effective Perimeter P_{eff} (rod units)	Curvature C_{MS-P}
min				
30.00	2.000	0.499	5.049	10.106
31.00	2.060	0.592	4.914	8.583
32.00	2.120	0.642	4.805	7.476
33.00	2.179	0.710	4.717	6.641
34.00	2.237	0.775	4.646	5.993
35.00	2.294	0.837	4.589	5.477
36.00	2.351	0.898	4.544	5.059
38.00	2.463	1.011	4.484	4.432
40.00	2.571	1.116	4.456	3.989
42.00	2.667	1.213	4.453	3.670
44.00	2.779	1.301	4.469	3.435
46.00	2.877	1.379	4.501	3.262
48.00	2.925	1.449	4.545	3.136
50.00	3.064	1.509	4.600	3.047
52.00	3.152	1.559	4.662	2.989
54.00	3.236	1.600	4.732	2.956
56.00	3.316	1.631	4.808	2.947
58.00	3.392	1.652	4.889	2.959
60.00	3.464	1.663	4.975	2.990
62.00	3.532	1.664	5.065	3.043
64.00	3.595	1.656	5.159	3.115
66.00	3.654	1.637	5.257	3.210
68.00	3.709	1.609	5.359	3.329
70.00	3.759	1.572	5.465	3.475
72.00	3.804	1.525	5.575	3.653
74.00	3.845	1.470	5.690	3.868
76.00	3.881	1.407	5.811	4.129
78.00	3.913	1.335	5.938	4.446
80.00	3.939	1.256	6.073	4.835
82.00	3.961	1.169	6.217	5.317
84.00	3.978	1.075	6.372	5.925
85.00	3.985	1.026	6.455	6.291
86.00	3.990	0.975	6.541	6.708
87.00	3.995	0.922	6.632	7.189
88.00	3.998	0.868	6.727	7.747
89.00	3.999	0.812	6.827	8.400
90.00	4.000	0.755	6.935	9.178
max				

Table I.2 MS-P predictions for the three equal rod arrangement containing a *type A* TM.

Half Angle ϕ (deg)	Outer Rod spacing L_2 (rod units)	Effective Area A_{eff} (rod units)	Effective Perimeter P_{eff} (rod units)	Curvature C_{MS-P}
30.00	2.000	0.310	2.164	6.970
31.00	2.060	0.348	2.292	6.577
32.00	2.120	0.390	2.426	6.218
33.00	2.179	0.436	2.569	5.886
34.00	2.237	0.488	2.724	5.579
35.00	2.294	0.547	2.896	5.294
36.00	2.351	0.616	3.097	5.026
37.00	2.407	0.707	3.375	4.771

Table I.3 MS-P predictions for the three equal rod arrangement containing a *type B* TM.

Half Angle ϕ (deg)	Outer Rod spacing L_2 (rod units)	Effective Area A_{eff} (rod units)	Effective Perimeter P_{eff} (rod units)	Curvature C_{MS-P}
30.00	2.000	0.117	1.325	11.319
30.50	2.030	0.126	1.379	10.896
31.00	2.060	0.137	1.438	10.487
31.50	2.090	0.148	1.501	10.093
32.00	2.120	0.161	1.571	9.712
32.50	2.149	0.176	1.649	9.314
33.00	2.179	0.193	1.740	8.979
33.50	2.208	0.214	1.852	8.622
34.00	2.237	0.245	2.025	8.263
34.50	2.266	0.276	2.177	7.888
35.00	2.294	0.288	2.177	7.554

Table I.4 MS-P predictions for the three equal rod arrangement containing a *type D* TM.

Half Angle ϕ (deg)	Outer Rod spacing L_2 (rod units)	Effective Area A_{eff} (rod units)	Effective Perimeter P_{eff} (rod units)	Curvature C_{MS-P}
30.00	2.000	0.152	2.619	17.169
30.50	2.030	0.172	2.495	14.497
31.00	2.060	0.190	2.379	12.519
31.50	2.090	0.206	2.268	11.001
32.00	2.120	0.220	2.162	9.798
32.50	2.149	0.233	2.059	8.823
33.00	2.179	0.244	1.960	8.019
33.50	2.208	0.253	1.864	7.344
34.00	2.237	0.261	1.770	6.769
34.50	2.266	0.267	1.679	6.275
35.00	2.294	0.271	1.589	5.845
35.50	2.323	0.274	1.501	5.468
36.00	2.351	0.275	1.414	5.136
36.50	2.379	0.274	1.329	4.839
37.00	2.407	0.272	1.245	4.574

Table I.5 MS-P predictions for the three equal rod arrangement containing a *type F* TM.

Half Angle ϕ (deg)	Outer Rod spacing L_2 (rod units)	Effective Area A_{eff} (rod units)	Effective Perimeter P_{eff} (rod units)	Curvature C_{MS-P}
80.00	3.939	0.595	3.126	5.255
81.00	3.951	0.547	2.967	5.416
82.00	3.961	0.508	2.837	5.578
83.00	3.970	0.474	2.725	5.741
84.00	3.978	0.444	2.625	5.906
85.00	3.985	0.417	2.534	6.074
86.00	3.990	0.392	2.450	6.245
87.00	3.995	0.369	2.372	6.420
88.00	3.998	0.348	2.299	6.599
89.00	3.999	0.328	2.230	6.782
90.00	4.000	0.310	2.164	6.970

Table I.6 MS-P predictions for the three equal rod arrangement containing a type G TM.

Half Angle ϕ (deg)	Outer Rod spacing L_2 (rod units)	Effective Area A_{ϕ} (rod units)	Effective Perimeter P_{ϕ} (rod units)	Curvature C_{MS-P}
83.00	3.970	0.234	1.171	4.987
83.50	3.974	0.206	1.127	5.460
84.00	3.978	0.179	1.082	6.017
84.50	3.982	0.154	1.033	6.682
85.00	3.985	0.131	0.982	7.488
85.50	3.988	0.109	0.928	8.484
86.00	3.990	0.089	0.870	9.742
86.50	3.993	0.071	0.808	11.379
87.00	3.995	0.054	0.742	13.589
87.50	3.996	0.039	0.668	16.728
88.00	3.998	0.027	0.587	21.507
88.50	3.999	0.016	0.495	29.606
89.00	3.999	0.008	0.388	46.145
89.50	4.000	0.002	0.253	97.126

I.2.2 Three Unequal rods and a plate, symmetrical - $R_1 = 0.5R_2 = R_3$

Table I.7 MS-P predictions for the three unequal rods symmetrically arranged ($R_1/R_2 = 0.5$) containing a type E TM.

Half Angle ϕ (deg)	Outer Rod spacing L_2 (rod units)	Effective Area A_{eff} (rod units)	Effective Perimeter P_{eff} (rod units)	Curvature C_{MS-P}
min				
19.47	2.000	0.561	5.401	9.622
19.50	2.003	0.565	5.394	9.543
21.00	2.150	0.755	5.135	6.793
22.50	2.296	0.936	4.990	5.326
24.00	2.440	1.110	4.922	4.433
25.50	2.583	1.277	4.909	3.844
27.00	2.724	1.437	4.938	3.435
28.50	2.863	1.591	4.998	3.141
30.00	3.000	1.738	5.083	2.924
31.50	3.135	1.878	5.187	2.762
33.00	3.268	2.009	5.307	2.640
34.50	3.398	2.132	5.440	2.551
36.00	3.527	2.246	5.583	2.485
37.50	3.653	2.349	5.735	2.441
39.00	3.776	2.442	5.894	2.413
40.50	3.897	2.524	6.060	2.400
42.00	4.015	2.595	6.230	2.401
43.50	4.130	2.653	6.406	2.414
45.00	4.243	2.700	6.586	2.439
46.50	4.352	2.733	6.770	2.476
48.00	4.459	2.754	6.957	2.525
49.50	4.562	2.762	7.148	2.587
51.00	4.663	2.757	7.343	2.662
52.50	4.760	2.739	7.541	2.753
54.00	4.854	2.707	7.743	2.860
55.50	4.945	2.662	7.949	2.985
57.00	5.032	2.604	8.159	3.132
58.50	5.116	2.532	8.374	3.306
60.00	5.196	2.447	8.594	3.511
61.50	5.273	2.349	8.821	3.754
63.00	5.346	2.238	9.056	4.045
64.50	5.416	2.115	9.299	4.396
66.00	5.481	1.978	9.552	4.827
67.50	5.543	1.829	9.818	5.365
69.00	5.601	1.668	10.100	6.052
70.50	5.656	1.495	10.401	6.955
70.53	5.657	1.491	10.407	6.977
max				

Table I.8 MS-P predictions for the three unequal rods symmetrically arranged ($R_1/R_2 = 0.5$) containing a *type A* TM.

Half Angle ϕ (deg)	Outer Rod spacing L_2 (rod units)	Effective Area A_{eff} (rod units)	Effective Perimeter P_{eff} (rod units)	Curvature C_{MS-P}
19.47	2.000	0.310	2.164	6.970
19.50	2.003	0.312	2.170	6.950
20.00	2.052	0.343	2.274	6.628
20.50	2.101	0.376	2.383	6.326
21.00	2.150	0.413	2.499	6.042
21.50	2.199	0.453	2.622	5.776
22.00	2.248	0.498	2.755	5.524
22.50	2.296	0.549	2.901	5.285
23.00	2.344	0.607	3.070	5.057
23.50	2.392	0.679	3.286	4.838
24.00	2.440	0.788	3.642	4.616
24.50	2.488	0.834	3.681	4.411
25.00	2.536	0.880	3.722	4.227

Table I.9 MS-P predictions for the three unequal rods symmetrically arranged ($R_1/R_2 = 0.5$) containing a *type B* TM.

Half Angle ϕ (deg)	Outer Rod spacing L_2 (rod units)	Effective Area A_{eff} (rod units)	Effective Perimeter P_{eff} (rod units)	Curvature C_{MS-P}
19.47	2.000	0.172	1.610	9.324
19.50	2.003	0.173	1.615	9.293
20.00	2.052	0.194	1.710	8.794
20.50	2.101	0.217	1.814	8.325
21.00	2.150	0.244	1.929	7.881
21.50	2.199	0.276	2.063	7.456
22.00	2.248	0.316	2.229	7.049
22.50	2.296	0.375	2.499	6.648
23.00	2.344	0.426	2.659	6.242
23.50	2.392	0.453	2.674	5.897
24.00	2.440	0.480	2.690	5.603
24.50	2.488	0.506	2.708	5.351
25.00	2.536	0.531	2.726	5.134

Table I.10 MS-P predictions for the three unequal rods symmetrically arranged ($R_1/R_2 = 0.5$) containing a *type D* TM.

Half Angle ϕ (deg)	Outer Rod spacing L_2 (rod units)	Effective Area A_{eff} (rod units)	Effective Perimeter P_{eff} (rod units)	Curvature C_{MS-P}
19.47	2.000	0.220	3.025	13.693
19.50	2.003	0.223	3.014	13.498
20.00	2.052	0.259	2.831	10.894
20.50	2.101	0.292	2.662	9.098
21.00	2.150	0.321	2.503	7.789
21.50	2.199	0.346	2.353	6.794
22.00	2.248	0.367	2.209	6.012
22.50	2.296	0.384	2.070	5.384
23.00	2.344	0.397	1.936	4.869
23.50	2.392	0.407	1.806	4.438
24.00	2.440	0.412	1.679	4.074
24.50	2.488	0.413	1.555	3.762
25.00	2.536	0.410	1.434	3.492
25.50	2.583	0.403	1.314	3.256
26.00	2.630	0.392	1.196	3.048
26.50	2.677	0.377	1.080	2.864
27.00	2.724	0.357	0.965	2.699
27.50	2.770	0.333	0.852	2.552
28.00	2.817	0.305	0.739	2.419
28.50	2.863	0.273	0.627	2.298
29.00	2.909	0.236	0.517	2.188
29.50	2.955	0.194	0.406	2.088
30.00	3.000	0.149	0.297	1.996

Table I.11 MS-P predictions for the three unequal rods symmetrically arranged ($R_1/R_2 = 0.5$) containing a *type F* TM.

Half Angle ϕ (deg)	Outer Rod spacing L_2 (rod units)	Effective Area A_{eff} (rod units)	Effective Perimeter P_{eff} (rod units)	Curvature C_{MS-P}
60.00	5.196	1.187	4.547	3.829
60.50	5.222	1.127	4.382	3.887
61.00	5.248	1.077	4.250	3.944
61.50	5.273	1.033	4.136	4.001
62.00	5.298	0.994	4.034	4.057
62.50	5.322	0.958	3.942	4.114
63.00	5.346	0.925	3.858	4.171
63.50	5.370	0.894	3.780	4.227
64.00	5.393	0.865	3.706	4.284
64.50	5.416	0.837	3.637	4.340
65.00	5.438	0.812	3.751	4.397
65.50	5.460	0.787	3.509	4.455
66.00	5.841	0.764	3.450	4.513
66.50	5.502	0.742	3.392	4.571
67.00	5.523	0.720	3.338	4.630
67.50	5.543	0.700	3.285	4.688
68.00	5.563	0.681	3.234	4.748
68.50	5.583	0.662	3.185	4.808
69.00	5.601	0.644	3.137	4.868
69.50	5.620	0.627	3.091	4.929
70.00	5.638	0.610	3.046	4.990
70.50	5.656	0.594	3.003	5.052

Table I.12 MS-P predictions for the three unequal rods symmetrically arranged ($R_1/R_2 = 0.5$) containing a *type G* TM.

Half Angle ϕ (deg)	Outer Rod spacing L_2 (rod units)	Effective Area A_{eff} (rod units)	Effective Perimeter P_{eff} (rod units)	Curvature C_{MS-P}
64.00	5.393	0.440	1.861	4.221
64.50	5.416	0.385	1.784	4.627
65.00	5.438	0.333	1.703	5.109
65.50	5.460	0.284	1.617	5.693
66.00	5.841	0.238	1.526	6.411
66.50	5.502	0.195	1.430	7.316
67.00	5.523	0.156	1.327	8.489
67.50	5.543	0.120	1.216	10.067
68.00	5.563	0.089	1.095	12.293
68.50	5.583	0.061	0.962	15.659
69.00	5.601	0.038	0.812	21.310
69.50	5.620	0.019	0.638	32.645
70.00	5.638	0.006	0.422	66.185
70.50	5.656	0.000	0.003	$= \infty$

I.2.3 Three Unequal rods and a plate, symmetrical - $R_1 = 2R_2 = R_3$

Table I.13 MS-P predictions for the three unequal rods symmetrically arranged ($R_1/R_2 = 2$) containing a type E TM.

Half Angle ϕ (deg)	Outer Rod spacing L_2 (rod units)	Effective Area A_{eff} (rod units)	Effective Perimeter P_{eff} (rod units)	Curvature C_{MS-P}
min				
41.81	2.000	0.445	4.658	10.453
42.00	2.007	0.454	4.638	10.215
43.50	2.065	0.517	4.499	8.688
45.00	2.121	0.577	4.383	7.593
46.50	2.176	0.632	4.287	6.775
48.00	2.229	0.684	4.206	6.146
49.50	2.281	0.732	4.138	5.651
51.00	2.331	0.776	4.080	5.256
52.50	2.380	0.816	4.031	4.935
54.00	2.427	0.853	3.990	4.674
55.50	2.472	0.887	3.955	4.458
57.00	2.516	0.917	3.926	4.280
58.50	2.558	0.944	3.902	4.133
60.00	2.598	0.967	3.882	4.013
61.50	2.636	0.987	3.866	3.915
63.00	2.673	1.004	3.853	3.836
64.50	2.708	1.018	3.844	3.775
66.00	2.741	1.028	3.836	3.730
67.50	2.772	1.036	3.831	3.698
69.00	2.801	1.040	3.829	3.679
70.50	2.828	1.042	3.828	3.673
72.00	2.853	1.040	3.828	3.678
73.50	2.876	1.036	3.831	3.696
75.00	2.898	1.029	3.835	3.724
76.50	2.917	1.020	3.840	3.764
78.00	2.934	1.008	3.847	3.817
79.50	2.950	0.993	3.855	3.880
81.00	2.963	0.976	3.865	3.957
82.50	2.974	0.957	3.876	4.047
84.00	2.984	0.936	3.888	4.152
85.50	2.991	0.913	3.902	4.274
87.00	2.996	0.887	3.917	4.412
88.50	2.999	0.860	3.934	4.571
90.00	3.000	0.832	3.953	4.752
91.50	2.999	0.801	3.974	4.958
93.00	2.996	0.769	3.998	5.193
94.50	2.991	0.736	4.023	5.462
96.00	2.984	0.702	4.052	5.771
97.50	2.974	0.666	4.083	6.126
99.00	2.963	0.629	4.118	6.537
100.50	2.950	0.592	4.157	7.019
102.00	2.934	0.553	4.200	7.584
103.50	2.917	0.514	4.249	8.256
105.00	2.898	0.474	4.303	9.066
106.50	2.876	0.434	4.365	10.053
108.00	2.853	0.393	4.434	11.278
109.47	2.828	0.352	4.511	12.796
max				

Table I.14 MS-P predictions for the three unequal rods symmetrically arranged ($R_1/R_2 = 2$) containing a *type A* TM.

Half Angle ϕ (deg)	Outer Rod spacing L_2 (rod units)	Effective Area A_{eff} (rod units)	Effective Perimeter P_{eff} (rod units)	Curvature C_{MS-P}
41.81	2.000	0.310	2.164	6.970
42.00	2.007	0.315	2.179	6.919
43.00	2.046	0.339	2.261	6.667
44.00	2.084	0.364	2.344	6.431
45.00	2.121	0.391	2.430	6.208
46.00	2.158	0.419	2.518	5.999
47.00	2.194	0.449	2.609	5.802
48.00	2.229	0.481	2.703	5.616
49.00	2.264	0.515	2.803	5.441
50.00	2.298	0.551	2.908	5.275
51.00	2.331	0.590	3.022	5.117
52.00	2.364	0.634	3.150	4.967
53.00	2.396	0.685	3.305	4.822
54.00	2.427	0.798	3.598	4.680
55.00	2.457	0.804	3.655	4.541

Table I.15 MS-P predictions for the three unequal rods symmetrically arranged ($R_1/R_2 = 2$) containing a *type B* TM.

Half Angle ϕ (deg)	Outer Rod spacing L_2 (rod units)	Effective Area A_{eff} (rod units)	Effective Perimeter P_{eff} (rod units)	Curvature C_{MS-P}
41.81	2.000	0.068	1.014	14.812
42.00	2.007	0.070	1.027	14.647
43.00	2.046	0.079	1.098	13.800
44.00	2.084	0.090	1.182	12.993
45.00	2.121	0.105	1.283	12.213
46.00	2.158	0.124	1.424	11.447
47.00	2.194	0.157	1.677	10.644
48.00	2.229	0.167	1.661	9.924
49.00	2.264	0.175	1.646	9.355
50.00	2.298	0.183	1.631	8.905
51.00	2.331	0.189	1.617	8.549
52.00	2.364	0.193	1.602	8.271
53.00	2.396	0.197	1.587	8.059
54.00	2.427	0.198	1.572	7.906
55.00	2.457	0.199	1.556	7.807

Table I.16 MS-P predictions for the three unequal rods symmetrically arranged ($R_1/R_2 = 2$) containing a *type D* TM.

Half Angle ϕ (deg)	Outer Rod spacing L_2 (rod units)	Effective Area A_{eff} (rod units)	Effective Perimeter P_{eff} (rod units)	Curvature C_{MS-P}
41.81	2.000	0.091	2.155	23.529
42.00	2.007	0.095	2.121	22.162
43.00	2.046	0.115	1.950	16.936
44.00	2.084	0.131	1.793	13.672
45.00	2.121	0.143	1.645	11.446
46.00	2.158	0.153	1.505	9.836
47.00	2.194	0.158	1.369	8.618
48.00	2.229	0.161	1.238	7.667
49.00	2.264	0.160	1.111	6.904
50.00	2.298	0.157	0.987	6.281
51.00	2.331	0.150	0.865	5.761
52.00	2.364	0.140	0.746	5.322
53.00	2.396	0.127	0.629	4.946
54.00	2.427	0.111	0.514	4.622
55.00	2.457	0.092	0.400	4.339

Table I.17 MS-P predictions for the three unequal rods symmetrically arranged ($R_1/R_2 = 2$) containing a *type F* TM.

Half Angle ϕ (deg)	Outer Rod spacing L_2 (rod units)	Effective Area A_{eff} (rod units)	Effective Perimeter P_{eff} (rod units)	Curvature C_{MS-P}
90.00	3.000	0.484	2.630	5.434
91.00	3.000	0.470	2.621	5.568
92.00	2.998	0.457	2.612	5.715
93.00	2.996	0.443	2.603	5.875
94.00	2.993	0.428	2.593	6.050
95.00	2.989	0.413	2.584	6.242
96.00	2.984	0.399	2.575	6.453
97.00	2.978	0.383	2.566	6.684
98.00	2.971	0.368	2.557	6.939
99.00	2.963	0.319	2.296	7.198
100.00	2.954	0.289	2.158	7.450
101.00	2.945	0.266	2.053	7.703
102.00	2.934	0.246	1.963	7.959
103.00	2.923	0.229	1.885	8.223
104.00	2.911	0.213	1.814	8.491
105.00	2.898	0.199	1.748	8.767
106.00	2.884	0.186	1.687	9.051
107.00	2.869	0.174	1.629	9.345
108.00	2.853	0.163	1.575	9.647
109.00	2.837	0.152	1.523	9.961
109.47	2.828	0.148	1.500	10.112

Table I.18 MS-P predictions for the three unequal rods symmetrically arranged ($R_1/R_2 = 2$) containing a type G TM.

Half Angle ϕ (deg)	Outer Rod spacing L_2 (rod units)	Effective Area A_{eff} (rod units)	Effective Perimeter P_{eff} (rod units)	Curvature C_{MS-P}
102.00	2.934	0.125	0.724	5.758
102.05	2.929	0.111	0.700	6.307
103.00	2.923	0.097	0.675	6.949
103.05	2.917	0.084	0.649	7.708
104.00	2.911	0.072	0.621	8.617
104.05	2.904	0.060	0.591	9.721
105.00	2.898	0.050	0.560	11.091
105.05	2.891	0.041	0.526	12.929
106.00	2.884	0.032	0.489	15.103
106.05	2.876	0.024	0.449	18.186
107.00	2.869	0.017	0.405	22.589
107.05	2.861	0.012	0.357	29.351
108.00	2.853	0.007	0.301	40.937
108.05	2.845	0.003	0.235	65.035
109.00	2.837	0.001	0.151	142.743
109.47	2.828	0.000	0.076	$\approx \infty$

I.2.4 Three Unequal rods and a plate, non-symmetrical - $R_1 = R_2 = 2R_3$

Table I.19 MS-P predictions for the three unequal rods non-symmetrically arranged ($R_1/R_3 = 2$) containing a type E TM.

Half Angle ϕ (deg)	Outer Rod spacing L_2 (rod units)	Effective Area A_{eff} (rod units)	Effective Perimeter P_{eff} (rod units)	Curvature C_{MS-P}
min				
24.09	1.414	0.252	3.599	14.271
24.50	1.437	0.271	3.554	13.108
26.00	1.519	0.338	3.428	10.125
27.50	1.600	0.403	3.348	8.301
29.00	1.679	0.465	3.301	7.089
30.50	1.758	0.525	3.279	6.238
32.00	1.836	0.583	3.277	5.617
33.50	1.912	0.638	3.291	5.151
35.00	1.987	0.691	3.317	4.795
36.50	2.061	0.742	3.353	4.519
38.00	2.133	0.789	3.398	4.303
39.50	2.203	0.834	3.450	4.136
41.00	2.273	0.875	3.508	4.006
42.50	2.340	0.913	3.571	3.908
44.00	2.406	0.948	3.639	3.835
45.50	2.471	0.979	3.709	3.786
47.00	2.533	1.006	3.783	3.757
48.50	2.594	1.030	3.860	3.746
50.00	2.654	1.049	3.939	3.752
51.50	2.711	1.065	4.021	3.775
53.00	2.767	1.076	4.104	3.813
54.50	2.820	1.083	4.189	3.866
56.00	2.872	1.086	4.276	3.936
57.50	2.922	1.084	4.365	4.024
59.00	2.969	1.079	4.456	4.128
60.50	3.015	1.069	4.548	4.253
62.00	3.059	1.055	4.642	4.399
63.50	3.100	1.036	4.739	4.570
65.00	3.140	1.014	4.837	4.768
66.50	3.177	0.987	4.938	4.999
68.00	3.212	0.957	5.042	5.266
69.50	3.245	0.922	5.149	5.579
71.00	3.275	0.884	5.259	5.947
72.50	3.304	0.842	5.374	6.381
74.00	3.330	0.796	5.493	6.900
75.50	3.354	0.746	5.618	7.525
77.00	3.375	0.693	5.750	8.293
78.50	3.395	0.636	5.890	9.250
80.00	3.411	0.576	5.040	10.472
80.26	3.414	0.566	5.067	10.718
max				

Table I.20 MS-P predictions for the three unequal rods non-symmetrically arranged ($R_1/R_3 = 2$) containing a *type F* TM between R_1 and R_2 .

F1

Half Angle ϕ (deg)	Outer Rod spacing L_2 (rod units)	Effective Area A_{eff} (rod units)	Effective Perimeter P_{eff} (rod units)	Curvature C_{MS-P}
65.00	3.140	0.750	3.672	4.895
66.00	3.165	0.697	3.507	5.028
67.00	3.189	0.631	3.253	5.155
68.00	3.212	0.587	3.099	5.280
69.00	3.234	0.550	2.977	5.404
70.00	3.255	0.519	2.873	5.530
71.00	3.275	0.491	2.780	5.658
72.00	3.295	0.465	2.695	5.788
73.00	3.313	0.442	2.617	5.920
74.00	3.330	0.420	2.544	6.055
75.00	3.346	0.399	2.475	6.191
76.00	3.361	0.380	2.411	6.333
77.00	3.375	0.362	2.349	6.477
78.00	3.388	0.345	2.289	6.623
79.00	3.400	0.329	2.233	6.774
80.00	3.411	0.314	2.178	6.927
80.26	3.414	0.310	2.164	6.970

Table I.21 MS-P predictions for the three unequal rods non-symmetrically arranged ($R_1/R_3 = 2$) containing a *type F* TM between R_2 and R_3 .

F2

Half Angle ϕ (deg)	Outer Rod spacing L_2 (rod units)	Effective Area A_{eff} (rod units)	Effective Perimeter P_{eff} (rod units)	Curvature C_{MS-P}
65.00	3.140	0.391	2.426	6.191
66.00	3.165	0.386	2.453	6.347
67.00	3.189	0.380	2.480	6.526
68.00	3.212	0.372	2.505	6.732
69.00	3.234	0.363	2.531	6.969
70.00	3.255	0.353	2.555	7.239
71.00	3.275	0.316	2.389	7.541
72.00	3.295	0.276	2.162	7.824
73.00	3.313	0.250	2.025	8.096
74.00	3.330	0.229	1.920	8.367
75.00	3.346	0.212	1.831	8.638
76.00	3.361	0.196	1.754	8.910
77.00	3.375	0.183	1.686	9.186
78.00	3.388	0.171	1.623	9.465
79.00	3.400	0.160	1.566	9.748
80.00	3.411	0.150	1.513	10.036
80.26	3.414	0.140	1.500	10.112

Table I.22 MS-P predictions for the three unequal rods non-symmetrically arranged ($R_1/R_3 = 2$) containing a *type G* TM.

Half Angle ϕ (deg)	Outer Rod spacing L_2 (rod units)	Effective Area A_{eff} (rod units)	Effective Perimeter P_{eff} (rod units)	Curvature C_{MS-P}
70.00	3.255	0.315	1.274	4.044
71.00	3.275	0.264	1.212	4.578
72.00	3.295	0.218	1.146	5.250
73.00	3.313	0.175	1.073	6.120
74.00	3.330	0.136	0.994	7.287
75.00	3.346	0.101	0.906	8.929
76.00	3.361	0.071	0.808	11.384
77.00	3.375	0.045	0.696	15.428
78.00	3.388	0.024	0.564	23.230
79.00	3.400	0.009	0.399	44.006

Table I.23 MS-P predictions for the three unequal rods non-symmetrically arranged ($R_1/R_3 = 2$) containing a *type H* TM between R_2 and R_3 .

Half Angle ϕ (deg)	Outer Rod spacing L_2 (rod units)	Effective Area A_{eff} (rod units)	Effective Perimeter P_{eff} (rod units)	Curvature C_{MS-P}
65.00	3.140	0.358	1.605	4.475
66.00	3.165	0.366	1.723	4.706
67.00	3.189	0.371	1.840	4.961
68.00	3.212	0.373	1.958	5.247
69.00	3.234	0.372	2.075	5.566
70.00	3.255	0.370	2.193	5.927
71.00	3.275	0.364	2.311	6.337
72.00	3.295	0.357	2.430	6.806
73.00	3.313	0.346	2.549	7.349
74.00	3.330	0.334	2.669	7.983
75.00	3.346	0.319	2.791	8.733
76.00	3.361	0.302	2.914	9.634
77.00	3.375	0.283	3.040	10.732
78.00	3.388	0.261	3.168	12.105
79.00	3.400	0.238	3.300	13.862
80.00	3.411	0.212	3.436	16.186
80.26	3.414	0.205	3.472	16.920

I.3 EXPERIMENTAL RESULTS

Table I.24. Experimental results for the three equal rods and plate system.

Half Angle ϕ (deg)	Standard radius R_s (mm)	Test radii R_t (mm)	Standard rise $\Delta h_{s,c}$ (mm)	Test rise $\Delta h_{t,c}$ (mm)	Expt. curvature C_{exp}	MS-P curvature C_{MS-P}	% dev. (%)
31.01	0.800	1.582	23.11	11.03	6.548	6.577	-0.4
31.62	0.800	1.189	24.11	14.87	6.363	6.352	+0.2
33.40	0.800	1.148	24.30	14.17	5.804	5.761	+0.7
				18.51	7.581	7.479	+1.4
34.54	0.800	1.496	24.08	10.20	5.494	5.434	+1.1
				11.56	6.226	6.270	-0.7
35.66	0.800	1.470	24.12	9.70	5.125	5.114	+0.2
37.93	0.800	1.190	23.18	9.94	4.424	4.440	-0.4
40.16	0.800	1.396	24.24	7.97	3.974	3.961	+0.5
40.91	0.800	1.386	24.21	7.82	3.880	3.830	+1.2
43.10	0.800	1.347	23.99	7.26	3.534	3.533	+0.0
51.88	0.800	1.243	24.10	6.60	2.951	2.990	-1.3
56.96	0.800	1.197	24.03	6.91	2.984	2.950	+1.1
62.82	0.800	1.148	23.83	7.27	3.033	3.070	-1.2
70.76	0.800	1.100	23.87	8.86	3.540	3.540	-0.0
72.58	1.583	1.586	12.29	6.59	3.728	3.713	+0.4
74.63	0.800	1.190	24.13	9.28	3.967	3.950	+0.5
77.79	1.583	1.586	12.32	7.83	4.419	4.411	+0.2
78.36	0.800	1.190	24.71	10.73	4.480	4.510	-0.7
79.71	1.583	1.586	12.27	8.54	4.839	4.780	+1.2
83.28	1.583	1.587	12.29	9.93	5.618	5.690	-1.2
83.52	1.583	1.586	12.16	10.01	5.724	5.770	-0.8
83.84	1.583	1.587	12.22	10.30	5.861	5.873	-0.2
84.07	1.583	1.587	12.24	10.42	5.919	5.918	+0.0
85.22	1.583	1.587	12.21	10.74	6.116	6.112	+0.0
				15.15	8.581	7.926	+8.3
85.87	1.583	1.587	12.29	11.06	6.257	6.223	+0.5
				17.22	9.742	9.415	+3.3
86.79	1.583	1.587	12.19	11.16	6.369	6.383	-0.2
				22.68	12.937	12.661	+2.1
86.83	1.583	1.587	12.25	11.25	6.386	6.390	-0.1
87.02	1.583	1.587	12.28	11.27	6.385	6.420	-0.5
87.80	1.583	1.587	12.18	11.43	6.529	6.563	-0.5
90.00	1.583	1.587	12.17	12.18	6.598	6.970	-0.2

$$C_{exp} = 6.94 \Delta h_{s,c} R_t / \Delta h_{t,c} R_s \text{ where } \Delta h_{s,c} = \Delta h_s + 0.5$$

Table I.25 Experimental results for three unequal rods symmetrically arranged against a plate with $R_1/R_2 = 0.5$.

Half Angle ϕ (deg)	Standard radius R_s (mm)	Test radii R_t (mm)	Radius ratio R_1/R_2	Standard rise $\Delta h_{s,c}$ (mm)	Test rise $\Delta h_{t,c}$ (mm)	Expt. curvature C_{exp}	MS-P curvature C_{MS-P}	% dev. (%)
22.51	0.800	1.129	0.502	24.17	13.16	5.330	5.285	+0.8
25.90	0.800	1.046	0.499	24.02	9.97	3.766	3.735	+0.8
28.07	0.800	0.997	0.500	24.03	8.87	3.192	3.225	-1.0
31.28	0.800	1.251	0.497	23.98	6.13	2.772	2.786	-0.5
34.14	0.800	1.186	0.498	24.06	5.95	2.546	2.572	-1.0
37.04	0.800	1.128	0.501	24.05	5.98	2.435	2.454	-0.8
42.62	0.800	1.044	0.498	24.22	6.44	2.399	2.406	-0.3
45.14	0.800	0.996	0.500	24.22	6.96	2.481	2.442	+1.6
47.31	0.800	0.983	0.498	23.92	6.96	2.480	2.502	-0.9
57.56	0.800	0.889	0.500	24.20	10.00	3.184	3.197	-0.4
60.65	1.583	0.789	0.500	12.22	12.89	3.651	3.616	+0.1
61.57	1.583	0.789	0.500	12.27	13.24	3.750		
62.19	1.583	0.789	0.500	12.21	13.25	3.768	3.767	+0.0
62.53	1.583	0.789	0.500	12.20	13.62	3.868		
63.20	0.800	0.657	0.499	23.98	13.72	3.889	3.888	+0.0
63.64	1.583	0.789	0.500	12.27	14.19	4.022		
64.19	1.583	0.789	0.500	12.26	13.99	3.969	3.915	+1.4
64.60	1.583	0.789	0.500	12.24	14.42	4.091		
65.28	1.583	0.789	0.500	12.27	17.22	4.090	4.092	-0.0
66.82	1.583	0.789	0.500	12.24	14.84	4.186	4.195	-0.2
69.14	1.583	0.789	0.500	12.28	15.67	4.420		
70.14	1.583	0.789	0.500	12.23	15.47	4.367	4.323	+1.0
					16.79	4.740		
					17.08	4.823	4.351	+0.3
					15.69	4.426	4.723	+2.2
					19.67	5.549	4.429	-0.1
					16.48	4.660	5.436	+2.0
					28.72	8.116	4.609	+1.1
					17.27	4.868	8.066	+0.6
					17.98	5.060	4.885	-0.3
							5.014	+0.9

$C_{exp} = 6.94 \Delta h_{s,c} R_1 / \Delta h_{t,c} R_s$, where $\Delta h_{s,c} = \Delta h_s + 0.5$

Table I.26 Experimental results for three unequal rods symmetrically arranged against a plate with $R_1/R_2 = 2.0$ and $R_1/R_3 = 1.0$.

Half Angle φ (deg)	Standard radius R_s (mm)	Test radii R_t (mm)	Radius ratio R_1/R_2	Standard rise $\Delta h_{s,c}$ (mm)	Test rise $\Delta h_{t,c}$ (mm)	Expt. curvature C_{exp}	MS-P curvature C_{MS-P}	% dev. (%)
49.80	0.800	1.183	1.998	24.39	12.47	5.244	5.308	-1.2
51.60	0.800	1.183	1.998	24.33	12.16	5.126	5.027	+1.9
52.51	0.800	1.183	1.998	24.37	11.59	4.878	4.893	-0.3
56.87	0.800	1.183	1.998	24.33	10.08	4.249	4.295	-1.0
60.09	0.800	1.183	1.998	24.27	9.57	4.044	4.007	+0.9
60.84	0.800	1.183	1.998	24.40	9.47	3.981	3.958	+0.5
62.22	0.800	1.183	1.998	24.26	9.23	3.902	3.877	+0.6
64.76	0.800	1.183	1.998	24.37	8.98	3.779	3.767	+0.3
70.38	0.800	1.183	1.998	24.28	8.65	3.654	3.675	-0.6
70.63	0.800	1.183	1.998	24.29	8.74	3.690	3.675	+0.4
73.85	0.800	1.183	1.998	24.27	8.73	3.689	3.702	-0.4
78.90	0.800	1.183	1.998	24.33	9.09	3.832	3.855	-0.6

$$C_{exp} = 6.94\Delta h_{s,c} R_t / \Delta h_{t,c} R_s \text{ where } \Delta h_{s,c} = \Delta h_s + 0.5$$

Table I.27 Experimental results for three unequal rods non-symmetrically arranged against a plate with $R_1/R_2 = 1.0$ and $R_1/R_3 = 2.0$.

Half Angle φ (deg)	Standard radius R_s (mm)	Test radii R_t (mm)	Radius ratio R_1/R_3	Standard rise $\Delta h_{s,c}$ (mm)	Test rise $\Delta h_{t,c}$ (mm)	Expt. curvature C_{exp}	MS-P curvature C_{MS-P}	% dev. (%)
46.44	1.188	1.588	1.994	16.42	6.64	3.748	3.768	-0.5
47.07	1.188	1.580	2.000	16.40	6.62	3.725	3.756	-0.8
51.90	1.188	2.247	1.996	16.35	4.64	3.725	3.785	-1.6
57.21	1.188	1.795	2.002	16.57	6.27	3.967	3.978	-0.3
60.83	1.188	2.094	2.000	16.50	5.67	4.203	4.285	-1.9
63.75	1.188	1.587	1.994	16.37	8.14	4.609	4.603	+0.1
66.54	1.188	1.587	1.994	16.54	8.87	4.971	5.006	-0.7
69.19	1.188	1.587	1.994	16.47	9.63	5.420	5.428	-0.2
70.25	1.188	1.587	1.994	16.45	9.86	5.556 ^{-F₁}	5.562	-0.1
					10.81	6.080 ^{-H₂}	6.029	+0.8
71.24	1.188	1.587	1.994	16.40	10.05	5.680 ^{-F₁}	5.689	-0.2
					11.52	6.511 ^{-H₂}	6.450	+0.9
72.38	1.188	1.587	1.994	16.55	10.36	5.802 ^{-F₁}	5.838	-0.6
					12.76	7.147 ^{-H₂}	7.012	+1.9
74.14	1.188	1.587	1.994	16.48	10.74	6.041 ^{-F₁}	6.074	-0.6
					14.48	8.144 ^{-H₂}	8.088	+0.7
75.56	1.188	1.587	1.994	16.53	11.12	6.236 ^{-F₁}	6.271	-0.6
					15.72	8.815 ^{-F₂}	8.790	+0.3
					19.49	10.929 ^{-C}	10.304	+5.7
77.08	1.188	1.587	1.994	16.57	11.61	6.489 ^{-F₁}	6.489	-0.0
					16.52	9.234 ^{-F₂}	9.208	+0.3
78.21	1.188	1.587	1.994	16.49	11.80	6.628 ^{-F₁}	6.655	-0.4
					17.02	9.559 ^{-F₂}	9.524	+0.4
80.32 (max)	1.188	1.587	1.994	16.45	12.41	6.969 ^{-F₁}	6.969	-0.0
					18.04	10.130 ^{-F₂}	10.112	+0.2

$$C_{exp} = 6.94\Delta h_{s,c} R_t / \Delta h_{t,c} R_s \text{ where } \Delta h_{s,c} = \Delta h_s + 0.5$$

